CYRIC

ANNUAL REPORT

1998

(January 1998 - December 1998)

CYCLOTRON AND RADIOISOTOPE CENTER
TOHOKU UNIVERSITY

ТРАВЫ ДАГЕСТАНА

ТОМ I

PREFACE

In this nineteenth issue of the CYRIC Annual Report, we summarize the activities for research and development and results of training for radioisotope safe-treatment at Cyclotron and Radioisotope Center, Tohoku University during the calendar year 1998.

The year 1998 was special one which we have so far passed through in CYRIC. As mentioned in the last issue of CYRIC Annual Report 1997, the budget to replace the old K=50 MeV AVF cyclotron with a K=130 MeV AVF cyclotron was authorized by Japanese government in the 1998 school year. On April 9, 1998, the last acceleration by the 680-AVF cyclotron finished. The shut-down ceremony was held in the cyclotron vault. A photograph illustrated in the back-page shows its climax event. Every body was full in appreciation to steady work of the cyclotron up to almost 80,000 hours, and made an offering of bottles of Japanese Sake for the cyclotron.

Then, removal of the old cyclotron was a big operation. The time available was limited to the end of December 1997, to keep a new place for coming installation of the K=130 MeV cyclotron. After clean up, some improvements of the cyclotron vault were needed for the larger scale new cyclotron. Waste included, of course, was radioactive. Works were supervised by the stuff members of Division of Radiation Control of CYRIC under the guidance of the related regulation laws. We are deeply indebted as well to Facilities Department of Tohoku University Administration Bureau and Japan Radiation Protection Co., ltd.

In the case of the renewal of the main facilities of an institute, it is of importance to keep activities as much as possible in various research fields even in the years-long construction period. Fortunately, studies with PIXE technique have been continuously carried out by using electrostatic accelerator, installed at FNL (Fast Neutron Laboratory) in Graduate School of Technology, Tohoku University, under the scientific tie-up between CYRIC and FNL. Indeed, more than six groups are running under this project using a total of its 250 hours beam-time. The other good news was installation of the small size AVF cyclotron HM-12 requested by Institute of Development, Aging and Cancer (IDAC), Tohoku University under scientific and technical tie-up among IDAC, CYRIC and Sumitomo Heavy Industry Co., ltd. After a half year shut-down, some clinical-works with short-lived positron emitters and PET scanner have already restarted at the end of November.

During 1998 school year, 553 of staff members and students of Tohoku University were trained at this Center in the beginner's course of safe handling of radiation and radioisotopes, while 213 staff members and students in the "x-ray course". In addition, 87

of staff members and students were trained in the course of safe handling of radiation from a SOR (Synchrotron Orbital Radiation).

It is our great pleasure to inform that the budget is going to be authorized for facilities to construct the new water-cooling system for the power-upped accelerator and improved beam-transport system equipped with higher K-number electromagnets. Also authorized are high-intensity negative ion-source together with ECR heavy-ion source. Related experimental facilities such as neutron time of flight analyzing system including the beam swinger, automated synthesis system for short-lived positron emitter labeled compounds, on-line electromagnetic mass separator, high-energy γ-ray detector, and neutron-induced reaction-product analyzing system are altogether included in the same category of this budget. In addition, construction of thermal and epi-thermal neutron sources is planned. Brief introduction for these projects is given in this issue.

We are very grateful to Tohoku University and to the Ministry of Education, Science, Sports and Culture for their continuous support.

January 1, 1999

Hikonojo ORIHARA

Director

Cyclotron and Radioisotope Center, Tohoku University

Photograph illustrates the climax event of the shut-down ceremony for 680-cyclotron on April 9, 1998.

EDITORS:

Hikonojo ORIHARA
Manabu FUJIOKA
Tatsuo IDO
Takashi NAKAMURA
Masatoshi ITOH

WORD PROCESSED BY

Yu-ko YAMASHITA

CONTENTS

IV. MEDICINE AND BIOLOGY (Basic)

V. MEDICINE AND BIOLOGY (Clinical)

VI. RADIATION PROTECTION AND TRAINING OF SAFE HANDLING

VII. PUBLICATION

VIII. MEMBERS OF COMMITTEE

IX. PERSONNEL

I. Project for Heavy Charged-particle Beam Multi-purpose Use

Orihara H.

Cyclotron and Radioisotope Center, Tohoku University (http://www.cyric.tohoku.ac.jp)

A brief summary is given for the results of multi-purpose use of a cyclotron and RI in past two decades. This report presents as well a preliminary planning of further development by introducing the facilities, being under construction or consideration, and scientific motivations.

CYRIC (Cyclotron and Radioisotope Center) was established in 1977 as an institution for carrying out research studies in various fields by the use of a cyclotron and radioisotopes, and also for training researchers of Tohoku University for safe treatment of radioisotopes and radiation. The CYRIC cyclotron is a variable energy AVF machine with a K value of 50 MeV; being capable of acceleration protons up to 40 MeV, deuterons to 25 MeV, α-particles to 50 MeV, and He-3 particles to 65 MeV.

During the past two decades, refereed 501-papers written in English have been published in scientific journals in the world. Ninety-six dissertations for D.Sc.(37), D.M.(38), D.Eng.(11), D.Agr.(6), Pharm.D.(2), etc. have been accepted based on the research in CYRIC, while 154-thesises for master's degree have been presented.

Based on the successful results of the 20 years-long multi-purpose use of Cyclotron and Radioisotopes, replacement of the present cyclotron with a larger dimension K=130 MeV one, and construction of experimental facilities have been authorized by Japanese government in 1998 and 1999 financial years.

Since 1979, we have an apparatus for fast neutron time-of-flight analysis equipped with a 40m long flight path, an electromagnetic isotope separator (EMIS) for on-line and off-line uses, and an x ray detection system for atomic physics and for element analysis by PIXE method. Fully automated positron emitter labeled compound synthesis systems is installed for the studies of biology and medicine. A positron tomograph ECAT-II was installed in 1981. Another four-rings PET(PT931) and TOF type PET (PT711) scanners were installed in 1986 and 1987, respectively. Since 1983 school year, these scanners have been extensively used for clinical researches; for cancer diagnosis and for brain researches, etc., supported by steady operation of the cyclotron, and by reliable supply of short-lived positron emitter labeled compounds. Recently, a system of the high-resolution positron-emission tomograph SET 2400W-S has been installed.

With fast neutron time of flight measurement, we have explored isospin- and spin-isospin excitation in nuclei by (p,n) charge-exchange reactions at 35 MeV. Our interests have been focused on: (1) Isospin mixing effect in the width of IAS, (2) 0^+ to 1^+ Gamow-Teller type transition, (3) Stretched particle-hole excitation, and (4) 0^+ to 0^- or $\Delta J^\pi = 0^-$ pion-like transition. These works have established a research field of spin-isospin excitation of nuclei in low energy (p,n) reaction. In addition, spectroscopic works by the (d,n) reaction have been carried out to investigate single particle nature of nuclei. Atomic and molecular physics with charged particles from an AVF cyclotron started at CYRIC exploring inner-shell ionization mechanism, results have been and extended over applications with the particle induced x-ray emission (PIXE) method for element analysis.

Researches using an EMIS equipped with a tape-transport and an ion-guide systems are: (1) Discovery of the heaviest two "mirror-decay" nuclei, ^{57}Cu and ^{59}Zn.(2) Implantation of radioactive isotopes to make good-quality samples for precision measurement of conversion-electrons up to the atomic valence shells to derive the Mössbauer isomer-shift scales $\Delta R/R$. Researches in the field of nuclear spectroscopy, using perturbed angular correlation (PAC) and perturbed angular distribution (PAD) methods with a magnet, are measurement of fifteen samples of magnetic-moments of nuclear isomeric-states. In a field of solid-state physics, PAC measurements, after EMIS for acceleration of RI, have been carried out to examine the orientation and magnitude of the electric field gradient created by a vacancy at RI-probe impact. Efforts to accelerate light heavy-ion has been continued for further application to scattering experiments. Heavy ions of ^{12,13}C, ^{15}N and ^{16}O were extracted successfully, and used for elastic scattering on ^{28}Si at small angles in order to obtain total reaction cross-sections model independently.

Using 36-MeV α-particles with an energy degrader system to obtain an uniform depth distribution in the specimen, He implantation effects on mechanical properties of a number of composites have been studied to apply these composites on structural materials of a fusion reactor. As a new type of isotope effect in metal acetylacetonates, time-dependent isotope effect in recoil implantation was studied, and it was found that the decay products ^{99m}Tc and ^{96}Tc tended to form pertechnetate in comparison with the direct nuclear reaction product ^{95}Tc, by water soluble species of Tc nuclides produced by the (d,xn) reaction on Mo. Further recent topics in RI-production with 12-MeV protons and 16-MeV deuterons is insertion of radioactive atoms in C_{60} and C_{70} fullerenes. Such endohedral fullerenes ^{7}Be@C_{60}, ^{127}Xe@$C_{60,70}$ and ^{79}Kr @$C_{60,70}$ and their dimers were detected.

With the neutron facilities in CYRIC, neutron dosimetry and monitoring were studied, and activation and spallation cross-sections have been measured. Also investigated were neutron absorption and leakage for purposes of radiation shielding. By combination with clinical PET studies, absorbed dose in humans due to intravenous administration of positron emission radiopharmaceuticals were measured.

One of major programs has been instrumental development of positron emission tomograph and automated labeling system of radiopharmaceuticals with cyclotron-produced positron emitters for nuclear medicine as listed in the following Table.

Nuclide	Radiopharmaceuticals	Imaging Target
C-11	[^{11}C]Methionine	Tumor
	[^{11}C]Doxepin	Histamine H_1 receptor
	[^{11}C]Nemonapride(YMO9] 51-2)	Dopamine D_2 receptor
	[^{11}C]Benztropin	Muscarinic acetylcholine receptor
F-18	[^{18}F]FDG	Energy metabolism in brain, heart and tumor
	[^{18}F]FDOPA	Presynaptic dopamine synthesis
	[^{18}F] Fluorodeoxyuridine	tumor
O-15	[^{15}O]Oxygen	Cerebral oxygen consumption
	[^{15}O]Carbon dioxide	Cerebral blood flow
	[^{15}O]Carbon monooxide	Cerebral blood volume
	[^{15}O]Water	Cerebral blood flow

These tracers have been successfully applied to several clinical researches including diagnosis of malignant neoplasms and neuro-pshyhiatrical diseases. The measurement of whole-body metabolism is an especially powerful technique not only for early and qualitative diagnosis (tissue characterization) of cancer but also for optimization of rational treatment and its evaluation. We were the one of the first research groups to have revealed neuronal receptor dysfunction in dementia of Alzheimer' s type. Research of central histamine H_1 receptors has been extensively investigated in our institute with collaboration of department of cellular pharmacology, school of medicine. Imaging analysis showed that H_1 receptors increased in the epileptic foci, which possibly reflects important role of histamine neurons in metabolic suppression of electrically over-discharge.

Development of a new PET with three-dimensional (3D) data acquisition and 3D-reconstruction capability was another success of our engineering group. 3D-reconstruction time was only 1 min for 63 sliced volume, which we believe a world record. Increase of sensitivity of this PET prompted us to apply this technique for sport science. Regional metabolic activation of muscles as well as in brain by physical exercise was successfully imaged.

We investigated the change of various neurotransmitter and receptors in the brain of several experimental models such as MPTP-induced Parkinsonian mice, 6-hydroxydopamine -treated rats, rats or gerbils subjected to cerebral ischemia and aged rats. Our results indicate that the dysfunction of neurotransmitter receptor systems plays a key role in the age-related neurodegenerative processes of several experimental animal models. Thus, these experimental study may provide an important information in age-related neurodegenerative diseases, such as Parkinson's and Alzheimer's disease.

1. AVF Cyclotron

Figure 1 illustrates a layout of the new AVF cyclotron and injection- and extraction-lines. Ion sources are located on the under ground level, then ions are injected upward into the central acceleration-region through an inflector. There are two modes of acceleration: one is positive-ion acceleration, being extracted at R=930 mm by a deflector, while negative ions are accelerated up to a radius of 680 mm corresponding to K = 50 MeV in magnetic rigidity, then stripped their electrons by a carbon foil, thus being extracted through the residual magnetic field as shown in the figure.

A negative ion source is located on the BF1 floor just below the accelerator. A conventional type Electron Cyclotron Resonance (ECR) source is installed in another room on the same BF1 floor, while a more high-power ECR course are under consideration. The conventional one is planned to be used for RI beam acceleration of light-heavy ion.

In the positive-ion's straight line through the first switching dipole-magnet, a beam-emittance measuring-port are equipped for tine tuning of the cyclotron to match acceptance of the beam transport system. One of the special features of our transport is beam time-sharing by a dipole-magnet with alternating current, by which a beam is injected into all beam courses available in a time interval of several seconds. Utilizing this equipment, a long-shift experiment and short-time radioisotope production may be possible simultaneously.

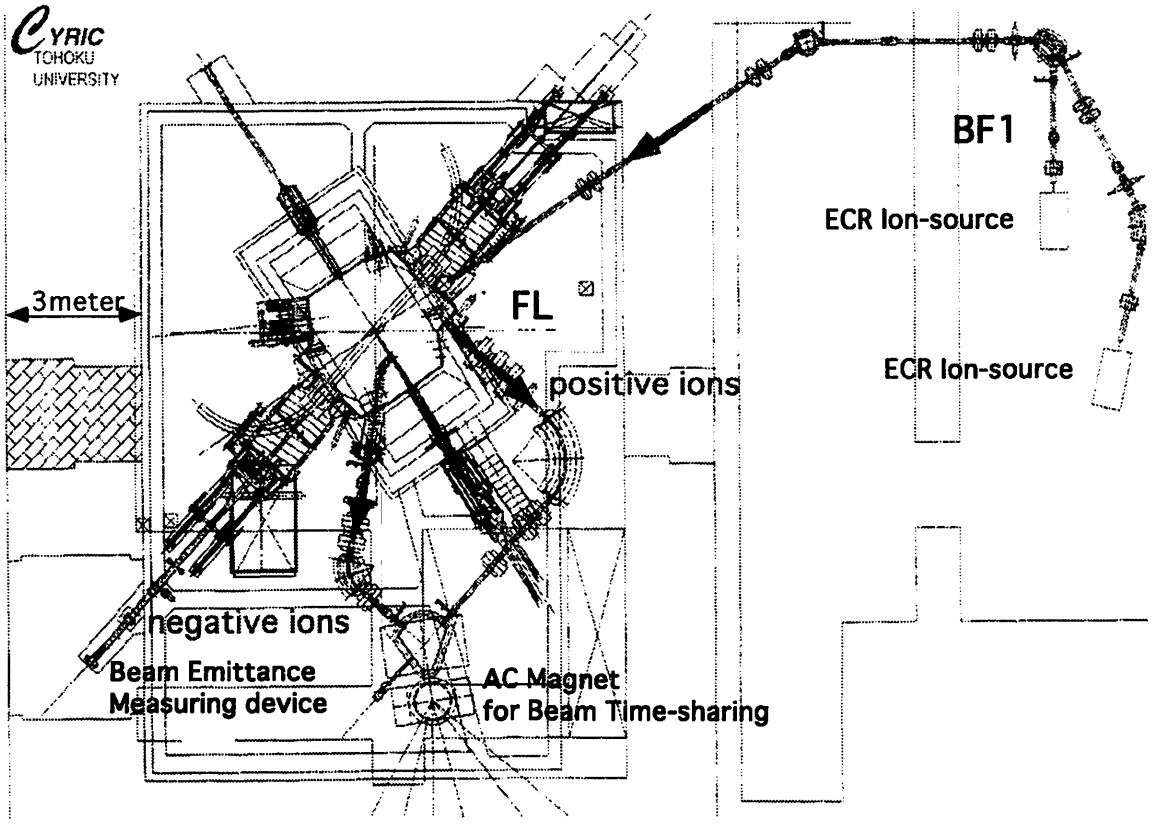

Fig 1. Layout of the new AVF cyclotron and injection- and extraction-lines.

Tables 1 and 2 list the specifications and beam characters of the new cyclotron.

Table 1. Specification of the new AVF cyclotron.

Electromagnet System		
	Weight	200 ton
	Extraction Radius	923 mm
	Number of Sector	4
	Max. Average Induction	19.6 kG (over Hill)
	Main Coil Power	230 kW
	Number of Trim Coil	12 pairs
Radio-Frequency System		
	Number of Dee's	2
	Frequency	11-22 MHz
	Max. Dee Voltage	50 kV
	Max. RF Power	70 kW x 2
External Ion Source		
	Negative ion	Cusp-type
	Positive ion	ECR, 10GHz
		ECR, 14GHz

Table 2. Beam energies of the new AVF cyclotron.

a) Positive ion acceleration.

Accelerated Particle	Energy (MeV)	Beam intensity(μA)
p	10-90	50
d	10-65	50
^{3}He	20-170	50
^{4}He	20-130	50
^{12}C	20-397	5p
^{14}N	20-463	5p
^{16}O	20-530	5p
^{20}Ne	20-662	5p
^{32}S	20-698	3p
^{40}Ar	20-744	3p
^{84}Kr	20-695	3p
^{129}Xe	20-748	1p

a) Negative ion acceleration.

Accelerated Particle	Energy (MeV)	Beam intensity(μA)
p	10-50	300
d	10-25	300

2. Beam Swinger and Large Solid-angle Neutron Detection System for Time-of-Flight Experiments

As one of the main facilities of the new System for Heavy Charged-particle Multi-purpose Use in CYRIC, construction the beam swinger, being capable for rotating the beam axis from -5deg. to 145deg. with K= 130 MeV, is under progress. The other new feature of this system is the neutron detector matrix, being located at a distance of 44 meter after the neutron flight path, and consisting of 32 pieces of the counter which contain 50 litter of liquid scintillater in its total volume.

This system may be a powerful tool to investigate isospin and spin-isospin excitation in nuclei through the (p,n) reaction in a wide range of incident proton energies. With energetic and high-intensity monochromatic neutron beams, neutron scattering experiments with high sensitivity provide a new field to explore charge-symmetry and charge-independent character of the nuclear forces, and to work with other engineering studies.

Figure 2 shows a lay out of the beam swinger and detector matrix.

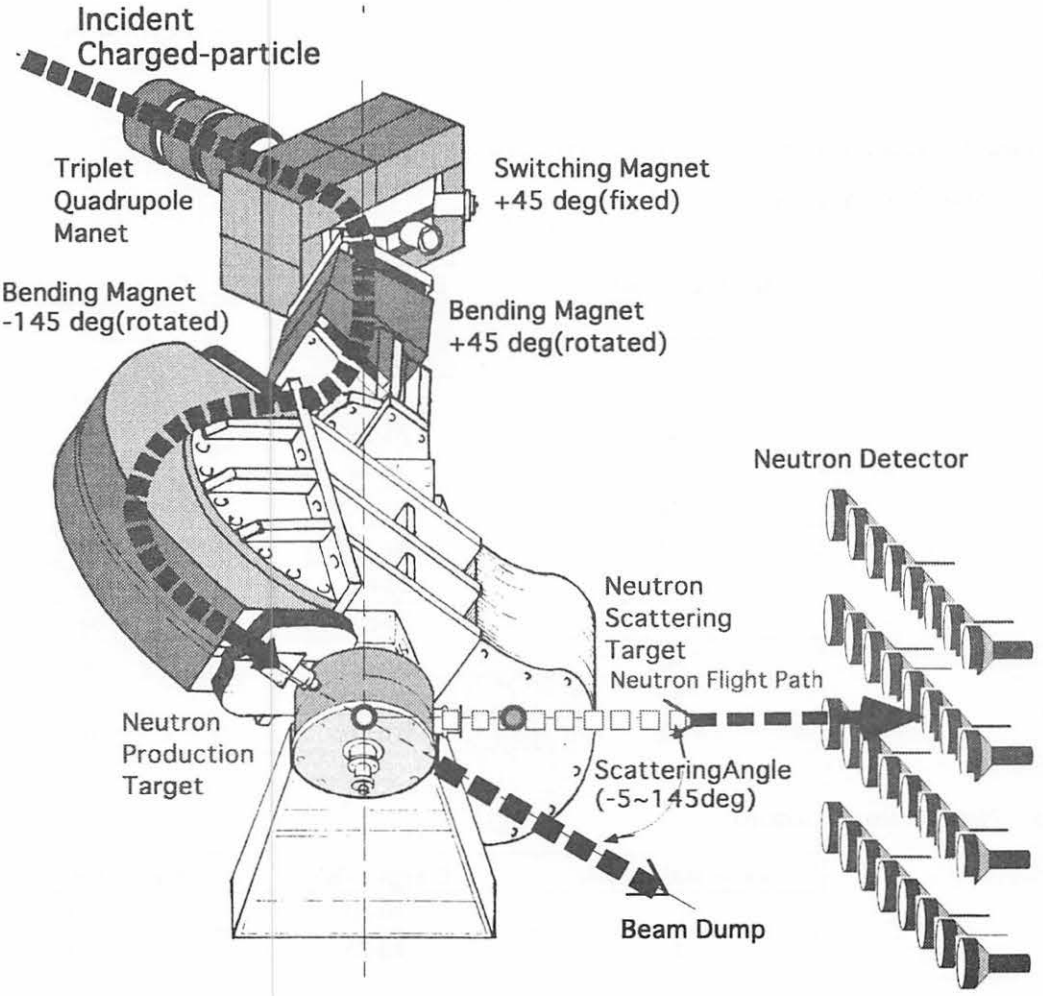

Fig. 2. Lay out of the beam swinger and detector matrix.

3. On-line Electric and Magnetic Isotope-separator

Study for unstable nuclei provide us with information of such nuclei that have decayed in the course of history of universe by producing them artificially with an accelerator or reactor. Energetic and high intensity charged-particle are considered to be the best candidate to explore such unstable nuclei far from the stability line. Many facilities in the world are oriented to the accelerated charged-particles, heavy-ions especially, for this purpose. On the other hand, production of unstable nuclei by neutrons may be more efficient, though it has been limited to a few cases with nuclear reactors due to the experimental difficulties to combine neutron beams with an on-line electromagnetic isotope separator.

The new cyclotron at CYRIC provide us with a sufficient high-intensity neutron beam to investigate unstable nuclei close to the neutron drip-line, together with the on-line electromagnetic isotope separator (EMIS) equipped with the ion-guide ion-source, and the high-speed tape-transport system. The additional powerful equipment is a high-resolution and large solid angle gamma ray detection system consisting of three pairs of four hold clover-type pure-Ge crystal, each of which is surrounded by 12 pieces of BGO Crystal. Figure 3 shows a layout of EMIS together with the new Ge-detector ball.

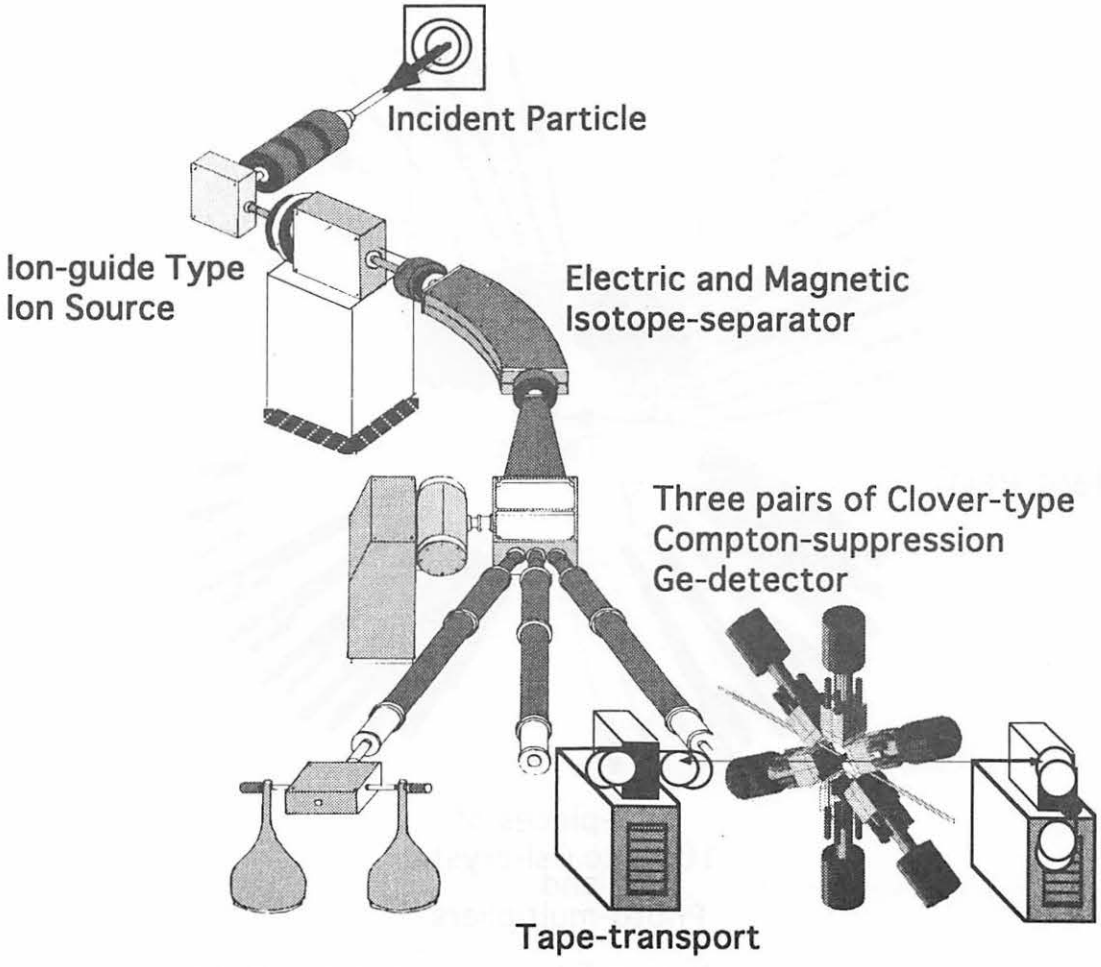

Fig. 3. Layout of EMIS, tape-transport and Ge-ball .

4. High-energy γ-ray Detection System

The system is capable for detecting and analyzing high-energy γ-rays, up to e. g. 500 MeV, and neutral mesons produced by nuclear reactions. It contains 148 pieces of CsI crystal, the volume of each detector being 1000 cm^3, and they are segmentaized into four blocks so as to cover a half π-radian in solid angle. The minimum internal radius is 55 cm. These four blocks are mounted on a stem, and each block is separately removable.

Equipped on a beam course of the K=130 MeV, AVF cyclotron facility of CYRIC, this system is applied for studies of high energy γ-rays production by energetic heavy ion impact up to the maximum energy kinetically allowed, and η- and π-mesons production energetically available. Thus, this system is expected to explore interesting phenomena of *coherent extreme* in nuclei. It should be noted that the beam transport system with time-sharing AC magnet is expected to work efficiently for such an experiment with quite rare events. Figure 4 shouws a schematic view of the CsI crystal high energy γ-ray detector.

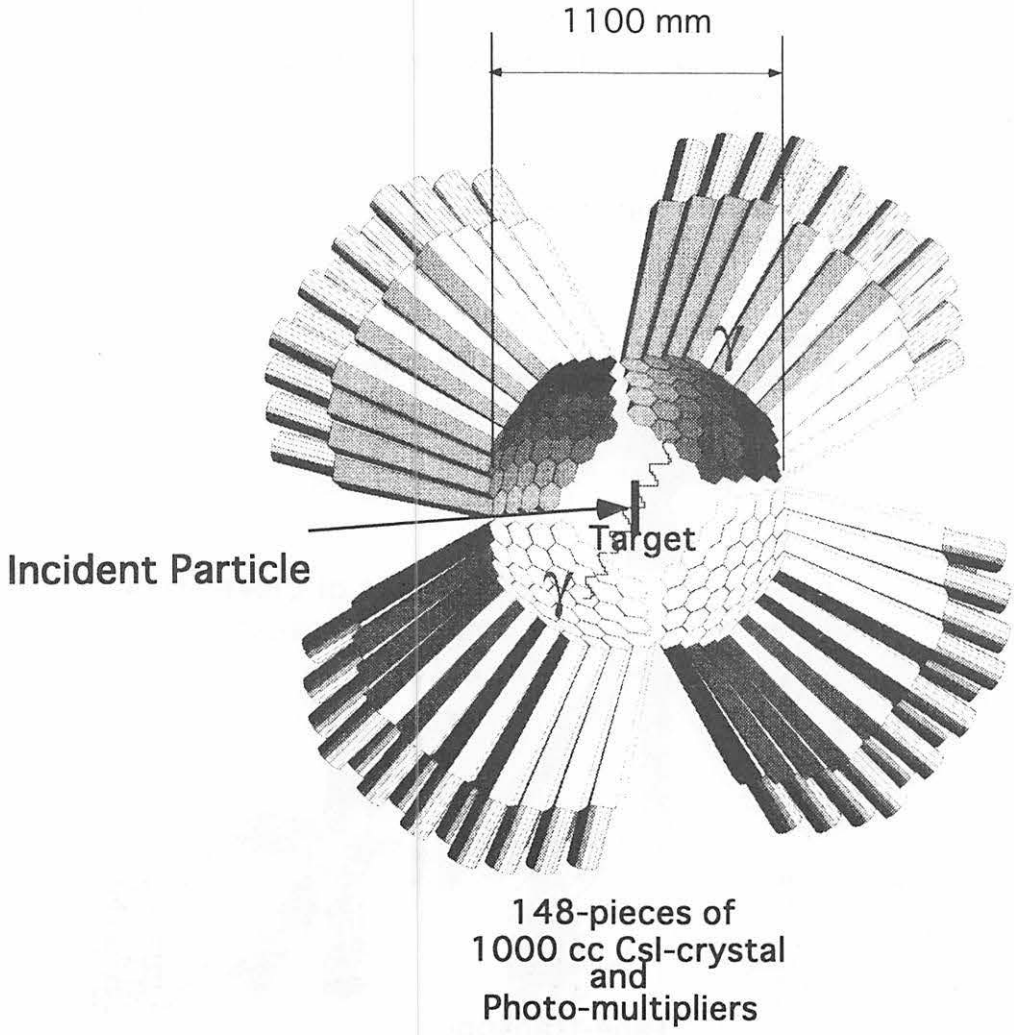

Fig. 4. Scematic view of the present CsI crystal high energy γ-ray detector.

5. Neutron-life and Neutron-induced Reaction Analyzing Facility

Energetic and high-intensity charged particle beam, negative ion beam in particular, provide as well high-intensity white and monochromatic neutron beam, thus enabling us to carried out a number of neutron induced experiments. The main part of the .spectrometer is the electromagnet which have been used as that of our old K=50 MeV, AVF cyclotron. Charged particles emitted from different points along with the plane perpendicular to the incident direction have a focal plane, where a detector array as calorie meter is located.

A challenging project with this large solid angle magnetic spectrometer and high-intensity monochromatic neutron beams is measurement of the life-time of neutrons in flight. Accurate and comprehensive neutron life-time data are of crucial importance for current science including astrophysics, cosmology, particle and nuclear physics, etc.

Monochromatic 30-MeV neutrons are produced, then they flight through the 20m-long evacuated tube, reaching to the spectrometer in an average flight-time of ~1 μsec. One neutron per hour may change to a proton. The neutron flight time, measured in a resolution of 10^{-3} is used to identify protons from neutron-decay. The most important point for this experiment is to measure the total amount of neutrons with sufficient accuracy as high as several 0. 1%. Figure 5 shows a cross-sectional layout of the facility.

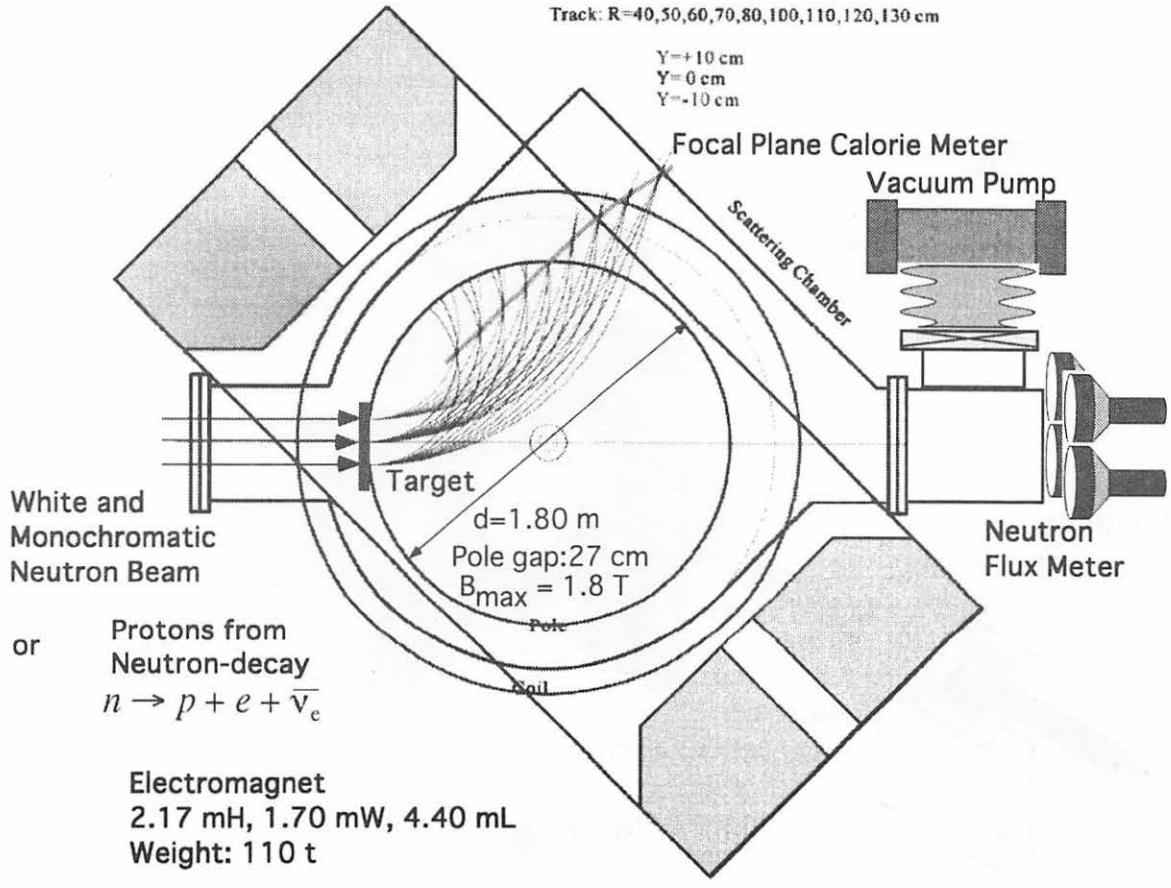

Fig. 5. Cross sectional view of magnetic spectrometer and neutron flux meter.

6. High Intensity Thermal and Epi-thermal Neutron Source

High intensity proton and deuteron beams by the negative ion acceleration mode provide a good place for production of thermal and epi-thermal neutrons. Recent development of high intensity charged-particle accelerator make it possible to use such a neutron beam with almost equivalent intensity as that by a nuclear reactor.

Figure 6 shows a target and moderator system to produce thermal and epi-thermal neutrons from high-energy neutrons by a configuration of Al/Pb, Iron, graphite, heavy-water, and Bi, etc. Of course, there should remain a lot of developing studies to thermalize several tenth MeV neutrons to thermal ones. Especially, minimization of high-energy neutron background is the most important point in these studies.

Utility of high-intensity thermal and epi-thermal neutrons may spread over many research fields, in which activation analysis combined with that by PIXE for medium and heavy elements, and radiography for light elements may be good candidates. Final goal of application of these neutrons is that for the study of Boron Neutron-capture Cancer Therapy (BNCT). Even limited to selective melanoma therapy, collaborations among physicists, pharmacologist, radiologist, and medical scientists are essential. This project is under consideration, being discussed in a working-group organized in CYRIC.

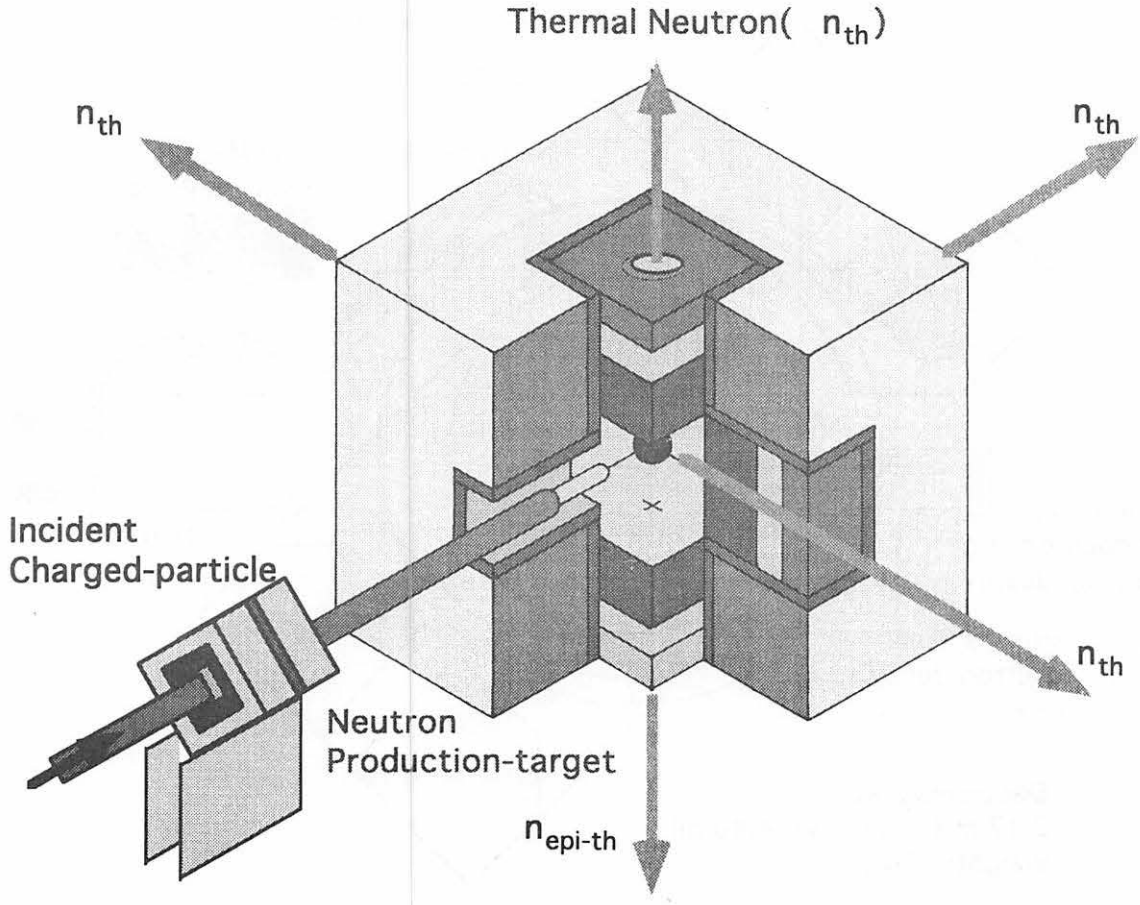

Fig. 6. Sketch of thermal and epi-thermal neutron source.

7. Medical Research by Simultaneous Synthesis of Multiple Radiotracer

Energetic beams may open a new field for production of radiotracers through, for example, (p,xn,yp) reactions on medium and heavy nuclei. With the additional small-size cyclotron already working, multiple production of radionuclides is possible.

Simultaneous measurement of cerebral blood flow gives an estimate of regional tracer delivery and thus improves accuracy of the receptor quantification. For quantitative assessment of neuronal transmitter and receptors, neuronal receptor quantification are made by ^{11}C-labeled receptor ligand and ^{15}O-labeled water are produced, respectively, by K=130 and K=120MeV cyclotrons. As such quantitative evaluation of clinical neuro-psychiatricaldiseases such as dementia, other degenerative disease and psychosis will be carried out. The ^{45}Ti nuclide is suitable for antibody labeling thanks to a longer half-life and high affinity with proteins. Intravascular radioactivity of ^{45}Ti can be connected by measurement of tissue vascular fraction using [^{15}O]carbon monoxide which tightly binds to hemoglobin. Cancer diagnosis using radiolabeled monoclonal antibody may be performed with ^{45}Ti-monoclonal antibody and [^{15}O]-CO produced by K=130 and K=12 MeV cyclotrons, respectively. Figure 7 shows a flow-chrat for nuclear medicine by PET and related facilities.

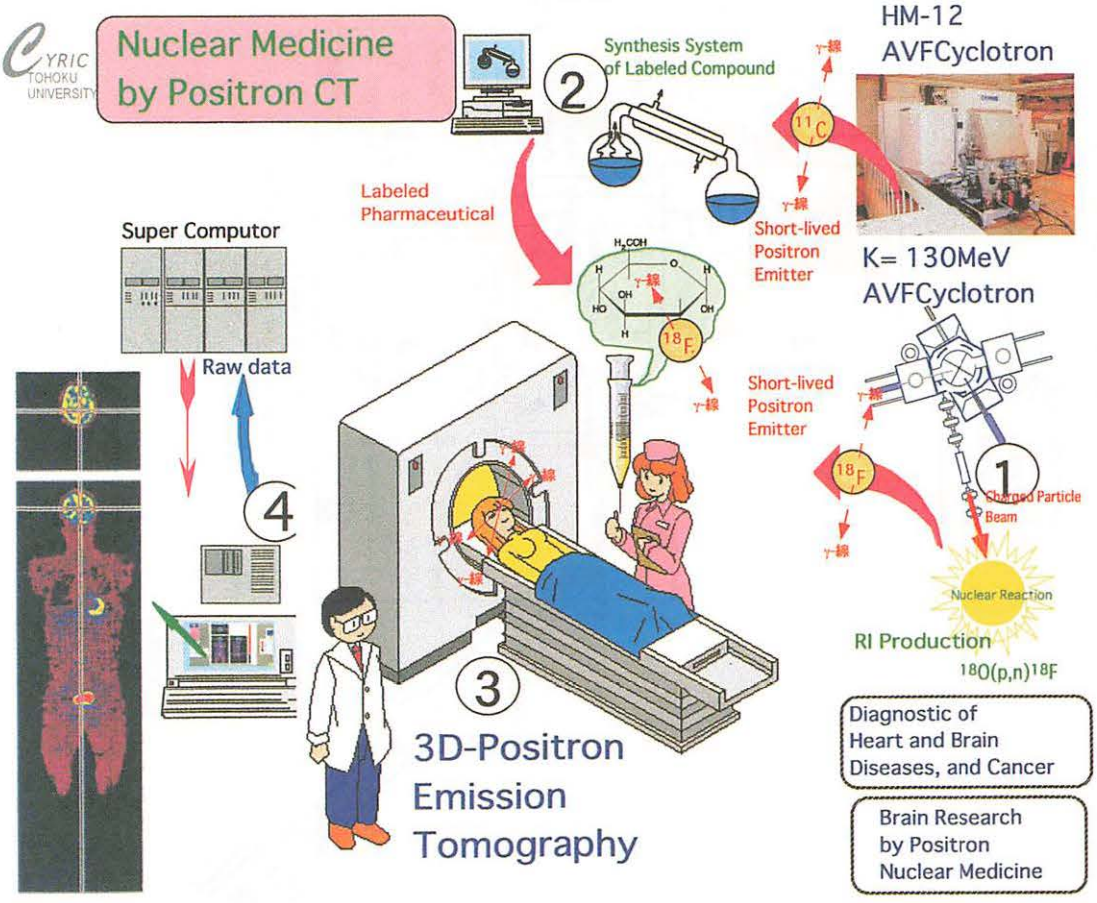

Fig. 7. Illustration for nuclear medicine by PET and related facilities.

As a summary, a layout of building and facilities for "Project for Heavy Charged-particle Beam Multi-purpose Use" are illustrated in the next page.

System for Heavy Charged-particle Beam Multi-purpose Use

CYRIC TOHOKU UNIVERSITY

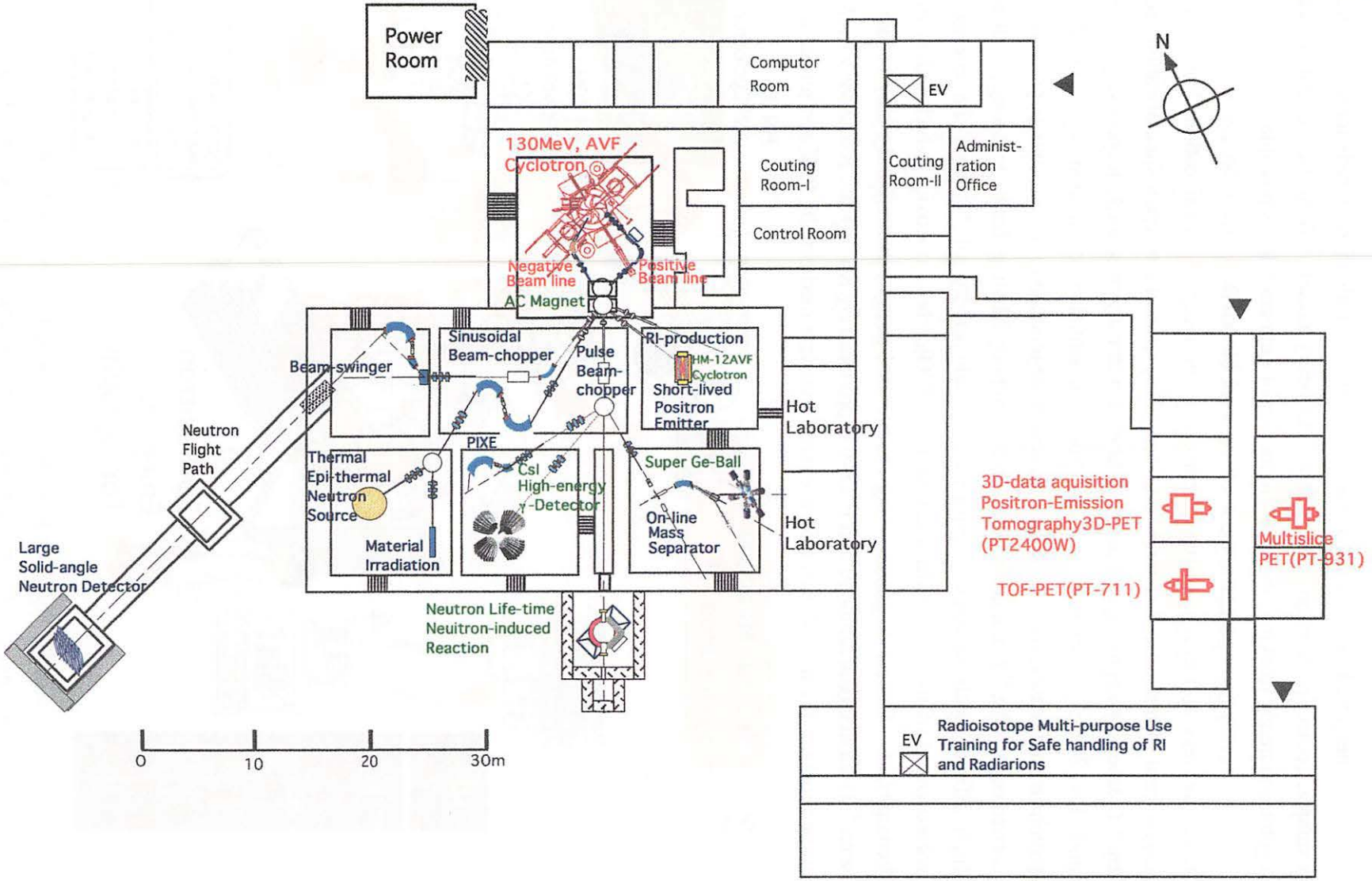

II. PHYSICS AND TECHNOLOGY

II. 1. Comparison of (p,n) Cross-section with Gamow-Teller β-decay Rates among T_z=-1, 0 and 1 Isobar Triplet

Orihara H., Suzuki H., Terakawa A., Jon G. C., and Ohnuma H.***

Cyclotron and Radioisotope Center, Tohoku University
*Institute of Physics, Academia Sinica, Nankang Taipei, Taiwan 11529**
*Department of Physics, Chiba Institute of Technology, Chiba 275-0023, Japan ***

Strong Gamow-Teller(GT) type β-decay, having log *ft* values ranging 3.0 to 3.5, are known in 9 sets of the T_z=-1, 0 and 1 isobar triplet[1], an example for which is illustrated in Fig. 1 for the case of the ^{38}Ar-^{38}K-^{38}Ca triplet. It is noteworthy that four characteristic nuclear states are connected by strong, weak and electro-magnetic interactions. The 0^+, T=1 ^{38}Ca ground state decays though positron emission into the 1^+, T=0 second excited state at E_x=1.6983 MeV with a log *ft* value of 3.40, while it decays as well into the 0^+, T=1 first excited state at E_x=0.1302 MeV. The former refers to the GT-transition, while the latter refers to the Fermi (F) transition with the standard log *ft* value of 3.49. This 1^+ state decays quickly through M_1 transition emitting a 1.5677-MeV γ-ray, hence the GT-transition rate between ^{38}Ar and ^{38}K is inaccessible by β-decay experiments. A high-resolution (p,n) study may resolve this difficulty. There are another 8 sets of the triplet: they are ^{10}Be - ^{10}B - ^{10}C, ^{14}C-^{14}N - ^{14}O, ^{18}O - ^{18}F - ^{18}Ne, ^{22}Ne - ^{22}Na - ^{22}Mg, ^{26}Mg - ^{26}Al - ^{26}Si, ^{30}Si - ^{30}P - ^{30}S, ^{34}S - ^{34}Cl - ^{34}Ar, and ^{42}Ca - ^{42}Sc - ^{42}Ti. Beyond the nuclei heavier than A=48, no such simple nuclear structure appear. Except the case of the ^{10}Be-^{10}B -^{10}C triplet, where target materials are not avairable in an ordinary manner, others all GT- and F-transitions among triplets may be explored by the (p,n) reaction. For some cases decribed above (p,n) stuies have been carried out at low and intermediate energies[2-7].

The (p,n) reaction has provided us with information about spin-isospin, as well as isospin excitation modes in nuclei. One can selectively excite the spin-flip components in the (p,n) reaction at intermediate energies through the relatively strong spin-isospin effective interaction ($V_{\sigma\tau}$). Low energy (p,n) reactions, due to the strong spin non-flip isovector effective interaction (V_τ), give us equivalent information on both excitation modes. Moreover, it gives us a sufficient energy resolution to discuss (p,n) strength for individual nuclear levels[2-4], although exchange contributions are important at low energies. Various problems associated with the distorted-wave (DW) analysis of low-energy (p,n) data were discussed in detail by Ohnuma et al[8]. It has been found possible to obtain basically the same information as that at intermediate energies if careful analysis including exchange terms is

carried out.

In this report we discuss prominent GT-type $0^+ \rightarrow 1^+$ transitions observed in the (p,n) reactiones on ^{14}C, ^{18}O, ^{22}Ne, ^{26}Mg, ^{30}Si, ^{34}S, ^{38}Ar and ^{42}Ca, among which those for (p,n) reactions on ^{14}C, ^{18}O and ^{34}S have been published in our previous papapers[2-4].

The experiment was performed at the Cyclotron and Radioisotope Center, Tohoku University, with a 35-MeV proton beam from an AVF-cyclotron and a beam swinger system. The details of the experimental setup have been described previously[9,10]. Neutron energies were measured by the time-of-flight technique (TOF), where neutrons were detected by a detector array located at 44.3 m from the target. The detectors, 23.2 ℓ in a total sensitive volume, were filled with organic liquid scintillator NE213. The absolute efficiencies of the detectors were obtained from the $^7Li(p,n)^7Be$ activation analyses with an error less than ± 6%. Errors in the absolute magnitude of (p,n) cross sections were estimated to be less than 12%. All the targets were enriched isotopes with enrichments higher than 95%. Figure 2 shows an excitation energy neutron spectrum measured for the $^{38}Ar(p,n)^{38}K$ reaction at 25-degrees. A prominent isolated peak of neutrons leading to the 1.6983-MeV, 1^+ state is senn to be excited, together with those to the first excited 0^+, IAS.

As an example of experimental results, Fig. 3 shows angular distributions for neutrons leading to the 1^+ states in ^{38}K and ^{42}Sc excited by the (p,n) reactions on ^{38}Ar and ^{42}Ca. The data are compared with the DW results calculated by the computer code DWBA-74[11], which includes knock-on exchange effects in an exact manner. N in the figure is the normalization factor introduced to fit calculated cross-sections to the experimental data. Note that fully antisymmetrized calculations are made in the present DW analysis, in which non-normal parity terms such as $\Delta J(\Delta L, \Delta S) = 1(1, 0)$ for the $0^+ \rightarrow 1^+$ transition also contribute to the cross section. They indeed play important roles in some cases. Optical potential parameters of Becchetti and Greenlees[12] are used for the entrance channel. Those for the exit channel were self-consistent potential parameters derived by Carlson et al[13]. The effective nucleon-nucleon interactions used in the present DW analysis are those by Bertsch et al. (M3Y)[14]. Sensitivity of such calculations to the optical-potential parameters is elaborated in Ref. 7. One body transition densities (OBTD) for microscopic DWBA calculation have been obtained by shell-model computer code OXBASH[15]. For the (p,n) reactions on ^{18}O, ^{22}Ne, ^{26}Mg, ^{30}Si and ^{34}S, full sd-shell calculations were carried out with the SD-interaction by Brown and Wildenthal[16] for both initial and final states, while OBTD for the $^{14}C(p,n)^{14}N$reaction was obtained with the interaction by Millener and Kurath[17], then finally, for the (p,n) reactions on ^{38}Ar and ^{42}Ca, $2\hbar\omega$-jump into fp-shell were taken into accounts with the SDPF model-space and by the SDPFMW interactions[18].

OBTD is defined as;

$$OBTD = < f \,||| [a^+(j')a(j)]^{\Delta J, \Delta T} ||| \, i > / \sqrt{(2\Delta J + 1)(2\Delta T + 1)} \,. \qquad (1)$$

With OBTD we obtain the Z(j',j)-coefficient for microscopic DWBA calculation;

$$Z(j',j) = \mathrm{OBTD}\langle T_i T_{iz} \Delta T \Delta T_z \mid T_f T_{fz} \rangle / \sqrt{(2J_i + 1)(2T_{fz} + 1)}\ , \tag{2}$$

where $\Delta T_z = T_f - T_i$. Then, Gamow-Teller matrix elements are;

$$B(GT) = |\sum_{j',j} \mathrm{OBTD}(j', j)\langle j' \| \sigma \| j \rangle|^2, \tag{3}$$

while differential (p,n) cross sections for a $0^+ \rightarrow 1^+$ transition are schematically expressed as;

$$(\frac{d\sigma}{d\Omega})_{(p,n)} \propto |\sum_{j',j} \mathrm{OBTD}(j', j)\langle j' | V_{\sigma\tau} f(q) | j' \rangle|^2, \tag{4}$$

where f(q) means q-dependensy of individual particl-hole xcitation peculier to the (p,n) reaction. Equations (3) and (4) suggest that there are close relationship between B(GT) and (p,n) cross sections for a $0^+ \rightarrow 1^+$ transition. In a limit of $q \rightarrow 0$, the proportional relationship has, indeed, discussed by many othors[19].

Table 1 summarize the present results. Data for β-decay were taken from recent review by Singh et al[20]. We translate the experiental log *ft* values into $B_\beta(GT)$, assuming the *free* values for vector and axial-vector coupling constants as $(g_A/g_V)^2 = (1.251)^2$. The experimental $B_\beta(GT)$ values systematically smaller than those by predictions, The average of their ratio is 0.74 ± 0.06, error being the standard deviation over eight samples. Meanwhile for the (p,n) reaction, a normalization factor *N* was introduced to fit the theoretical cross sections by DWBA calculation to the data. We list, in the 8th column in Table 1, our suggestion for the B(GT) values for each transition obtained by multiplying $B_{th}(GT)$ by the normalization factor *N*, the average value for which is 0.62 ± 0.04. Generally speaking, the present results for the B(GT) values are reasonable. However, they are systematically smaller than those $B_\beta(GT)$. We introduce further normarization constant *K* obtained by 0.74/0.62 = 1.19, then finally we obtain our recomended B(GT) values listed in the 9th column in Table 1. The log *ft* values, thus obtained for each isobar triplet, are quite reasonable comparing with those by β-decay experiments.

We have introduced two kinds of normalization factor for the experimental GT matrix elements in the course to deduce the final B(GT) value with (p,n) cross-sections. The first one is obtained for the individual transition, its averaged value being 0.62, and ranges over 0.51 through 0.81, with the standard deviation of 6.3%, while the second one is a common factor of 1.19 for all transitions. As listed in Table 1, the quenching factor for β-decay rate ranges over 0.61 through 1.03, and their average is 0.74 with the standard deviation of 8.1%. Quenching in (p,n) cross-section needed in the first normalization seems to have same origin with that in β-decay rate, and considered to be inadequate choice of wave functions. On the other hand, requirement for the second normalization or difference

between 0.62 ± 0.04, and 0.74 ± 0.06 is peculiar to the (p,n) reaction, presumably due to the choice of effective interaction.

In summary, experimental results for prominent GT-type $0^+ \rightarrow 1^+$ transitions observed in the (p,n) reactions on ^{14}C, ^{18}O, ^{22}Ne, ^{26}Mg, ^{30}Si, ^{34}S, ^{38}Ar and ^{42}Ca were discussed by comparing them with analog GT-transition strengths among T=-1, 0 and 1 isobar triplet. Reasonable B(GT) values for the energetically inaccessible β^--decay were obtained for almost all T=-1, 0 and 1 isobar triplets by shell-model and DWBA calculations. In order to fit the B(GT) values by the (p,n) reaction to those analog β^+-decay completely, further normalization of 1.19 was needed.

References

1) Table of Isotope Eigh Edition (1996), ed. by Firestone et al.
2) Kabasawa M. et al., C **45** (1992) 1220.
3) Oura M. et al., Nucl Phys. Nucl. Phys. **A586** (1995) 20.
4) Furukawa K. et al., Phys. Rev. **36** (1987) 1686.
5) Anderson B. D. et al., Phys. Rev. C **27** (1983) 1387.
6) Madey R. C. et al., Phys. Rev. C **35** (1987)2011.
7) Anderson B. D. et al., Phys. Rev. C **54** (1986) 602.
8) Goodman C. D. et al., Phys. Lett. **107B** (1981) 406.
9) Ohnuma H. et al., Nucl. Phys. **A467** (1987) 61.
10) Orihara H. et al., Nucl Instrum. Methods **188** (1981) 15.
11) Orihara H. et al., Nucl. Instrum. Methods **A257** (1987) 189.
12) Schaeffer R. and Raynal J., the computer program DWBA70 unpublished.
13) Becchetti F. D. and Greenlees G. W., Phys. Rev. **182** (1969) 1190.
14) Carlson J. D., Zafiratos C. D. and Lind D. A., Nucl. Phys. **A249** (1975) 29.
15) Bertsch G., Borysowics J., McManus H. and Love W. G., Nucl. Phys. **A284**, 399 (1977).
16) Echegoyen A. E. et al., The shell model code OXBASH.
17) Brown B. A. and Wildenthal B. H., Phys. Rev. C **27** (1983) 269.
18) SDPFMW., Phys. Rev. C **41** (1990) 1147.
19) Cohen S. and Kurath D., Nucl. Phys. **A101** (1967) 1.
20) Taddeucci T. N. et al., Nucl. Phys. **A469** (19879 125.
21) Singh B. et al., Nuclear Data Sheets **84** (1998) 487.

Table 1. Comparison of GT matrix elements obtained by the (p,n) reaction with those by super-allowed β-decay.

β-decay				Shell-Model	(p,n)Reaction				
decay	E_x(MeV)	log *ft*	$B_{\beta}(GT)^{\#1}$	$B_{th}(GT)$	Reaction	$N^{\#2}$	$N\times B_{th}(GT)$	$K^{\#3}\times N\times B_{th}(GT)$	log *ft* $^{\#4}$
$^{14}O(0^+)\rightarrow{}^{14}N(1^+)$	3.9478	3.13	2.922	4.805	$^{14}C(p,n)^{14}N(1^+)$	0.51	2.451	2.917	3.13±0.05
$^{18}Ne(0^+)\rightarrow{}^{18}F(1^+)$	0.0	3.09	3.204	5.058	$^{18}O(p,n)^{18}F(1^+)$	0.50	2.529	3.010	3.12±0.05
$^{22}Mg(0^+)\rightarrow{}^{22}Na(1^+)$	1.9362	3.44	1.431	1.705	$^{22}Ne(p,n)^{22}Na(1^+)$	0.60	1.023	1.217	3.51±0.06
$^{26}Si(0^+)\rightarrow{}^{26}Al(1^+)$	1.0577	3.55	1.111	1.910	$^{26}Mg(p,n)^{26}Al(1^+)$	0.60	1.146	1.363	3.46±0.05
$^{30}S(0^+)\rightarrow{}^{30}P(1^+)$	3.0194	3.56	1.086	1.466	$^{30}Si(p,n)^{30}P(1^+)$	0.70	1.027	1.222	3.51±0.05
$^{34}Ar(0^+)\rightarrow{}^{34}Cl(1^+)$	3.1291	3.45	1.399	1.355	$^{34}S(p,n)^{34}Cl(1^+)$	0.81	1.097	1.305	3.48±0.06
$^{38}Ca(0^+)\rightarrow{}^{38}K(1^+)$	1.6983	3.40	1.570	2.031	$^{38}Al(p,n)^{38}K(1^+)$	0.70	1.422	1.692	3.37±0.06
$^{42}Ti(0^+)\rightarrow{}^{42}Sc(1^+)$	0.6111	3.17	2.665	3.746	$^{42}Ca(p,n)^{42}Sc(1^+)$	0.57	2.135	2.541	3.19±0.05

#1 derived from log *ft* through the relation:

$$B(GT) = \frac{6170}{\left(\frac{g_A}{g_V}\right)^2 ft}$$

#2 normalization factors to fit the theoretical cross sections by DWBA to the data.

#3 averaged constant to fit $N\times B_{th}(GT)$ to $B_{\beta}(GT)$: $K = 1.19 \pm 0.12$, where error denotes the standard deviation.

#4 obtained from $N\times B(GT)$ by the relation:

$$ft = \frac{6170}{\left(\frac{g_A}{g_V}\right)^2 K \times N \times B(GT)}$$

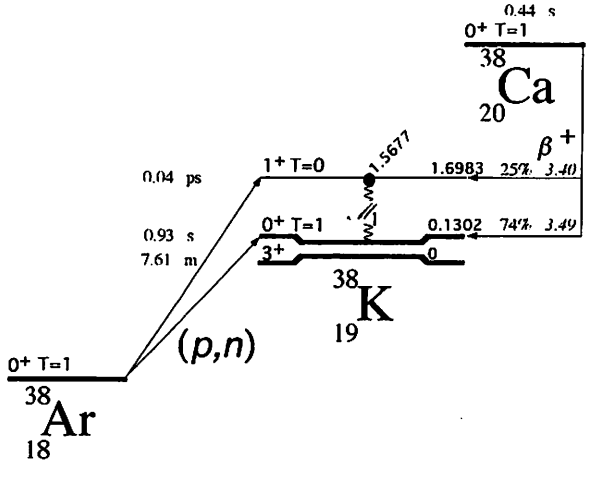

Fig. 1. Level diagram of ^{38}Ar - ^{38}K - ^{38}Ca, A = 38 isobar triplet.

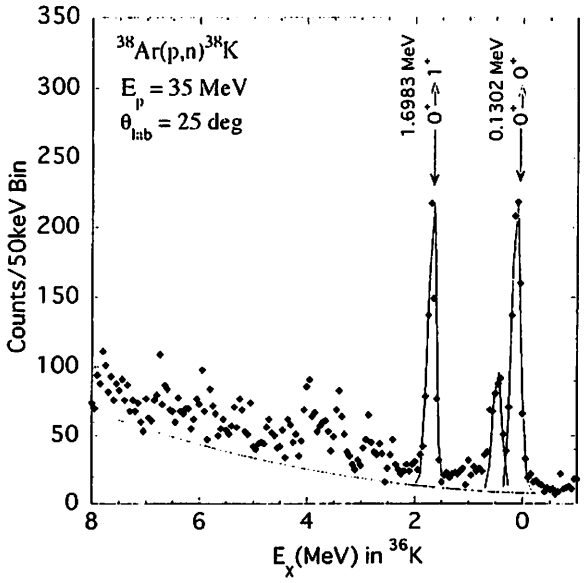

Fig. 2. A sample energy spectrum for the $^{38}Ar(p,n)^{38}K$ reactions at 25° with a flight path of 44.3 m. Energy per channel is 50 keV.

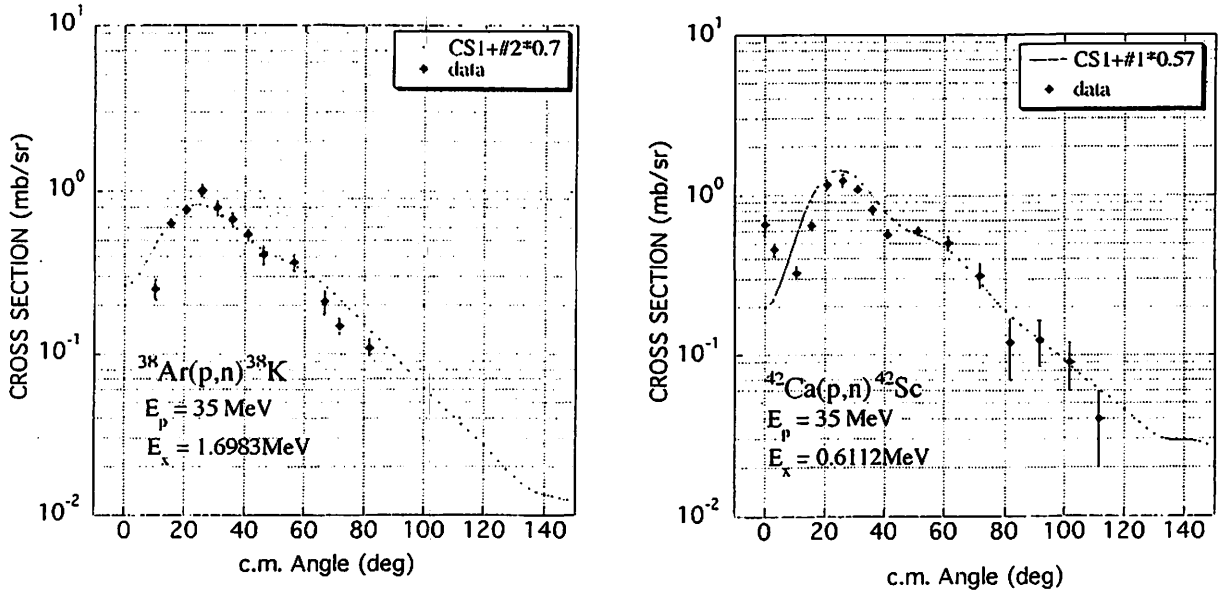

Fig. 3. Differential cross sections for neutrons leading to the 1.6983-MeV states in ^{38}K and to the 0.611-MeV states in ^{42}Sc. The curves are DWBA results described in text.

II. 2. Nuclear Structure Study of ^{36}K by Charge-exchange (p,n) Reaction on ^{36}Ar

Orihara H., Suzuki H., Jon. G. C., Terakawa A., Yamamoto A., Mizuno H., Kamurai G., Kikuchi Y., Ishii K.**, and Ohnuma H.****

Cyclotron and Radioisotope center, Tohoku University
*Institute of Physics, Academia Sinica, Nankang Taipei, Taiwan 11592**
*Department of Quantum Science and Energy Engineering, Tohoku University***
*Department of Physics, Chiba Institute of Technology, Chiba 275-0023, Japan ****

The charge-exchange (p,n) reaction is one of the powerful tools to explore the nuclear structure of neutron deficient nuclei, especially selecting spin-isospin excitation in the residual nucleus. The nuclear structure experiment for the neutron deficient ^{36}K nucleus has so far been limited to a few cases with e. g. the (^{3}He,t) reaction, where twelve levels are reported[1].

The (p,n) reaction has provided us with information about spin-isospin, as well as isospin excitation modes in nuclei. One can selectively excite the spin-flip components in the (p,n) reaction at intermediate energies through the relatively strong spin-isospin effective interaction ($V_{\sigma\tau}$). Low energy (p,n) reactions, due to the strong spin non-flip isovector effective interaction (V_{τ}), give us equivalent information on both excitation modes. Moreover, it gives us a sufficient energy resolution to discuss (p,n) strength for individual nuclear levels[2,3], although exchange contributions are important at low energies. Various problems associated with the distorted-wave (DW) analysis of low-energy (p,n) data were discussed in detail by Ohnuma et al[4]. It has been found possible to obtain basically the same information as that at intermediate energies if careful analysis including exchange terms is carried out.

The experiment was carried out using a 35 MeV proton beam from the AVF cyclotron and the time-of-flight facilities[5,6] at the Cyclotron and Radioisotope Center at Tohoku University. A beam swinger system was used to measure angular distributions of emitted neutrons between 0° and 140° (lab). The target was argon gas enriched to 99 % in ^{36}Ar. It was contained in a 20 cm long cylindrical cell which allowed us to shield the neutron detectors against neutrons emitted from the window foils. In all the cases the effective target thicknesses were of the order of 1 mg/cm^2. The window material was Havar foil for the cylindrical cell, their thicknesses being ~10 mg/cm^2.

Neutrons were detected by an array of twelve detectors, which were located at 44.3 m from the target and contained a total of 23.2 liters of NE213 scintillator. The detector efficiencies were obtained from Monte Carlo calculations for monoenergetic neutrons with E $\leq$ 34 MeV. Absolute detector efficiencies were also measured by counting neutrons from the ^{7}Li(p,n)^{7} Be reaction and comparing its yield with the absolute neutron fluence determined by activation. They were in good agreement with the Monte Carlo calculations. Overall time resolution was typically 1.3 ns corresponding to 174 keV for the most energetic neutrons. Main contributions to this resolution were attributed to the energy loss and straggling of incident protons in the entrance-window of the target gas cell. Errors in the absolute scale of the cross sections were estimated to be less than 15%. Further experimental details have been given in a previous report[2,3].

Figure 1 shows an excitation energy neutron spectrum measured at 25-degrees. Referring the level sequence of the isobar nucleus ^{36}Cl, low-lying ($E_x \leq 1$ MeV) levels are considered to be positive states due to the $d_{3/2}$ valence orbit, while the lowest $1\hbar\omega$ jump negative-parity states are expected to appear at $E_x \leq 2$ MeV. As shown in Fig. 1, the weakly populated low-lying states are masked by background neutrons from target-window materials. We discuss for these 11 levels strongly populated by the present (p,n) reaction, and give spin-parity assignments for these levels based on the shell-model calculation and DWBA analysis for the (p,n) cross sections neutron described below.

Figures 2 and 3 show angular distributions for neutrons leading to the 11 levels discussed in the present report. The data are compared with the DW results calculated by the computer code DWBA-74[7], which includes knock-on exchange effects in an exact manner. Note that fully antisymmetrized calculations are made in the present DW analysis, in which non-normal parity terms such as $\Delta J(\Delta L, \Delta S) = 1(1, 0)$ for the $0^+ \rightarrow 1^+$ cases. Optical potential parameters of Becchetti and Greenlees[8] are used for the entrance channel. Those for the exit channel were self-consistent potential parameters derived by Carlson et al[9]. The effective nucleon-nucleon interactions used in the present DW analysis are those by Bertsch et al. (M3Y)[10]. Sensitivity of such calculations to the optical-potential parameters is elaborated in Ref. 4. One body transition densities (OBTD) for microscopic DWBA calculation have been obtained by shell-model computer code OXBASH[11]. For positive parity transitions, full sd-shell calculations were carried out with the SD-interaction by Brown and Wildenthal[12] for both initial and final states. As for negative parity transition, on the other hand, OBTD for $1\hbar\omega$-jump into fp-shell were taken into accounts with the SDPF model-space and by the SDPFMW interactions[13]. Note that full sd-shell wave functions were applied for the latter target state.

Shell-model calculation gives us OBDT and energy eigen-values for each transition, then we are able to estimate its (p,n) strength provided by DWBA calculation with Z-coefficient derived from the OBTD. The deepest eigen-value in positive-parity states is that

for the lowest 2^+ state, while that in negative-parity states is for the 2^- state. We regard the first theoretical 2^+ corresponds to the ground state of ^{36}K, while the calculated lowest 2- state corresponds to the 1.677 MeV-state, neutrons for which form a prominent peak as seen in Fig. 1. The cross section magnitudes and its angular distribution shown in Fig. 2 give indeed reasonable fit. As such, we are now able to predict a energy spectrum for the state prominently excited by the (p,n) reaction as shown in Fig. 4.

Also illustrated in Fig. 4 are the present spin-parity assignments for each observed state. Among them, assignments of $J^\pi = 1^-$ and 0^- states at E_x = 3.93 and 4.13 MeV are tentative, since their excitation energies are rather high and hence possibilities of another spin-parity assignments are not rejected. Three 1^+ state, corresponding to GT-type transition, are observed, though that to the 1.92-MeV state show L=2 angular distribution with ΔJ (ΔL, ΔS) = 1(2,1). Two prominent $0^+ \rightarrow 1^+$ transitions, which have log*ft* values of 3.68 and 3.54, leading to E_x=3.61 and 6.06 MeV state respectively, are predicted by shell-model as the forth and sixth members of the 1^+ state. We have assigned these to 3.37- and 5.75-MeV states with normalization factors ~0.5 as shown in Fig. 3. As for the 2^+ state, only one transition to E_x=2.00 MeV has sizable (p,n) strengths, as fitted to the observed 2.42-MeV state shown in Fig. 3.

Starting at E_x = 1.67 MeV as a 2^- state, three negative parity states of $1\hbar\omega$-excitation character are identified from their cross section magnitudes, angular distributions and excitation energies. Comparison for the excitation energy, cross section and its angular distribution with those predicted by shell-model and DWBA theory is reasonable as shown in Figs. 2 though 4, and Fig. 5. An exception is the case of $\Delta J^\pi = 3^-$ excitation. Shell-model predicts two 3^- states at E_x ~ 3MeV, while $\Delta J^\pi = 3^-$ strength is concentrated experimentally in one transition leading to the 3.65-MeV state. Thus, we have fitted data with the sum of two transition strengths. To resolve this discrepancy, more detailed shell-model calculation including e. g. $3\hbar\omega$-excitation.

In summary, experimental study has been carried out in order to make clear the nuclear structure of the neutron deficient ^{36}K nucleus, including spin-isospin excitation in such a nucleus. Shell-model calculation and analysis by DWBA theory have provided a set of spin-parity assignments over 11 levels presently observed.

References

1) Table of Isotope Eigh Edition, ed. by Firestone et al.
2) Orihara H. et al., Phys. Rev. Lett. **47** (1981) 301.
3) Furukawa K. et al., Phys. Rev. C **36** (1987) 1686.
4) Ohnuma H. et al., Nucl. Phys. **A467** (1987) 61.
5) Orihara H. et al., Nucl Instrum. Methods **188** (1981) 15.
6) Orihara H. et al., Nucl. Instrum. Methods **A257** (1987) 189.
7) Schaeffer R. and Raynal J., the computer program DWBA70 unpublished.
8) Becchetti F. D. and Greenlees G. W., Phys. Rev. **182** (1969) 1190.
9) Carlson J. D., Zafiratos C. D. and Lind D. A., Nucl. Phys. **A249** (1975) 29.
10) Bertsch G., Borysowics J., McManus H. and Love W. G., Nucl. Phys. **A284**, 399 (1977).
11) Echegoyen A. E. et al., The shell model code OXBASH.
12) Brown B. A. and Wildenthal B. H., Phys. Rev. C **27** (1983) 269.
13) SDPFMW., Phys. Rev. C **41** (1990) 1147.

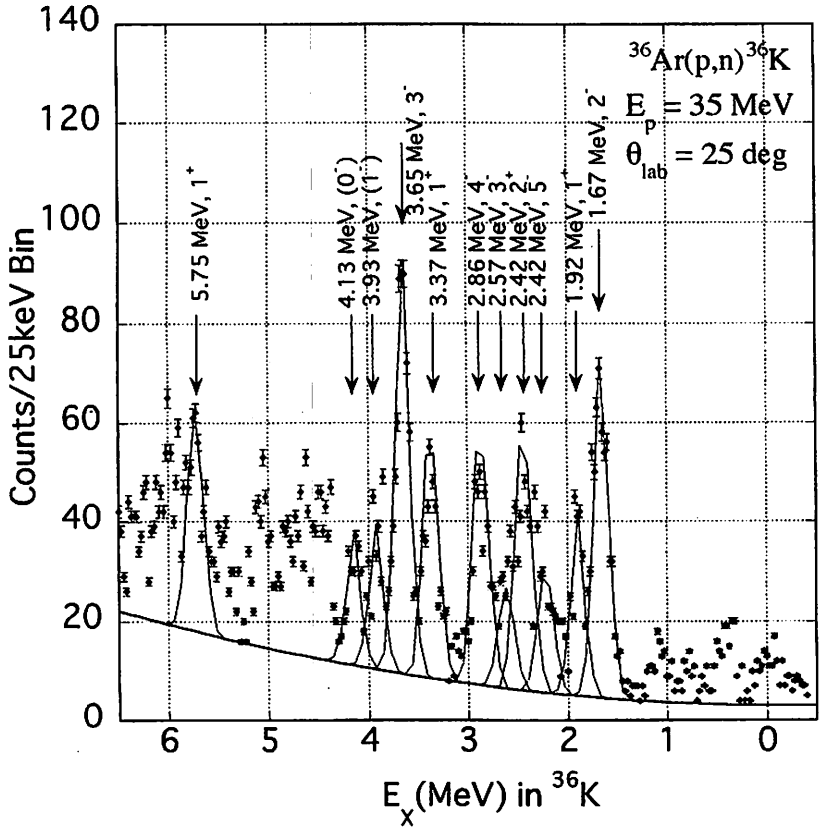

Fig. 1. A sample energy spectrum for the ^{36}Ar(p,n) ^{36}K reactions at 25° with a flight path of 44.3 m. Energy per channel is 25 keV.

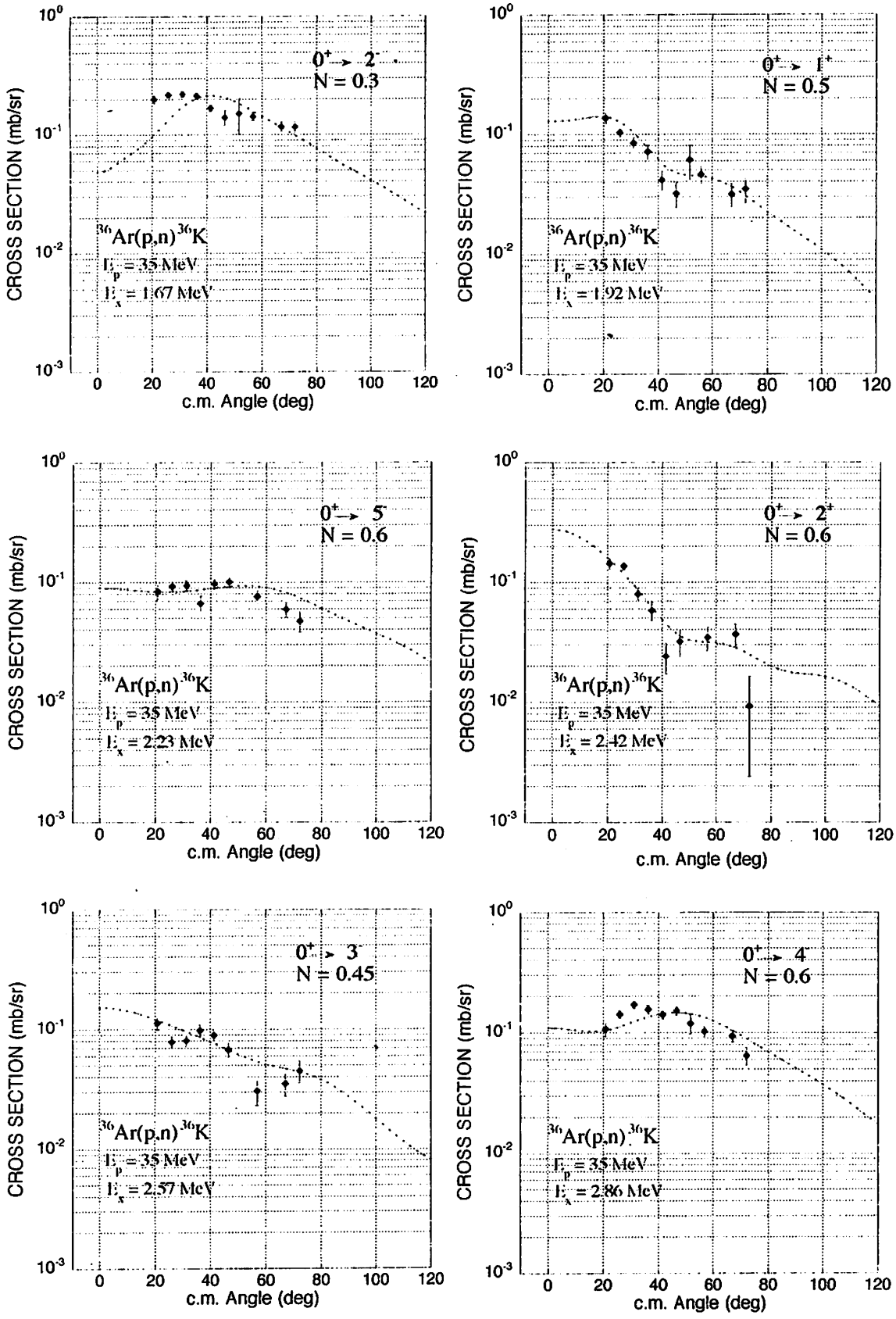

Fig. 2. Differential cross sections for neutrons leading to the 1.67-, 1.92-, 2.23-, 2.42-, 2.57-, and 2.86-MeV states in ^{36}K. The curves are DWBA results described in text. N denotes the normalization factor introduced to fit data.

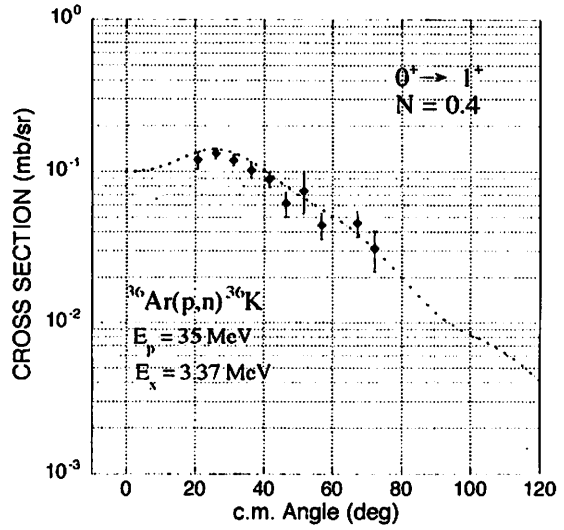

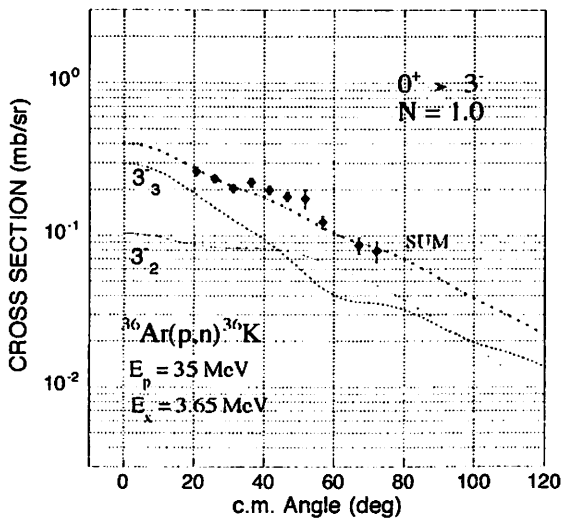

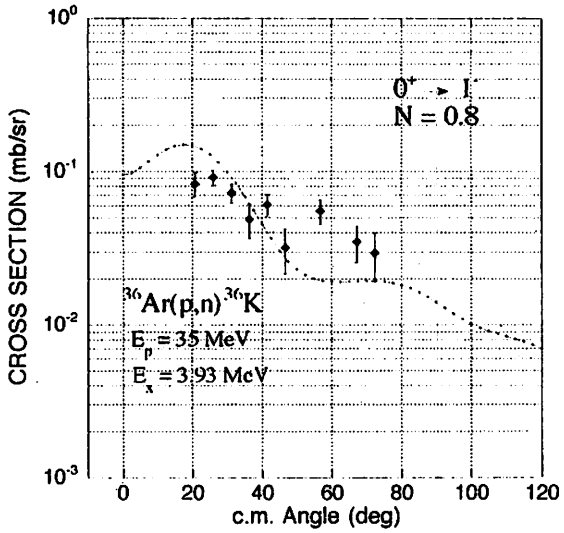

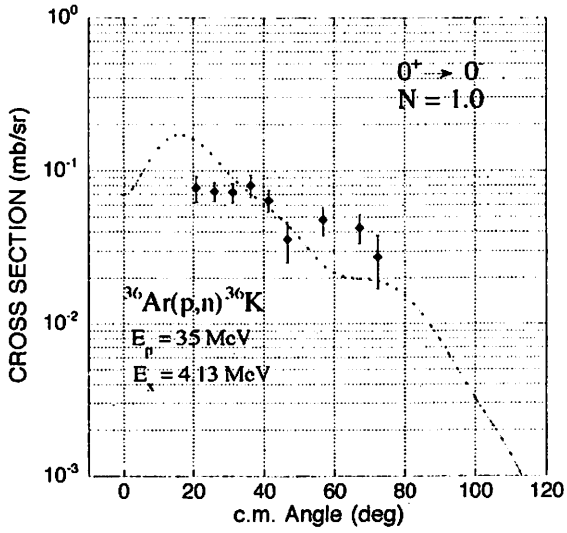

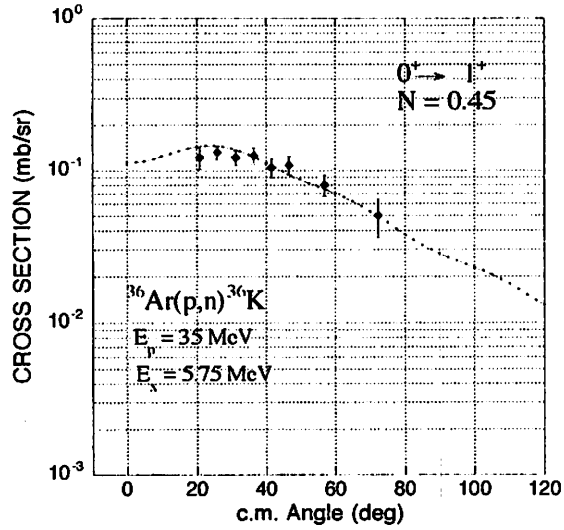

Fig. 3. Same with Fig. 2 but for neutrons leading to the 3.37-, 3.65-, 3.93-, 4.13-, and 5.75-MeV states in ^{36}K.

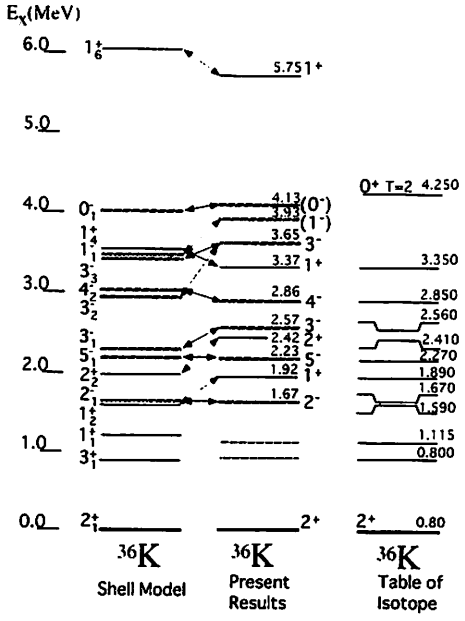

Fig. 4. Level diagram of ^{36}K nucleus. Levels by shell-model denote those having prominent (p,n) cross sections.

II. 3. Single-Particle States in the ^{51,53}Mn Nuclei

Hirai M., Nakagawa T., Fujii Y., Yamazaki A., Matsunaga M., Kumagai K., Orihara H., Terakawa A.*, Itoh K.*, Yun C.C.*, Yamamoto A.*, Kawami K.*, Suzuki H.*, Kamurai G.*, Mizuno H.*, Kikuchi Y.*, Aoisotope Center, Tohoku University**
*Department of Nuclear Engineering, Tohoku University***
*Tohoku Institute of Technology, Sendai, Japan****
*Chiba Institute of Technology, Chiba, Japan*****

A deuteron stripping reaction at higher incident energies is a very useful tool to study one-proton states as the target nucleus plus one nucleon. From spectroscopic factors derived as a ratio of experimental differential cross-sections to those calculated by distorted wave Born approximation, we can get information for the ground state of a target nucleus, such as proton occupation probabilities and single-particle energies of shell-model orbits. Therefore, a detail study of the (d,n) reaction plays an important role in nuclear spectroscopy.

In the nuclear shell-model, Z or N=20-28 nuclei are expected to have simpler configurations in its ground state wave function, because of large energy gaps between orbits above and below $1f_{7/2}$ and itself. From this point of view, the spectroscopic studies for the Sc, Co, and Cu isotopes have been done through the (d,n) reactions in the Ca (Z=20), Fe (Z=26) and Ni (Z=28) isotopes at E_d =25MeV, so far[1-5].

Previous studies have indicated that the ground state wave function for a nucleus cannot be described by a simple shell model, because of change of proton single-particle energies with neutron number, even if the nucleus has the same proton number. Therefore, it is a very interesting problem how much are the proton occupation probabilities and energy gaps between each shell-model orbit in $1f_{7/2}$ shell nuclei. This time, based on above systematic results, a spectroscopic study has been done by the (d,n) reaction for the^{50,52} Cr (Z=24) target at E_d =25MeV.

The experiments were performed with a 25MeV deuteron beam from the CYRIC AVF cyclotron and 44m-long time-of-flight facility[6,7]. The targets consisted of self-supporting foils with 3.66mg/cm^2 thick metallic ^{50}Cr (95.3% enriched) and 4.86mg/cm^2 metallic Cr in natural abundance. Angular distributions of the differential cross section were measured between 0° and 60° at laboratory angles. Achieved energy resolutions for the states were 200-250keV. The angular distributions were measured for states up to 11 and 15MeV in their excitation energy ranges for ^{51}Mn and ^{53}Mn, respectively.

Theoretical calculations for the differential cross section were done using the code

DWUCK4[8,9] in the framework of the adiabatic deuteron breakup approximation (ADBA) by Johnson & Soper[10]. Finite range and nonlocality corrections were applied to these calculations and the method of Vincent & Fortune[11] was used for ADBA calculations for unbound states. In this treatment, the optical model potential parameters for a proton and neutron in the incident channel were taken from the systematics of Becchetti & Greenlees[12] and Carlson et al[13], respectively. The potential parameters of Carlson et al. were also used for the outgoing neutron. Typical differential cross sections for the ^{50,52}Cr(d,n)^{51,53}Mn reactions have been shown in Fig. 1 and Fig. 2, respectively.

The information for the transfer momentum ℓ and spectroscopic factor, obtained by (^{3}He,d) reaction, has been so far restricted up to about 6MeV in ^{51}Mn and 12MeV in ^{53}Mn. In the present work, we have observed many proton single-particle states over the unexplored region. And we obtain transfer momenta ℓ's and get spectroscopic factors for many states, which have never been assigned by one-proton transfer reactions up to this time.

Obtained spectroscopic factors for ^{51,53}Mn are listed in Table 1 and 2, together with the (^{3}He,d) data. Excitation energy distributions of the spectroscopic factors for each transfer momentum ℓ are presented in Fig. 3. As shown in Fig. 3, fragmentations of the strength occur especially in the ℓ =1 orbits. The spectroscopic factors are dispersed over a lot of weak states in a wide excitation energy region. In the ℓ =3 orbits, the tendency that the $1f_{7/2}$ strength almost concentrates in the first excited state in ^{51}Mn and the ground state in ^{53}Mn has been observed.

The sums of the spectroscopic factors for each orbit are shown in Fig. 4. In the figure, the dotted lines show the simple shell-model limits and the solid lines show derived values in the present work. That for the $1f_{7/2}$ and $1f_{5/2}$ orbits reach the sum rule limits, so almost all strength for these states are considered to be observed. In ^{51}Mn, the strength for the 2p orbits is smaller than the shell-model limit. This may imply that there exist many weak peaks, which have not been observed in the present measurement, or the strength distributes also in the excitation region above 11MeV.

In conclusion, we have observed many proton single-particle states in the ^{51,53}Mn nuclei by the (d,n) reaction at E_d =25MeV in the excitation energy region up to 11MeV for ^{51}Mn and to 15MeV for ^{53}Mn, and newly assigned the transfer momentum ℓ for each state.

References

1) Mori S., Phys. M. thesis, Tohoku University 1988.
2) Hino T., Phys. M. thesis, Tohoku University 1995.
3) Aizawa T., Phys. M. thesis, Tohoku University 1996.
4) Matsunaga M., Phys. M. thesis, Tohoku University 1997.
5) Inomata T., Phys. M. thesis, Tohoku University 1992
6) Orihara H. and Murakami T., Nucl. Instrum. and Meth. **188** (1981) 15.
7) Orihara H. et al., Nucl. Instrum. and Meth. **A257** (1987) 189.
8) Kunz P. D., a DWBA code. Univ. Colorado, unpublished.
9) Comfort J. R., Extended version for the program DWUCK4. unpublised.
10) Johnson R. C. and Soper P.J.R., Phys. Rev. **C1** (1970) 976.
11) Vincent C. M. and Fortune H. T., Phys. Rev. **C2** (1970) 782.
12) Becchetti F. D. and Greenlees G. W., Phys. Rev. **182** (1969) 1190.
13) Carlson J. D. et al., Nucl. Phys. **A249** (1979) 15.
14) J. E. Park, W. W. Daehnick, and M. J. Spisak, Phys. Rev. **C19** (1979) 42.
15) S. Gales, S. Fortier, H. Laurent, J. M. Maison, and J. P. Schapira, Phys. Rev. **C14** (1976) 842.

Table 1. Experimental spectroscopic factors for ^{51}Mn.

Present work E_d = 25MeV					^{50}Cr(^{3}He, d)^{51}Mn J.E.Park et al.[14] $E_{^3He}$ = 18MeV			
No.	Ex	ℓ	j^π	$(2j+1)C^2S$	Ex	ℓ	j^π	$(2j+1)C^2S$
					0	3	$5/2^-$	0.15
1	0.24	3	$7/2^-$	2.20	0.240	3	$7/2^-$	2.25
2	1.83	1	$3/2^-$	0.53	1.823	1	$3/2^-$	0.63
3	1.96	1	$1/2^-$	0.14	1.958	1	$1/2^-$	0.24
4	2.14	1	$3/2^-$	0.30	2.139	1	$3/2^-$	0.36
					2.275	0	$1/2^+$	0.06
5	2.42	3	$7/2^-$	0.18	2.416	3	$7/2^-$	0.08
6	2.84	1	$1/2^-$	0.17	2.841	1	$1/2^-$	0.22
					2.913	1	$3/2^-$	0.05
					2.984	1	$5/2^+$	0.05
7	3.05	3	$(5/2^-)$	0.47	3.048	1+3	$(3/2^-)$+?	0.004+0.16
			$(7/2^-)$	0.37				
8	3.29	3	$5/2^-$	0.89	3.293	3	$5/2^-$	1.28
9	3.51	1+3	$(1/2^-)+(5/2^-)$	0.03+0.12	3.426	1+3		0.01+0.11
			$(3/2^-)+(5/2^-)$	0.03+0.12	3.556	1		0.07
			$(1/2^-)+(7/2^-)$	0.02+0.10				
			$(3/2^-)+(7/2^-)$	0.04+0.09				
10	3.70	1	$(1/2^-)$	0.08	3.698	(1)		0.05
			$(3/2^-)$	0.07				
11	3.90	1	$(1/2^-)$	0.10	3.896	1		0.09
			$(3/2^-)$	0.09				
					4.017	(1)		0.04
12	4.09	3	$(5/2^-)$	0.28	4.095	(3)		0.18
			$(7/2^-)$	0.20				
					4.362	(1)		0.02
13	4.45	3	$7/2^-$	0.63	4.449	3		0.54
14	4.95				4.523	1		0.03
15	5.13	1	$3/2^-$	0.61				
16	5.48	1	$(1/2^-)$	0.22				
			$(3/2^-)$	0.19				
17	5.67	1	$(1/2^-)$	0.29				
			$(3/2^-)$	0.24				
18	5.86	1+3	$(1/2^-)+(5/2^-)$	0.09+0.55				
			$(3/2^-)+(5/2^-)$	0.14+0.49				
			$(1/2^-)+(7/2^-)$	0.13+0.38				
			$(3/2^-)+(7/2^-)$	0.13+0.38				
19	6.07	3+4	$(5/2^-)+(9/2^+)$	0.77+0.66				
			$(7/2^-)+(9/2^+)$	0.48+0.75				
20	6.36	1	$(1/2^-)$	0.21				
			$(3/2^-)$	0.18				
21	6.84	1	$(1/2^-)$	0.22				
			$(3/2^-)$	0.20				
22	7.15	1+3	$(1/2^-)+(5/2^-)$	0.10+0.10				
			$(3/2^-)+(5/2^-)$	0.11+0.09				
			$(1/2^-)+(7/2^-)$	0.09+0.07				
			$(3/2^-)+(7/2^-)$	0.09+0.08				
23	7.39	2+3	$(5/2^+)+(5/2^-)$	0.11+0.20				
			$(5/2^+)+(7/2^-)$	0.09+0.17				
24	7.59	1+3	$(1/2^-)+(5/2^-)$	0.15+0.19				
			$(3/2^-)+(5/2^-)$	0.15+0.18				
			$(1/2^-)+(7/2^-)$	0.14+0.15				
			$(3/2^-)+(7/2^-)$	0.14+0.14				
25	7.82	3	$(5/2^-)$	0.14				
			$(7/2^-)$	0.11				
26	8.04	3+4	$(5/2^-)+(9/2^+)$	0.15+0.08				
			$(7/2^-)+(9/2^+)$	0.10+0.09				
27	8.21	1	$(1/2^-)$	0.16				
			$(3/2^-)$	0.15				
28	8.45	3+4	$(5/2^-)+(9/2^+)$	0.74+0.48				
			$(7/2^-)+(9/2^+)$	0.49+0.56				
29	8.94	3	$(5/2^-)$	0.20				
			$(7/2^-)$	0.15				
30	9.20	3	$(5/2^-)$	0.17				
			$(7/2^-)$	0.13				
31	9.36							
32	9.62	3	$(5/2^-)$	0.15				
			$(7/2^-)$	0.11				
33	9.89							
34	10.09	3	$(5/2^-)$	0.17				
			$(7/2^-)$	0.13				
35	10.30	3+4	$(5/2^-)+(9/2^+)$	0.04+0.10				
			$(7/2^-)+(9/2^+)$	0.02+0.10				
36	10.57	4	$(9/2^+)$	0.14				
37	10.78	3	$(5/2^-)$	0.21				
			$(7/2^-)$	0.21				
38	10.98	4	$(9/2^+)$	0.14				
39	11.22	3	$(5/2^-)$	0.15				
			$(7/2^-)$	0.15				

Table 2. Experimental spictroscopic factors for ^{53}Mn.

Present work E_d = 25MeV					^{52}Cr(^{3}He, d)^{53}Mn J.E.Park et al.[14] $E_{^3He}$ = 18MeV			
No.	Ex	ℓ	j^π	$(2j+1)C^2S$	Ex	ℓ	j^π	$(2j+1)C^2S$
1	0	3	$7/2^-$	4.52	0	3	$7/2^-$	3.00
					0.378	(3)	$(5/2^-)$	(0.15)
2	1.29	1	$3/2^-$	0.25	1.290	1	$3/2^-$	0.19
3	2.41	1	$3/2^-$	1.64	2.406	1	$3/2^-$	1.45
4	2.67	1+3	$1/2^- + 5/2^-$	0.33+0.54	2.672	1	$1/2^-$	0.30
					2.707	0	$1/2^+$	0.06
5	2.88	1	$3/2^-$	0.13	2.875	1	$3/2^-$	0.06
					3.007	2	$3/2^+$	0.04(1d)
						2	$5/2^+$	0.002(2d)
6	3.13	1+3	$3/2^- + (5/2^-)$	0.13+0.26	3.097	1	$3/2^-$	0.04
					3.127	3		0.17
7	3.48	1	$1/2^-$	0.37	3.480	1	$1/2^-$	0.25
8	3.67	3	$(5/2^-)$	1.80	3.666	3		1.76
					3.709	(3)		0.10
					3.896	1		0.08
9	4.06	1+3	$(3/2^-) + (5/2^-)$	0.11+0.86	4.064	(1)+(3)		0.04+0.52
		1+3	$(1/2^-) + (5/2^-)$	0.12+0.87				
					4.268	(3)		0.08
10	4.30	3	$(5/2^-)$	0.42	4.298	3		0.13
					4.348	(1)		0.03
11	4.43	1	$(3/2^-)$	0.27	4.429	1		0.19
			$(1/2^-)$	0.29				
					4.552	(3)		0.08
					4.574	1		0.07
12	4.65	1+3	$(3/2^-) + (5/2^-)$	0.29+0.19	4.635	(3)		0.06
		1+3	$(1/2^-) + (5/2^-)$	0.29+0.21				
					4.720	1		0.24
					4.783	(1)		0.04
					4.931	3		0.42
13	4.95	1+3	$(3/2^-) + (5/2^-)$	0.29+0.40	4.958	1		0.14
		1+3	$(1/2^-) + (5/2^-)$	0.30+0.46				
14	5.10	1	$(3/2^-)$	0.09	5.081	(1)		0.12
		1	$(1/2^-)$	0.10				
					5.320	(1)		0.04
15	5.49	1	$(3/2^-)$	0.08	5.476	(1)		0.04
		1	$(1/2^-)$	0.08				
16	5.85				5.894	(0)+(1)		0.07(3S)+0.39
17	6.33	1+4	$(3/2^-) + (9/2^+)$	0.08+0.52				
		1+4	$(1/2^-) + (9/2^+)$	0.08+0.55	^{52}Cr(^{3}He, d)^{53}Mn S.Galès et al.[15] $E_{^3He}$ = 25MeV			
18	6.52	2+4	$(5/2^+) + (9/2^+)$	0.16+0.54				
19	6.98	1	$(3/2^-)$	0.92	6.997	1	$(3/2^-)$	0.60
		1	$(1/2^-)$	0.99				
					7.028	4	$(9/2^+)$	0.30
20	7.26	1+4	$(3/2^-) + (9/2^+)$	0.06+0.37	7.277	3	$(5/2^-)$	0.36
		1+4	$(1/2^-) + (9/2^+)$	0.06+0.38				
21	7.55	1	$(3/2^-)$	0.34	7.548	1	$(1/2^-)$	0.26
		1	$(1/2^-)$	0.37				
22	8.00	3	$(5/2^-)$	0.90	8.000	3	$(5/2^-)$	0.12
23	8.24	1	$(3/2^-)$	0.13	8.188	1	$(3/2^-)$	0.08
		1	$(1/2^-)$	0.14		1	$(1/2^-)$	0.06
					8.516	3	$(5/2^-)$	0.18
24	8.56	1	$(3/2^-)$	0.37				
		1	$(1/2^-)$	0.41				
25	8.81	2+4	$(5/2^+) + (9/2^+)$	0.08+0.14	8.883	2(3)	$(5/2^+)$	0.06
26	8.98	2+4	$(5/2^+) + (9/2^+)$	0.07+0.19	8.982	2(3)	$(5/2^+)$	0.06
27	9.27	1	$(3/2^-)$	0.63	9.282	1	$(3/2^-)$	0.28
		1	$(1/2^-)$	0.70				
28	9.63	2+4	$(5/2^+) + (9/2^+)$	0.11+0.29	9.656	3	$(5/2^-)$	0.42
29	9.87	2+4	$(5/2^+) + (9/2^+)$	0.03+0.16	9.837	4	$(9/2^+)$	0.12
					10.190	2(3)	$(5/2^+)$	0.06
30	10.23	3	$(5/2^-)$	0.24	10.320	2(3)	$(5/2^+)$	0.06
					10.604	4	$(9/2^+)$	0.10
31	10.64	2+4	$(5/2^+) + (9/2^+)$	0.23+0.76	10.662	4	$(9/2^+)$	1.20
32	10.84	2	$(5/2^+)$	0.11				
33	11.04	2+4	$(5/2^+) + (9/2^+)$	0.20+0.15	11.033	2(3)	$(5/2^+)$	0.06
34	11.23	3	$(5/2^-)$	0.16				
35	11.41	3	$(5/2^-)$	0.24				
36	11.61	2+4	$(5/2^+) + (9/2^+)$	0.21+0.22	11.654	3	$(5/2^-)$	0.18
37	11.80	1	$(3/2^-)$	0.22				
		1	$(1/2^-)$	0.26				
38	12.00	2	$(5/2^+)$	0.19				
39	12.18	4	$(9/2^+)$	0.24				
40	12.38	1	$(3/2^-)$	0.25				
		1	$(1/2^-)$	0.30				
41	12.75	4	$(9/2^+)$	0.13				
42	12.97	4	$(9/2^+)$	0.23				
43	13.15	4	$(9/2^+)$	0.12				
44	13.35							
45	13.59	4	$(9/2^+)$	0.16				
46	13.79	2+4	$(5/2^+) + (9/2^+)$	0.04+0.11				
47	13.99	2	$(5/2^+)$	0.13				
48	14.16	4	$(9/2^+)$	0.15				
49	14.40							
50	14.68	2+4	$(5/2^+) + (9/2^+)$	0.06+0.08				

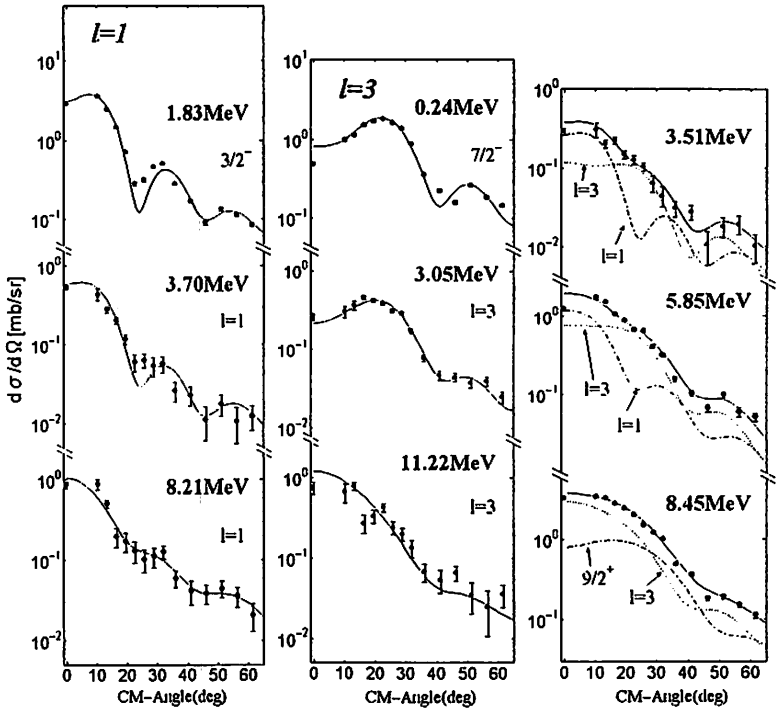

Fig. 1. Typical differential cross sections for the ℓ = 1-4 transitions in the ^{50}Cr(d,n) ^{51}Mn reaction.

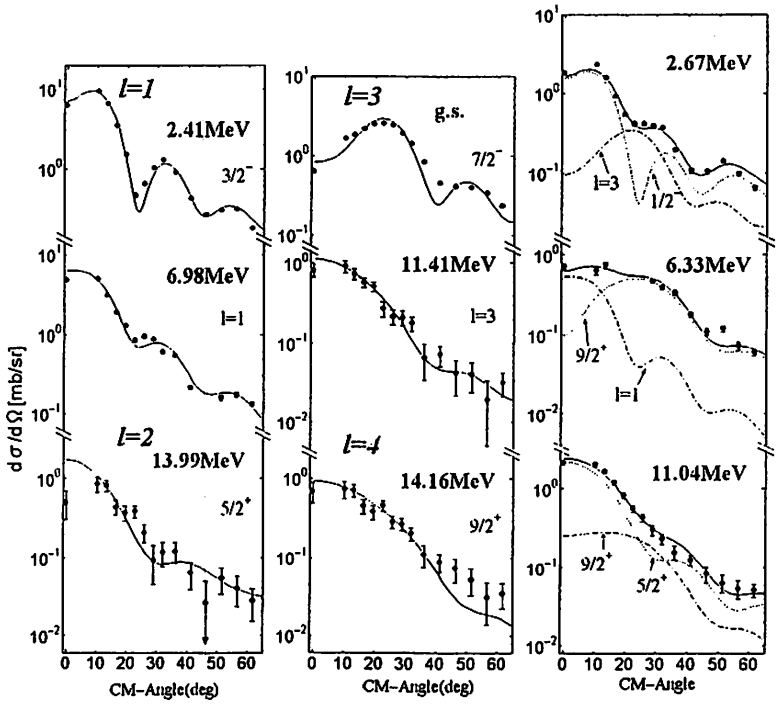

Fig. 2. Typical differential cross sections for the ℓ = 1-4 transitions in the ^{52}Cr(d,n) ^{53}Mn reaction.

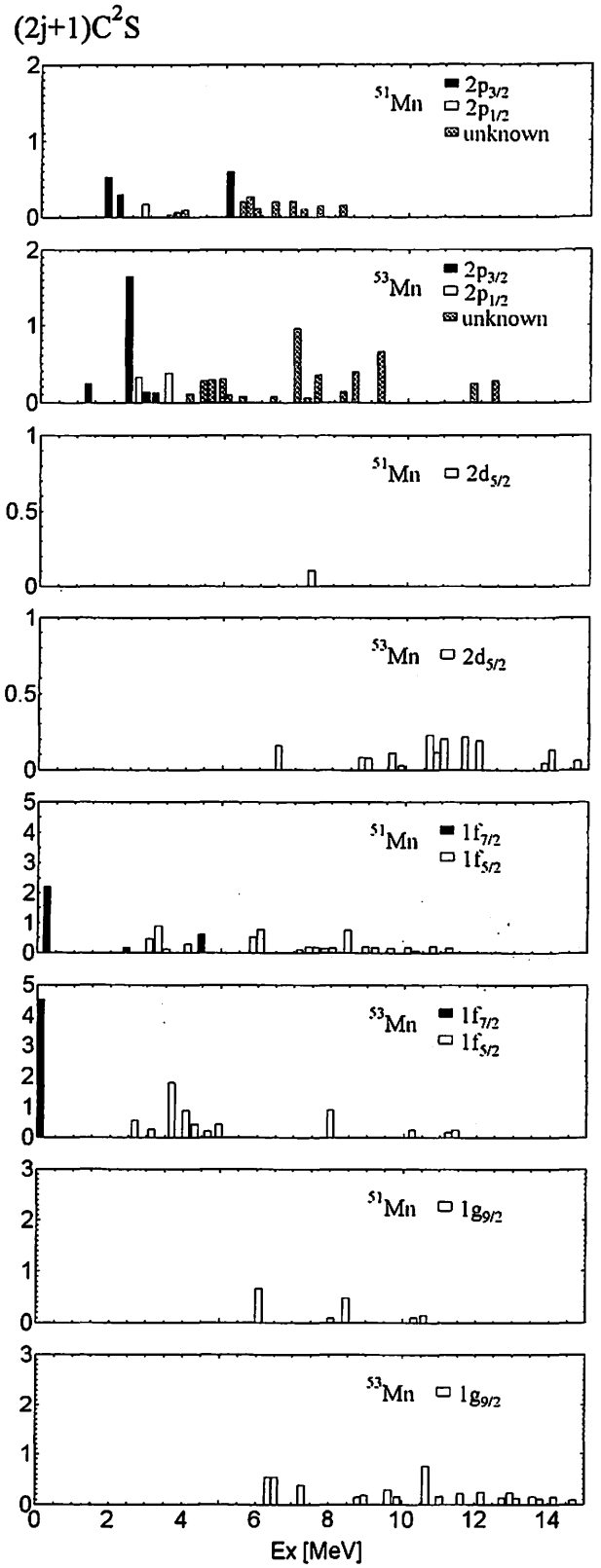

Fig. 3. Excitation energy distributions of single particle strengths for each orbit in ^{51,53}Mn.

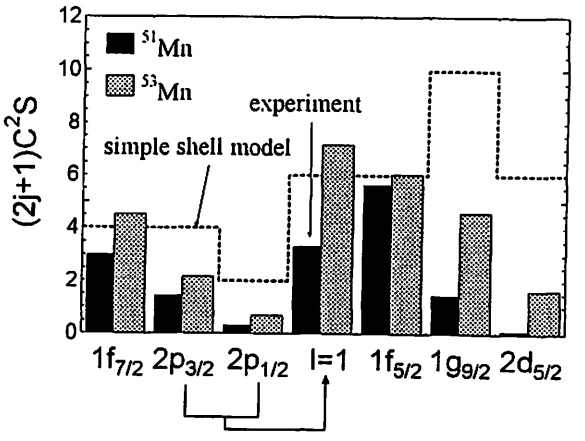

Fig. 4. Summed spectroscopic factors of ^{51,53}Mn for each ℓ.

II. 4. Gamow-Teller Transition in the ^{92}Zr(p, n)^{92}Nb Reaction at 35 MeV

Mizuno H., Orihara H., Terakawa A., Yamamoto A., Suzuki H., G. Kamurai, Kikuchi Y., G. C. Jon., Ishii K.**, and Ohnuma H.****

Cyclotron and Radioisotope center, Tohoku University
*Institute of Physics, Academia Sinica, Nankang Taipei, Taiwan 11592**
*Department of Quantum Science and Energy Engineering, Tohoku University***
*Department of Physics, Chiba Institute of Technology, Chiba 275-0023, Japan ****

Gamow-Teller(GT) β-decay is one of the simple transitions carrying information about spin-isospin excitation in nuclei. It is significant to accumulate β-decay data through out periodic table for our better understanding of the nuclear structure. As far as low lying nuclear states are concerned, β-decay rates have been directly measured in many cases. In some cases, however, such a GT type $\Delta J^{\pi}=1^{+}$ transition is energetically inaccessible by β-decay. Recently (p,n) reactions at low and intermediate energies have been extensively used to study GT strength distribution in nuclei. One can selectively excite the spin-flip components through (p,n) reactions at intermediate energies due to the strong spin-isospin part of the effective nucleon-nucleon interaction for nuclei in almost entire region of the periodic table with some exceptions of N = Z nuclei[1]. Low energy (p,n) reactions, on the other hand, give much better energy resolution, making it possible to discuss (p,n) strength for individual nuclear levels[2]. Various problems associated with the distorted-wave (DW) analysis of low-energy (p, n) data were discussed in detail by Ohnuma et al[3].

Proportionality relationship between β-decay matrix elements B(GT) and low-energy (p,n) reaction cross sections have been reported[4] for the cases of A ~ 100 nuclei by the (p,n) reactions on ^{110,112,114,116}Cd and ^{116,118,120}Sn at E_p = 35 MeV. Several odd-odd nuclei in A = 110 - 120 region have, indeed $\Delta J^{\pi}=1^{+}$ ground states. The β-decay rates of these nuclei leading to the even-even daughter nuclei have been measured. ^{112,114}In and ^{118,120}Sb are such examples. In A=92 nuclei, prominent GT-type β-decay are observed with log *ft* = 4.3 in ^{92}Kr – ^{92}Rb and ^{92}Sr – ^{92}Y pairs. However, the ground state of ^{92}Nb, the ground-state spin-parity of which is 7^{+}, is higher energetically than those of ^{92}Zr and ^{92}Mo. As such, no $1^{+} \rightarrow 0^{+}$ or $0^{+} \rightarrow 1^{+}$ transition is observed through β-decay experiments. The (p,n) study may provide a good place to explore such a prominent GT-type transition for ^{92}Nb. In this report we discuss on the spin-isospin excitation in the ^{92}Zr(p,n)^{92}Nb reactions at E_p = 35 MeV, and obtain GT-matrix elements for β-decay starting ^{92}Nb by using a scaling factor connecting the (p,n) cross section to B(GT) value.

The experiment was carried out using a 35 MeV proton beam from the AVF cyclotron and the time-of-flight facilities[5] in the Cyclotron and Radioisotope Center at Tohoku University. A beam swinger system was used to measure angular distributions of emitted neutrons between 0° and 55° (lab). Neutrons were detected by an array of twelve detectors, which were located at 44.3 m from the target and contained a total of 23.2 liters of NE213 scintillator. The targets were metallic foils of ^{92}Zr with a thickness of 5.66 mg/cm^2 and enrichment of 95.13 %.

Figure 1 shows an excitation energy neutron spectrum measured at 0-degrees. The most prominent peak is due to the neutrons leading to the isobaric analog state at 9.01 MeV in the residual nucleus. In the low excitation energy region, lower than $E_x \cong$ 1MeV, peaks corresponding to the $\pi g_{9/2}$-particle $\nu g_{7/2}$- hole states are seen, though they are unresolved by the limited experimental conditions. Among them, a peak corresponding to the 1,09-MeV, 1^+ state in ^{92}Nb is clearly resolved. In addition, forward peak neutrons are observed at an excitation energy of 3.08MeV, suggested an extra GT-type transition with L=0 as discussed below.

Figure 3 shows angular distributions for neutrons leading to the IAS and the 1^+ states. The curve for the IAS transition is macroscopic DWBA prediction by DWUCK-4[6], where optical potential parameters of Becchetti and Greenlees[7] are used for the entrance channel. Those for the exit channel are self-consistent potential parameters derived by Carlson et al[8]. As for the isovector potential parameters for IAS excitation, those obtained by Jon et al.[9] are used. Also shown in Fig. 2 are theoretical predictions by microscopic DWBA calculation wiyh the computer code DWBA-74[10]. The effective nucleon-nucleon interactions used in the present DW analysis are those by Bertsch et al. (M3Y) [11].

Since one body transition densities (OBTD) are not available in these medium heavy mass nuclei, the microscopic DWBA predictions provide just qualitative conclusion with analyses. The main component of OBDT in the $0^+ \rightarrow 1^+$ transition leading to the 1.09-MeV state may be $(\pi g_{9/2}, \nu g_{7/2})$, while those to the 3.08-MeV state may be mixing of $(\pi g_{9/2}, \nu g_{7/2})$ and $(\pi g_{9/2}, \nu g_{9/2})$. The normalized fittings in Fig. 2 give reasonable accounts for the L=0, GT type transition. After assignment for L=0 for these two transitions, we estimate their GT-matrix elements corresponding to b-decay rates. The scaling factor obtained in Ref. 4 is,

$$[\mathrm{B(GT)for}\ 1^+ \rightarrow 0^+\ []/\sigma(\mathrm{p, n})(\mathrm{in\ mb/sr})] = 0.255,$$

then

B(GT) = 0.0582 for the 1.09 MeV transition, and 0.0640 for 3.08 MeV.

By using the relation,

$$(g_A/g_V)^2\ \mathrm{B(GT)} = 6170\ /ft \quad \text{and} \quad (g_A/g_V)^2 = 1.251^2,$$

where g_V and g_A are weak vector and axial-vector coupling constants, respectively, we obtain log ft = 4.83 for the 1.09 MeV transition, while it is 4.79 for 3.08 MeV. Note that these log ft values correspond to, respectively, 4.35 and 4.31 for the $0^+ \rightarrow 1^+$, 1.09 MeV

transition and for $0^+ \rightarrow 1^+$, 3.08 MeV, being close magnitudes to those β-decay rates among A=92 nuclei.

In summary, neutrons from the ^{92}Zr(p,n) ^{92}Nb reactions at E_p = 35 MeV were observed by high resolution TOF technique. Three L=0 transitions were identified from the angular distributions of emitted neutrons and DWBA analysis for them. Cross section magnitudes for the GT-like transition gave us new information of B(GT) values for b-decay of ^{92}Nb.

References

1) Taddeucchi T. N. et al., Nucl. Phys. **A469** (1987) 125.
2) Furukawa K. et al., Phys. Rev. C**36** (1987) 1686.
3) Ohnuma H. et al., Nucl. Phys. **A467** (1987) 61.
4) Orihara H. et al., Nucl. Phys.
5) Orihara H. et al., Nucl. Instrum. Methods **A257** (1987) 189.
6) Kuntz P. D., The code DWUCK-4, unpublished.
7) Becchetti F. D. and Greenlees G. W., Phys. Rev. **182** (1969) 1190.
8) Carlson J. D., Zafiratos C. D. and Lind D. A., Nucl. Phys. **A249** (1975) 29.
9) Jon G. C. et al., CYRIC Annual Report 1997, to be published in Phys. Rev. C.
10) Schaeffer R. and Raynal J., the computer program DWBA70 unpublished.
11) Bertsch G., Borysowics J., McManus H. and Love W. G., Nucl. Phys. **A284**, 399 (1977).

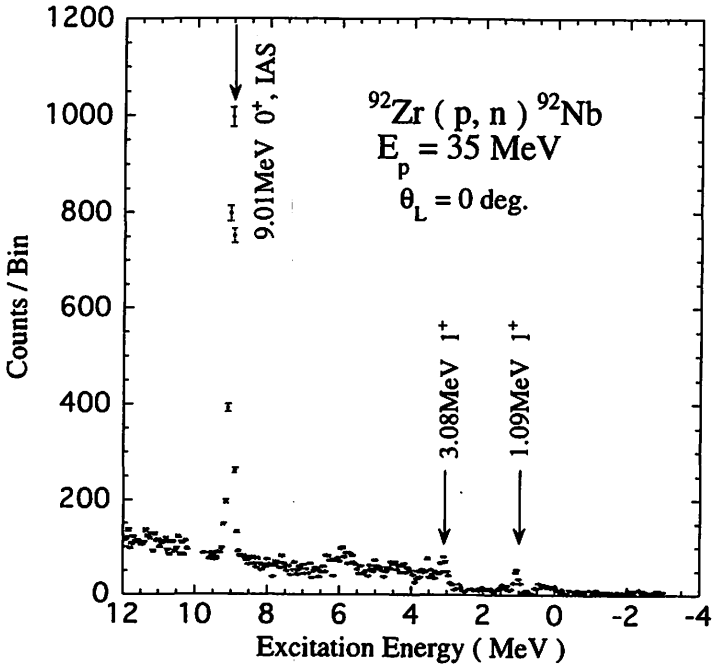

Fig. 1. A sample energy spectrum for the ^{92}Zr(p,n) ^{92}Nb reactions at 0° with a flight path of 44.3 m. Energy per channel is 50 keV.

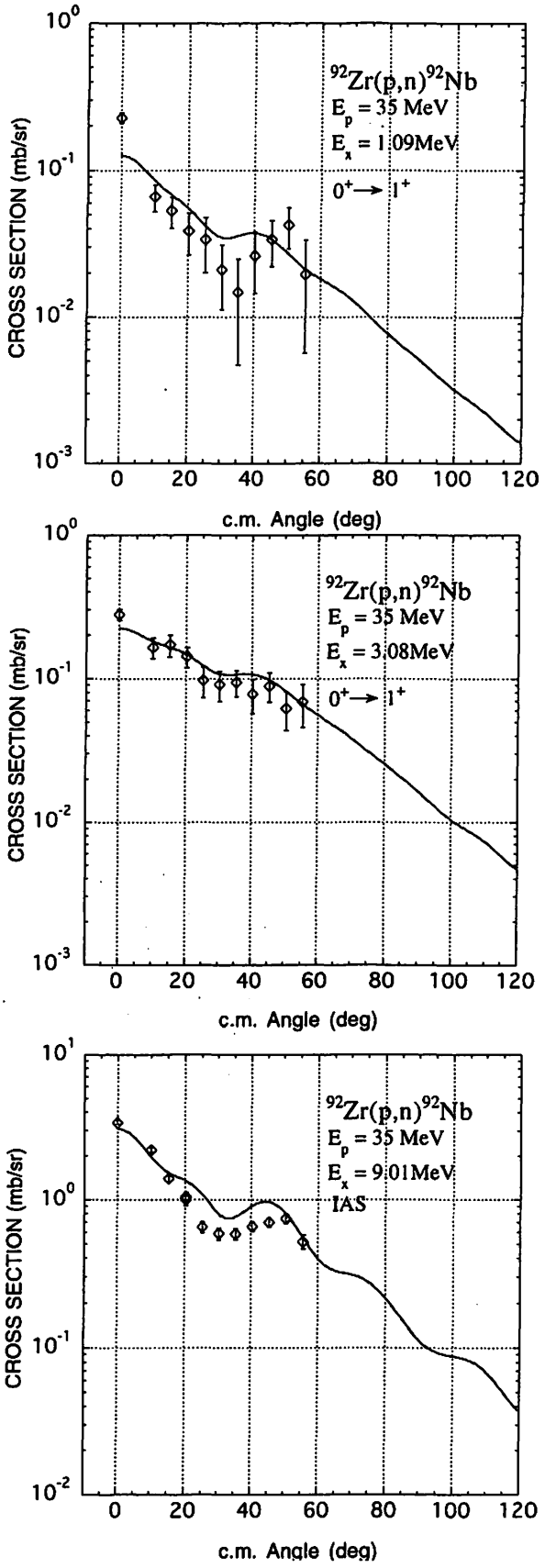

Fig. 2. Differential cross sections for neutrons leading to the IAS at E_x=9.01 MeV in ^{92}Nb and those for neutrons leading to the 1^+ states at 1.09 and 3.08 MeV in ^{92}Nb. The curves are DWBA results described in text.

II. 5. Charge Polarization of Fission Products in Proton-Induced Fission of ^{238}U and ^{232}Th

Kaji D., Goto S., Kudo H., Fujita M., Shinozuka T.*, Fujioka M.**

Department of Chemistry, Faculty of Science, Niigata University
*Cyclotron and Radioisotope Center, Tohoku University**

The charge distribution of fission products in proton-induced fission of ^{238}U and ^{232}Th was measured by the use of IGISOL in the incident proton energy of 13-26 MeV. Yields of fission products were determined by a γ-ray spectrometry. The analysis was performed by assuming a Gaussian function with representative parameters Z_p and C, where Z_p is the most probable charge of a given mass chain and C is the width parameter of the charge dispersion. The same kind of method as Kudo et al[1] was used for the evaluation of Z_p.

The obtained Z_p was compared to the charge Z_{UCD} expected from UCD model. It was found that Z_p's mainly lay on the side of higher charge density in a light fragment mass region and on the side of lower charge density in a heavy one in all systems. This observation implies that the charge polarization occurs in all systems. The deviation of Z_p from Z_{UCD} has similar tendency as the proton-to-neutron ratio of stable nuclei. Therefore, it is expected that the nuclear stability of fission fragments reflect the charge polarization in fission.

The charge polarization was examined with respect to ground-state Q values. The results were shown in Fig. 1, where Z_{Qgg} was estimated from the most energetically favorable combination of complementary fragments. The experimental Z_p was found to be fairly well reproduced by the estimated charge, Z_{Qgg}, except in the system of 13 MeV proton-induced fission of ^{238}U and ^{232}Th. Although Z_p dose not seem to correlate with Z_{Qgg} in Fig. 1 (D), this is probably because of the inadequate correction of emitted neutrons. These results suggest that the fission path to the most favorable charge division may go through the most energetically favorable path. On the other hand, some structure in Fig. 1 (C) and (F) was recognized in vicinity of spherical closed shell and $A'=142$. This region of $A'=142$ is coincident with the neutron closed shell of the deformed nuclei, N = 86-88, suggested by Wilkins et al. [2]. These systems were obtained for the lowest proton energy in the present work. Therefore, the effect such as a shell effect which is emphasized in low energy region may affect the most probable charge.

The probability of charged particle emission is quite small in fission process, so that it is expected that the nuclear charges of fragments are determined before scission. As fission fragments are expected to be considerably deformed at scission point, masses at scission point are expected to be different from ground-state masses. Therefore, the explanation by the use of ground-state masses seems to be inadequate. The detailed analysis about deformation at scission point is now in progress.

References

1) Kudo H., Phys. Rev. **C57** (1998) 178.
2) Wilkins., et al., Phys. Rev. **C14**, (1976) 1832.

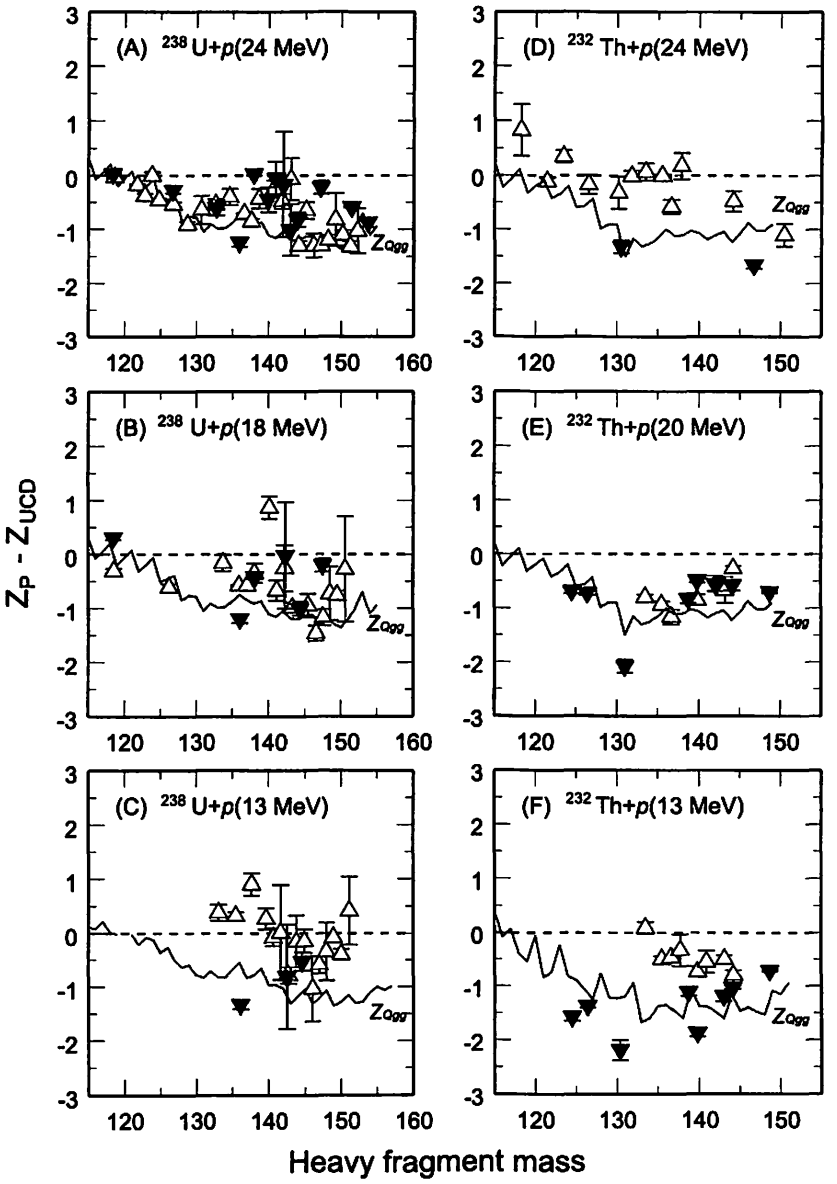

Fig. 1. Deviation of Z_p from Z_{UCD} plotted versus heavy fragment mass for various systems. The light mass products, which are folded at the symmetric mass and superimposed, are indicated by closed symbols. The solid curve is the result of the estimation using production Q values.

II. 6. Semiclassical Origin of Quantum Shells in the Elliptic Billiard

Misu T., Arita K. and Matsuyanagi K.***

Cyclotron and Radioisotope Center, Tohoku University
*Department of Physics, Nagoya Institute of Technology**
*Department of Physics, Graduate School of Science, Kyoto University***

Introduction

The shell structure in finite fermion system like atomic nuclei and metallic clusters has been widely demonstrated in numerous calculations by using Strutinsky's shell correction method. The semiclassical periodic orbit theory (POT), developed by Gutzwiller[1,2] for chaotic systems, by Balian and Bloch[3] for cavities, and by Berry and Tabor[4] for integrable systems, is shown to be an useful tool to understand such shell effects and leads to the semiclassical interpretation of deformation process and equilibrium deformations of fermion systems. The POT also provides a link between quantum and classical mechanics in the form of the so-called trace formula, which expresses the oscillating parts of level density and energy in terms of sums over the classical periodic orbits. However, difficulties of the conventional POT, i.e., divergencies and discontinuities of the amplitudes in the trace formulas due to the bifurcations of the periodic orbits[5], have not yet been overcome. One faces these critical phenomena for some shapes of the potential well for which the orbits bifurcate into the ones and newly created periodic orbits with higher degeneracies. For instance, for the elliptic billiard it is due to the short diameter orbits bifurcating into the ones and hyperbolic orbits (see Fig. 1) and for the spheroidal cavities the equatorial orbits bifurcating into the ones and 3-dimensional orbits[6-10].

Recently, significance of these bifurcation effects for the emergence of the superdeformed shell structure in finite fermion systems was reported[9,10]. In order to varify the importance of such orbital bifurcations in the appearance of quantum shells one needs to construct a more general POT, which is capable of describing bifurcations of stable periodic orbits. We have recently developed and suggested a successfully modified POT starting from the trace formula in the phase space variables, and its theoretical details can be found elsewhere[11].

In this report, to stress the importance of orbital bifurcations in the emergence of deformed nuclear shell formations, we omit the details of our semiclassical frame works but only present below some quantitative results indicating the correspondence between quantum spectra and classical periodic orbits for the elliptic billiard.

Methods and Results

Numerical method for the spectra calculation

Single-particle energies ε of a particle of mass m moving freely inside of the elliptic boundary can be obtained by number of numerical methods. In the present analysis, we employed, in addition to the circular-wave decomposition method[9,10], the numerical procedure based on the separation of Schrödinger equation in elliptic coordinate system[12-14]. The coordinate transformation between the elliptic coordinates (u,v) and the cartesian coordinates (x,y) reads

$$x = f\cosh u\cos v,\ y = f\sinh u\sin v, \tag{1}$$

which represent the confocal ellipses with foci at $(0, \pm f)$. For the following discussion, we introduce the deformation parameter η defined as the ratio between major axis and minor axis under the area-conservation condition. In terms of the elliptic coordinates, Schrödinger equation can be separated into two ordinary differential equations and solved exactly. By imposing usual boundary conditions on the radial wave functions, one finds the eigenenergies ε.

Strutinsky's smoothed level densities and shell energies

In terms of the occupation particle number N one can also obtain the shell-structure energy δE defined as the difference between the sum of single-particle energies filling N states from the bottom of the well and the Strutinsky averaged energies, i.e.,

$$\delta E = 2\sum_{i=1}^{N}\varepsilon_i - \tilde{E}, \quad \tilde{E} = 2\int_{-\infty}^{\tilde{\varepsilon}_F} d\varepsilon'\varepsilon'\tilde{g}(\varepsilon'), \tag{2}$$

with the Fermi energy $\tilde{\varepsilon}_F$ satisfying

$$N = 2\int_{-\infty}^{\tilde{\varepsilon}_F} d\varepsilon'\tilde{g}(\varepsilon'). \tag{3}$$

Figure 2 illustrates the oscillating pattern of the shell-structure energy δE as functions of both deformation η and particle number N. It is clear from the figure that the distance between major shell gaps shrink with increasing deformation.

Shell Structure and Fourier Spectra

Single-particle equations of motion in the cavity are invariant with respect to the scaling transformation $(\mathbf{r},\mathbf{p},t)\rightarrow(\mathbf{r},\alpha\mathbf{p},\alpha^{-1}t)$. The action integral S_β for a periodic orbit β is proportional to its length L_β,

$$S_\beta\left(E = p^2/2m\right) = \oint_\beta dr\cdot p = pL_\beta = \hbar kL_\beta, \tag{4}$$

and the semiclassical trace formula for the level density $g_{scl}(\varepsilon)$ is written as

$$g_{scl}(\varepsilon) = \tilde{g}(\varepsilon) + \sum_{\beta} A_{\beta}(kR)\cos\left(kL_{\beta} - \frac{\pi}{2}\mu_{\beta} \right), \qquad (5)$$

where $\tilde{g}(\varepsilon)$ denotes the smooth part corresponding to the contribution of zero-length orbit, A_β the amplitude, R the radius at circular limit, and μ_β the Maslov phase.

In order to examine the classical-quantum correspondence on shell structure, one can perform the Fourier transform $F(L)$ of the quantum level density $g(\varepsilon)$ with respect to the wave number k,

$$F(L) = \int dk e^{-ikL} g(\varepsilon) e^{-\frac{1}{2}\left(\frac{k}{k_c}\right)^2}, \qquad (6)$$

which may be regarded as 'length spectrum' exhibiting peaks at lengths of individual periodic orbits. Here the Gaussian factor is imposed to smoothly cutoff the spectrum in high energy region. In numerical calculation, we use $k_c = k_{max}/\sqrt{2}$, k_{max} being the maximum wave number calculated. The above method of taking Fourier transform of the quantum level density is shown to be a powerful tool to investigate the role of classical periodic orbits in the appearance of shell fluctuations in quantum systems, and from such observations one can also extract the semiclassical contributions of individual periodic orbits.

Figure 3(a) demonstrates the deformation-dependence of Fourier amplitudes calculated from the quantum single-particle spectra. The enhancement of peaks indicates the greater contribution from the corresponding classical periodic orbits β of length L_β to the shell structure. Here closed orbits are classified by two positive integers (n_v, n_u), which represent number of rotations and vibrations with respect to two elliptic coordinates in one revolution. With increasing its deformation from a circular shape, the short diameter orbits of M revolutions M(1,2) also bifurcate into the ones and hyperbolic orbits at the critical axis ratios η_{bif} given by

$$\eta_{bif} = \frac{1}{\sin(\pi n_u / n_v)}. \qquad (7)$$

The length of those classical periodic orbits as a function of deformation can be calculated[7] as shown in Fig. 3(b). It is clearly seen from both figures that the bifurcations of stable periodic orbits give rise to the increase in Fourier amplitudes. The remarkable enhancements seen in the figure exactly coincide with the corresponding lengths of the newly created hyperbolic orbits, and hence stress the importance of the orbital bifurcations. In this context, similar enhancements for the case of a spheroidal cavity at superdeformed shape were also reported in the previous work[9] by some of the present authors, where superdeformed shell structure is associated with bifurcations of periodic orbits with two repetitions on the equatorial plane. In the present work, particular attention is paid to investigate such correlations between bifurcations of stable periodic orbits and quantum level-density oscillations.

Shell valley and constant-action lines

Suppose some classical periodic orbits β of length L_β are the dominant components in the semiclassical trace formula for oscillating level density, then the shell valley maxima/minima follows the constant-action lines $S_\beta(k,\eta)$=const of those dominating classical periodic trajectories. Refering to Eq. 5 such constant-action lines are determined by

$$kL_\beta - \pi\mu_\beta/2 = (2n+1)\pi, \quad n=0,1,2,... \qquad (8)$$

We shall now demonstrate the above dependence in Fig. 4(a), where the smoothed level densities are plotted on the k-η plane. As indicated in Fig. 4(b), it is interesting to note that the shell valley structures seen in Fig. 4(a) can be described by the constant-action lines of three major periodic orbits; near the circular limit the shell valleys vary along those of elliptic (mainly triangular and rhombic) orbits; in the right-half region of Fig. 4(a) the influence of newly created (1,4) hyperbolic orbits is visible; the contribution of short diameter orbits are less pronounced but certainly non-negligible throughout the considered range of deformation. The equality, Eq. 8, indicates the inverse-proportionality relation between the orbital length L_β and wave number k. As the length of a trajectory β increases, the values of k decrease and consequently the smoothed level densities show more oscillations. In particular, since the length of the (1,4) hyperbolic orbits gradually increases within $\eta \approx \sqrt{2} - 1.7$ and then slowly decreases for η>1.7, the corresponding constant-action lines also behave in the same manner, indicating the essential role of the orbital bifurcations in quantal shell formations.

Discussion

We performed the Fourier analysis on quantum level density and demonstrated the importance of bifurcations of the repeated short diameter orbit for the emergence of shell structure at large deformations. To support our conclusion in the frame work of semiclassical POT, we have recently improved the POT by taking into account the two additional (second and third) terms in the trace formula for the elliptic billiard[11]. The validity and usefulness of this approach have been demonstrated by the success in describing the bifurcations of the short diameters in the elliptic billiard. The semiclassical shell corrections obtained with our improved semiclassical approach are in good agreement with their quantum-mechanical counterparts[11], as shown in Fig. 4. Our investigation is currently extended to similar bifurcation effects in general axially-symmetric, but non-integrable cavities, such as more realistic shapes of nuclear fission.

References

1) Gutzwiller M. C., J. Math. Phys. **12** (1971) 343.
2) Gutzwiller M. C., *Chaos in Classical and Quantum Mechanics*, Springer-Verlag, New York, 1990.
3) Balian R. B,. and Bloch C., Ann. Phys. (N.Y.) **69** (1972) 76.
4) Berry V. M., and Tabor M., J. Phys. **A10** (1977) 371.
5) Brack M., and Bhaduri R. K., *Semiclassical Physics*, Addison and Wesley, Reading, 1997.
6) Strutinsky M. V., et al., Z. Phys. **A283** (1977) 269.
7) Okai S., Nishioka H. and Ohta M., Mem. Konan Univ. Sci. Ser. **37(1)** (1990) 29.
8) Nishioka H., Ohta M. and Okai S., Mem. Konan Univ. Sci. Ser. **38(2)** (1991) 1.
9) Arita K., and Matsuyanagi K., Nucl. Phys. **A592** (1995) 9.
10) Sugita A., Arita K. and Matsuyanagi K., Prog. Theor. Phys. **100** (1998) 597.
11) Magner A. G.,et al., to appear in Prog. Theor. Phys. Vol. 102, No.3.
12) Morse P. H. and Feshbach H., *Methods of theoretical physics*, McGraw-Hill, New York, 1953.
13) Misu T., Nazarewicz W. and Aberg S., Nucl. Phys. **A614** (1997) 44.
14) Merchant A. C., and Rae W. D. M., Nucl. Phys. **A 571** (1994) 43.

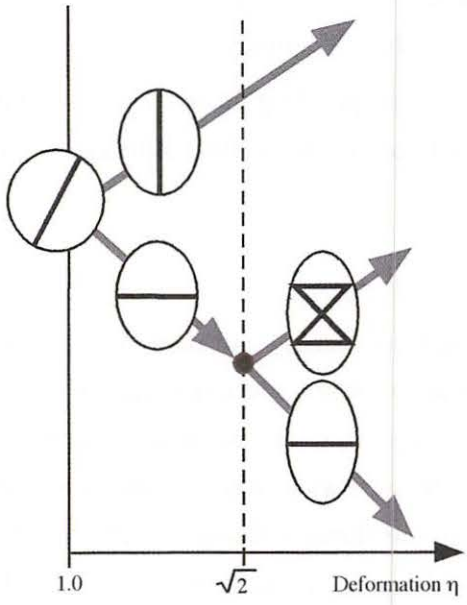

Fig. 1. Bifurcation of classical orbits in the elliptic billiard. Near the circular limit the diameter orbits bifurcate into long and short diameters. At superdeformation ($\eta = \sqrt{2}$) the repeated short diameter orbits bifurcate into the ones and hyperbolic (1,4) orbits.

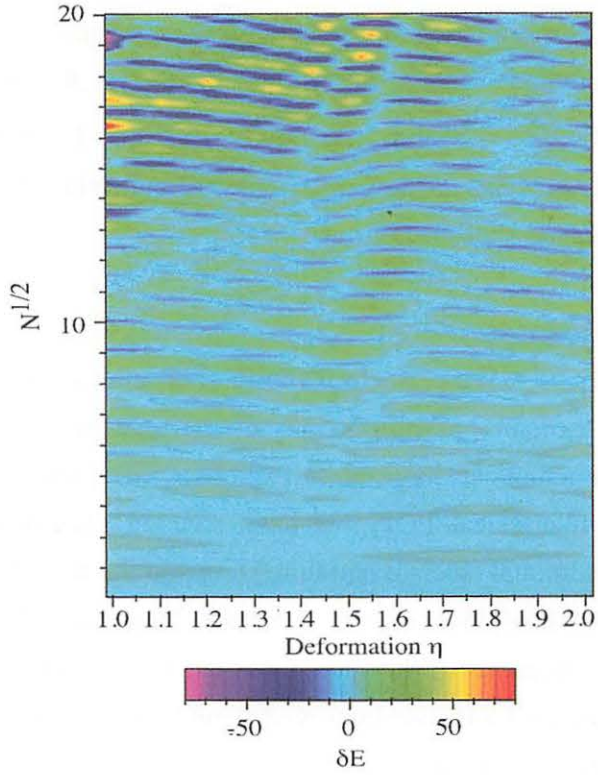

Fig. 2. Shell-structure energy δE plotted as function of both η and $N^{1/2}$.

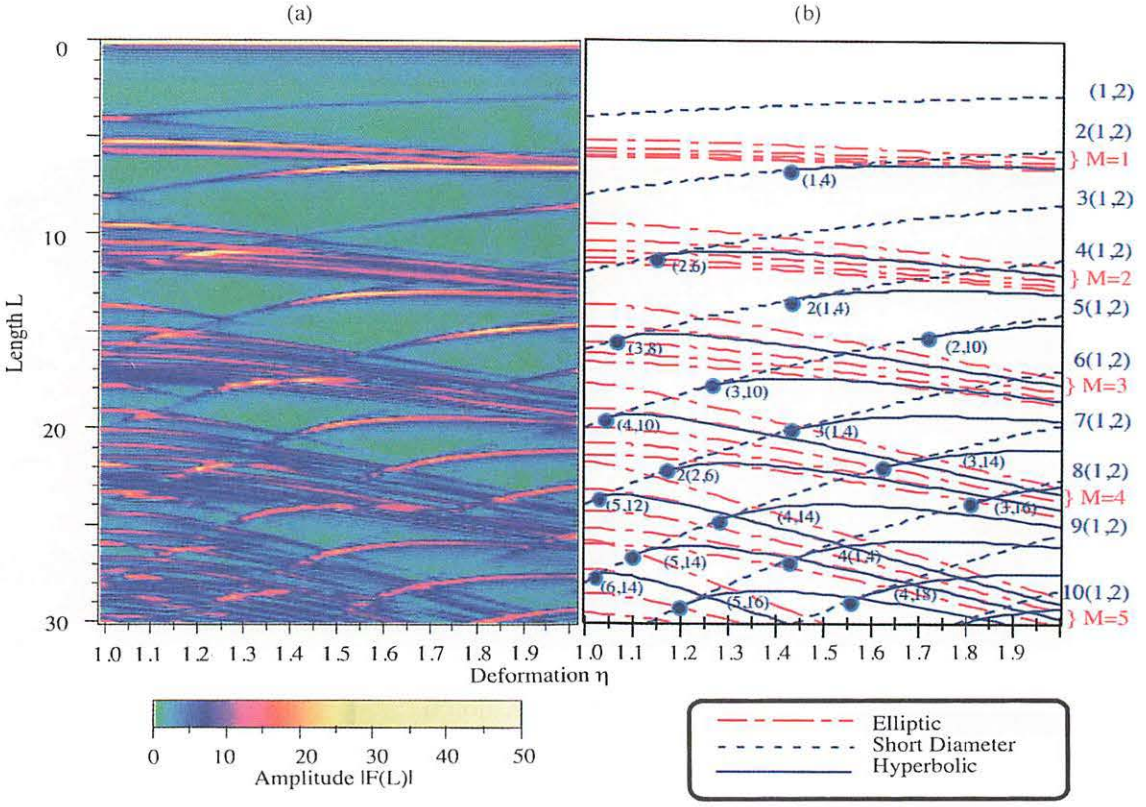

Fig. 3. (a) Modulus of the Fourier amplitudes plotted as functions of both L and η. (b) Lengths L of classical periodic orbits calculated as function of deformation η. Solid, dashed and dash-dotted lines correspond to hyperbolic, short-diameter, and elliptic orbits, respectively.

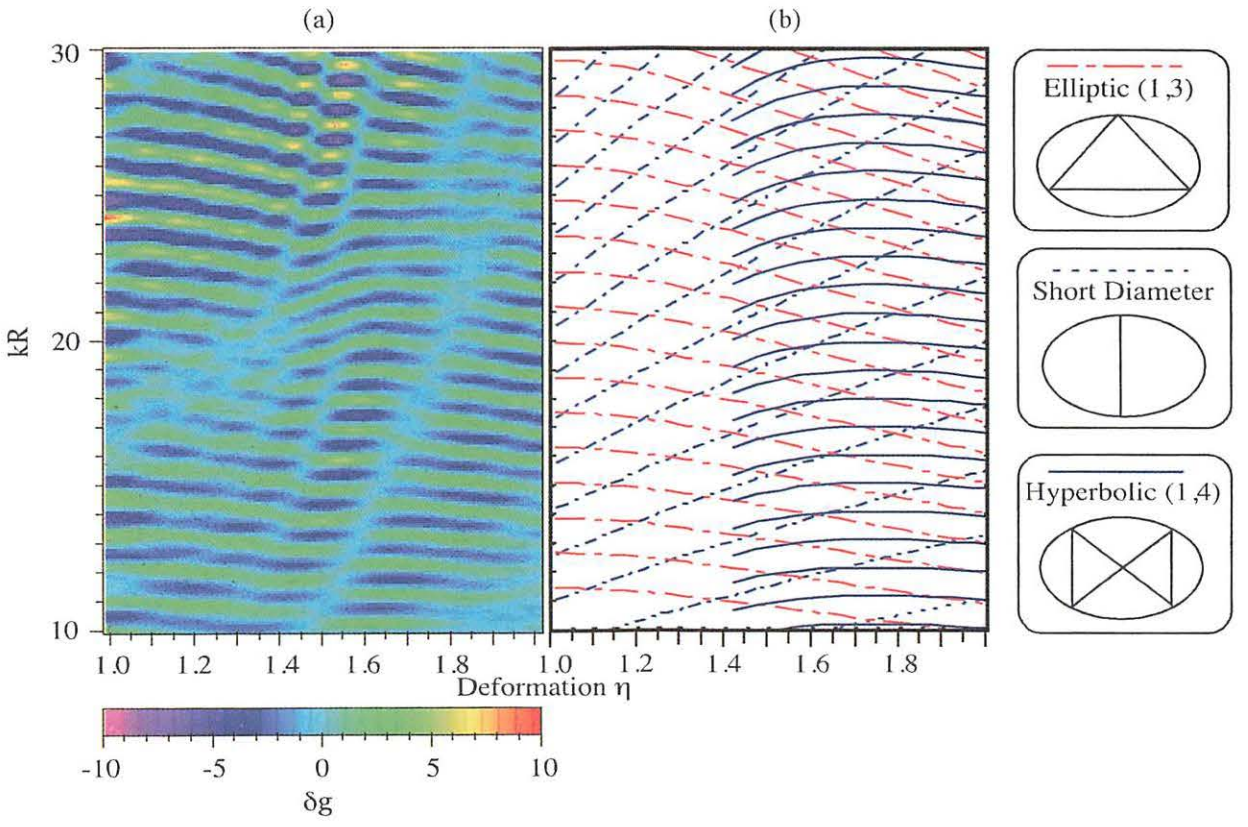

Fig. 4. (a) Smoothed level density plotted on the k-η plane. (b) Constant-action lines on the k-η plane for the elliptic (1,3) orbit (dash-dotted lines), the primitive short diameter (1,2) orbit (dotted lines) and the hyperbolic (1,4) orbit (solid lines).

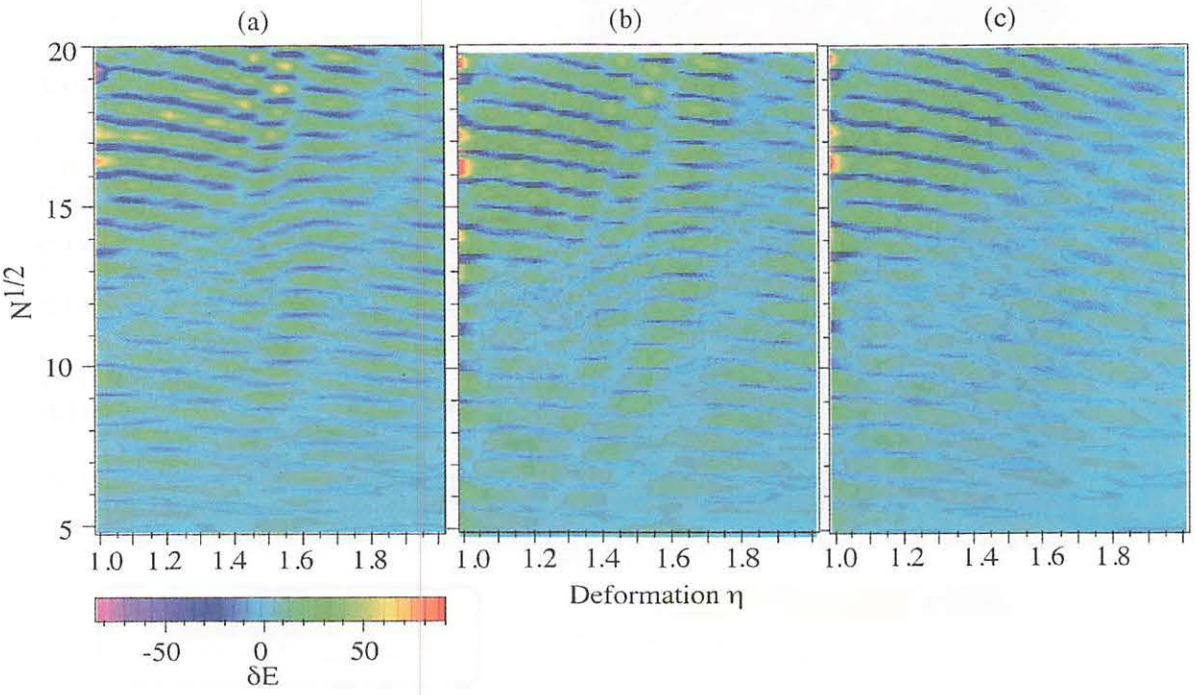

Fig. 5. Shell energy maps δE plotted as function of particle number N and deformation η. Quantum results (a) are compared with semiclassical results[11] with (b) and without (c) taking into account the bifurcating orbits, respectively.

II. 7. A Peak-intensity Oriented Least-squares Fitting

Fujita M. and Fujioka M.

Cyclotron and Radioisotope Center, Tohoku University

The least-squares method (LSM) is one of the most popular fitting technique for data analysis. For example, it is used to obtain peak intensities from measured spectrum in many fields. In order to apply LSM for such a situation, a fitting function must be determined. Generally, a peak shape can be considered as a Gaussian curve. Then three independent parameters are needed to determinate the Gaussian shape, and usually a parameter set of "height (h)", "average (x_0)" and " standard deviation (σ)" is used. Then the Gaussian is rewritten as

$$g(x) = h \cdot \exp\left[-\frac{1}{2}\left(\frac{x-x_0}{\sigma}\right)^2\right]. \tag{1}$$

A peak intensity (S) is obtained from these parameters using the relation,

$$S = \sqrt{2\pi}\, h \cdot \sigma .$$

Considering a quantity $u = f(x, y)$ where x and y are quantities having errors σ_x and σ_y, the variance σ_u^2 can be found as[1)]

$$\sigma_u^2 \cong \left(\frac{\partial f}{\partial x}\right)^2 \sigma_x^2 + \left(\frac{\partial f}{\partial y}\right)^2 \sigma_y^2 + 2cov(x,y)\frac{\partial f}{\partial x}\frac{\partial f}{\partial y} .$$

The errors therefore are added quadratically with a modifying term due to the covariance. Depending on its sign and magnitude, the covariance should increase or decrease the errors by appreciable amounts. A covariance can be calculated in the fitting procedure and a non-diagonal element of the error matrix should supply this information.

When an error of a peak intensity is calculated from those of the fitting parameters, one must take into account of the correlation among them. If a gross area of the Gaussian, instead of a height, is chosen as a parameter, one can determine easily the error of it, because diagonal element of the error matrix shows the square of the error. In that case, the Gaussian is rewritten as

$$f(x) = \frac{S}{\sqrt{2\pi}\,\sigma} \cdot \exp\left[-\frac{1}{2}\left(\frac{x-x_0}{\sigma}\right)^2\right]. \tag{2}$$

A sample spectrum, which is generated by random numbers, are fitted by function (1) and (2)

in Fig. 1, and the result of the error matrices are also shown in Table 1. Then the background component of the spectrum are considered as a quadratic function.

As a result, both fitting methods are seen to give the same peak area and the error of it, though the complication of the procedure to obtain it differs.

Reference

1) William R. Leo, Techniques for Nuclear and Particle Physics Experiments, pub. by Springer-Verlag (1987).

Table 1. External error matrices. A) and B) show the result with fitting function (1) and (2), respectively.

A)

σ	$0.197E^{-1}$	$-0.450E^{-3}$	-0.247	0.161	$-0.217E^{-1}$	$0.291E^{-3}$
x_0		$0.145E^{-1}$	$-0.338E^{-2}$	$0.702E^{-1}$	$-0.185E^{-2}$	$0.827E^{-5}$
h			65.7	7.14	-0.720	$0.717E^{-2}$
BG(constant)				22.3	-1.12	$0.975E^{-2}$
(first-order)					$0.830E^{-1}$	$-0.794E^{-3}$
(second-order)						$0.779E^{-5}$

B)

σ	$0.202E^{-1}$	$-0.366E^{-3}$	20.4	0.187	$-0.236E^{-1}$	$0.236E^{-3}$
x_0		$0.144E^{-1}$	-0.549	$0.764E^{-1}$	$-0.224E^{-2}$	$0.119E^{-4}$
S			$0.459E^{5}$	376	-44.1	0.441
BG(constant)				23.8	-1.20	$0.105E^{-1}$
(first-order)					$0.892E^{-1}$	$-0.852E^{-3}$
(second-order)						$0.834E^{-5}$

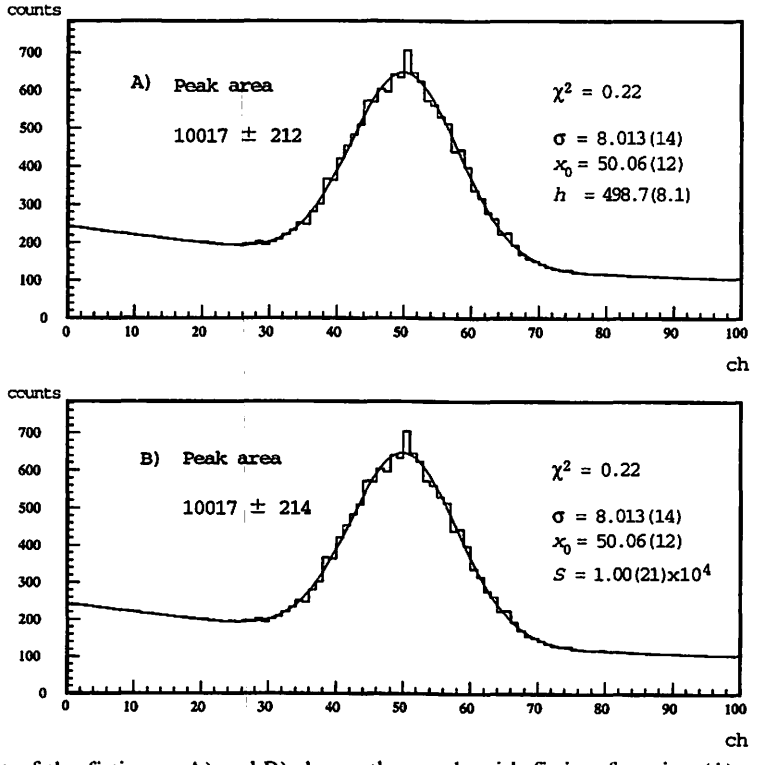

Fig. 1. Result of the fitting. A) and B) shows the result with fitting function (1) and (2) respectively.

II. 8. Schottkey-CdTe Detector (Pt/CdTe/In) for Angular Correlation Measurement

Hoshino T., Tanigaki M., Fujita M.*, Sonoda T., Baba T., Shinozuka T. * and Fujioka M. **

Depart~nent of Physics, Tohoku University
*Cyclotron and Radioisotope Center, Tohoku University**

CdTe has been known as a versatile semi-conductor. The use of semi-conductor, e.g. CdTe, has therefore been studied for application to gamma-ray spectrometry. Small size, good energy resolution and, above all, operation at room temperatures, render the CdTe detectors suitable for many angular correlation measurement system (e.g., crystal ring system). The present study is a pre-experiment for a crystal ring system. We tried to establish coincidence system, to investigate gamma-gamma angular correlation on the decay of ^{133}Ba with the CdTe detectors.

In the experiment, 7mmϕ×50mm CdTe detectors made in JAPAN-ENRGY [1] were used. The CdTe crystals in the detectors are 2mmx2mm×0.5mm Schottkey-CdTe (Pt/CdTe/In). One of the spectra with a CdTe detector is shown in Fig. 1.

The CdTe detectors were studied; leakage current data (I≈ lnA at 600V), intrinsic efficiencies (0.29% at gamma ray-356keV, 600V), spectra with time dependence, and gamma-gamma angular correlation data on the decay of ^{133}Ba.

As it is known, the longer the Schottkey-CdTe detectors are biased, the worse and worse becomes the energy resolution. (called as 'polarization effect'). This polarization effect recovers, once the detectors are de-biased and are re-biased[2]. So we made programs for automatic operating bias system.

The gamma-gamma angular correlation on the decay of ^{133}Ba were measured and investigated[3,4]; we used a ^{133}Ba gamma-ray source for system verification. The directional correlation of the 356keV-81 keV gamma-gamma cascade has been measured as

$$W(\theta) = 1 + (0.038 \pm 0.016)P_2(\cos\theta) + (0.019 \pm 0.021)\,P_4(\cos\theta).$$

This experimental data agreed with the past experimental data (see Fig. 2). The gamma-gamma angular correlation measurement with CdTe detectors is therefore available.

It is expected that the crystal ring system be developed on the base of this experiment.

References

1) Private communication from Ozaki T. (Japan Energy Ltd.).
2) Arlt R., Rundquist D. E., NuclearInstruments and Methodsin Physics Research **A380** (1996) 455.
3) Bodenstedt E., Komer H. J. and Matthias E., Nuclear Physics **11** (1959) 584.
4) Thun J. E., Tornkvist S., Bonde Nielsen K., Snellman H., Falk F. and Mocoroa A., Nuclear Physics **88** (1966) 289.

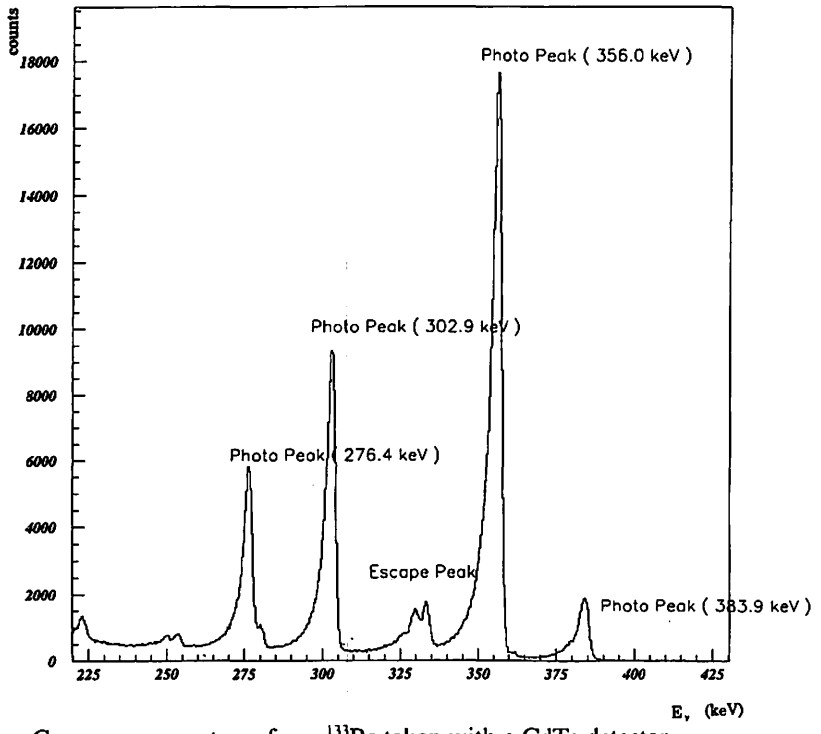

Fig. 1. Gamma-ray spectrum from ^{133}Ba taken with a CdTe detector.

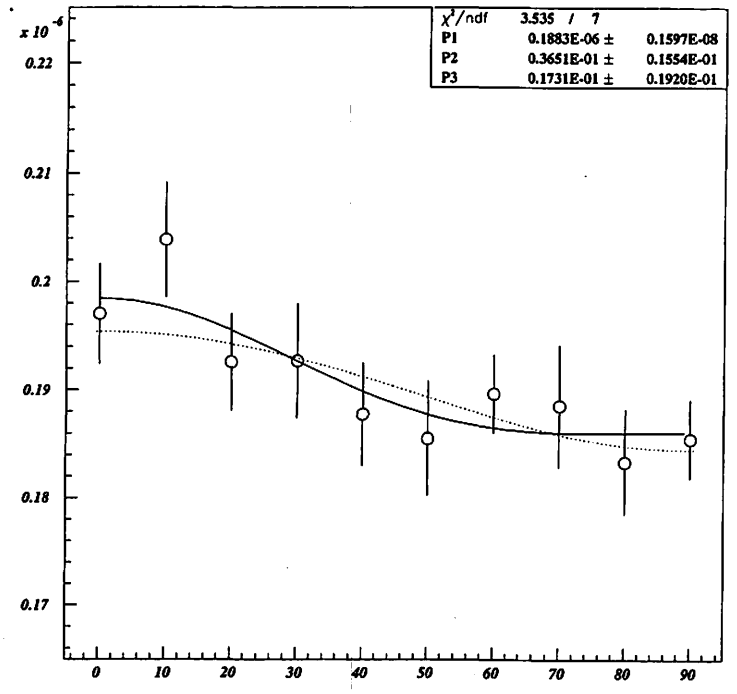

Fig. 2. 356KeV-81KeV angular correlation in ^{133}Cs taken three CdTe detectors.

II. 9. Preparation of ^{111}In Source by a Melting Method for PAC Spectroscopy

Hanada R.

Institute for Materials Research, Tohoku University

Introduction

Preparation of ^{111}In sources is one of the most important step to apply PAC spectroscopy to various topics in materials science or solid state physics. So far the present author has applied three different methods. Namely, (1) the nuclear reaction method (2) the diffusion method and (3) the implantation method. Among them, the implantation method with an ISOL (isotope separator) is the most convenient method since ^{111}In can be implanted into any materials. However, as has been shown by the present author, the implanted ^{111}In with several 10 keV was found to diffuse away from Fe specimens at about 500C[1]. So for the research subjects on Fe which need heat treatments above this temperature, some other method of specimen preparation must be devised. Recently, a Krakow-Göttingen group has reported a simple but an unique method of the preparation. Namely, they have melted Fe foils with ^{111}In deposited on the surface[2]. The foil is melted so fast that part of ^{111}In remain in the bulk before they evaporated away thus forming a good PAC source with a high enough activity for the spectroscopy. They have applied the method to determine the solubility of In or Rh in Fe.

This method of the fast melting has been applied by the present author of that technical part will be described in this report. The results of the applications to (1) Fe-carbon martensite (2) Fe-Si alloys (3) other Fe-alloys (4) Ni-alloys and (5) Si-alloys will be described in the following 5 reports.

Experimental

Fe foils, 25×25 mm^2×50μm, were prepared from a Johnson Matthey high purity rod. 0.02-0.1ml of $^{111}InCl_2$ (the specific activity, 4mCi/ml) was dropped and dried on the surface. In the case of alloy study, a controlled amount of alloying elements (either the element itself or the Fe mother alloys with the known alloy concentration) was added to it with weighing by a micro-balance. Subsequently, the foil is folded several times to form "a ball" as called by K-G group with about 5mm diameter. The ball was placed in an alumina crucible of which diameter is 10mm around which 1mmϕ×180mm Ta wire was wounded about 4-5 times. Some thermal insulation by isolite around the crucible has been found helpful to reduce the power input. The crucible was

set in a transparent quartz tube (22mmϕ×700mm) which is known to be stable against a thermal shock. The tube was evacuated and flushed by Ar gas several times to prevent the oxidation during the subsequent heating. Next, 40A of AC current were applied to the Ta heater to heat up the crucible. The temperature of the crucible, monitored by a two-color thermometer, reached to 1600-1800C within 5 sec. The crucible was kept at the temperature for several 10 sec and the current was switched off. The total power input was estimated as 400W and the total running time was less than 90sec. For the case of pure Fe, the foil was found to melt to form a sphere with about 3mm diameter. The ^{111}In activity dissolved in the specimen was found high enough to measure several PAC spectra. The specimen shows a metallic color to verify the oxidation during the melting procedure was negligible. The yield of ^{111}In (the ratio of ^{111}In solved in the specimen/ that initially applied on the surface) was found somewhat to depend strongly on the kind of the alloying element, of which details will be described later.

The same procedure was also applied to Ni and Si. For the case of Si, the powder with the alloying elements was pressed to form a disk to which ^{111}In was dropped and dried before the melting. BN (boron nitride) crucibles were used for the Si case since melted Si was found to sinter to the alumina crucible.

Results and Discussion

PAC Spectrum for pure Fe, Ni and Si

Fig. 1 shows PAC spectra for a pure Fe specimen prepared by the present melting method and the corresponding Fourier spectra in Fig. 2. All spectra are nothing but that of ^{111}In at the substitutional site in α-Fe (bcc). Namely ^{111}In are at the substitutional site after the melting procedure and give rise to the 11 nsec precession signal with the hyperfine field of -39 T. The amplitude of the precession signal is about 2 times larger than that after the implantation. This shows that the melting method is superior to the implantation method in that no damage effect is present. (An annealing at 400C is necessary after the implantation to obtain the same amplitude as in Fig. 1. see Ref. 3). No significant change is present in the spectra after the heat treatments in Fig. 1 (slow cool, quenching and annealing at several temperatures). Namely, any change in the spectra in the following 3 reports for the Fe alloys after the heat treatments may be taken as due to the effect of the alloying elements.

The only difference from the spectrum after the implantation is the presence of the low frequency component of several 10 M rads^{-1} as shown in Fig. 2, which is noticed as the upward bending of the spectrum base line near t=0 in Fig. 1. The cause of the low frequency component is not known at present. The clusters of ^{111}In is one possibility. Also one notes the amplitude of the 1st harmonic ($2\omega_L$) is much smaller than that expected for the present measurement. Namely, without an external magnetic field, the amplitude of the 1st harmonic should be the same with the basic (ω_L). This is probably due to the poor time resolution in the present set up using NaI detectors and not due to the method of the specimen preparation. Namely, such a lack of the $2\omega_L$

term has also been noticed in the implanted specimens. The lack, however, is not serious problem since most of the new components in Fe alloys are found near the basic.

For the case of pure Ni, a large precession signal was found, of which amplitude and the period are exactly the same with those in the specimens prepared by a diffusion or implantation method. So the present melting method is also useful to Ni and applied to several Ni-alloys, the details of which will be described in one of the following reports. The cold work at RT or hydrogen charging on Ni, however, caused only a slight change in the spectra. So no further details will be reported here.

For the case of pure Si, a flat spectrum without any precession signal was obtained. This is reasonable since no EFG should be present in the substitutional site of Si cubic lattice. The addition of Cu, however, was found to give rise to a clear precession signal, of which details will be described in one of following reports.

The yield dependence on alloying elements

During the several runs in the present melting method, the yield of ^{111}In was noticed strongly to depend on the kind of the alloying element added on the Fe foil or Si disk. Since no systematic study has been performed on the subject, only qualitative and empirical results will be remarked as;

Fe-host: Very high yield: Mn, high: Ti, V, Nb, Cu, medium: Si low:C, B, Mo, As, P.

Si-host: Very high yield: Au, high: Cu, Mn, medium: Fe, low As, P, B.

Once one notices the tendency, it can be utilized to adjust the amount of the ^{111}In solution to obtain a PAC specimen with a proper amount of the activity. For instance, only 0.01ml of ^{111}In solution was used for Fe-Mn alloy contrary to Fe-C alloys where 0.2ml was necessary. So in a favorable combination of alloying elements, about 10 specimens can be prepared using 1 ml ^{111}In solution.

For Ni alloys, the yield was found as high as 30 %. So, ^{111}In solution of less than 0.01 ml was necessary to prepare the PAC Source. Also volatile elements as As, P were noticed to evaporate away from the specimens during the melting procedure and hence it is likely that alloys with the aimed composition have not been formed.

With proper modifications, this method of melting for PAC spectroscopy source preparation may be extended to other elements of which melting point is below 1600C. (Fe: 1535C, Si: 1410C, Ni: 1453C) In principle, however, the melting method can not be applied to single crystals or amorphous alloys.

Further works are now in progress to develop the melting method.

Acknowledgement

The author is indebted to Professor P.Wodniecki (H. Niewodniczanski Institute of Nuclear Physics, Krakow, Poland) for his specific information concerning the melting method.

References

1) Hanada R., CYRIC Annual Report-1997, p40 (1998).
2) Wodniecki P., Wodnieka B., Kuliñska A., Lieb K. P., Neubauer M. and Uhrmacher M., to be published in Hyp. Int. (Proc. Durban Conf. On HFI-1998) 1999.
3) Hanada R., CYRIC Annual Report-1995, p36 (1996).

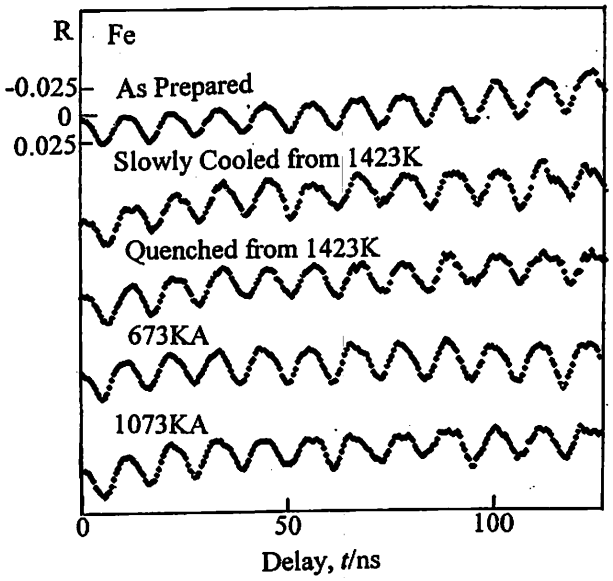

Fig. 1. PAC spectrum for pure Fe prepared by the melting method.

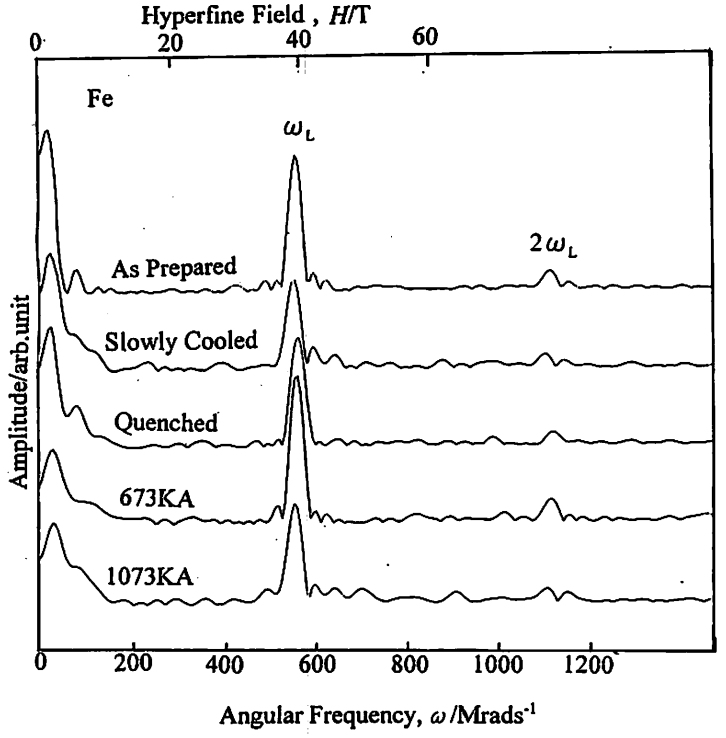

Fig. 2. Corresponding Fourier spectrum for Fig. 1.

II. 10. PAC Spectroscopy of Iron-Carbon Martensite

Hanada R.

Institute for Materials Research, Tohoku University

Introduction

Fe-C martensite has been a subject of materials science for a long time, since the formation of martensite is utilized to harden steels as best exemplified by the process of manufacturing Japanese sword. The bcc (body centered cubic) α-Fe transforms into fcc (face centered cubic)γ-Fe at 910C. If carbon is present and also the specimen is cooled quite fast (quenched) across the transformation temperature, an intermediate bct (body centered tetragonal) phase is formed which is named as martensite phase and has been known to cause the steels hardening.

Fe-C martensite has been extensively studied by Mössbauer spectroscopy. The accomplishment and the controversy among research groups with the spectroscopy have been summarized in Ref. 1.

So far no PAC spectroscopy has been performed on Fe-C martensite and hence attempted in the present. This kind of study has become possible only with the application of the new technique of PAC specimen preparation, namely, the melting method, of which details are described in a preceding report.

Experimental

Fe-C alloys for the ^{111}In PAC spectroscopy were prepared by the method in the preceding report. Namely, graphite powder (C) or the powder of Fe-C mother alloy (C content 4.7wt%) was deposited on a Fe foils together with ^{111}In. Since no significant difference was noticed in the results between them, the latter method was usually utilized since C distribution is expected more uniform. Although several runs have been performed, here the result on a specimen with 2-wt % C will be reported. As well known from the Fe-C phase diagram, the maximum solubility of C in γphase Fe is 2.08wt% (8.99at.%) at 1154C. So the effect of C on the PAC spectrum is expected to be maximum at this concentration. The results on other alloys with different C concentrations are found qualitatively the same with the present.

After measuring the spectrum right after the melting, the specimen was quenched from 1150C into ice brine to form the martensite phase. Also an isochronal annealing between RT and

600C(80C/30min) was given to the specimen. After each heat treatment, PAC spectrum was measured at RT without an external magnetic field. As shown in the preceding report, no significant change was observed for pure Fe specimen given the similar heat treatment. So any change in the present Fe-C alloys should be ascribed to the effect of C.

Result

Fig. 1 shows PAC spectra for the Fe-C alloy after several heat treatments. Right after the specimen preparation by the melting method, the spectrum is that of ^{111}In at the substitutional site (S-site) of α-Fe. Namely, the cooling rate after the melting is not fast enough to retain C atoms as a solid solution. All C atoms precipitate as Fe_3C (cementite) and hence only few of them are near ^{111}In probes. So the hyperfine field at most of ^{111}In site is the same with that in pure Fe. This is clearly shown in Fig. 2, Fourier spectrum for Fig. 1, where only the S component is prominent at-39T except the low frequency component of which nature is speculated in the preceding report.

After the quenching into an ice brine from 1150C, namely with the formation of martensite, the PAC spectrum shows a significant change of the amplitude damping as shown in Fig. 1 (the 2nd spectrum). This trend of the amplitude damping is clearly observed up to the delay time 70ns in the 3rd spectrum (after the annealing at 80C). Also note in the spectrum, the amplitude tends to recovers between the delay time 70 and 120ns. Namely we are observing a beating phenomenon in the 3rd spectrum. The cause of the amplitude beating is well understood if the corresponding Fourier spectra (the 3rd in Fig. 2) are examined. Namely, in that Fourier spectrum , two satellites, the one below ω_L and the other above ω_L, take place to cause the beating. As well known, the superposition of multiple cosine curves with slightly different angular frequency results in the beating which appears as amplitude damping near the delay time t=0 and the recovery with increasing time. Indeed, such a beating can be reproduced in the calculated PAC spectrum with the hyperfine distributions with satellites. (See a following report for the comparison between calculated and measured spectra for several Fe alloys.) The angular frequency ω_L is directly related to the hyperfine field H as $\omega_L=g\mu H/\hbar$ in the present magnetic interaction. So the present results have revealed that two new sites with slightly different hyperfine field than that of S site take place in martensite, of which nature will be discussed in the next section.

Discussion

Nature of the Satellites

Since Fe-C alloys have been extensively studied by Mössbauer spectroscopy using ^{57}Fe probes and the interpretation of the similar satellites in the spectrum has been well established, we will apply their argument to the present ^{111}In probe case.

In the bct martensite phase, the interstitial C atoms occupy the octahedral site. So there

exist two Fe atoms at the 1st nearest site to C atom and four Fe atoms in the 2nd neighbor site. C atom pushes away the 1st neighbor Fe atoms resulting in the bct structure elongated along the c-axis. The Fe atoms at the 2nd neighbor site are pushed toward to C atom because the repulsive force by the 1st neighbor Fe atoms are reduced. The hyperfine field of Fe nucleus strongly depends on the distance between Fe atoms. So if one sums up the contribution of neighboring Fe atoms to the hyperfine field with the presence of the C atom, the reduction in the 1st neighbor and the increase in the 2nd neighbors result in. This may be directly applied to the present ^{111}In case with substituting Fe atoms in the 1st or 2nd neighbor Fe atoms. Namely, the component with the lower hyperfine field corresponds to the ^{111}In at the 1st neighbor to C atom and the higher to the 2nd neighbor. If ^{111}In are randomly distributed in the lattice, namely neither attractive nor repulsive to C atoms, the probability ratio for them to occupy 1st and 2nd neighbor is 1:2. This relation seems to be qualitatively fulfilled in the present experiment result, as the higher frequency population is larger than that of the lower as sketched in Fig. 2.

The annealing behavior of the present PAC spectroscopy is also in accord with the proposal that the beating is caused by martensite. Namely as shown by a resistivity measurement, C atoms in the martensite precipitates to ε carbide between RT and 120C and further re-precipitates to cementite below 400C[2]. The satellites also show the same annealing behavior that they exist in the as quenched state or after 80C annealing but disappear after 120C annealing as shown in Fig. 2 as well as in Fig. 1 where no beating is present after 120C annealing. Namely C atoms coagulate to form ε carbides at 120C and hence the lattice recovers to the bcc α phase. Since α phase component is still present after the C precipitation, one can conclude that ^{111}In are still in the bulk not in the precipitates.

After the annealing at 600C, where ^{111}In have been known to migrate a long distance in Fe [3], however, the S component is reduced to show that part of them migrates to some unknown sites. These ^{111}In may give rise to several components seen in Fig. 2, though the reproducibility of them must be examined in the further study.

References

1) Ron M., : "Iron-Carbon and Iron Nitrogen System" in Application of Mössbauer Spectroscopy vol.II p329 ed by Cohen R. L., Academic Press (1980).
2) Fujita F. E., : "Mössbauer Spectroscopy in Physical Metullurgy" in Mössbauer spectroscopy p201 ed by Gonser U., pub. by Springer Verlag (1975).
3) Hanada R., : CYRIC-Annual Report 1997, p40 (1998).

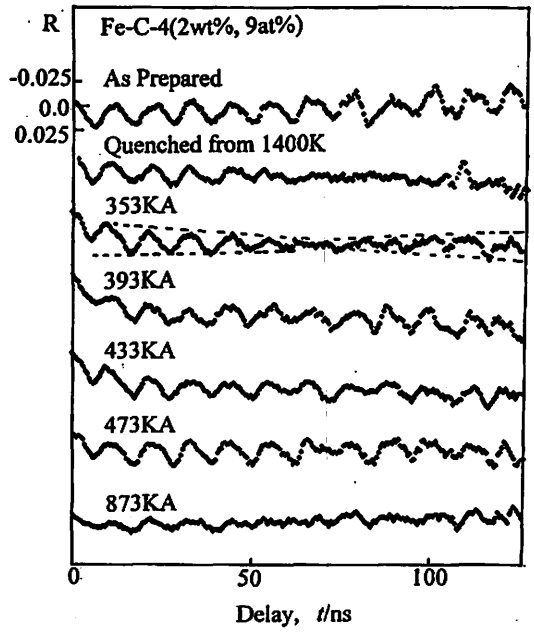

Fig. 1. PAC spectrum for a Fe-C alloy after various heat treatments.

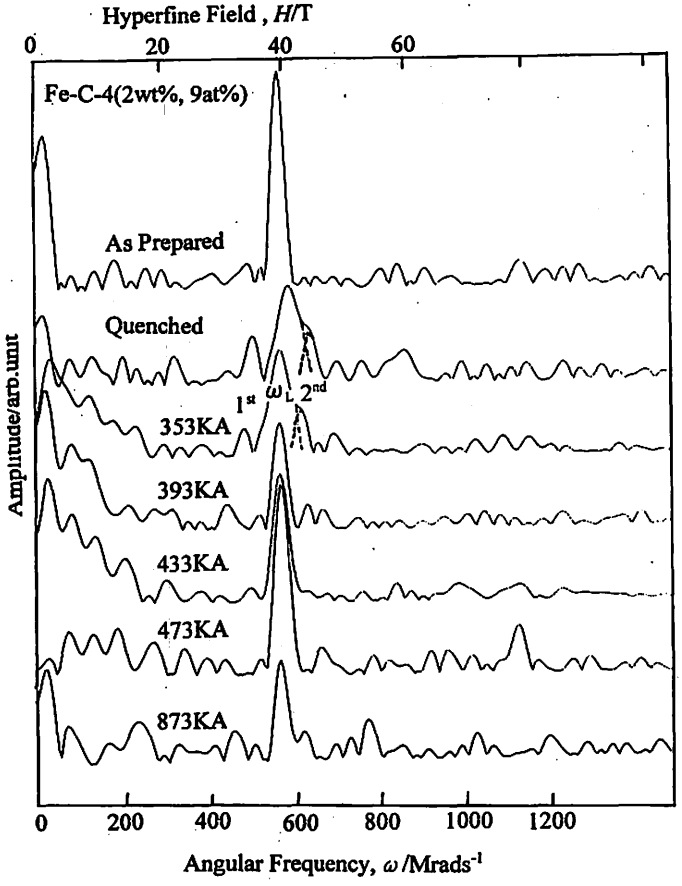

Fig. 2. Corresponding Fourier spectra for Fig. 1.

II. PAC Spectroscopy of Fe-Si Alloys

Hanada R.

Institute for Materials Research, Tohoku University

Introduction

Fe-Si alloys have been one of the most extensively studied materials because of its use as transformers core. Also it is one of the oldest materials studied by Mössbauer spectroscopy[1]. Unfortunately, to the knowledge of the preset author, no PAC spectroscopy has yet been reported and hence attempted here.

Also the author has reported results of Mössbauer and PAC spectroscopy on several Fe based amorphous alloys[2]. The alloying elements are mainly Si and B and so the study of the crystalline Fe-Si alloys reported here will be useful to examine the role of Si in the magnetic properties of the amorphous alloys.

Experimental

Fe-Si alloys for PAC specroscopy were prepared by the melting method as described in the preceding report. Namely, a known amount of Fe-Si mother alloy (75wt. % Si) powder was mixed with ^{111}In solution on a Fe foils and melted in an alumina crucible. Four alloys of which Si concentrations were between 4 and 14 at. % were prepared. Several heat treatments between 400C and 1150C followed by quenching to ice brine or fast cooling by removing the furnace were given to each specimen for the PAC spectroscopy. Since the hyperfine field distribution was found not to depend on the heat treatment strongly, only representative examples will be reported here.

Result

Fig. 1 shows the PAC spectra for four Fe-Si alloys with different Si concentrations together with that for pure Fe for comparison. As revealed in Fig. 1, amplitude damping is present only for PAC spectra in Si alloys. The rate of the damping is enhanced with the Si concentration. Fig. 2 shows the corresponding Fourier spectra revealing the cause of the damping. Namely, a new component develops below the substitutional (S) component. This new component is observed as a small bulge in the 4 at.% alloy but develops to comparable amplitude with the S component in 9 at.% alloy. For the alloys of 12 or 14 at.%, the S component almost disappears and several components with the lower hyperfine fields

develops.

These observations are in agreement with the proposed model of the effect of alloying elements on the hyperfine field by Mössbauer spectroscopy. Namely, the substitution of Fe atoms by non-magnetic impurities as Si reduces the hyperfine field at the nucleus of neighboring Fe atoms. Since a quantitative model has already been established[3], this will be applied to the present PAC case.

Discussion

Hyperfine Field in Fe-Si Alloys by PAC Spectroscopy.

Let us consider a bcc α-Fe lattice of which the body centered site is occupied by the probe ^{111}In. Then we have eight nearest neighbors sites occupied by Fe atoms in pure Fe. With adding alloying elements, n sites out of the eight sites are occupied by the alloying element. The probability that the n sites are occupied is given by a binomial distribution as eq. (1).

$$P(n,c) = {}_8C_n\, c^n(1-c)^{8-n} \qquad (1)$$

where c is the concentration of the alloying element in atomic fraction. Eq. (1) is shown in Fig. 3 as a function of c. The formula is based on an assumption that the alloying element atoms distribute randomly in the Fe lattice. This assumption is correct for ^{57}Fe probe in Fe alloy but not necessarily holds for the present ^{111}In probes. So any deviation from the assumption may tell us that the alloying atoms act as repulsive or attractive to the ^{111}In probe atoms.

Next let us assume that the hyperfine field at the ^{111}In nucleus is proportional to the number of Fe atoms at the 1st nearest neighbor 8 sites. (Some models take into account the 2nd nearest neighbor 6 sites additionally thus 14 Fe atoms contribute to the hyperfine field but neglected here[4]). Then, the hyperfine field at the ^{111}In with n alloying atoms is given as eq (2).

$$F(H,n,w) = (w/2)^2/\,[(H-H_0(1-n/8))^2+(w/2)^2] \qquad (2)$$

Here, a Lorentz distribution is assumed for the hyperfine field with the FWHM, w. H_0 is the hyperfine field for Fe atoms with no impurity in the nearest neighbor. Then the hyperfine field distribution in the alloy of the concentration c is given as eq (3).

$$HFD(H,c,w) = \sum_n P(n,c)\, F(H,n,w) \qquad (3)$$

The eq. (3) was calculated as in Fig. 4 as the Si concentration as the parameter. The w was

fixed at 10% of H_0 typically observed in Mössbauer spectrum. The calculated results show a qualitative agreement with the observed in Fig. 2 up to the concentration of 12 at. % in a sense that 1,2 and 3 Si components gradually grow with the concentration. The result for 14at. % alloy shows, however, a deviation from the calculated. Namely, a low frequency component centered at around $H_0/2$ dominates with the population exceeding the calculated. Inspection of the Fe-Si phase diagram reveals that ordered phases are formed in this range of Si concentration, the one is FeSi (B2 type) and the other is Fe_3Si (DO_3 type). For FeSi, the Fe atom in the body-centered position is substituted by Si atom. This structure is not ferromagnetic and hence not considered here. For Fe_3Si, four body centered Fe atoms out of eight bcc unit cells are substituted by Si atoms. So four Si and four Fe atoms surround the half of the Fe sites. So within the present naive model of the hyperfine field, one can expect $H_0/2$ hyperfine field for the ^{111}In in the ordered structure Fe_3Si in agreement with the present result for 14 at% alloy.

Comparison with Amorphous Alloys.

In the present light of the Fe-Si alloys study that are definitely crystalline, some remark can be made on the PAC spectrum for Fe based amorphous alloys reported by the present author. Although not shown here, the PAC spectra for amorphous alloys, of which alloying elements are Si and B (Si+B=~20at. %), have shown quite similar damping signals that can not be distinguished from the present on the crystalline. This strongly suggests that the non-magnetic alloying elements are the primary cause for the damping in the amorphous alloys and the non-crystalline nature is only the secondary. Namely, primarily, the number of the alloying element atoms around the probe determines the mean value of the hyperfine field. Secondarily, the broadening of the hyperfine field, w, due to the non-crystalline nature determines the hyperfine distribution around the mean value. Indeed, one can distinguish 1,2 and 3 Si components in the Fourier spectra for the present crystalline alloys but not in those for amorphous alloys. Namely, the width w becomes so large in amorphous alloys that each components merge into one broad distribution of Gaussian type. It should be noted that the non-crystalline nature is too much stressed to explain the magnetic properties of amorphous alloys and most of them are due to the high concentration of alloying elements[5].

The present result on Fe-Si is very encouraging to apply the PAC technique to study the hyperfine interactions in magnetic materials. Since only a few 100 mg of the specimen is needed for the spectroscopy, the preparation of alloys, the heat treatments etc can be performed rather easily. Also with the progress of the damped signal analysis, new components might be discovered in the Fourier spectra. This may give a new insight for the hyperfine field distribution around an impurity in Fe or other magnetic materials. Further works are now in progress.

References

1) Stearns M. B., Phys. Rev. **129**, 1136 (1963).
2) Hanada R., CYRIC Annual Report 1996 p **44** (1997).
3) Mössbauer spectoroscopy ed. by Gonser U., Springer-Verlag (1975).
4) Wertheim G. K., et al Phys. Rev. Lett. **12**, **24**, (1964).
5) Chikazumi S., *Physics of Ferromagnetism* vol. I. chapt. 4-11 Syokabo 1978.

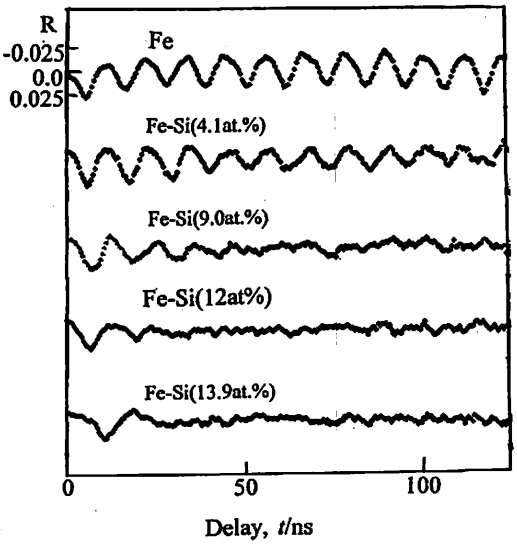

Fig. 1. PAC spectra for Fe-Si alloys.

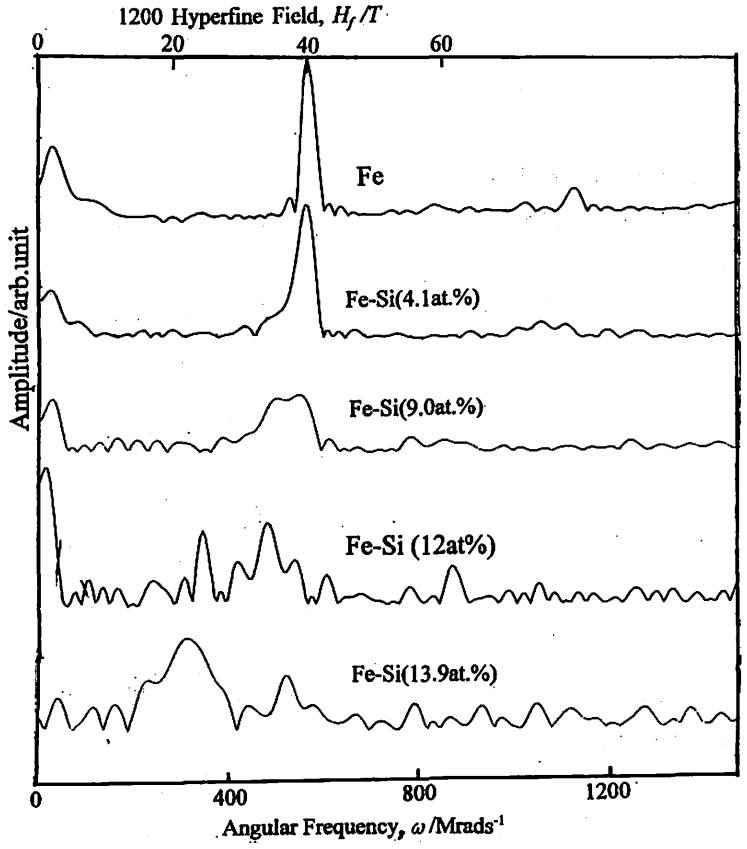

Fig. 2. Corresponding Fourier spectra for Fig. 1.

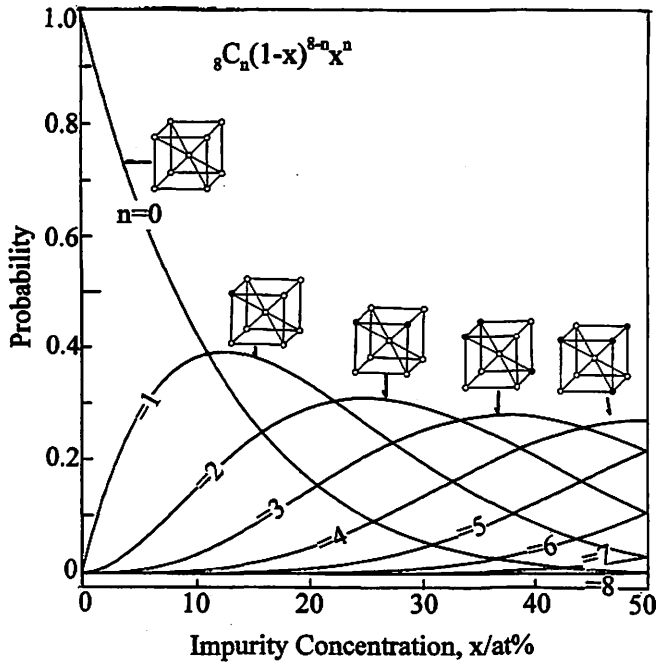

Fig. 3. Calculated binomial distribution as a function of alloying element concentration.

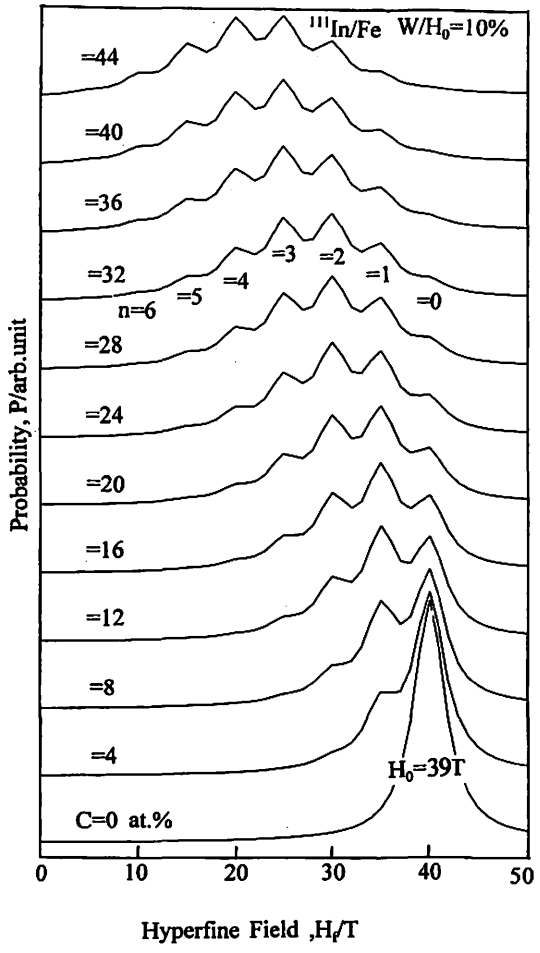

Fig. 4. Calculated hyperfine distribution for alloys. (For details see text).

II. 12. PAC Spectroscopy of Fe Binary Alloys

Hanada R.

Institute for Materials Research, Tohoku University

Introduction

As shown in previous two reports on Fe-C martensite and Fe-Si alloys, the method of melting for ^{111}In PAC source is quite useful to study effects of impurities on the hyperfine field of Fe. In this report, the results of PAC spectroscopy on several other Fe binary alloys prepared by the melting method will be described. Although only a limited number of Fe binary alloys have been studied, some general trend has been observed in the PAC spectra. In these PAC spectrum measurements in the alloys as well as in Fe-C or Fe-Si alloys, measured PAC spectra show several variation. Namely, (i) only with a low frequency component (ii) the one looks like to that in pure α-Fe (iii) a precession with a monotonous damping (a simple decay of the amplitude) (iv) a precession with a beating (a damping near the delay time 0 with the amplitude recovery at the later delay time). The spectra for the case (iii) and (iv) will be referred as S like spectrum since the period of the precession is more or less alike with that in pure Fe.

The case (i) and (ii) will be interpreted as due to the precipitation of impurities. Namely, there exists an interaction between ^{111}In and precipitates for the case (i) and no interaction for the case (ii).

The case (iii) and (iv) will be interpreted as due to the change in the hyperfine field by impurities in the α phase of Fe. Examples of the analysis for these cases have already given in Fe-C or Fe-Si cases in this volume.

Experimental

The alloying elements investigated are in the concentration in at. % ;

(I) B(4.4), Au(3.3) and Nb (0.44, 4.2, 12): limited solubility in Fe.

(II) Ti (4.4, 8.0, 12.0), Mo (8.0), Be (4.5): a high solubility at a high T and a low one at low T.

(III) V(3.7, 8.3, 12.0) Cr(4.8), Ni(3.4): a high solubility at all T.

Here, the alloying elements are classified according to their solid solubility in Fe[1], of that details will be discussed later.

The specimens were prepared by the method described in a preceding report. After

the spectrum measurement in the as prepared state, the specimen was quenched with a rate of several 10^4K/s into an ice brine when the temperature is above 1000C. When it is below 1000C, they were annealed for 4 hrs and cooled fast (several 10^2K/s) by moving the furnace. The spectrum was measured after each treatment at RT without an external magnetic field.

Result and Discussion

Fe-Ti Alloys

Fig. 1 shows the PAC spectrum for Fe-Ti (8.0at. %) alloy and the corresponding Fourier spectrum in Fig. 2. Although many spectrum measurements were performed for the alloys described above, this Fe-Ti system represents the basic aspects of them. Namely after the quench from 1150C, we see a precession pattern of that period is close to that of α-Fe although the amplitude shows a trend of the beating. The corresponding Fourier spectrum shows that the spectrum mainly consists of two components, one for that of pure Fe (S component) and the other a satellite. The magnitude of the hyperfine field for the satellite is 87% of that for the S component. So as shown in a previous report on Fe-Si alloys, the satellite can be concluded as due to the ^{111}In that has one Ti atom which substitutes one of 8 Fe atoms in the nearest neighbor sites. If we look up the Fe-Ti phase diagram, Ti is soluble up to 8% at 1150C. So all of Ti atoms are present as a random solution in Fe and hence the above explanation based on the binomial distribution is consistent with the phase diagram.

With decreasing temperature, however, the solid solubility decreases quite fast for Fe-Ti case. For instance, it is null at 400C and 4 at% at 970C (the annealing temperature for the 2nd spectrum in Fig. 1 and 2). So about the half of Ti precipitates to $TiFe_2$ and the other half are in solution at this temperature. The PAC spectrum after the 970C annealing, however, shows only a large low frequency component and a trace of S and the satellite components (the 2nd in Fig. 2). One way to explain the result is to assume that the low frequency component is due to the ^{111}In incorporated in to the precipitates. Namely, if precipitates are present, almost all ^{111}In probes are absorbed them to give only the low frequency component. In discussing the other alloy systems, however, we have to distinguish the two cases between (a) ^{111}In has an attractive interactions with the precipitates as Fe-Ti and (b) no interactions.

Other Alloys

The class (I) alloying elements (B, Au, Nb) have a very limited solid solubility (less than 1 at%) at all temperatures. So in the range of temperatures and the concentration investigated in the present, precipitates should be present in these binary alloy systems. Indeed, we observe only the similar low frequency component as the 2nd one in Fig. 2 in Fe-Au and Fe-Nb alloys for all concentrations (except for Nb (0.44)). So these cases may be classified as I- (a). On the other hand, Fe-B alloys always show S like spectrum despite of

that most of B is precipitated because of the low solid solubility. (Null for all temperatures) So in this case we have to conclude that ^{111}In are not in the precipitates or there is no attractive interactions between them. So Fe-B system is classified as I- (b) case.

For the class II elements (Ti, Mo, Be), a high solid solubility (10%) at high temperatures (1000C) and a low one at low temperature (500C). Fe-Ti case is classified as II- (a) as described above. Within the limited concentrations and temperatures investigated, Fe-Mo and Fe-Be always have shown S like spectrum. So these should be classified as II-(b).

For the class III (V, Cr, and Ni) elements, a complete solid solution at all compositions and temperatures, we should always have S like spectrum since there should be no precipitates in these alloys. Indeed, S like spectrum always has been observed in these alloys although the trends of the damping or beating are present as in the cases of Fe-Si or Fe-Ti, respectively. So the analysis for Fe-Si alloy should apply to these alloys although the magnitude of the hyperfine field reduction will depend on the kind of the alloying elements.

Further Subjects to Study

The above discussion is based on an assumption that in some cases ^{111}In probes have attractive interactions with precipitates (metallic compounds). Even when this is the case, questions remain as whether ^{111}In are inside the precipitates or on the surface. To answer for these questions, PAC spectroscopy for the metallic compounds might be useful. For this purpose, the spectroscopy in Fe_3Si compounds is now in progress.

Also the classification of the alloying elements based on the primary solid solubility is too simple for Fe binary alloy system. Namely, many complications arise depending on the alloying element as γ or σ phase formation. So Fe-Mn alloys are now being studied since Mn is a strong γ phase former in Fe.

Reference

1) Binary Alloy Phase Diagrams, Ed. by Massalski T. B (ASM 1986).

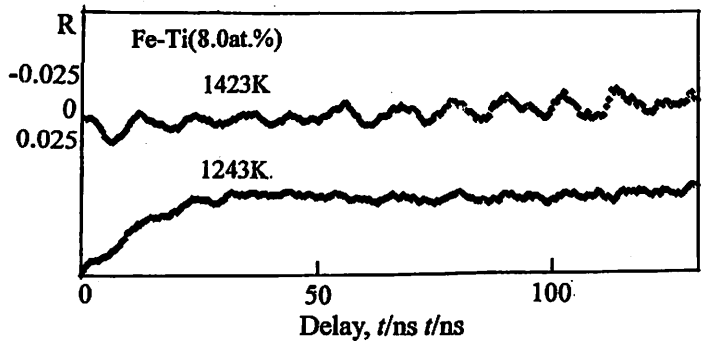

Fig. 1. PAC spectra for Fe-Ti(8.0at.%) alloy. Upper:Quenched from 1150C. Lower: Fast cooled from 970C.

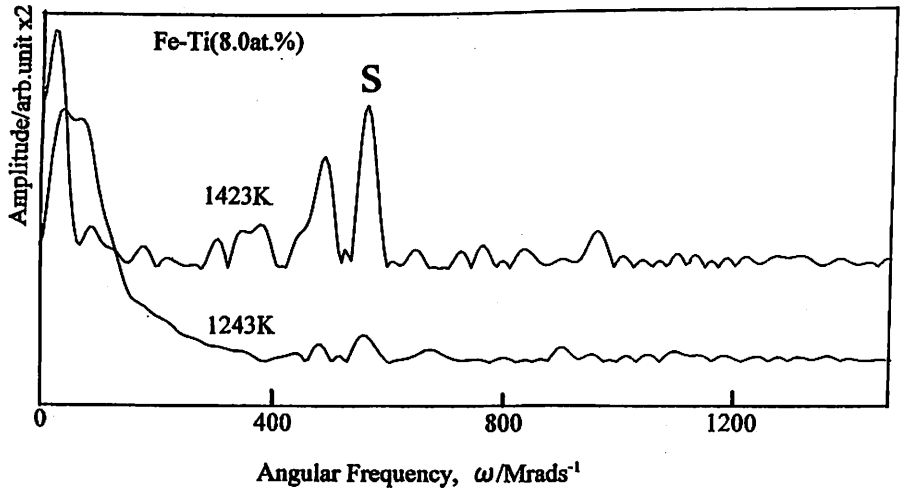

Fig. 2. Fourier spectra for Fig. 1.

II. 13. PAC Spectroscopy of Ni Alloys

Hanada R.

Institute for Materials Research, Tohoku University

Introduction

As shown in the preceding reports on Fe alloys, the new method of PAC source preparation, namely, a melting method, is quite useful to study the effect of the alloying elements on the magnetic hyperfine field in ferro-magnets. In this report, the method has been extended to other ferromagnetic metals alloys, Ni.

Different from bcc Fe, Ni has a fcc structure and hence the effect of the alloying elements on the hyperfine field is expected to be different from that in Fe. So a hyperfine field distribution was calculated with taking into consideration the crystal structure and compared with the experimental results.

Experimental

The method of the PAC source preparation is exactly the same with that described in Fe alloys. Different from Fe, Ni has a high solid solubility for In and so the source can be prepared by a conventional diffusion method. Here, however, the merit of the melting method, the simultaneous preparation of the alloy and the source, has been utilized to study many different kind of Ni alloys. Because of the high solid solubility, only 0.01ml or less amount of ^{111}In solution (4mCi/ml) was found necessary to prepare the Ni alloy sources that have a high enough activity for the PAC spectroscopy.

Results

Fig. 1 shows Fourier spectrum for a Ni-Cu (7at.%) alloy after several heat treatments as well as with or without the external magnetic field vertical to the detectors plane. For comparison, the spectrum for pure Ni without the field is also shown. For the case of pure Ni, we see two components at about 100 (ω_L) and 200 ($2\omega_L$) Mrads^{-1} that have been known as the precession signals for ^{111}In at the substitutional site (S site) in Ni[1]. Without the external field, we see the basic component (ω_L) as well as the 1st harmonic ($2\omega_L$) in accord with the theory of the magnetic interactions[1,2]. So this result confirms that ^{111}In resides at the S site of Ni after the present melting method.

Next let us see the results on the Ni-Cu alloy. In the as prepared state (the melting

followed by the cooling to 400C in 10sec and another several minutes to RT), we see two broad components of which centers are at about 70% of pure Ni (the thin vertical lines are for pure Ni). From this, one can conclude that the alloying element Cu reduces the magnitude of the hyperfine field by 30%. Also without the external field, both the basic and the 1st harmonic are present for the case of the alloy. No significant change is observed in the spectrum after the heat treatments (800C×2hrs annealing and the fast cooling or the water quenching from 1150C). This is an expected result for Ni-Cu alloy where Cu is completely soluble in Ni lattice for all composition at all temperature[3]. Namely, Cu atoms are distributed in Ni lattice as a random solid solution.

With the application of the external magnetic field, the 1st harmonic ($2\omega_L$) grows with the expense of the basic(ω_L), which is also in accord with the theoretical prediction for the magnetic interaction[2].

Inspection of the basic component as well as the 1st harmonic reveals that the broad components consist of several finer ones as revealed in Fig. 1. These finer components are reproducibly observed in the spectra given different heat treatments although the populations seem to depend on them. These components will be interpreted as due to ^{111}In probes with different number of Cu atoms in the 12 nearest neighbor site as will be shown in the next section.

Discussion

Hyperfine Field Distribution in FCC Ferromagnetic Alloys

The hyperfine field distribution for fcc Ni is calculated with the same assumptions as bcc Fe. Namely, (i) impurity atom distributes randomly in Ni lattice. Or similarly, the concentration dependence of the nearest neighbor occupation probability is given by a binomial distribution. (ii) The magnitude of the hyperfine field is proportional to the number of Ni atoms in the 12 nearest neighbor sites or the occupancy of one non-magnetic atom as Cu reduces the hyperfine field by 1/12 H_0 , where H_0 for pure Ni.

Fig. 2 is the calculated result for fcc lattice where the hyperfine distribution is shown with the impurity concentration as a parameter. For the case of Ni, 12 different components overlap each other thus resulting in a broader distribution than the case of bcc Fe. (see Fig. 3 for the Fe-Si alloy report in this volume). The center of the distribution shifts to the lower side with increasing impurity concentration as expected. Also each component corresponding to different impurity atom in the nearest neighbor site is still visible.

The experimental result in Fig. 1 for Ni-Cu alloy shows a qualitative agreement with the calculated (Fig. 2). Namely, (i) the center of the distribution shifts to the lower side with the addition of the non-magnetic alloying element. (ii) the distribution consists of the finer components corresponding to the different number of impurity atoms in the nearest neighbor site.

Quantitatively, however, the experimental result shows a disagreement with the calculated. The Cu concentration for Fig. 1 is 7 at.%. So the center of the hyperfine distribution should be $(11/12)H_0$ as the case of c=8 at.% in Fig. 2. The result in Fig. 1 , however, shows the center is at about 0.7 H_0 corresponding to c=32.at% in Fig. 2. Namely. the effect of the impurity on the hyperfine field is much larger than the calculated.

This disagreement suggests us an interesting insight about the state of the impurity atoms in the alloy. Namely, the calculation described above is based on the assumption that the impurity distribution is completely random in the alloy. The higher concentration observed in the experiment suggests that this assumption does not hold for Ni-Cu alloy.

The possibility is that there is an attractive interaction between Cu atoms and the probe ^{111}In atom and so the Cu concentration is higher in the ^{111}In neighboring sites than the average.

The other possibility is that Cu distribution can not be made uniform during the melting procedure and so there exist two regions in the specimen, one with a higher Cu concentration and the other without Cu. This case is, however, unlikely. Namely, if this the case, we should see pure Ni components in Fig. 1 together with the Cu components, which is against the observation in Fig. 1.

Other Ni Alloys

Several other Ni alloys prepared by the melting method have been studied by PAC spectroscopy of which results will be briefly summarized as: (the concentrations in at.%);
Case I (large hyperfine field shift to the lower side)

Cu(7.0, Fig.1), Be(5.2), Si(5.4,8.3), Nb(5.3), Al(3.5)

Case II (slight hyperfine field shift to the lower side)

C (3.0,10.4), Re(3.4)

Case III (no shift)

B(6.4), Fe(7.7), Rh(5.9)

The case I may be interpreted as in the present case of Ni-Cu. For the case II, C is an interstitial atom and hence should be treated differently from the present. The random distribution may apply to the other case II. For case III, B has a limited solubility in Ni and hence precipitated out leaving the probe in pure Ni lattice. This also suggests there is no attractive interactions between ^{111}In and B precipitates (BFe_2).

Rh and Fe have a large solid solubility in Ni and yet have no effect on the hyperfine field. This suggests either (i) these impurities are repulsive to the probe ^{111} In or (ii) do not reduce the hyperfine field even when they are in the nearest neighbor site.

Several other systems including Co alloys are now being investigated.

References

1) Matthias E., et al :Phys.Rev.Lett.**1 4** (1965) 46.
Hanada R., CYRIC Annual Report-1994 (1995) 44.
2) Frauenfelder H., and Steffen R M., in alpha, beta and gamma ray spectroscopy vol. II, Ed by Siegbahn Kai., (North-Holland 1968) p1113.
3) Binary Alloy Phase Diagram ed by Massalski T. B., (ASM,1986).

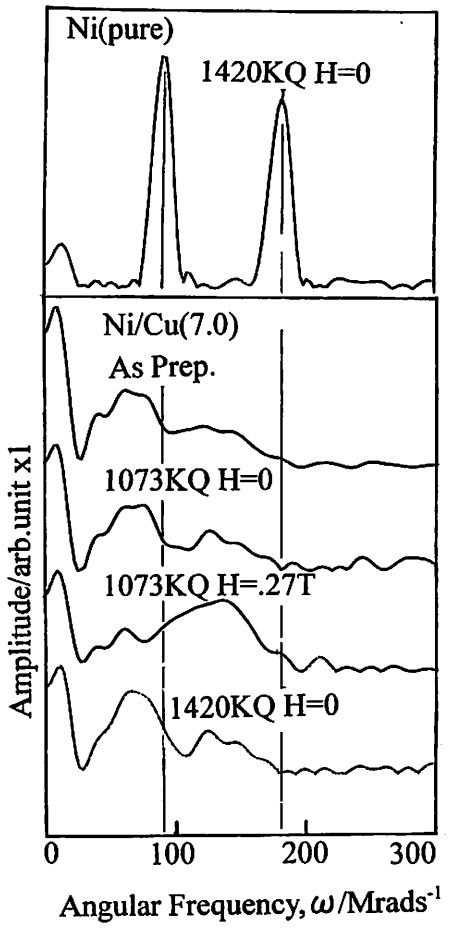

Fig. 1. PAC Fourier spectrum for pure Ni (top) and a Ni-Cu (7 at.%) alloy (bottom four) prepared by the melting method.
TQ: water quenched from the temperature T.
H: an external magnetic field vertical to the detectors plane.

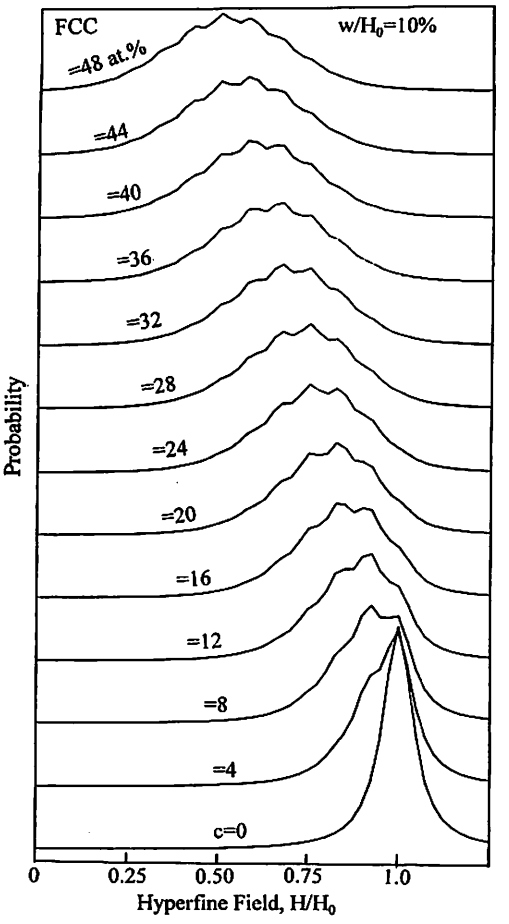

Fig. 2. A calculated hyperfine field distrib ution for fcc lattice. c: alloying elements conc. in at. %.

II. 14. PAC Spectroscopy of Si alloys

Hanada R.

Institute for Materials Research, Tohoku University

Introduction

Needless to say, Si is one of the most important materials in the modern technology. So extensive and detailed researches have been and being performed on the material.
The application of the hyperfine interaction technique, PAC or Mössbauer spectroscopy, on Si has also been extensively done, of which part of the accomplishment are summarized in[1]. In these works, the ion implantation technique has been usually applied to incorporate the probes, ^{111}In or ^{57}Fe, into the specimen.

In the present, the new technique of the PAC source preparation, the melting method, has been applied to Si alloys, of which part of the results will be described.

Experimental

Si powder (99.999%) was mixed well with a known amount of alloying elements and pressed to a disk. ^{111}In solution was dropped on the disk and dried for the melting. For the preparation of very dilute alloys, a special care was taken. Namely, a well mixed 1 at.% powder was prepared first. Next, a known but small amount of the powder was mixed with that of pure Si.

The melting procedure is almost the same with Fe or Ni alloys, though BN crucible was used for Si.

As, P, Fe, Rh, Mn, Au and Cu have been chosen as the alloying elements. Among them, Cu doped Si specimens show well defined PAC signals and hence studied in details, where the Cu concentration was varied between 20 at.ppm and 6 at.%, of which a result for 0.80 at.% alloy will be described in the followings.

As and P have been known to form a pair with ^{111}In[2]. Unfortunately, these elements are quite volatile and found to evaporate away during the melting procedure. So no well-defined PAC signal was observed for Si-As and Si-P alloys in the present.

Result and Discussion

Si-Cu Alloys.

Fig. 1 shows PAC spectra for a Si-Cu (0.80 at.%=8000 at.ppm) alloy after several

heat treatments. Right after the specimen preparation (a), we see a well-defined precession signal, of which period is 33 nsec. Since Si lattice has a cubic symmetry, there should be no EFG for ^{111}In at the substitutional site and hence no precession signals. So the precession signal must be related to the presence of Cu. Since we have only one frequency, ^{111}In should be feeling a unique EFG. A possible species for the signal is a Pair of ^{111}In and Cu atoms (complexes), although how many Cu atoms are trapped to ^{111}In is not known at present.

Next, the specimen was quenched from 1200C into liquid nitrogen and the spectrum was measured at 77K. The quenching to or the measurement at 77K is to prevent possible reactions of Cu at RT, since Cu atom dissolves interstitially in Si and mobile at RT with the migration energy of 0.43eV[3]. After the quench, the amplitude of the signal is considerably reduced as in (b). This shows that the In-Cu complex is not stable and both atoms dissolve as isolated atoms at 1200C. With the annealing at RT (c) or higher temperature (d), (e), (f), the amplitude gradually recovers to the initial value of (a). This shows that Cu atoms migrate to ^{111}In to form the complex again. The fact that most of the recovery takes place after RT and 200C annealing confirms that Cu migration energy is quite low in Si. The presence of the signal in the as prepared state (a) merely shows that an equilibrium state at an unspecified temperature during the cooling after the melting is frozen in.

Next let us discuss about the species of Cu-In complex in the present. The metallurgical phase diagram for Si-Cu system shows that the solid solubility of Cu in Si is none[4]. However, a microscopic study has revealed that Cu atoms are soluble in Si, though the maximum solubility is as small as 20 at.ppm (10^{18}/cm^3) at 1300C[5]. Although 20 at.ppm solubility sounds quite low in usual applications, it is not so for the hyperfine interaction works. The activity of ^{111}In in the present specimen (a sphere with 5mm diameter) is estimated as 50 μCi and so the ^{111}In concentration is estimated as 6.5×10^{11}/cm^3 far below the Cu concentration. So we have enough amount of Cu atoms to form a complex of multiple Cu atoms with ^{111}In probes. The total Cu concentration in the present specimen is 8000at.ppm that are far above the maximum solubility of Cu in Si. So most of them precipitate to Cu_3Si phase even at 1300C, where the maximum solid solubility is achieved. So the results in Fig.1 may be interpreted as follows. At the quenching temperature of 1200C, Cu atoms are present in forms of both a solid solution with nearly 20 at.ppm concentration and Cu_3Si precipitates. This state is frozen in by the quench to 77K. In the following annealing below 200C, Cu atoms migrate to ^{111}In probes to form ^{111}In-Cu atoms complexes thus giving rise to the precession signal. The other possibility of ^{111}In migration to Cu atoms is unlikely, since In migration energy in Si is as high as several eV[6] and hence it should not be mobile below 200C.

Next let us compare the present result with others. Keller et al have performed PAC spectroscopy on boron doped Si-Cu system where ^{111}In was implanted at the depth of

150nm and Cu ions at the energy of 0.2keV almost on the surface[7]). The Cu low implantation energy is to relate their work to the other PAC work on ^{111}In-X observed in a Si wafer given mechano-chemical polishing. After the subsequent annealing at RT, they have found two precession signals with η=0 (ω_1=223,ω_2=315 Mrads^{-1} at 77K) that are ascribed to Cu-^{111}In pairs. The signals, however, disappear in the annealing up to RT. Namely, the pair dissociates between 200K and RT with the dissociation energy of 0.69eV. Also ingeniously, they have extended the work to study the jumping process of Cu atoms around ^{111}In in the pair[8,9]. Namely, they measured the broadening of the basics and their harmonics in the PAC signals below 200K to obtain the activation energies of the jump as 0.09, 0.13 and 0.21 eV.

Comparing with theirs, the present results on the Si-Cu system prepared by the melting method show different behaviors. They are:

(1) Our ^{111}In-Cu complex is stable at RT.

(2) The angular frequency (183Mrads^{-1}) is close to but lower than theirs.

(3) No significant difference is observed in the spectrum measured at 77K and RT

So we can conclude that our complex in Si-Cu system is different from theirs, namely, a pair of one Cu atom with ^{111}In.

Adding to these we have found that:

(4) The signal is visible down to the Cu concentration of 100 at.ppm but not in 50 and 20 at.ppm Cu.

(5) The angular frequency gradually shifts to lower with the decreasing Cu concentration, 128Mrads^{-1} at 100 at.ppm.

So tentatively, we ascribe the complex as the pair of multiple Cu atoms with ^{111}In, although the number of Cu atoms varies with the Cu concentration in the specimen.

Among several elements studied in the present, only Cu gives a well-defined PAC signal reproducibly down to the concentration of 100 at.ppm. So this system is considered to be the best among Si-impurity systems to apply the PAC technique. On the other hand, the present results also warn that one must be careful for Cu contamination in the PAC application for Si using ^{111}In as the probe.

Further works are now in progress.

References

1) *Hyperfine Interaction of Defects in Semiconductors*, ed. by Langouche G. (Elsevier, 1992).
2) See the article by Wichert et Th. et al., in Ref. 1.
3) Landolt-Börnstein Vol22 subvol b"*Impurities and Defects in Group IV Elements and III-V Compounds*" ed. by Schulz M. (Springer-Verlag).
4) Si-Cu binary alloy in *Binary Alloy Phase Diagram ed.* by Massalski T. B. (ASM,1986).
5) Waber E. R.: Appl. Phys. A**30** (1983) 1.
6) See Ref. 3.

7) Keller R. et al., Phys. Rev. Lett. **65** (1990) 2023.
8) Keller R. et al., Nucear Inst. Method, B**63** (1992) 202.
9) Deicher M. Hyperfine Interactions **79** (1993) 681.

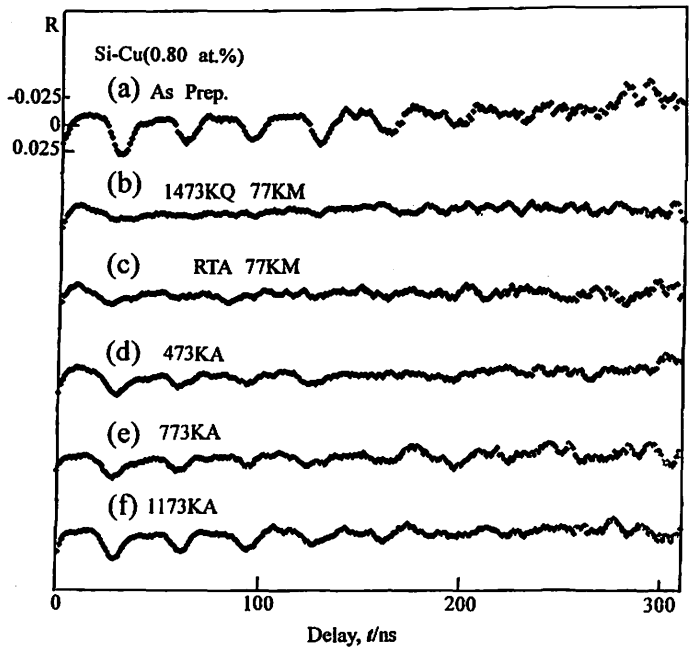

Fig. 1. PAC spectrum for a Si-Cu (0.80at.%)alloy.
TQ: Quenched to 77K from the temperature T.
TA: Annealed for 4hrs at the temperature T.
(b)(c) 77K measurements. (a)(d)(e)(f) RT measurements.

II. 15. Mössbauer Spectroscopy of Oxidation of ^{57}Fe on Au Surface.

Hanada R.

Institute for Materials Research, Tohoku University

Introduction

Lattice defects in Au have been a subject of research from the beginning of defect physics. At the first time, the existence of lattice vacancy in metals has been proved in this material. During the subsequent vast researches on Au lattice defects, an annealing in air has been found to purify the Au specimen. Namely, the resistivity ratio of a specimen, a measure for a specimen purity, is more increased after an air annealing than in a vacuum annealing. The purification has been explained as due to the internal oxidation of impurities in the bulk.

In the present Mössbauer spectroscopy, the behavior of ^{57}Fe in Au annealed in air has been studied. There, the migration of ^{57}Fe atoms to Au surface and the trapping on the surface with the formation of the Fe-oxides have been found. This gives an alternative explanation for the Au purification upon air annealing. Namely, Fe impurities are removed from the bulk to the surface thus not to contribute to the resistivity.

Experimental

Several mg of metallic ^{57}Fe was melted with Au and rolled to a 10μm foil for the transmission Mössbauer spectroscopy after annealing between 400 and 1000C in either vacuum or in 1atm air. The ^{57}Fe concentration was estimated as 5 at.%.

Result and Discussion

Fig. 1 (a)-(i) shows the spectra after each annealing at the temperature, the duration and the atmosphere (in air or in vacuum) as indicated in the figure. After the annealing at 970C in a vacuum to anneal out the cold work effect for the foil preparation, Fig. 1- (a), or the annealing in air at 400C, Fig. 1- (b), we see only a paramagnetic line near v=0mm/s. Since Fe atoms have a high solid solubility in Au host (25 at. % at 600C), the line is due to ^{57}Fe atom in the substitutional site of Au. Namely, ^{57}Fe atoms are still in the bulk at this stage. With proceeding the annealing in air at 600C, Fig1-(c), a sextet takes place. By the magnitude of the separation between the line 1 and 6, the sextet is as due to Fe_2O_3. The Fe_2O_3 sextet grows with the annealing at higher temperatures, Fig. 1- (d) for 700C and Fig. 1-

(e) for 800C with the expense of the paramagnetic line. At 800C, the paramagnetic line disappears completely. Note that the sextet takes place only when the specimen is annealed in air. So the ^{57}Fe atoms that was initially in the bulk to give the paramagnetic line now transforms to Fe_2O_3 after the air annealing.

Then a question arises that where this Fe_2O_3 is present, in the bulk or at the surface? The Mössbauer spectrum itself does not give the answer. However, the inspection of the Au specimen after the air annealing gives the answer at once. Namely the shiny gold color of the specimen is lost after the annealing and the surface color becomes completely black, the color of Fe_2O_3, after the annealing at 800C. Note that the blackening takes place only when the Au specimen contains ^{57}Fe.

So one can explain the present result as follows. At 600C, ^{57}Fe atoms start to migrate and some of them reach to the Au surface to be oxidized by the oxygen in the air. Once they are oxidized, they never diffuse back to the bulk and stay at the surface. This process proceeds with a higher rate at higher temperatures, since ^{57}Fe atoms migrate to the surface with a higher diffusion rate. So after the 800C annealing, all ^{57}Fe atoms reach to the surface to form Fe_2O_3 only to give the sextet.

The trial to diffuse back the ^{57}Fe atoms in the oxide to the bulk, the annealing at higher temperatures in vacuum, did not work. Namely, we still see the sextet at 900C, Fig. 1- (f). However, after a long time annealing at 970C, Fig. 1- (g), (h) and (i), the Fe_2O_3 spectrum gradually changes into that of Fe_3O_4, magnetite. This behavior of the reduction of Fe_2O_3 into Fe_3O_4 by a vacuum annealing is exactly the same those found in the PAC and Mössbauer studies of the oxides on Fe surface[1]. Once Fe oxides are formed, they are quite stable and can not be reduced to metallic Fe by a vacuum annealing. Only a hydrogen annealing was found effective.

After a very prolonged annealing at 970C, a small paramagnetic line takes place near v=0 mm/s as in Fig. 1- (i). At present, however, the absorption is too small to distinguish between as due to ^{57}Fe atom in the bulk or by FeO that is formed by a further reduction of Fe_3O_4. At RT, FeO spectrum appears as paramagnetic because the Curie temparature is below RT.

The present Mössbauer spectroscopy as well as the visual inspection clearly show that Fe atoms in Au tend to be removed from the Fe bulk to form Fe oxides on the surface. Such a process may take place for other kind of impurities in Au. Then it may explain the observed purification of an Au specimen after the air annealing, since the resistivity usually measures the impurities only in the bulk.

This observed surface oxidation of Fe impurity probably takes place only in Au, since it is unlikely that oxygen atoms diffuse into Au bulk for the internal oxidation. Indeed, a similar experiment in ^{57}Fe doped Cu has revealed that the whole bulk is oxidized to be brittle and yet Fe_2O_3 or Fe_3O_4 spectrum is observed. The case of Cu is one of the usually observed

internal oxidation, of which details will be reported elsewhere.

The present result also shows that the diffusion rate of Fe in Au is quite high, since it migrates a macroscopic distance of 10μm at 600C.

Reference

1) Hanada R., CYRIC Annual Report- 1997, p.34 (1998). Also see Proc. Hyp. Int. Durban 1998 to be published 1999.

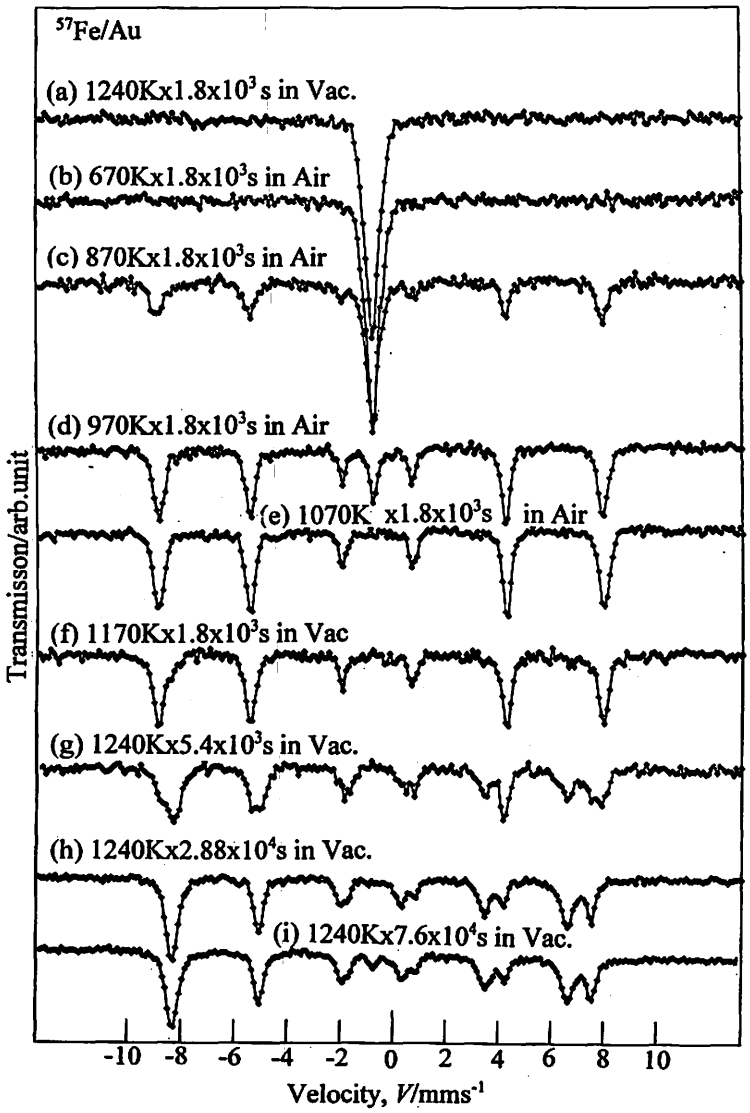

Fig. 1. Mössbauer Spectrum for ^{57}Fe doped Au after various heat treatments. The temperature, the duration and the atmosphere as indicated.

II. 16. PIXE Analysis of Thorium and Uranium in Drainage from a Radioisotope Laboratory

Yamazaki H., Takahashi Y., Ishii K., Matsuyama S., Sato T., and Orihara H.*

Department of Quantum Science and Energy Engineering, Tohoku University
Cyclotron and Radioisotope Center, Tohoku University

Introduction

Nuclear materials such as ^{232}Th and ^{238}U and many kinds of radioisotopes are used in experimental studies at a radioisotope laboratory of Engineering Department of Tohoku University. It is legally demanded by Atomic Energy Acts to control leakage of radioactivity into surface water as low as possible. The highest limit of radioactivity in drainage from a laboratory is 1×10^{-3} Bq/cm^3 for ^{232}Th and 2×10^{-2} Bq/cm^3 for ^{238}U. Radiation monitoring is not effective for these extremely long-lived nuclides. The half lives for ^{232}Th and ^{238}U are, respectively, 1.41×10^{10} and 4.47×10^{9} years, so the permissible concentrations in drainage are 0.246 ppm for ^{232}Th and 1.61 ppm for ^{238}U. These concentrations can be easily determined by absorptiometry using a coloring reagent of both Arsenazo III for Th(IV)[1] and 5-bromo-PADAP for U(VI)[2], and they also are much higher than the lower detection limits for these elements by ICP-MS and ICP-AES[3]. Since a sample of drainage from a laboratory contains a detergent, many kinds of metals, and reagents used in an experiment, these substances cause a severe problem such as a matrix effect for determination of Th and U by the analytical methods mentioned above. So that, some chemical process separating Th and U from other substances in drainage is essential to absorptiometry, ICP-AES and ICP-MS, which results in a rather impractical contamination monitoring for drainage from a radioisotope laboratory.

The PIXE analysis permits the convenient routine work for monitoring contamination of Th and U due to relatively high sensitivity to these elements[4] and direct determination of these elements independently of matrix elements of samples. The PIXE technique is conveniently applied to the analysis of thin uniform samples. In our previous studies,[5-7] complexation by dibenzyldithiocarbamate (DBDTC) ions with subsequent condensation into dibenzylidene-D-sorbitol (DBS) gels has been developed for preconcentration of trace amounts of heavy metals in water samples, in conjunction with rapid preparation of thin uniform targets containing zirconium as an internal standard for PIXE analysis. We also have developed a simple preparation method for a thin polycarbonate film and used it as target backing in the PIXE analysis of anions such as sulfate, chromate and

arsenate in a wide concentration range (10-2000 ppb).

In this paper, we report the PIXE analysis of Th(IV) and U(VI) with two kinds of targets prepared by the method mentioned above, and the performance for elemental analysis of drainage from our radioisotope laboratory.

Experimental

Target preparation

In order to evaluate reliability of quantitative PIXE analysis, calibration curves were measured for targets made from standard solutions of thorium and uranium, and then the quantitative performance of the present technique was checked using targets of drainage with and without addition of a known amount of thorium and uranium. The concentrations of Th^{4+} and UO_2^{2+} in the stock solutions were determined by spectrophotometry respectively using Arsenazo III [1] and 5-bromo-PADAP[2]. Two types of targets were used in these experiments. The first type of target was prepared by depositing 30-μl solution containing 2.5 ppm Ga-internal standard four times after dried at 60℃ on a hand-made polycarbonate film (0.27 mg/cm^2). This kind of target is called "deposit target" in the following section. The second type of target was prepared by a preconcentration technique developed in our previous studies,[5-6] which is called "preconcentration target" in the following. The processes in the preconcentration step are as follows. To a 25-ml solution, 2.5 ml of 0.1% (w/v) DBDTC solution was added with stirring and then either 25μl of 1000 ppm Zr or 50μl of 1000 ppm Pd standard solutions was pipetted as an internal standard. After the pH of solutions was adjusted to around 5 with an acetate buffer, the solution is kept stirred for 4 minutes. The solution gels immediately after the addition of 10μl of 4% (w/v) DBS in DMSO solution. The DBS gels containing the DBDTC complexes of metals and the internal standard are filtered on a Nuclepore filter of 0.4-μm pores. The filter is mounted on a Mylar target frame and kept in desiccator to dry for the PIXE measurement.

PIXE analysis

Here, we used a vertical beam-type in-air PIXE system[8]. A target was bombarded by 3 MeV protons (beam current, 5 nA; beam diameter, 2mm) from the 4.5-MV Dynamitron of Tohoku University. The irradiation time was 10 minutes, unless otherwise noted. In this PIXE system, X-rays from a target passed through a 100 μm Mylar sheet and were measured with a Si(Li) detector (4-mm diam. x 5-mm thick Crystal with 25μm Be window), which viewed a target at 135 degree with respect to the beam axis at a distance of approximately 3 cm.

For PIXE-spectrum analysis, we used a least-squares fitting computer program, which has been developed in our laboratory based on the pattern analysis method[9]. In this program, a background function for elements with atomic number Z=6-30 was obtained as a

function of Z and X-ray energy from bremsstrahlung emission cross-sections derived by the theoretical formula based on PWBA and BEA[10-11]. Then, the spectra of continuous and characteristic X-rays of elements were formed with the background functions and were used to the least-squares fit to a measured PIXE spectrum. Intrinsic efficiency of the detector and the transmission through absorbers were determined experimentally in the X-ray range of 1-60 keV. The values for the total production cross-sections of X-rays of interest and the correction factors for the relative intensity of multiplets for each characteristic X-ray were obtained from the text book by S. A. E. Johansson and J. L. Campbell[12].

Results and Discussion

In order to evaluate reliability of quantitative analysis by PIXE for thorium and uranium ions, calibration curves were measured for deposit targets and preconcentration targets, which were made from standard solutions of these elements. Figure 1 shows the results for the calibration measurements; the experimental concentration (C_{exp}) is plotted against the nominal one (C_{th}). The straight line corresponds to the relation of $C_{exp} = C_{th}$.

For the deposit targets (A and B), the difference between the nominal and the analyzed concentrations is within the quoted error (3σ) estimated from counting statistics in the wide concentration range of 40-1000 ppb. No detectable peak characteristic to thorium or uranium was found when the deposit targets made from 10 ppb solutions were irradiated up to accumulated charges of 3μC. It is appropriate from the experimental result to judge the lower detection limit of thorium and uranium to be 40 ppb for the deposit target. This means that the PIXE analysis for deposit targets has a good sensitivity enough to detect the legally permissible concentrations of these elements in drainage from a radioisotope laboratory. The reproducibility of the PIXE analysis was examined using four deposit targets separately prepared under the same condition, and the deviation is found to be $\pm 12\%$ of the mean analyzed value. A relatively large deviation is probably due to inhomogeneity caused by multiple deposition of the test solution on the film.

Uranium in the preconcentration targets (C and D) is shown in the concentration range from 10 to 1000 ppb for the internal standards of Zr and Pd, respectively. The statistical counting error (3σ) is much smaller for preconcentrated samples than for the deposit targets due to larger yield of uranium L_α X-rays resulting from large amount of U in the beam spot on the preconcentration target. Hence, the preconcentration step increases precision and sensitivity of the PIXE analysis. In the sample of 4-ppb U, however, the experimental concentration is around two times higher than the nominal concentration. This is ascribed to the interference of Br K_β X-rays appearing from Nuclepore filter, as will be shown below. The Br-contribution fluctuates widely at each Nuclepore filter used, and it results in a severe interference in determination of very low concentration of uranium. On the basis of these experimental results, the lower detection limit of PIXE analysis for the preconcentration

targets turns out around 10 ppb, above which the analyzed concentrations show satisfactory good agreement with the nominal values. The preconcentration technique was used for the solutions of thorium, but the recovery of thorium came to be utterly imperfect. This is possibly due to extreme hydrolysis of Th^{4+} ions in a solution at pH≈4[13]; the pH value of solution in preconcentration step is chosen to avoid an undesirable precipitation of carbamic acid with the small dissociation constant ($2.95 \leq pK_a \leq 5.19$)[14].

The PIXE measurement for the deposit target of drainage alone simultaneously detected 13 elements as well as very low concentrations of Th and U originally present in drainage. The addition of around 0.4 ppm of each Th and U to the drainage sample came to the distinct peaks of *L* X-rays of these elements, even though the spectrum was very complicate due to the presence of Br, Pb, Rb and Sr. These results indicate that the PIXE analysis for the deposit target has a reasonable sensitivity useful for monitoring an actinide-contamination in drainage. On the other hand, peaks corresponding to characteristic X-rays of heavy metals including U originally present in the drainage sample were clearly recognized comparing with the deposit targets. The preconcentration step consequently has a beneficial effect on the detection limit of U in drainage. In addition to this, palladium serves as more suitable internal standard than zirconium because of *K* X-rays with energies far from those of X-rays of Th and U. A relatively large yield of bromine K_α X-ray originated from a Nuclepore filter, since the PIXE measurement of the filters arbitrarily sampled from the Costar's serial number of 5775, which were used currently in a series of the preconcentration targets, showed a high bromine content.

The elemental concentrations in drainage with and without addition of a known amount of Th and U are tabulated in Table 1. The samples of drainage were collected from two different reservoirs of the radioisotope laboratory of Tohoku University; No. 1-drainage is more aged than No.2-drainage. The average and the variation (numerical value) of analyzed concentrations are listed for three targets of each of drainage samples. For deposit targets, concentrations of Th and U, which are originally present in No. 1-drainage, are determined to be 0.11 and 0.06 ppm, although a relatively large variation (more than ± 30 %) is observed from the average of three targets. Based on the original concentrations, it is clear that the amounts of Th and U added to No. 1-drainage can be quantitatively determined by the PIXE analysis. The concentrations of many other elements also are reproducibly obtained by the PIXE analysis for deposit targets, as shown in the first and second lines of Table 1. For the preconcentration targets, on the other hand, concentrations of U added to No.2-drainage and heavy metals originally present are determined in higher reproducibility comparing with the analyzed values for the deposit targets. The analyzed concentrations of heavy metals including U originally present in No. 1-drainage are much lower for preconcentration targets than those for deposit ones, as shown in the second and third lines of Table 1. These experimental results suggest the hydrolysis or coprecipitation of heavy

metals in drainage having a neutral pH during storage in a reservoir. The preconcentration step selectively collects unhydrolyzed components in ionic form to react with DBDTC ions and the insoluble particles large enough to be filtered out on a Nuclepore filter of 0.4-μm pores. Anyhow, heavy metals having these two chemical forms are considerably small in number, but the detection of thorium in preconcentration targets indicates the existence of Th-hydroxide polymers to be collected on the filter. It can be considered that a large deviation of the analyzed concentrations for the deposit targets comes out due to variation in the amount of insoluble particles of heavy metals in drainage samples used for the target preparation. It is highly recommended to analyze duplicate targets of one drainage sample by PIXE and use the average on actinide-contamination monitoring.

In conclusion, a procedure has been developed and tested for the PIXE analysis of Th and U in drainage from a radioisotope laboratory. The deposit target is simply made up without any chemical procedure except addition of an internal standard and preparation of thin polycarbonate films. The PIXE analysis of the deposit target offers a promising prospect of determining concentrations of Th and U, regardless of the chemical form, below their legally permissible concentrations in drainage from a radioisotope laboratory. Uranium ions can be further precisely analyzed by the combined use of the PIXE measurement and the preconcentration technique. The methodology developed in this study can be applied to a routine work for contamination control of drainage from a radioisotope laboratory with a special regulation to use nuclear materials in experiments.

References

1) Sandell E. B. and Ohnishi H., *"Photometric Determination of Traces of Metals, PART I,"* John Wiley & Sons, New York (1978), Chap. 6.
2) Johnson D. A. and Florence T. M., " Talanta, **22,** 253 (1975).
3) Haraguchi H. and Inagaki K., *Bunseki,* **1998**, 494.
4) Ishii K. and Morita S., and Orihara H., *Int. J. PIXE,* **1**, 1(1989).
5) Yamazaki H., Tanaka M., Tsutsumi K., Ishii K., Matsuyama S., Iwasaki S., Inoue J., Murozono K., and Orihara H., *Int. J. PIXE,* **6**, 483 (1996).,
6) Yamazaki H., Tanaka M., Tsutsumi K., Ishii K., Matsuyama S., Iwasaki S., Inoue J., Murozono K., *Int. J. PIXE,* **7**, 31 (1997).
7) Yamazaki H., Tsutsumi K., Ishii K., Matsuyama S., Murozono K., Inoue J., Iwasaki S. and Orihara H., *Int. J. PIXE,* **7**, 101 (1997).
8) Iwasaki S., Ishii K., Matsuyama S., Murozono K., Inoue J., Tanaka M., Yamazaki H. and Orihara H., *Int. J. PIXE,* **6**, 117 (1996).
9) Murozono K., Iwasaki S., Inoue J., Ishii K. and Kitamura M., *Int. J. PIXE,* **6**, 135 (1996).
10) Ishii K. and Morita S., Nucl. Instrum. Meth. **B3**, 57-61 (1984).
11) Hamanaka H., Ohura M., Yamamoto Y., Morita S., Iwamura K. and Ishii K. Nucl. Instrum.
12) Johansson S. A. E. and Campbell J. L., *"PIXE. A Novel Technique for Elemental Analysis,"* John Wiley & Sons, New York (1989), 313-329.
13) Baes C. F. and Mesmer R. E., "The Hydrolysis of Cations," John Wiley & Sons, New York, 158-168.
14) Hulanicki A., Talanta, **14**, 1371 (1967).

Table 1. PIXE analysis for drainage from a radioisotope laboratory.

Deposit Target	Analyzed Concentration (ppm)												
	S	Cl	K	Ca	Cr	Mn	Fe	Cu	Zn	Sr	Pb	Th	U
No.1-drainage + 0.37 ppm Th + 0.40 ppm U	6.5 ±3.2	4.6 ±2.5	15.8 ±8.6	13.5 ±5.8	0.24 ±0.14	0.28 ±0.16	0.40 ±0.22	0.12 ±0.06	0.76 ±0.35	0.09 ±0.03	0.38 ±0.14	0.45 ±0.04	0.43 ±0.05
No.1-drainage	5.6 ±3.0	3.7 ±2.3	10.1 ±5.6	9.2 ±3.9	0.23 ±0.13	0.27 ±0.17	0.39 ±0.23	0.13 ±0.05	0.61 ±0.09	0.08 ±0.03	0.38 ±0.16	0.11 ±0.05	0.06 ±0.02

Preconcentration Target	Analyzed Concentration (ppm)								
	Cr	Mn	Fe	Ni	Cu	Zn	Pb	Th	U
No.1-drainage	0.005 ±0.001	0.034 ±0.001	0.118 ±0.081	0.017 ±0.011	0.012 ±0.005	0.578 ±0.049	0.137 ±0.019	0.018 ±0.003	0.012 ±0.001
No.2-drainage + 0.20 ppm U	0.005 ±0.001	0.038 ±0.002	0.158 ±0.011	0.013 ±0.002	0.029 ±0.003	0.817 ±0.054	0.503 ±0.039	0.091 ±0.004	0.225 ±0.013
No.2-drainage + 0.10 ppm U	0.008 ±0.002	0.040 ±0.006	0.189 ±0.005	0.011 ±0.001	0.022 ±0.001	0.891 ±0.021	0.619 ±0.007	0.079 ±0.003	0.129 ±0.008
No.2-drainage	0.007 ±0.002	0.043 ±0.005	0.504 ±0.334	0.044 ±0.039	0.026 ±0.004	0.840 ±0.051	0.516 ±0.104	0.057 ±0.017	0.016 ±0.008

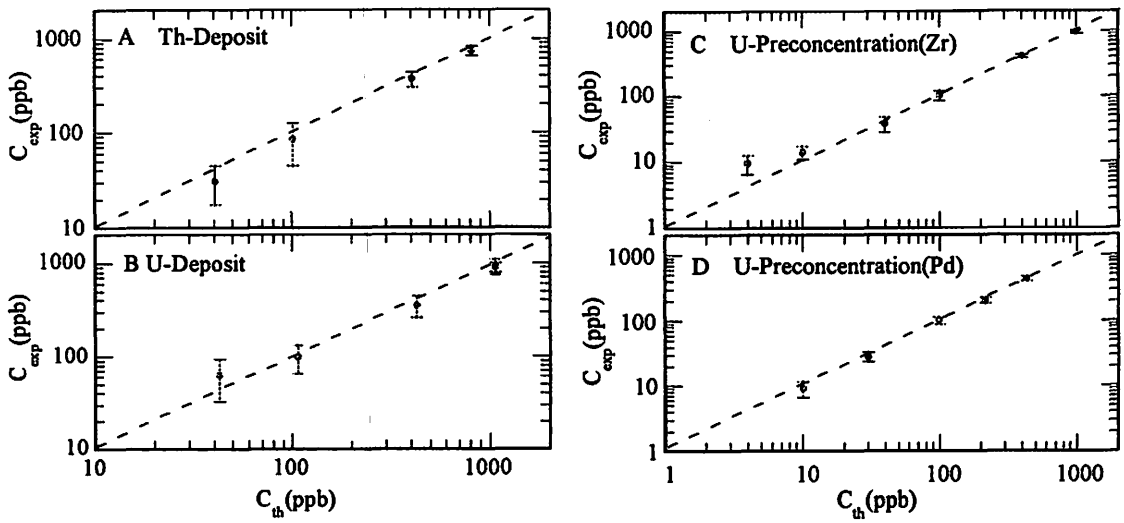

Fig.1. Calibration curves for PIXE analysis of Th and U. The quoted error is 3σ from counting statistics in a single 3-μC run.

II. 17. An Endurance Test of Kapton Foil in In-Air PIXE System

*Matsuyama S., Inoue J., Ishii K., Yamazaki H., Iwasaki S., Goto K., Murozono K., Sato T. and Orihara H.**

Department of Quantum Science and Energy Engineering, Tohoku University
*Cyclotron and Radioisotope Center, Tohoku University**

Introduction

Particle-induced X-ray emission (PIXE) is a useful technique for multielemental analysis with high sensitivity[1]. Generally samples to be analyzed are irradiated in vacuum. Samples which contain moisture cannot be analyzed in the vacuum chamber. Sample size is limited because of the difficulties of placing it in a vacuum chamber. These problems can be solved by extracting the beam into the laboratory atmosphere. We call this arrangement an in-air PIXE analysis. In-air PIXE analysis is attractive especially for biological, botanical and archeological fields than vacuum PIXE.

The easiest way to realize the in-air PIXE analysis is to extract the beam through a thin window into the laboratory milieu. While metallic foils are strong enough to withstand beam damage, their characteristic X-rays from strong background in PIXE analysis. On the other hand, greatly reduced background is achieved using polymer foil. It is known that among polymers, a polyimide such as Kapton (manufactured by Dupont) has the highest radiation resistivity and is suitable for exit window in in-air PIXE system[1,2]. It is a serious problem that the beam exit foil breaks during the experiment, so it is very important to know its lifetime until breakdown. Studies on radiation deterioration of the Kapton foil has been performed from viewpoint of mechanical properties[1,2]. However, there is scarce study on its lifetime as an exit window.

Here, we irradiated the Kapton foil until it was broken and measured total charge through the foil under various beam parameters. We define the total charge through the Kapton foil until breakdown as its lifetime. The average beam current was varied from 10 nA to 1000 nA. Beam size was 0.5 to 3 mm in diameter. The total charge until breakdown of the Kapton foil was analyzed in consideration of current, diameter and energy loss of the beam.

Experiment

Endurance tests were made using a vertical in-air PIXE (ViaPIXE) system at Tohoku university[3,4]. ViaPIXE is the vertical beam type in-air PIXE system. A single-ended type Dynamitron accelerator in Tohoku University was used in this study. The proton beam from the accelerator is bent by 30 degree using a switching magnet, further bent by 10 degree and led to a beam exit assembly through a vertical dipole magnet by 90 degree. A fast valve closing system was set just downstream of the switching magnet to protect the accelerator from the vacuum break due to destruction of the exit window. Figure 1 shows the beam exit assembly consisting of a beam viewing port, a Faraday cup, a carbon beam collimator, a beam exit window assembly and an in-air Faraday cup. The exit foil was glued on a copper or aluminum metal ring with a 5 mm inner diameter hole. The exit foil is a Kapton foil of 12.5 or 7.5 μm. The exit window assembly can be changed within a few minutes from the beam exit assembly. Beam current can be measured by the Faraday cup just before the carbon collimator or the in-air Faraday cup (see Fig. 1). Beam currents measured by these Faraday cups were consistent with each other.

Irradiation with 2 or 3 MeV proton was performed until the foil was broken. The average current varied from 10 to 1000 nA. The beam size was 0.5 to 3 mm in diameter. The beam size larger than 0.5 mm was obtained by the carbon collimator. In order to get uniform beam, the beam was defocused by using a thin (50 mg/mm^2) carbon diffuser foil settled just downstream of a quadrupole doublet lens. An actual beam size was obtained by measuring diameter of a mark burning black on the Kapton foil.

Results and Discussion

Typical results of the total charge until breakdown as a function of the beam current for the different beam spot size is shown in Figs. 2 and 3. Figure 2 shows the results of 7.5 and 12.5 μm Kapton foils for beam spot sizes of 3.2, 4.2 and 3.2 mm^2. While total charge until breakdown depends on the beam spot size, it does not depend on the beam current. Proton irradiation induced chain scission of the polymer and caused the changes in tensile parameters such as tensile strength, elongation and fracture energy[2,5]. Thus, the foil is destructed by radiation damage. Figure 3 shows the result of the 12.5 μm Kapton foil for beam spot size of 0.34 mm^2. Beam current density is about ten times higher than that of the former. In this case, total charge until breakdown decreased with increase in the beam current. Since rise in temperature of the Kapton foil also degrades its malleability and ductility, local heating by ion beam accelerates deterioration of the foil in addition to the radiation damage.

As shown in Figs. 2 and 3, the total charge until breakdown differs for various beam parameters. In order to research the total charge until breakdown at the different beam parameters, the following normalization may be useful. We introduce the following

normalization. The foil gets stress (F) from pressure difference (P) and withstands that stress by tensile strength. In ordinarily, the value of tensile strength at break (F') is larger than that of F. Beam irradiation decrease the value of F' and the foil is broken. The value of F is proportional to the beam spot size (S). The value of F' is proportional to the length of beam circumference ($\ell=2\pi r$, r=beam radius) times foil thickness (t). Furthermore, we introduce the effects of radiation and heat damage into such consideration. The fracture energy of the Kapton foil, which will affect the value of F', is almost in inverse proportion to radiation dose (G)[5]. The fracture energy of the foil decreases slowly with the temperature up to 200°C and decreases sharply with the temperature higher than 200°C. In this study, we assume F' is inversely proportional to temperature (T). While the foil thickness may change continuously with irradiation time, we assume the thickness to be constant. This assumption is sufficient for normalization on our experimental data to evaluate the life time of the foil. Thus, the following equation is derived.

$$F = P \cdot S = \text{const}\,\frac{\ell \cdot t}{G \cdot T} = F'. \qquad (1)$$

Radiation dose; total energy deposited to unit volume (G) is defined by energy loss of the proton beam in the foil (dE), total charge (Q), beam spot size (S) and foil thickness (t) :

$$G = \frac{Q \cdot dE}{S \cdot t}. \qquad (2)$$

From equation (1) and (2),

$$\frac{Q \cdot dE}{r \cdot t^2} = \text{constant}\,\frac{1}{T}. \qquad (3)$$

Temperature of the foil (T) depends on beam current (I) and energy loss in the foil. We assumed that all of the deposited energy to the foils is converted to heat in disregard of another physical process such as sputtering. Temperature of the foil is estimated by using the following equation based on heat transfer both foil surface and wall.

$$I \cdot dE = (h \cdot S + h' \cdot S\frac{2 \cdot t}{r})T, \qquad (4)$$

where h :heat transfer coefficient of air,

h ' :heat transfer coefficient of the kapton foil.

Since heat conductivity of Kapton foil is 6.5 times higher than that of air, h' is estimated 6.5h. Namely equation (4) become

$$I \cdot dE = (h \cdot S + 6.5 \cdot h \cdot S \cdot 2 \cdot R)T, \qquad (5)$$

where R is the ratio of t to r (R=t/r).

The equations (3) and (5) are reduced in the following equation

$$Y = \text{constant} \cdot X \qquad (6)$$

where $$Y = \frac{Q \cdot dE}{r \cdot t^2}$$

$$X = \frac{(1 + 13R)}{dE} \cdot \frac{1}{I/S}$$

Figure 4 shows the normalized results for various beam parameters with least square fitting curves. The data are normalized for 3 MeV proton beam with the beam diameter of 2 mm and 12.5μm foil thickness. While Y increases with X, the rate of increase decreases at the region of $X > 0.01$. It shows that temperature of the foil is not so high and does not cause degradation due to heating in the region of low current density. Standard deviations of the data are 31-49 % and 15-24 % for the region lower than 0.01 and higher than 0.01, respectively. Large deviation for the region of $X<0.01$ may be due to temperature fluctuation caused by instability of beam intensity. In the case of PIXE analysis where our usual beam current density is around 10 nA/mm^2 (7 nA in 1 mm beam diameter), the lifetime of the Kapton foil can be estimated longer than 2 days. It is sufficient for in-air PIXE analysis.

Conclusion

Endurance of the Kapton foil used as an exit window of in-air PIXE system for beam irradiation has been tested. The total charge until breakdown of the Kapton foil was analyzed in consideration of beam current, diameter and energy loss. The total charge until breakdown decreases with increase in the beam current in the beam current higher than 100 nA/mm^2. On the other hand, in the beam current density lower than 100 nA/mm^2, total charge until breakdown does not decrease so much. The lifetime of the Kapton foil can be estimated longer than 2 days for the beam current density of 10 nA/mm^2. Our results will be useful for the users who want to start an in-air PIXE experiment.

Aknowledgment

The authors are pleased to acknowledge the assistance of Messrs. M. Oikawa and T.Sasaki during the experiments. The authors wish to thank Messrs. R. Sakamoto and M. Fujisawa for their maintenance work for Dynamitron accelerator. The authors also wish to thank Messrs T. Takahashi, K. Komatsu, T. Nagaya and C. Akama for their supports in the fabrication of the beam exit assembly.

References

1) Sven A. E. Johansson and John L. Campbell, *PIXE:A Novel Technique for Elemental Analysis*, Singapore, John Wiley & Sons, 1988, chapter 3 and 7.
2) Sasuga.T., *Polymer*, **29**, 1562-1568, 1988.
3) Iwasaki S. et al., *International Journal of PIXE*, **6**, Nos. 1&2, 117-125, 1996.
4) Iwasaki S. et al., *International Journal of PIXE*, **5**, Nos. 2&3, 163-173, 1996.
5) David J. T. Hill and Jefferson L. Hopewell, *Radiat. Phys. Chem.*, **48**, No5, 533-537, 1996.

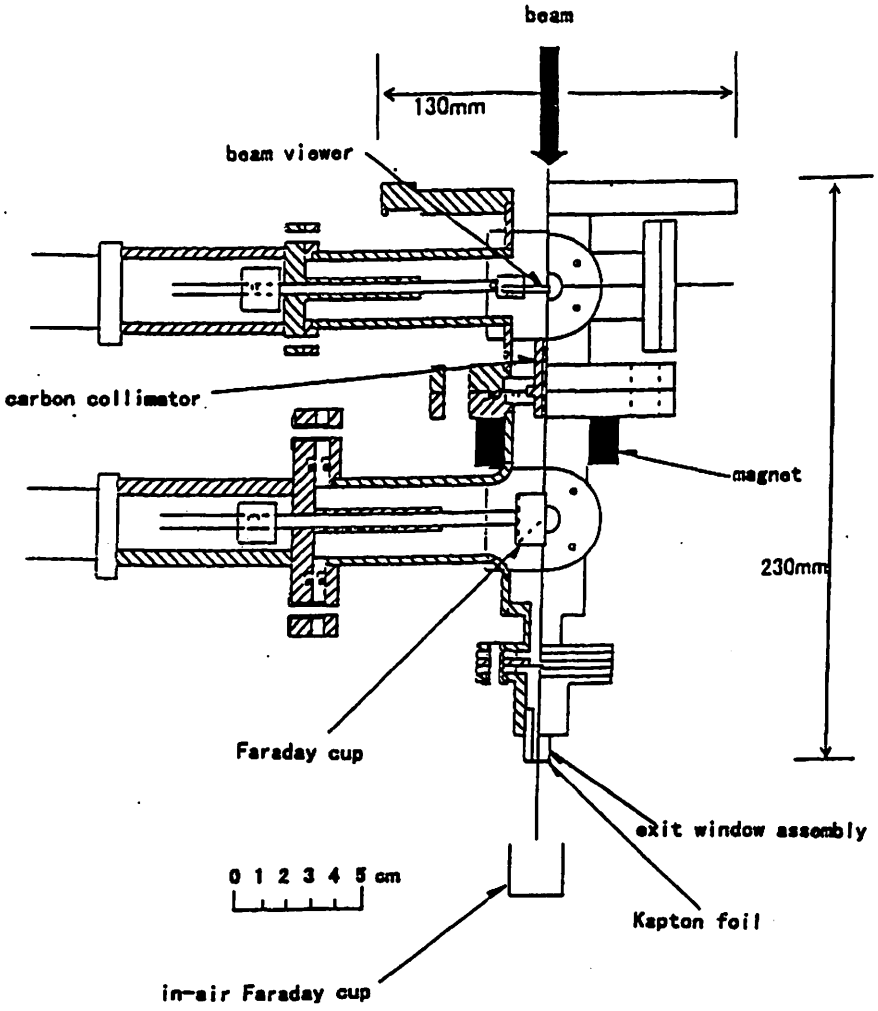

Fig. 1. A beam exit assembly.

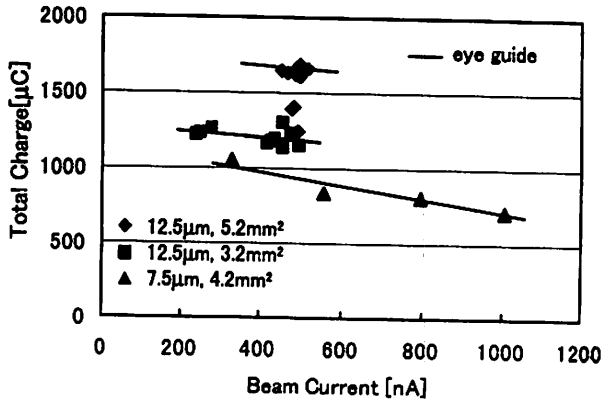

Fig. 2. The total charge until breakdown as a function of the beam current for 7.5 and 12.5 μm Kapton foil (large spot size).

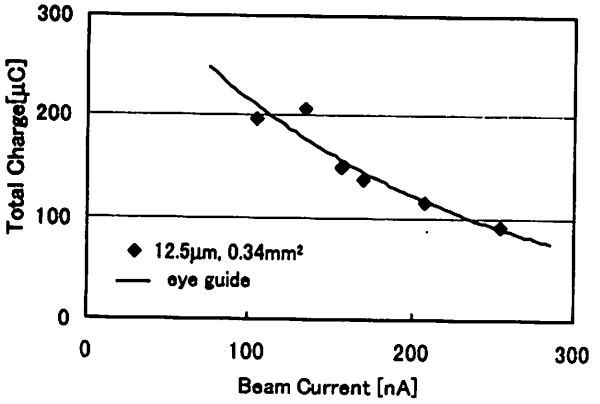

Fig. 3. The total charge until breakdown of 12.5 μm Kapton foil as a function of the beam current (small spot size).

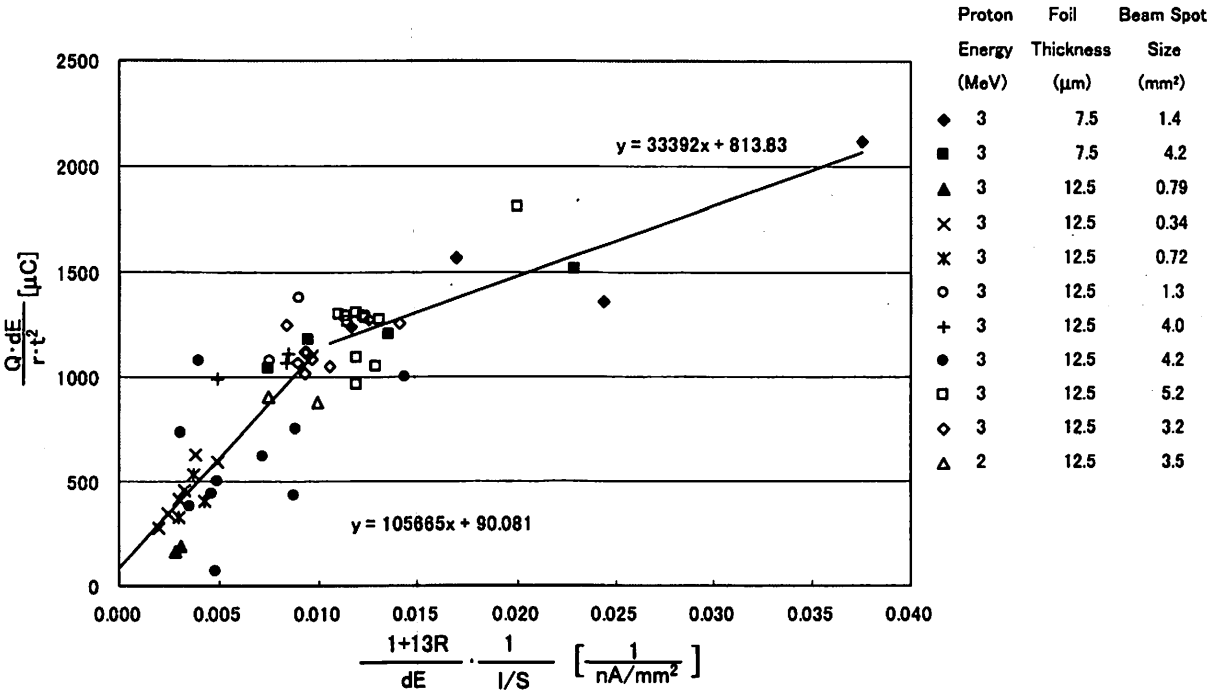

Fig. 4. Normalized results for various beam parameters with least square fitting curve.

II. 18. Development of a Submilli-PIXE Camera

*Matsuyama S., Gotoh K., Ishii K., Yamazaki H., Satoh T., Yamamoto K., Sugimoto A., Tokai Y. and Orihara H.**

*Department of Quantum Science and Energy Engineering, Tohoku University, Cyclotron and Radioisotope Center, Tohoku University**

Introduction

Particle-induced X-ray emission (PIXE) analysis is well known to be a novel technique for trace elemental analysis[1]. A beam spot size of a few mm diameters is usually used in the PIXE analysis. In this case, it is needed that the distributions of elements are uniform in the specimen. If spatial distributions of elements in a region of several cm^2 can be measured with a spatial resolution of submilli-meters, it will be a powerful means in the analysis of archeological samples, e.g., paintings, books and stamps. Such technique has been already developed for the PIXE analysis of the microscopic region[1,2]. Elemental analysis over the area of several cm^2 is possible by moving the specimen relative to the beam[3]. However, it has some technical problems such as damage of sample due to local heating with intense beam and distortion of spatial distribution images of elements induced by unperfect measurement of beam current.

Here, we developed a submilli-beam line with a high-speed scanning system and a spatial distribution imaging system of n elements with a spatial resolution of submilli-meters for 3 cmx3 cm area. Furthermore, we combined this system with an in-air PIXE analysis. The high-speed beam scanning and the in-air analysis reduce the risk of damaging the specimen.

Submilli-beam line

Figure 1 shows the layout of the PIXE analysis system newly developed at a Dynamitron laboratory in Tohoku university, which consists of a submilli-PIXE camera, a vertical in-air PIXE system[4], a target chamber for nuclear spectroscopy, a low Z PIXE system using a crystal spectrometer, a polarized-PIXE system using a crystal spectrometer with a position sensitive proportional counter, a PIXE background measurement system and a vacuum PIXE system. A single-ended type 4.5 MV Dynamitron accelerator with a high-current duo-plasmatron ion source was used in this work, which accelerates hydrogen, deuteron or helium ions. The maximum beam current is larger than 100 μA. The emittance

of the Dynamitron accelerator is 1mrad·cm·MeV$^{1/2}$. The submilli-beam line has been settled in a -40 degrees line which had been equipped with three types of PIXE chambers in series. In order to install the submilli-beam line, two of the chambers were moved to a -15 degrees line. Ion beams are bent by -30 degrees using a switching magnet, further bent by -10 degrees and led to the submilli-beam line (see Fig. 1). Two quadrupole doublet lenses are settled at the upstream side and downstream side of the switching magnet. The beam spot size is smaller than 6 mm in diameter at the end of the beam line. Figure 2 shows the detail of the submilli-beam line. The submilli-beams were formed by using two slits with the spacing of 1.5 m. A dipole magnet to bend the beams 90 degrees was installed between the slits, which is used for a vertical in-air PIXE (ViaPIXE) system[4] (see Fig. 1)5. The slit at upstream side is four-pole type copper jaws of 2 mm thick. The slit at downstream side consists of two wedge-shape jaws made by tantalum plates of 0.1mm thick. Both slits are remotely controlled at the control room of Dynamitron where we are monitor beam currents at each slit. The submilli-beams which are formed by passing through these two slits, are scanned horizontally and vertically on a specimen by two magnets.

Submilli-PIXE camera

In the submilli-PIXE camera, specimens can be irradiated either in vacuum or in atmosphere. To scan a wide area, we use two magnets which are an air-core coil and a laminate-core magnet for vertical (Y) and horizontal (X) scanning with high-speed, respectively. These magnets are controlled by a function generator. While a raster scanning mode is used for elemental imaging, patterns of beam scanning can be freely made by computational program. The maximum area of scanning region is 3×3 cm^2. A vacuum chamber (or a beam exit) assembly is placed at the end of the submilli-beam line for the PIXE analysis in-vacuum (or in-air). The vacuum chamber is a rectangular shaped aluminum chamber with a Si(Li) detector or a Si-PIN photodiode detector settled at the direction of 90 degrees with respect to the beam axis. The beam exit assembly is shown in Fig 3. A beam exit window is a Kapton foil of a thickness of 12.5 μm and its area is 16 cm^2. The lifetime of the Kapton foil window until breakdown by beam irradiation was longer than 2000 seconds under the beam current density of 300nA/mm^2 (100 nA for the beam spot size of 0.7 mm in diameter)[6]. Since the lifetime is made to elongate by beam scanning, the endurance of the Kapton foil window is sufficient for the submilli-PIXE analysis. The specimen is set just before the exit window. X-rays from the specimen are detected with a Si(Li) or a Si-PIN photodiode detector through the exit window and a detector window of a 7.5 μm Kapton foil (see Fig. 3).

Figure 4 shows a schematic diagram of the beam scanning system and the data acquisition system for elemental imaging. In the PIXE camera, the X-ray energy and beam position are simultaneously measured in order to obtain spatial distributions of elements.

The system consists of a multi-parameter data acquisition system, ADCs for X-ray detector signals and ADCs for position signals. The position signals are derived from the control signals for the X- and Y-magnets. Analog signals from the detectors trigger the ADCs to pick up scanning voltages. After conversion, the digital data are saved in a list file. It takes 20 μ seconds for one data acquisition cycle. The list mode data acquisition is useful to observe changes in elemental imaging during irradiation. This system can sort the data for selected element/energy region and generate elemental images even while the data are accumulated. A large memory size is required in the list mode data acquisition, but it is not so serious since we can use large capacity and removable media at the present.

Performance

The proton beams were first focused at the end of the submilli-beam line by using the two quadrupole doublet lenses with opening the slit maximally, and then the four-pole slit at upstream side was closed to 0.5 mm by monitoring the beam spot size at both X and Y axes. Finally, the slit at down stream side was closed.

The beam spot size was measured in vacuum by using a sharp (#) pattern which was made of a 1.5 mm wide tungsten ribbon. The FWHM of beam spot was obtained by differentiating the spectra derived from the cross section of the spatial distribution of characteristic X-ray yields from the # pattern which was measured by the Si-PIN photodiode detector settled 90 degrees with respect to the beam axis. A measured beam spot size was 0.25×0.48 mm^2 in FWHM for average beam currents of 1 nA. Current intensity of beam halo was three order lower than that of the beam center. Fig. 5 shows the photograph and corresponding elemental image of copper from a substrate. The printed pattern in 0.5-1.0 mm spacing is clearly seen in the measured elemental image.

Response of the magnetic field for a control voltage was studied by measuring elemental images of the copper mesh and by changing the scanning speeds. Fig. 6 and 7 show the control voltages of the magnets v.s. the positions of the copper mesh for the laminate-core magnet and the air-core coil, respectively. The position of mesh is proportional to its control voltage even at the scanning speed of 8.1 cm/sec for the laminate-core magnet. The air-core coil works at the scanning speed of 0.15 cm/sec without distortion of elemental images. It takes twenty seconds to scan the region of 3×3 cm^2.

A shell of short neck clam and a granite were analyzed to demonstrate the application of PIXE camera to the fields of biology and geology. The PIXE analysis was performed in-air. The beam spot size was 0.54×0.65 mm^2 and was rather large than an expected value which was estimated in consideration of diffuseness due to the scattering in the Kapton foil and air molecule. The samples were settled perpendicular to the beam axis and the X-ray detector was settled 135 degrees with respect to the beam axis. Fig. 8 shows elemental images of the Ca and Fe elements in the shell. It took 90 minutes to obtain these images

under the beam currents of 1 nA. The Ca element which is the main components of the shell is homogeneously distributed. On the other hand, the Fe element is locally distributed. Since shells concentrate the elements correlated to their circumstances, this shell had spent his life in water of Fe rich. Fig. 9 shows elemental images of the granite sample. It is seen in these images that the Fe and Ca elements are inhomogeneously distributed. Since the in-air PIXE analysis enables to measure such insulator sample without charge buildup, the submilli-PIXE camera in-air is applicable to measure elemental images contained in any sample.

Summary

The submilli-PIXE camera has been developed for measuring spatial distribution of elements in a specimen, which consists of the high-speed scanning system of the submilli-beam and the data acquisition system. The beam spot size of 0.25 mm×0.48 mm is obtained with a beam current of 1 nA. The maximum beam scanning area is 3 cm×3cm. The maximum scanning speed is 0.15 cm/sec and 8.1 cm/sec for vertical and horizontal scanning, respectively. In order to improve the spatial resolution, we are planning to install quadrupole doublet lenses at the downstream side of the slit of the submilli-beam line.

As the application of the submilli-PIXE camera to the fields of biological and geological sciences, a shell of short neck calm and granite were analyzed in-air. We got clear elemental images for both samples. This system will also be a powerful means for archeology and other fields.

Acknowledgements

The authors are pleased to acknowledge the assistance of Messrs. M.Oikawa and T.Sasaki during the experiments. We wish to thank to Mr. M.Fujisawa for his help in fabrication of the ADCs for scanning voltage signals and to T.Takahashi, K.Komatsu, T.Nagaya, R.Sakamoto and C.Akama for their work in fabricating the submilli-beam line. We are indebted to Dr. M.Baba for providing the multi-parameter data acquisition system for us. This work are partly supported by Tohoku power electric Co. Ltd.

References

1) Johansson S. A. E., Campbell J. L. and Malmqvist K. G., Particle-induced X-ray emission spectroscopy (PIXE) John Wiley and Sons, 1995.
2) Watt F., Grime G. W., Principle and Application of High Energy Ion Microbeames (Adam Hilger Bristol, 1995).
3) Lovestam N. E. G. and Swietlicki e., Nucl. Instrum. and Meth. B4 **3** (1989) 104.
4) Iwasaki S. et al., Int. J. PIXE **6** (1996) 117.
5) Cleland M. R. and Kiesling R. A., IEEE Trans. on Nucl. Science **6 0** (1996).
6) Matsuyama S. et al., Proc. 15th Intern. Conf. on Application of Accelerators in Research and Industry (Denton TX, 1998), pp.480-483.

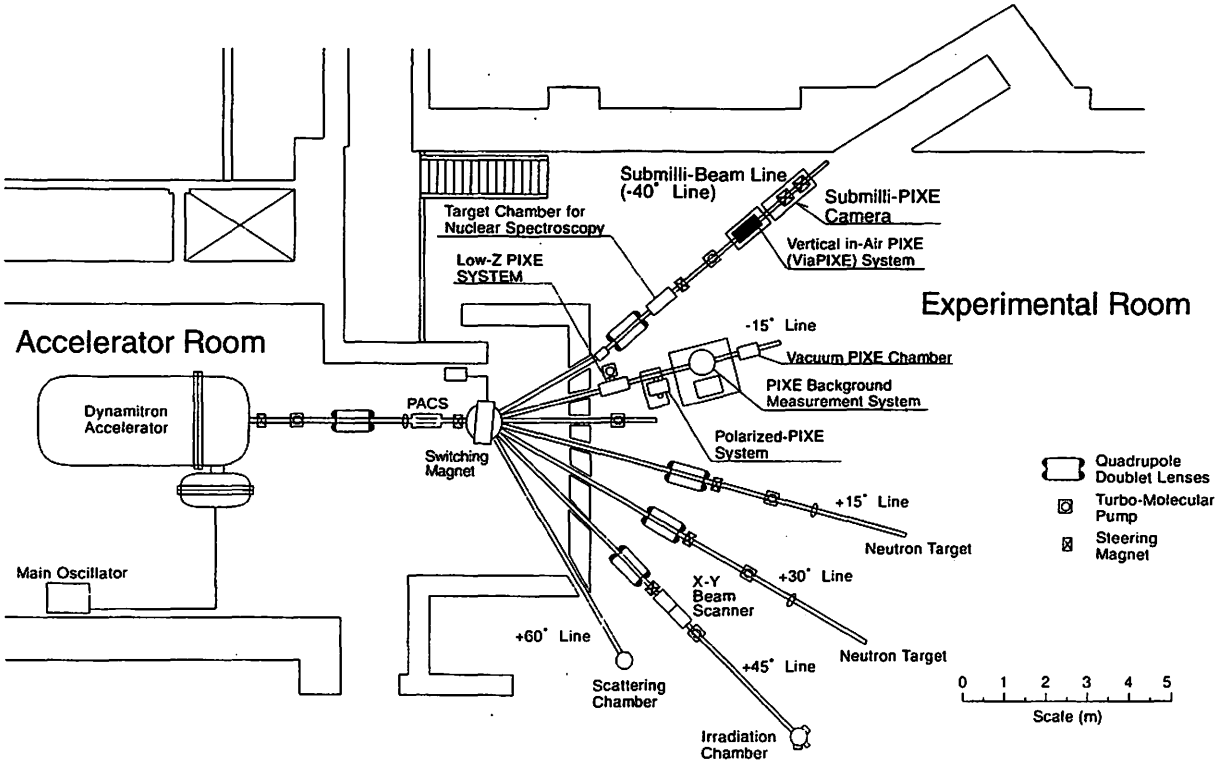

Fig. 1. Layout of the PIXE analysis system newly developed at the Dynamitron laboratory in Tohoku University.

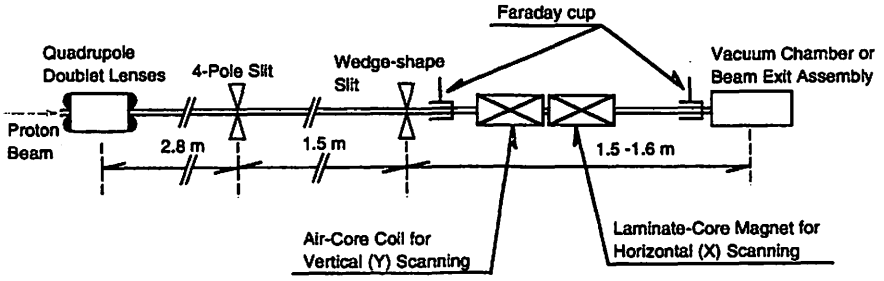

Fig. 2. Detail of the submilli-beam line.

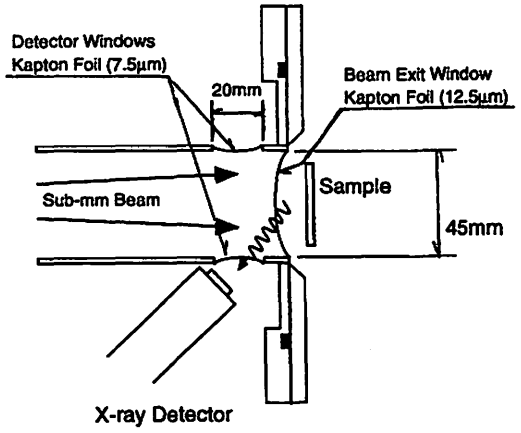

Fig. 3. Cross section view of the beam exit assembly.

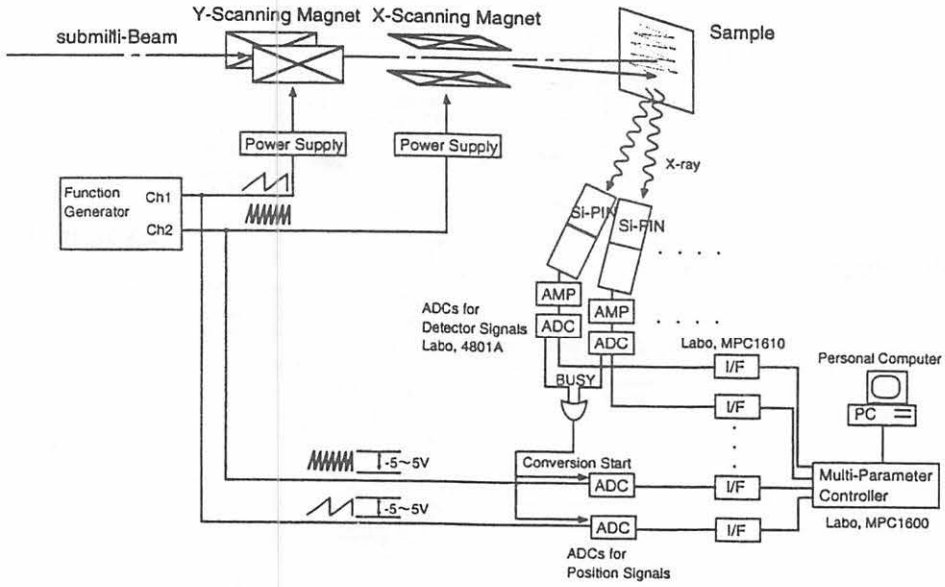

Fig. 4. Schematic diagram of the beam scanning system and the data acquisition system for elemental imaging

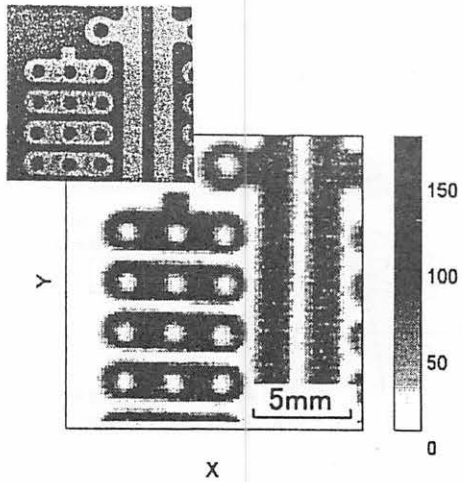

Fig. 5. Photograph of thesubstrare and the corresponding elemental image of Cu.

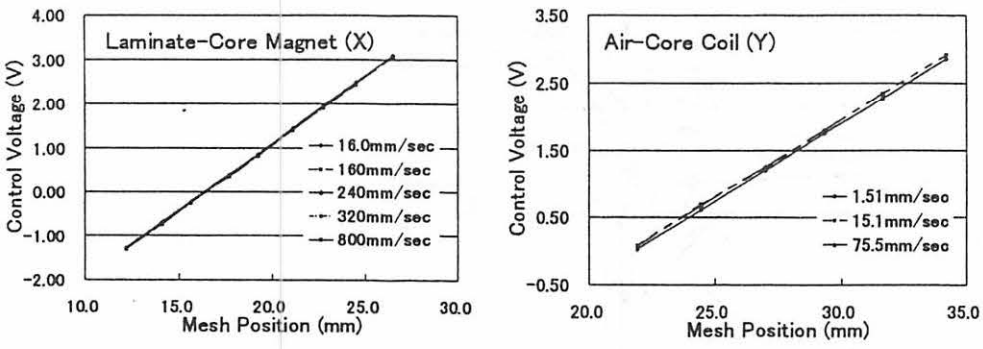

Fig. 6. Control voltages of the magnets v.s. the positions of the copper mesh for the laminate-core magnet.

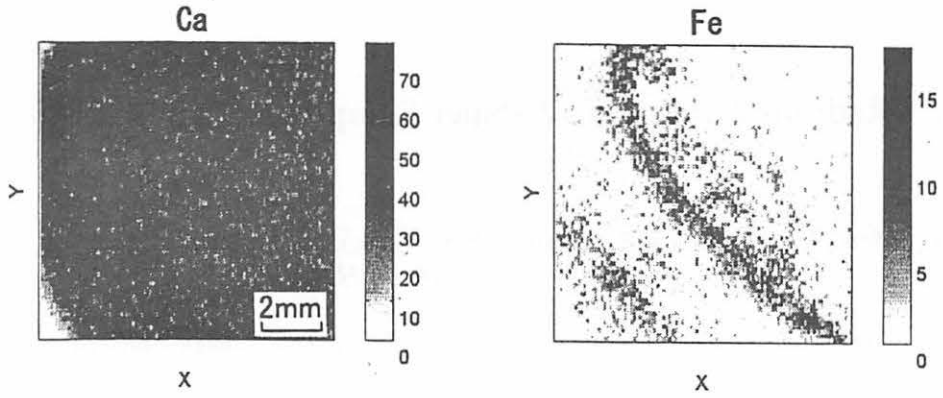

Fig. 7. Elemental images of Ca and Fe in the shell.

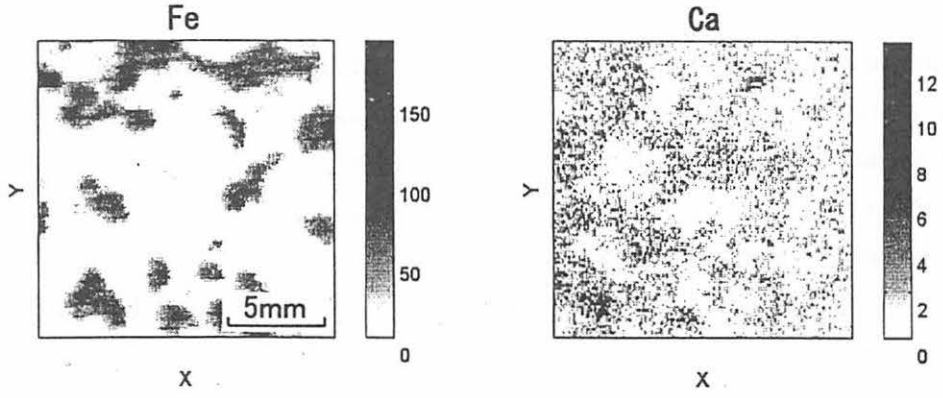

Fig. 8. Elemental images of Fe and Ca in the granite sample.

II. 19. Radiation Damage of Paper Samples in In-Air PIXE Analysis

*Endo H., Matsuyama S., Ishii K., Yamazaki H., Tokai Y., Sugimoto A., Yamamoto K., Sato T., and Orihara H.**

Department of Quantum Science and Energy Engineering, Tohoku University
*Cyclotron and Radioisotope Center, Tohoku University**

Introduction

Particle-induced X-ray emission (PIXE) analysis is well known to be a novel technique for trace elemental analysis. In quantitative analysis of PIXE method, the distribution of elements is required being uniform within the cross-sectional area of beams. Recently a submilli-PIXE camera has been developed at Tohoku University, which can measure spatial distributions of elements in a region of several cm^2 with a resolution of submilli-meters[1]. It will be a powerful tool in the analysis of archeological samples, *e.g.*, paintings, books, stamps, and paper currency. To analyze precious specimens like ancient writings, however we should consider their radiation damage caused by beam irradiation[2]. In this study, we investigated coloration of paper induced by beam irradiation.

Experiment

Three types of papers, Fine quality paper, *Houshosi*(Japanese paper), and Thick Japanese paper were irradiated in the In-Air submilli-PIXE camera, where 3MeV proton beams of a 0.5mm were scanned on a paper and the scanning area was $20\times20mm^2$. Irradiation conditions are listed in Table 1. Deterioration of paper was investigated from a viewpoint of coloration. After irradiation the degree of coloration was measured at the irradiated area and the non-irradiated area with a color meter (Model 520-02 Yokogawa Instruments). The color meter measures the reflected light from the paper and determines values on the color-coordinates. Since the value on color-coordinates depended on the intensity of light source, the light source had been fixed during the measurement. We introduced a relative value of the degree of coloration in the irradiated area and non-irradiated area.

Results

Relative values on color-coordinates for the tested papers are shown in Figs. 1 (a), (b), and (c) for various total beam charge. The degree of coloration for *Houshosi* and Fine

quality paper has a linear coloration with the total beam charge. On the other hand, that of Thick paper is independent with the total beam charge. This result suggests that proton beams cause the breakage of molecular chain of paper matrix and lead to coloration. The degree of coloration for *Houshosi* at the same beam charge is the largest among the papers. In the case of Thick paper, the coloration is easily achieved and this effect is saturated bellow the total beam charge of 2.5μC.

Relative values on the color-coordinates of *Houshosi* for total beam charge, beam currents and beam scanning speeds are shown in Fig. 2. The degree of coloration depends only on the total beam charge, but does not vary with beam currents and scanning speeds.

Time variations of relative values on color-coordinates of *Houshosi* and Fine quality paper are shown in Figs. 3 (a) and (b). The degree of coloration of the irradiated papers decreased with increase in days, and increased again after a few weeks of the irradiation.

Summary

As an application of the submilli-PIXE camera to archeological studies, the degradation of paper was investigated from a viewpoint of coloration. The degree of coloration was different for each the tested paper and was corresponding to the total beam charge. In another feature, the coloration of all types of irradiated papers decreased steadily as time at first and then increased after a few weeks. This shows a very important result for application of PIXE to archeological samples that the radiation damage of paper disappears but it appears again.

References

1) Matuyama S., Goto K., Ishii K., Yamazaki H., Yamamoto K., Sugimoto A., Tokai Y., Endoh H. and Orihara H., Internat. J PIXE, 8, 2&3, to be published.
2) Zeng X., Wu X., Shao Q., Tang J., and Yang F., Nucl. Instr. and Meth. B47 (1990) 143-147.

Table. 1. Irradiation conditions.

Irradiation condition	Beam charge(μC/cm^2)	Beam current (nA)	Scanning speed (Hz)
1	0.25	2.5	x:10 y:0.12
2	1	2.5	x:10 y:0.12
3	2	2.5	x:10 y:0.12
4	0.25	0.5	x:10 y:0.12
5	0.25	0.5	x:1 y:0.012

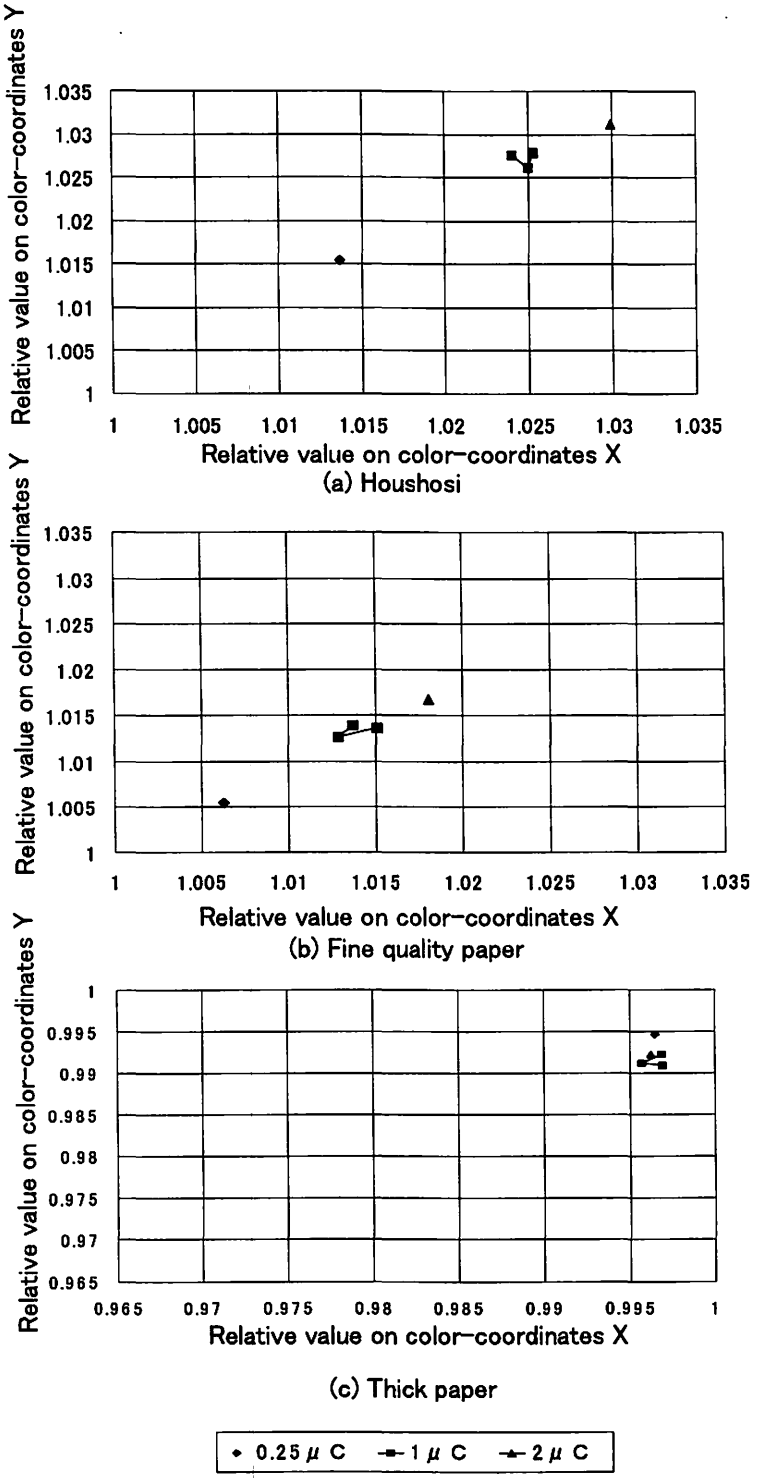

Fig.1 Relative values on color-coordinates for total beam charge. (a) Houshosi, (b) Fine quality paper, and (c) Thick paper.

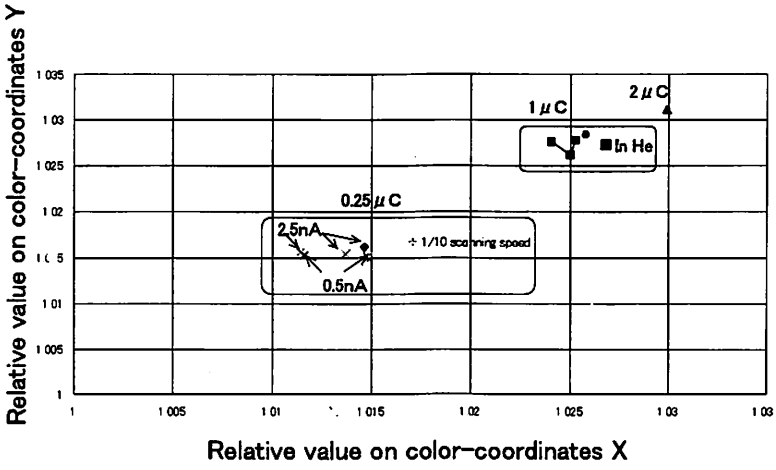

Fig.2 Relative values on color-coordinates of Hoshosi for various beam conditions.

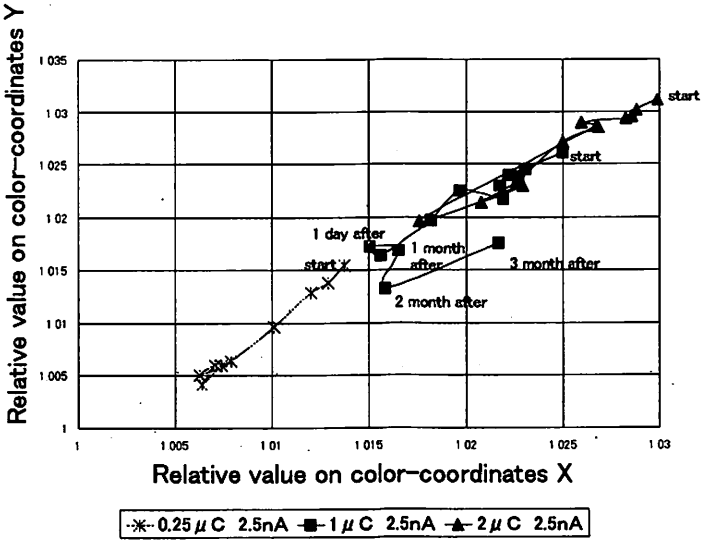

(a) Houshosi

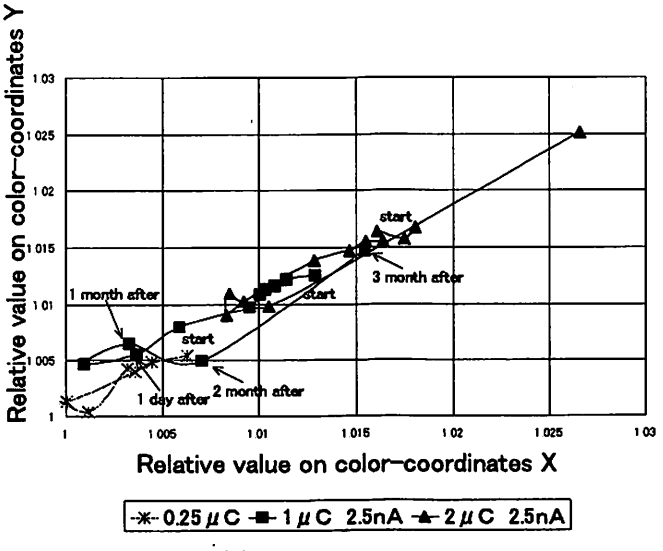

(b) Fine quality paper

Fig.3 Time variations of relative values on color-coordintaes.
(a) Houshosi, and (b)Fine quality paper.

II. 20. PIXE Analysis of Aerosol Samples Collected at the Suburbs of SENDAI City

Tokai Y., Matsuyama S., Ishii K., Yamazaki H., Gotoh K., Satoh T., Sugimoto A., Yamamoto K., Oikawa M., Iwasaki S., Orihara H., Jon G.C.**, Nakamura E.***, Futatsugawa S.****, and Sera K.*****,*

Dept. of Quantum Science and Energy Engineering, Graduate School of Engineering, Tohoku University
*Cyclotron and Radioisotope Center, Tohoku University**
*Institute of Physics, Academia Sinica***
*Miyagi Prefectural Institute of Public Health and Environment****
*Nishina Memorial Cyclotron Center, Japan Radioisotope Association*****
*Department of Cyclotron Research Center, Iwate Medical University******

Introduction

Aerosols are very small particles which are sandy dusts, smoke from factories, and exhaust gas of cars. They cause the acid rain and the greenhouse effect. Observation of air pollution will be possible by analyzing elemental concentrations in the aerosols continuously for a long period. We collected aerosol samples on Nuclepore filters by means of a step sampler and analyzed elemental concentrations in the aerosol samples by the Particle Induced X-ray Emission (PIXE) method which is known as a technique for multi-elemental analysis with extremely high sensitivity[1]. A method of PIXE analysis in air[2-4] is able to analyze a lot of samples quickly because it has no limit for the size and shape of samples, and the samples can be easily changed. So this method is suited to analyze the aerosol samples. In this study, we investigated the time variation of concentration of each element in aerosols collected at the suburbs of Sendai City. We tried to determine a place generating the pollution using time data for the wind direction.

Sampling and analysis

The step sampler is composed of a sampling unit, a control unit and a vacuum pump. The sampling unit is put in a case with a multi-storied roof to avoid sucking large particles that come from mainly natural origins. Atmosphere is sucked through the Nuclpore filter of pore size 1.0μm in diameter and the aerosols are collected on the surface of this filter. A suction nozzle of 4mm in diameter is mounted on either side of the sampling unit (see fig. 1). The aerosols were continuously collected for 2 or 3 hours with a constant flow rate of 1.0 l/min. The sampling of aerosols was performed during the periods of 4-27 August 1997 and of 23 March-2 April 1998 in Tagajo City (see fig. 5). At the sampling site,

meteorological data were also taken. The total number of aerosol samples obtained was about 300. The samples were analyzed by in-air PIXE systems at Tohoku University and at Nishina Memorial Cyclotron Center (NMCC) of Japan Radioisotope Association. The PIXE spectra were analyzed by using a program based on a pattern spectra analysis[5]. It takes only a few seconds to analyze a PIXE spectrum by this program. A typical X-ray spectrum of aerosol is shown in fig. 2.

Result and Discussion

Eleven elements (Si, S, Ca, Ti, Cr, Mn, Fe, Cu, Ni, Zn and Pb) were contained in the aerosol samples. Time variations in concentration were obtained for these elements. The result of Fe is shown in fig 3. It shows a diurnal pattern, namely, the concentration periodically is incleased in the daytime and decreased at night. Low concentrations were shown during the period of 8/11~ 8/17, which just corresponds to the summer holidays. This pattern coincides with the human activity. The time variations of Si, Ca and Mn elements showed a similar trend to the result of Fe. We investigated the correlation between the elemental concentration and the direction of the wind. The concenetrations of six elements (Fe, Mn, Ca, Cu, Pb, Zn) in the direction of the wind are shown in fig. 4. Here, the values of concentrations are the average of one month. This figure shows that the concentrations for Fe, Mn, Ca, and Pb became high when the southeast wind has blown. As shown in fig. 5, there is an industrial area in the southeastern side of Tagajo City. If we collect aerosol samples at multi-points in this region, it is able to determine the place generating the aerosols with these elements. Such a network of aerosol sampling sites enables us an air-pollution monitoring. To construct a network of air-pollution monitoring systems, however, it is necessary to reduce the manufacturing cost of samplers and its running cost which depends on the price of Nuclepore filters.

References

1) Johansson S. A. E. and Campbell J. L., PIXE:A Novel Technique for Elemental Analysis, Wiley, Chichester 1988.
2) Iwasaki S., Ishii K., Yoshizaki K., Fukuda H., Yokota H., Iwata Y., and Orihara H., International Journal of PIXE, Vol. 5, No. **2 & 3** (1995), pp. 163-173.
3) Iwasaki S., Ishii K., Matsuyama S., Murozono K., Inoue J., Tanaka M., Yamazaki H., Honma T., Fujioka M and Orihara H., International Journal of PIXE, Vol. 6, Nos. **1 & 2** (1996) 117-125.
4) Futatsugawa S., Hatakeyama S.,.Saitou S and Sera K., International Journal of PIXE, Vol.7, Nos. **3 & 4** (1997), pp. 171-177.
5) Murosono K., Iwasaki S., Inoue J., Ishii K., Kitamura M., Sera K., and Futatugawa S., International Journal of PIXE, Vol. 6, Nos. **1 & 2** (1996) 135-145.

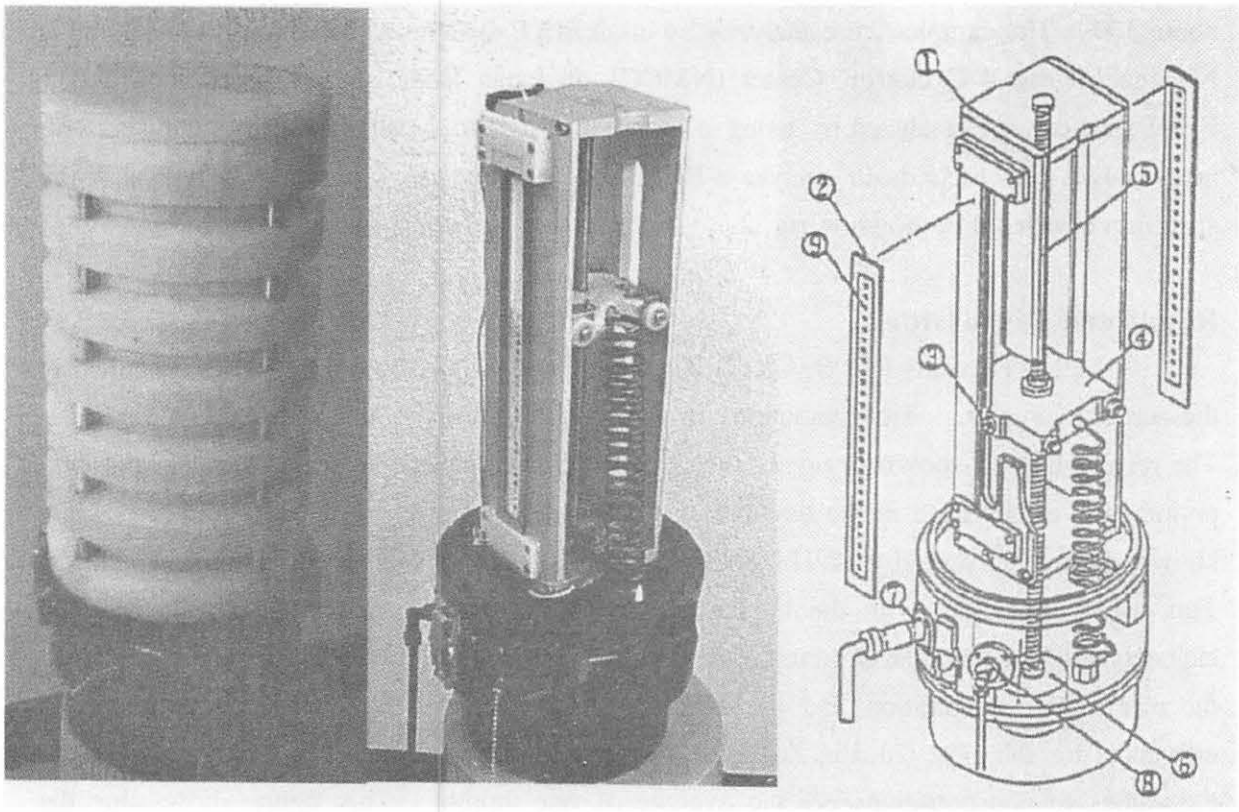

Fig. 1. Step Sampler.

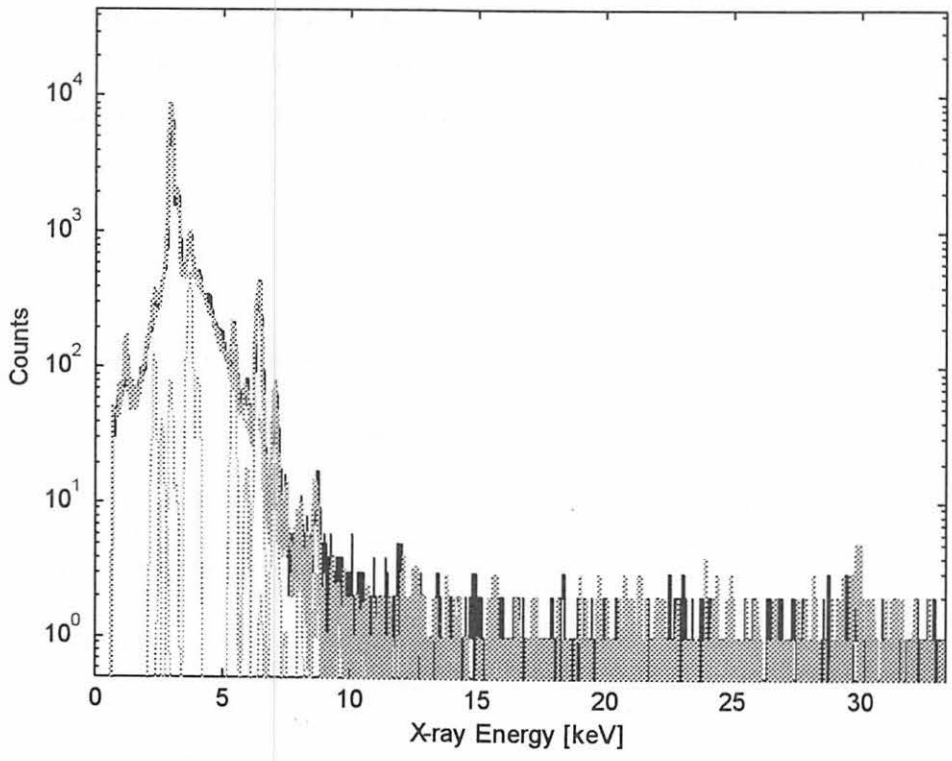

Fig. 2. IXE spectrum of atmospheric aerosol.

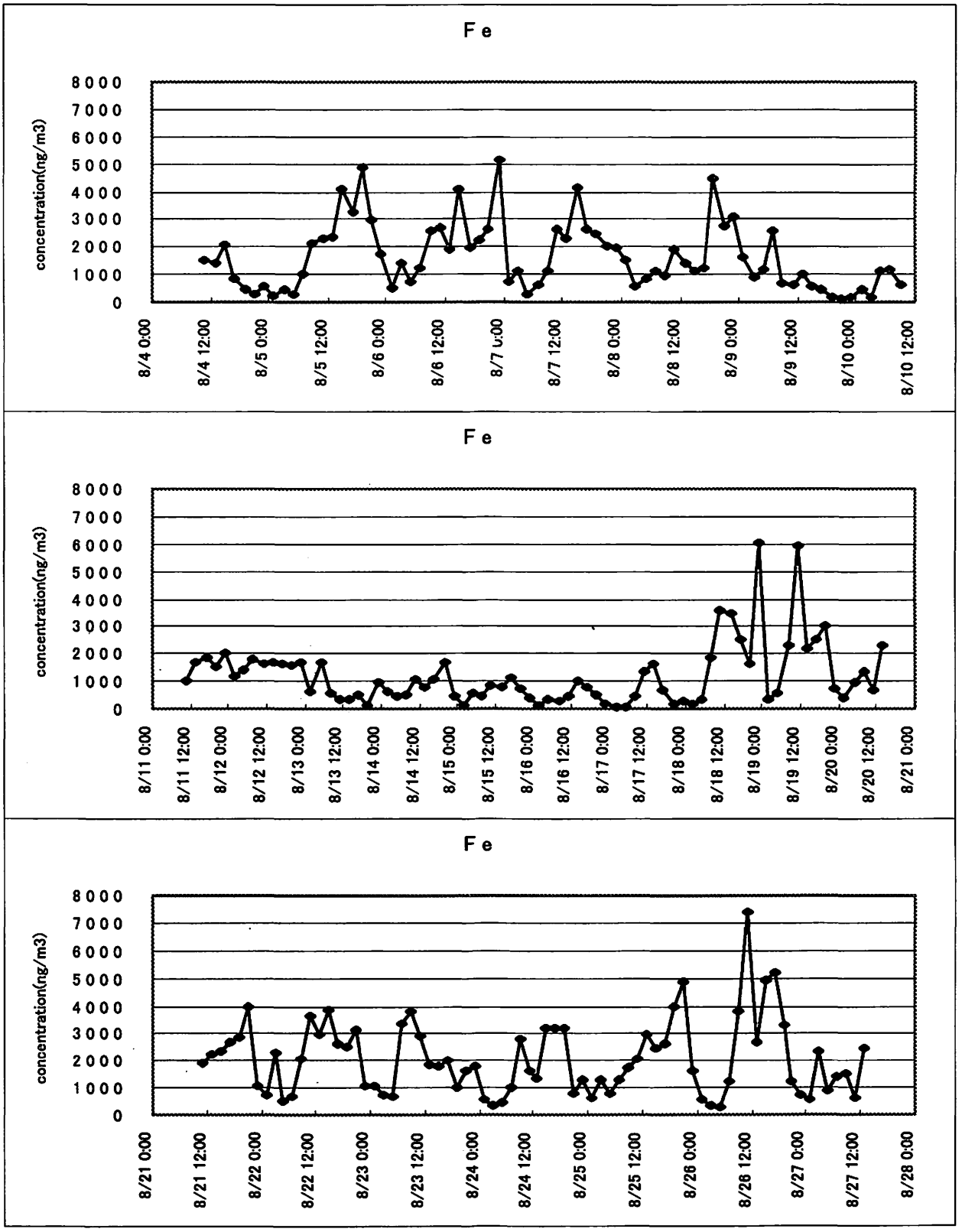

Fig. 3. Time variation in concentration of Fe in the aerosol.

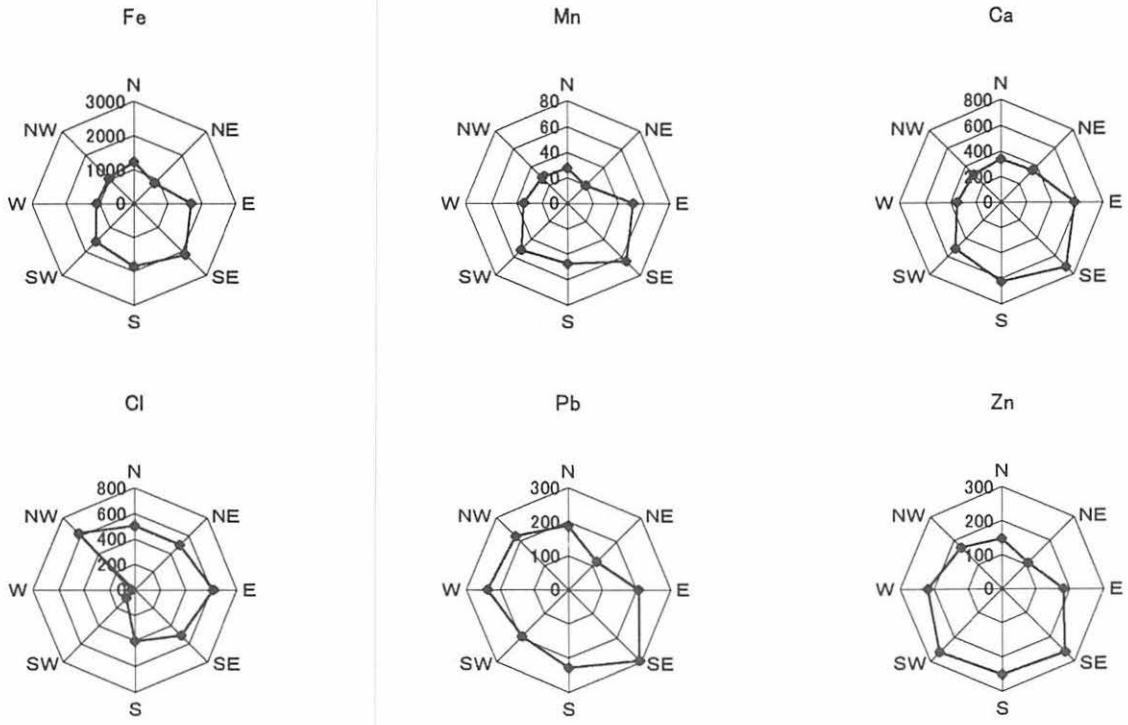

Fig. 4. Concentration (ng/m^3) of elements in aerosols as a function of wind direction.

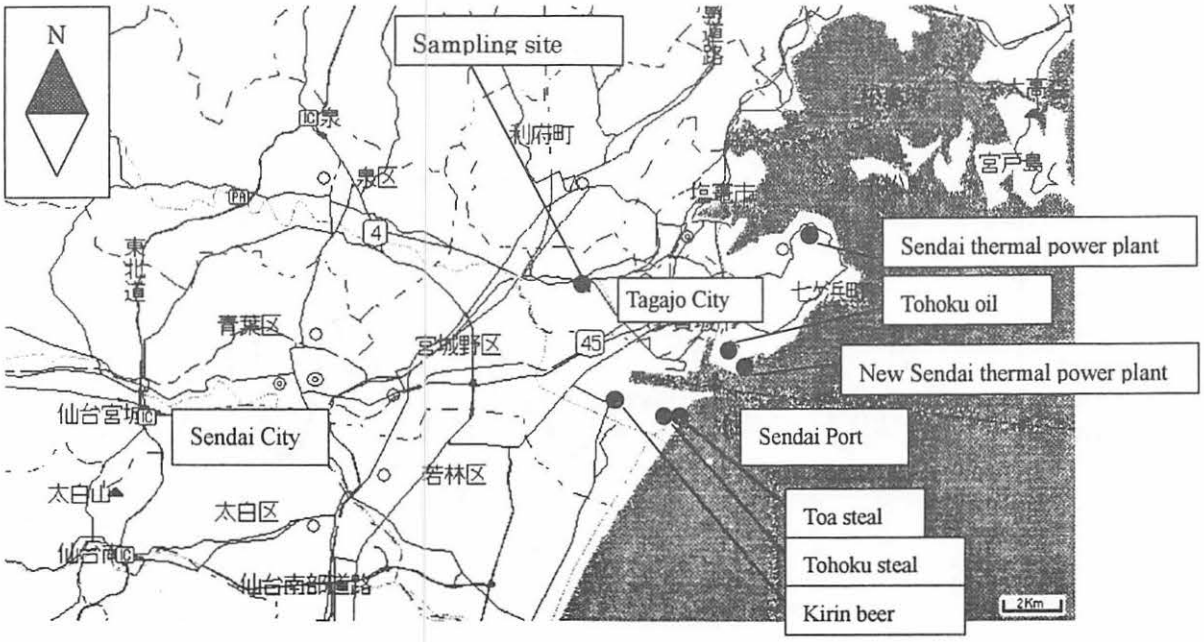

Fig. 5. Location of the Sampling site at the suburbds of Sendai City.

II. 21. Application of Vertical-beam In-air PIXE to Surface Analysis of Plant Root Exposed to Aluminum Stress

Yokota S., Inoue J., Murozono K.*, Matsuyama S.*, Yamazaki S.*, Iwasaki S.*, Ishii K.*, and Mae T.***

Laboratory of Plant and Environmental Research, Faculty of Agriculture, Tohoku University
*Department of Quantum Science and Energy Engineering, Tohoku University**
*Laboratory of Plant Nutrition, Faculty of Agriculture, Tohoku University***

Introduction

On acid soils, growth of plants is greatly reduced because of phytotoxicity of Al ions that tend to become soluble in acidic surroundings. Recently, acid rain is also problematical as a factor of environmental stress for crop production through acidification of soils and water. Development of acid-soil-tolerant crops is demanded for worldwide increase in food production, however, the molecular mechanism of Al toxicity has not been clarified yet.

We are trying to detect short-term responses of alfalfa root to Al stress. We previously reported that alteration of elemental composition especially in atomic ratio of potassium to phosphorus (K/P ratio) of whole root-tip occurs by 4-h Al treatment by application in-vacuum PIXE[1]. At that time, root-tips used were dry before and during measurement, hence what we could know was only bulk composition of whole root-tips. On the other hand, differences in elemental composition between surface and inner region of root-tip under Al stress were found to be important to interpret results obtained by non-destructive optical observation. Then techniques for in-situ microdetermination of elements of living cells or tissues have been desirable.

By using in-air PIXE method for surface analysis of samples can be achieved in air without any pre-treatment, information of in-situ spatial distribution of elements of biological tissues could be expected. Our preliminary experiments revealed that only a surface layer of root-tip cells is damaged by 5-min irradiation of a 3 MeV proton beam using newly developed vertical-beam in air (Via) PIXE system in Tohoku University[2].

Thus we tried to apply Via PIXE to determine elemental composition of root surface cells of alfalfa exposed to Al stress. Summary of Via PIXE method for in-situ elemental analysis of plant root will be reported.

Experimental

Plant material and Al treatment

Alfalfa seeds were germinated in distilled water. Aluminum stress was loaded to seedlings by solution experiments. Rooting solutions were prepared as follows; control solution: 1 mM $CaCl_2$ (pH was adjusted to 5.0 with HCl), Al-stressed solution: 1 mM $CaCl_2$ containing 0.02 mM $AlCl_3$ (pH 5.0). Samples were immediately used for Via PIXE analysis after brief wash with distilled water.

Via PIXE system

Via PIXE system in Tohoku University was used. A 3-MeV proton beam generated by Dynamitron accelerator was collimated to approximately 2 mm in diameter at the target.

Sample holder

Sample holder was assembled as illustrated in Fig. 1. A strip of filter paper (3 cm×3 cm, Toyo No.6 for quantitative use; Toyo Roshi Kaisha, Tokyo, Japan) was put between mylar plates with a center hole (20 mm in diameter). The target holder was irradiated for 15 min prior to use to visualize the beam position. Beam spot was easily recognized as browning of filter paper. Impurity of filter paper as a target holder was also examined by a long time irradiation (60 min) and any problematical peaks were not apparent.

Measurement of root samples

To avoid drying, filter paper of a target holder was moisten with distilled water, followed by placing a seedling of alfalfa. Root-tip region of the seedling was adjusted to the brown spot on the filter paper (Fig. 1). Beam current was kept in the range of 200-300 pA, and X-rays were detected using a Si(Li) detector. Each sample was irradiated for 5-7 min. Total measuring time (before and during irradiation) was less than 15 min and loss of cellular viability by natural drying could be negligible. Under this condition, damages caused by the irradiation per se were restricted within only surface cell layer (epidermal cells) of root-tip of alfalfa. In present experiment, total beam flux could be minimized less than 100 nC comparing to that in our previous report.

Standard solution for via PIXE

For energy calibration and elucidation of relative yield of K X-rays of phosphorus and potassium, standard solution containing 1 mM NaH_2PO_4 and 1 mM KCl (KP standard) was absorbed in a small piece of filter paper (5×8 mm, Toyo No.6, Toyo Roshi Kaisha), followed by Via PIXE. Measuring condition was same as described above. Chemicals (special grade) were purchased from Wako Pure Chemical Industry (Osaka, Japan).

Results and Discussion

Overview of Via PIXE spectra

Figure 2 shows Via PIXE spectra of wet or dry filter paper, standard solution absorbed in filter paper, time-zero root-tip, 8-h control root-tip and 8-h Al-treated root-tip. No problematical impurity peak was observed in wet or dry filter paper (Fig. 2, panels A and B). Especially, supply of water to samples through wet filter paper have a great effect to prevent them from drying, heat-up and charge-up. The K X-ray peaks of P, S, Cl, Ar, K and Ca were observable in spectra of root samples (Fig. 2, panels D,E and F). The K X-ray peak of Al that was apparent in in-vacuum PIXE spectra of Al-treated root was not observable in present experiment (Fig. 2, panel F). This may mainly come from absorption of low energy X-rays by air and window materials between the sample and a detector. The objective of this study is to know alterations of elemental composition (especially in the K/P ratio) of root surface cells under Al stress. Five to ten minutes irradiation of a 3 MeV proton beam at 300 pA was an experimentally suitable setting to satisfy this objective. Both peaks of P and K were detectable and net X-ray counts of P and K of plant samples were at least 76 and 264, respectively. Values of total beam flux of each root sample were suppressed lower than 100 nC. This greatly contributed to minimize damages of samples by beam irradiation.

Background spectra

All samples applied to this experiment are so-called "thick targets" which consist of water (H, O) and polysaccharides (for example, cellulose; C, H, O) as matrix substances. Those matrix substances cause continuous spectral X-ray in low energy region (below 6 keV). Unfortunately the region of interest in present study (from 1.5 to 4.0 keV, including P-, S-, Cl-, K- and Ca-K X-rays) and continuous background X-rays overlapped each other. Therefore, elucidation of BGF will have much importance on interpretation of spectrum data in this kind of experiment. Diameter of beam at the target was always larger than the width of root-tip region, therefore the background of root spectra must be consisted of X-rays from wet filter paper and plant root matrix.

Advantages and problems of Via PIXE as a tool for in situ analysis of biological samples

There must be no doubt that Via PIXE will be a powerful tool for in-situ non-destructive analytical method of biological samples. In order to assure the profits of Via PIXE, however, some problems as follows must be cleared. The concerned region of biologically living samples that are analyzed by use of advantages of in-air PIXE is the surface of highly organized tissues or organs. Excluding in the case of very thin samples, e.g. blood corpuscles and cultured single cells of plants or animals, ordinary ones are so-called "thick targets". It has been problematical how should we estimate the large continuous background X-rays in lower energy region (<10 keV) from constitutive components, that is water, proteins, lipids, polysaccharides etc. In root samples, the

intensity of signals of P, S, Cl in root samples is not large excess comparing to that of background X-rays (Fig.2, panels D-F). The background function (BGF) elucidated from wet filter paper (BGF-WFP) was also expected to be a simple model for plant roots because plant cells consist of water (approximately 90%), cellulose and other molecules. However, BGF-ZR and BGF-WFP were not identical (data not shown). Confirmation of exact origin of X-rays, that is position, width and depth within a target, is another problem. To know in-situ three-dimensional distribution of elements in organized structure of living things will help us to understand both physiological roles of elements and status of cells or tissues. The microbeam in-air PIXE will be the shortest way to fulfil this demand.

References

1) Yokota S. et al., International J. PIXE **4, 263** (1994).
2) Iwasaki S. et al., International J. PIXE **5, 163** (1995).

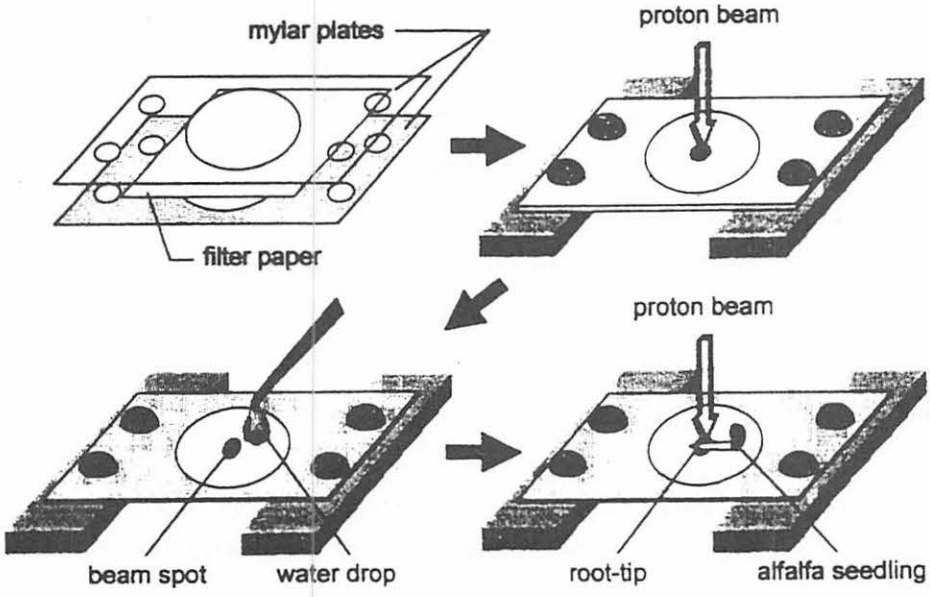

Fig. 1. Preparation of target holder and irradiation of plant root samples in Via PIXE method.

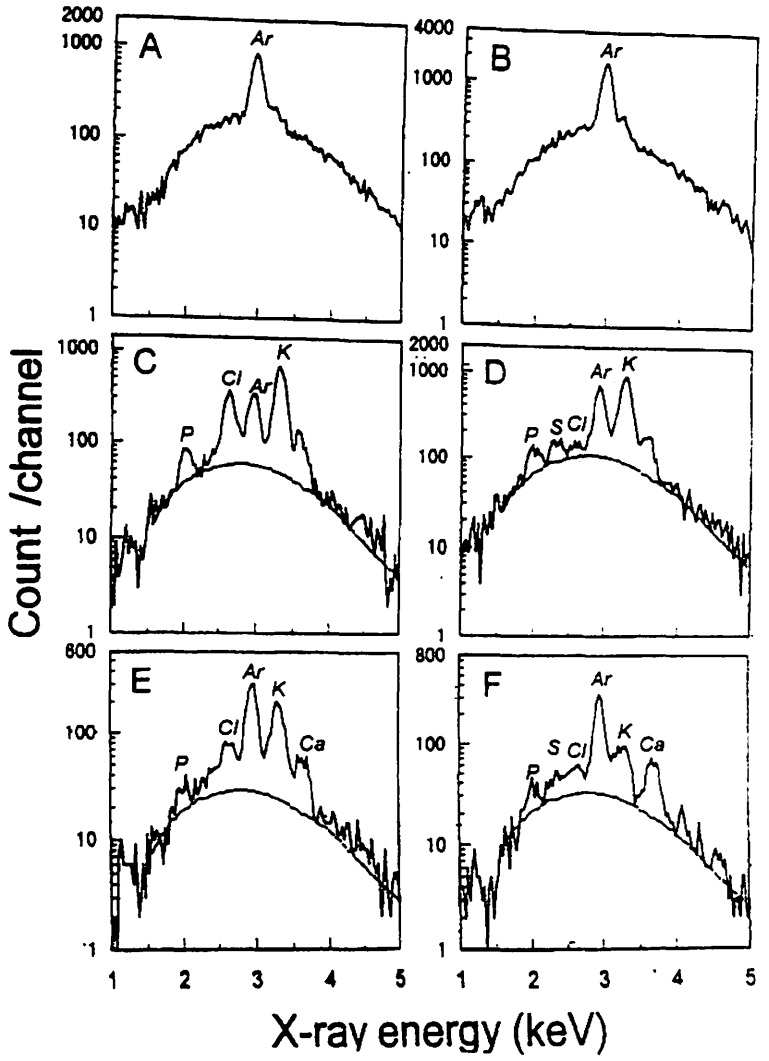

Fig. 2. Via-PIXE spectra of wet filter paper (A), dry filter paper (B), KP standard solution abosorbed in filter paper (C), time-zero root-tip of alfalfa (D), 8-h root-tip in control solution without Al (E) and 8-h root tip exposed to Al (F). Names of elements are designated at the top of their K X-ray peaks. The ordinate is expressed in log scale.

II. 22. Strontium-Calcium Ratios in Sagittal Otoliths of the JuvenileJapanese Flounder Exposed to Diluted Sea Water

Kakuta I., Chiba D., Ishii K. Yamazaki H.*, Iwasaki S.* and Matsuyama S.**

Department of Biotechnology, School of Science and Engineering, Senshu University of Ishinomaki
*Department of Quantum Science and Energy Engineering, Faculty of Engineering,Tohoku University**

Introduction

Sagittal otoliths in teleost fishes are located in the membranous labyrinth of the inner ear, where they function as a perceptive organ for stato-acoustic sensation and in the detection of orientation and acceleration. The otoliths have been used to estimate the age of fish, because of the internal formation of daily and annual rings.

Otoliths of teleost mainly consist of calcium carbonate in the aragonite crystal form[1] and contain other elements such as strontium, chloride, sodium, zinc at various concentrations[2-4]. Chemical composition of calcified tissue is controlled by the physiological activity of fishes. It is thought to be affected by environmental factors such as salinity and temperature. Therefore, the otoliths of fish contain large amount of ecological, metabolic and biological data.

Within the aragonitic crystals, strontium can be a contaminant at very low levels[2-4]. Strontium interchanges with calcium in otolith aragonite, due to its close proximity to calcium in terms of ionic radius size. It was found that strontium concentrations in coral aragonite are both temperature and salinity dependent, and it has been suggested that strontium incorporation was a physiological process which was controlled by theses temperature and probably by salinity[5,6]. The ratio of strontium to calcium (strontium/calcium) of otoliths will thus provide information on the temperature and the salinity of the environment experienced by a fish in its past.

Many attempts have been carried out to estimate a fish's history of temperature and salinity based on the strontium-alcium ratio in the otoliths[4, 7-12]. However, (i) the effect of the habitat water temperature on the strontium-calcium ratio in fish otoliths is different between the case of freshwater fish and marine fish[13], (ii) there have been few detailed studies of the relation between the salinity of breeding environments and strontium-calcium ratio of fish otoliths; and (iii) the composite effects of ambient temperature and salinity on the

strontium-calcium ratio of fish otoliths have hardly been investigated.

The Japanese flounder, *Paralichthys olivaceus*, is widely distributed at estuaries, inner bays and coastal regions from Hokkaido to the Kyushu. The flounder is an important fish species being cultured in Japan. At the present time, however, ecological and life history studies of the Japanese flounder are not sufficient to understand the population dynamics of the fish inhabiting in the Sendai Bay.

The particle induced X-ray emission (PIXE) technique is an effective tool for performing multielemental analysis in small amount of samples. In the present study, for the purpose of obtaining basic data for grasping the environmental history of the *Paralichthys olivaceus* habitat, the effect of the salinity of the environmental water on the strontium-calcium concentration ratios of the otoliths taken from the Japanese flounder were analysed using PIXE was investigated.

Matarials and Methods

One hundred and five the juvenile Japanese flounder, *Paralichthys olivaceus*, purchased from a commercial farm in September, 1996, being 1.3±0.3g in body weight and 55±4mm in body length, were used for the experiment. They were reared preparatively at 20±1°C for one month, with thirty-five fish being placed in three 60l tanks filled with filtered sea water. Half of the rearing water was exchange softly every 3 days. During this process, the fish were fed twice a day with dried commercial pellets at the daily amount of 2% of the body weight.

After the pre-rearing, otoliths were removed from fifteen fish (initial control), and the remaining fish (test) were divided into three 60ℓ experimental tanks. One of these tanks contained 50% sea water, one had 75% sea water and one had 100% sea water (control). The fish were reared at 20±1°C for one month. Half of the rearing water was exchanged softly every 3 days. The fish were fed twice a day with the same pellets administrated in the pre-rearing period amounting to 2% of the body weight every day. The otoliths from fifteen fishes in each tank were removed on day 7 and at the end of this rearing process.

The otoliths were cleaned by means of ultrasonication once in distilled water, once in 99% ethyl alcohol, and twice in ultra pure water for 10 min each, and then dried at room temperature for 72h. The left otolith from each fish was used for the analysis of the elemental composition of the portion formed during rearing by particle induced X-ray emmision (PIXE) method after pasting a thin otolith section onto a 2μm Makrofol film attached by a plastic bond to a Mylar frame of 45×32×0.5 mm having 20×20 mm hole in its center with the analysing surface upward. A 4.5 MeV Dinamitron accelerator at Tohoku University was used for this analysis. Bombardment was carried out with a 3 MeV proton beam in air with 0.1 to 5 nA for 300 to 1800 sec, and with a beam spot diameter of 3 mm for analysing the surface of fish otoliths. Induced X-ray were detected by an Si(Li) detector

through a 500μm Mylar absorber in order to attenuate X-ray intensities of calcium line.

A mixture of bovine liver (NBS), and a part of right otolith which was homogenized in an onyx mortar and the elemental compositions were analysed by Inductivity Coupled Atomic Emission Spectrometry (ICP, Seiko SPS-1200A) after ashing with HNO_3 and $HClO_4$ (5:1) in a Teflon vessele were used as a standard for determination of elemental compositions of the left otolith by the PIXE method.

Sea water (about 33‰) was collected at the coastal area of Ishinomaki Bay in Miyagi Prefecture. Ammonia-N and nitrite-N concentrations in the rearing water were kept below 0.05mg/l.

All data in this study were analysed statistically using Duncan's method with a significant limit of $p<0.05$, and were indicated as the mean ± SE, unless otherwise mentioned.

Results and Discussion

Body length, body weight and otolith weight of the Japanese flounder reared in 100% sea water were 71±7mm, 2.5±0.4g and 1.2±0.2mg at the end of the experiment. No significant differences in these parameters were found among 50%, 75% and 100% sea water groups.

Changes of the strontium and calcium compositions and the strontium-calcium ratios of the otoliths from fish in each group are shown in Figs. 1 and 2. No statistically significant changes were found in calcium concentration of otoliths from fish in each group. The strontium concentration and the strontium-calcium ratio of the otoliths at the end of the experiment (on day 30) were positively proportional to the rearing salinity. Significantly lower values for strontium concentration and strontium-calcium ratio (about 0.90 times as much) were found in 50% sea water compared with those in 100% sea water. Although slightly lower values (about 0.95 times) of these parameters were found, in 75% sea water no significant differences for these values were observed between 100% and 75% sea water groups.

On day 7, however, significantly higher values (about 1.17 times) of the strontium concentration and the strontium-calcium ratio of fish otoliths in 50% sea water were found compared with those in 100% sea water. No significant changes in these parameters were observed between 75% sea water and 100% sea water groups, though slightly higher values for these parameters were shown in 75% sea water.

The PIXE analysis of the element composition of the otolith portion formed during the rearing process showed a positive correlation between the salinity of the rearing water and the strontium concentration and the strontium-calcium ratio of otoliths taken from the fish acclimated to lower salinity. Therefore, it is thought that these otolith parameters reflect the chemical differences of the rearing water.

However, brief exposure to much lower salinity (50% sea water) increased these otolith parameters. There occurred severe physiological changes in the fish immediately after being transferred to 50% sea water. It is thought that the elemental compositions of otoliths are closely related to those of the blood plasma and the endolymp[2, 14-16]. It is thus suggested that the fluctuations of plasma and endolymph elemental compositions triggered by radical changes of enviromental salinity affect not only the growth of the otoliths but also the incorporation rate of various elements into the otobased on liths in direct or indirect ways.

This experiment was carried out to interpret the information on environmental salinity recorded in *Paralichthys olivaceus* otoliths, based on the elemental composition of the otolith. In the present study, it was found that the strontium concentration and the strontium-calcium ratio of fish otoliths are effective indices (information sources) for predicting the history of environmental salinity experienced by a fish in the past. However, these otolith parameters were seriously affected by severe physiological changes triggered by radical environmental fluctuations. Therefore, there is a possibility that these otolith parameters don' t exactly reflect the salinity history in the fish inhabiting the regions with large fluctuations in salinity level within a short period. The researcher must carefully consider the various physiological and environmental factors to each fish species before the interpretation of otolith element data is undertaken.

References

1) Carlstrom D., Biol. Bull. **125** (1963) 441.
2) Kalish J. M., Mar. Ecol. Prog. Ser. **74** (1991) 137.
3) Sie S. H. and Thresher R. E., Int. J. PIXE **2** (1992) 357.
4) Kakuta I., Bull. Soc. Sea Water Sci. Japan **50** (1996) 349.
5) Weber N. J., Geochim. Cosmochim. Acta. **37** (1973) 2173.
6) Schneider R. C. and Smith S. V., Mar. Biol. **66** (1982) 121.
7) Papadopoulou C. et al., Nar.Pollut. Bull. **11** (1980) 68.
8) Radtke R. L. et al., Env. Biol. Fish. **23** (1988) 205.
9) Radtke R. L., Comp. Biochem. Physiol. **92A** (1989) 189.
10) Sadovy Y. and Severin P., Bull.Mar. Sci. **50** (1992) 237.
11) Townsend D. W. et al., J.Exp. Biol.Ecol. **160** (1992) 131.
12) Arai N. et al., Fish. Sci. **61** (1995) 43.
13) Mugiya Y. and Tanaka S., Fish. Sci. **61** (1995) 29.
14) Mugiya Y., Nippon suisan Gakkaishi **60** (1994) 7.
15) Kalish J. M., U. S. Fish. Bull. **88** (1990) 657.
16) Kalish J. M., J. Exp. Mar. Biol. Ecol. **132** (1989) 151.

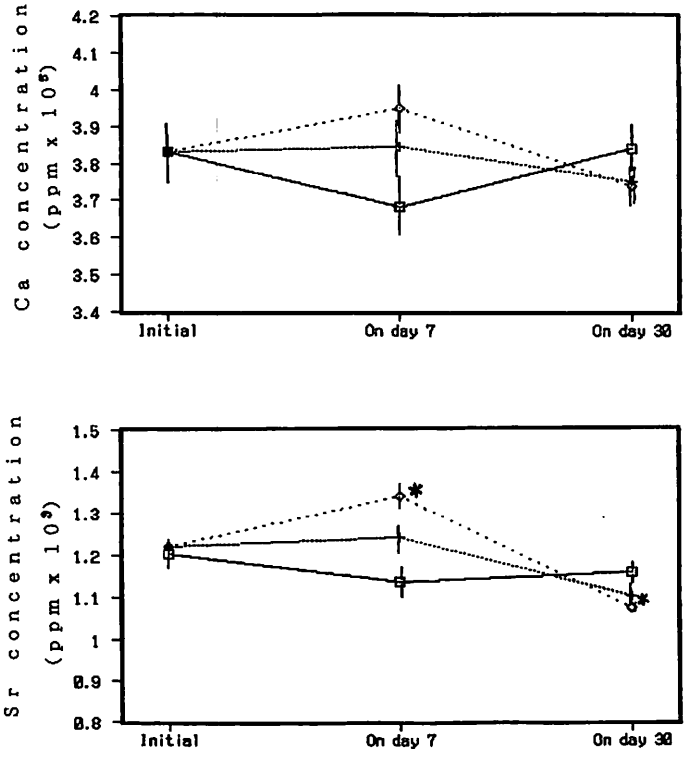

Fig. 1. Changes of strontium and calcium compositions in the surfaces of sagittal otoliths taken from ***Paralichthys olivaceus*** reared in 50%, 75% and 100% sea water for one month. Data are given as mean ± SE (N=15).

□, 50% sea water; +, 75% sea water; ◇, 100% sea water

*; Significant ($p<0.05$)

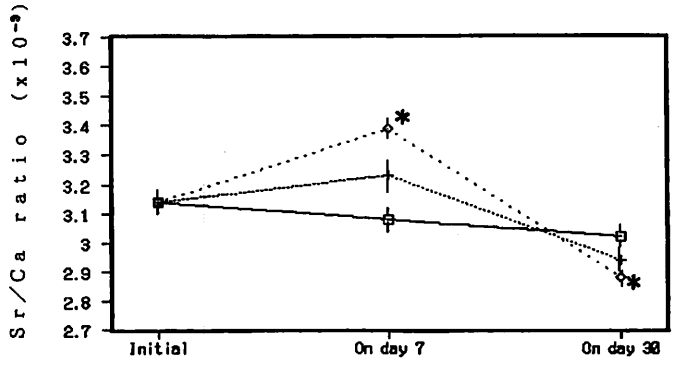

Fig. 2. Changes of strontium-calcium ratios in the surfaces of sagittal otoliths taken from ***Paralichthys olivaceus*** reared in 50%, 75% and 100% sea water for one month. Data are given as mean ± SE (N=15).

□, 50% sea water; +, 75% sea water; ◇, 100% sea water

*; Significant ($p<0.05$)

III. CHEMISTRY

III. 1. Are Polycyclic Aromatic Hydrocarbon (PAH) Precursors Produced by 15-MeV Proton Irradiation of Benzene ?

Ando Y., Ido T., Sekine T. and Kudo H.*

Department of Chemistry, Graduate School of Science, Tohoku University
*Cyclotron Radioisotope Center, Tohoku University**

A number of studies on radiolysis of liquid benzene have revealed that benzene is more radiation resistive than aliphatic compounds[1-3]. Although production of low-molecular weight products such as H_2, C_2H_2 and biphenyl is reported, little is known on the major products of viscous yellow liquid containing higher molecular weight "polymers". The polymerized products are of cosmological interest, because polycyclic aromatic hydrocarbons (PAHs) are predominant in organic compounds in space[4]. Cosmic or high-energy protons are supposed to be an initiator of reactions of PAHs synthesis. Despite theoretical and laboratory simulations[5-6], crucial explanation about the PAH synthesis in space has not yet been given. In this work, liquid benzene was irradiated with 15-MeV protons, and the non-volatile products ("polymers") were analyzed to get a clue to chemical processes of PAH synthesis.

Benzene (Wako Pure Chem. Ind. Ltd.) was carefully purified by dehydration and distillation followed by freezing and thawing in a vacuum to eliminate dissolved gas. The liquid benzene sealed in a helium gas atmosphere in a quartz cell was irradiated with 15-MeV protons for 30 min, at the current from 1 to 3 μA. The cell was cooled with ice to keep liquid the sample during the irradiation. The samples turned to viscous yellow liquid by the irradiation, and insoluble substances were not observed. The analysis of products in the irradiated liquid was performed a few days later after the induced radioactivity was decayed out.

When the irradiated sample was diluted with ethanol, yellow insoluble substances were rapidly precipitated. The yield was as high as 2-14 wt.%. The products in the filtrate (the ethanol-soluble fraction) were analyzed by reversed-phase high performance liquid chromatography (HPLC) (μBondapak C_{18}, 1/4 inchϕ×1 feet, Waters Co.), with a acetonitrile-water mixture (v/v=7/3) as an eluate at a flow rate of 1.0 ml min^{-1}. The products were identified based on the retention times of signals detected with UV (λ=254 nm). Mass spectrometric analysis of the products was also performed by EI-MS (70 eV). A typical chromatogram, shown in Fig. 1, indicates that the major product was biphenyl. The yield of

biphenyl increases linearly with an increase of the dose (Fig. 2(a)), and the *G*-value of biphenyl was determined as *G*(biphenyl) = 0.064±0.008. The *G*(biphenyl) values for liquid benzene reported in the literatures[1,2] (in Fig. 2(a)) are almost the same as the value obtained in this study, irrespective of a kind of radiation and energy.

Incident protons lose most of their kinetic energy through electronic stopping processes, giving phenyl radicals and hydrogen atoms. Since the yield of phenyl radicals should be proportional to the dose of protons, the reaction path to produce biphenyl is mainly attributed to the reaction of phenyl radicals with solvent benzene molecules (Scheme 1(a)). Further reactions with phenyl radicals would produce terphenyl as observed in the chromatogram (Fig. 1). Although the yield of terphenyl is much smaller than that of biphenyl, a linear relation between the yield of each isomer and the dose is clearly seen in Fig. 2(b), indicating the similar formation processes starting from phenyl radicals. The differences of yields between the isomers can be explained by introducing, at least, two formation schemes (scheme 1(b) and (c)).

A peak just after the benzene peak in the chromatogram (Fig. 1) was collected and analyzed again by HPLC with an eluate having a different mixing ratio (acetonitrile-water, v/v=1/1). The result of analysis reveals that the fraction contains toluene, 1,3,5-cycloheptatriene and styrene monomer, as shown in Fig. 3. Formation of toluene and 1,3,5-cycloheptatriene, which have not been observed in γ-ray-irradiated benzene[1], may be initiated by knock-on events of energetic protons accompanied with generation of C_1 radicals (Scheme 1(d)).

The other major product is the precipitate formed in the irradiated benzene by an addition of ethanol. The results of elementary analysis for this compound indicate that the atomic ratio of hydrogen to carbon was similar to that of benzene. The IR spectrum of the compound is quite similar to that of thin polystyrene film as shown in Fig. 4. The UV absorption spectrum of this compound in THF shows a maximum peak at 244 nm with an extinction coefficient of 26 L g^{-1} cm^{-1}, that is attributed to the $\pi \rightarrow \pi^*$ transition of an aromatic compound substituted by a chromophoric group[7]. On the other hand, the compound did not show clear melting point up to 1000°C, while gradual decomposition was observed. This feature disagrees with that of polystyrene that has lower melting point of 240°C (*it*-polystyrene) or 90°C (*at*-polystyrene)[8]. The discrepancy of melting behavior suggests that the compound has a structure similar to that of polystyrene but has highly cross-linked (three-dimensionally) and disordered structures. In addition, the compound showed a polystyrene-like solubility except for acetone; it is soluble in THF and chloroform, but insoluble in water, alcohol, acetonitrile, *n*-hexane and acetone.

The formation mechanisms of this compound are interesting. Acetylene(C_2H_2), as a main gaseous product of radiolysis of benzene[1], might explain the formation of aliphatic structure. Although mechanism of aromatic ring cleavage was not clarified in the literature, the existence of C_2 and C_4 radicals as intermediates can be speculated. These radicals would

play a role in the linkage benzene rings, and afford highly cross-linked polymers (Scheme1 (e)).

A log-log plot of the yield of the polymer against the dose rate gives a linear relation with a slope of 2, as shown in Fig. 5. Assuming that the radical yield is proportional to the dose rate, one can consider that the polymer is produced through radical-radical reactions.

Although PAHs were not directly observed in this work, the formation of polystyrene-like polymers reveals a possibility of the formation of PAHs by proton irradiation.

References

1) Cherniak E. A., Collinson E. and Dainton F. S., Trans. Faraday Soc. **60** (1964) 1408.
2) Gäumann T. and Schuler R. H., J. Phys. Chem. **65** (1961) 703.
3) LaVerne J. A. and Schuler R. H., J. Phys. Chem. **88** (1984) 1200.
4) Allamandola L. J., Tielens A. G. G. M. and Barker J. R., Astrophys. J. Suppl. **71** (1989) 733.
5) Strazzulla G. and Baratta G. A., Astron. Astrophys. **266** (1992) 434.
6) Henning Th. and Salama F., Science **282** (1998) 2204.
7) Silverstein R. M., Bassler G. C. and Morrill T. C., "Spectrometric Identification of Organic Compounds", Fifth Edition, John Wiley & Sons, Japan, 1991.
8) Yamamoto K., "Handbook of Polymer Data, Elementary Edition", Baifukan, Tokyo, 1986.

Table. 1. The reactions schemes.

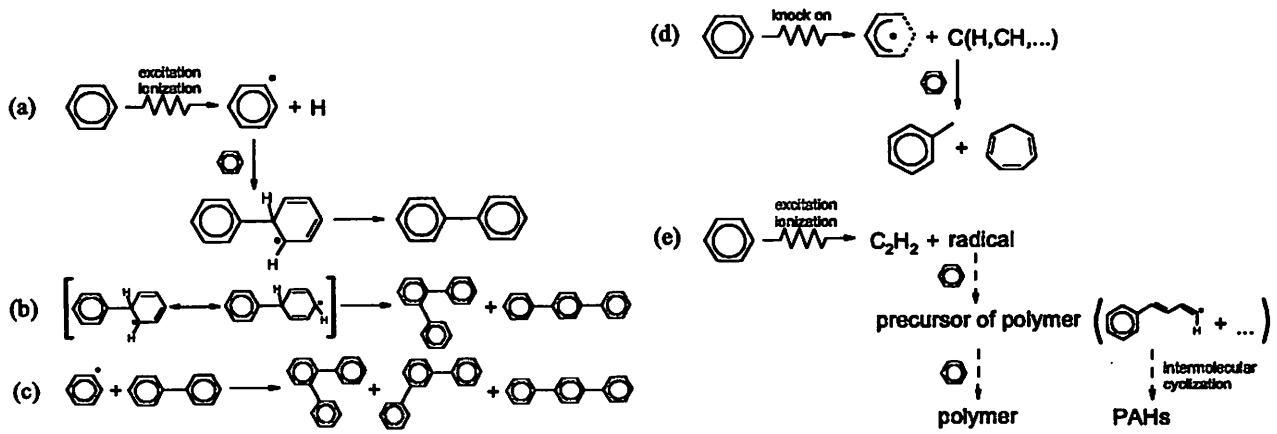

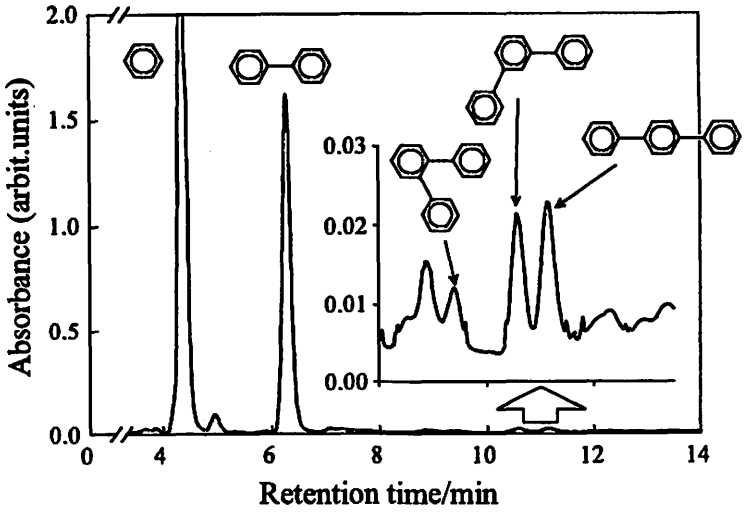

Fig. 1. The HPLC chromatogram of the proton-irradiated benzene. Column: μBondapak C_{18} (1/4 inchϕ × 1 feet, Waters). Eluate: CH_3CN/H_2O (v/v = 7/3). Flow rate: 1.0 ml min^{-1}. Detection: UV (λ = 254 nm).

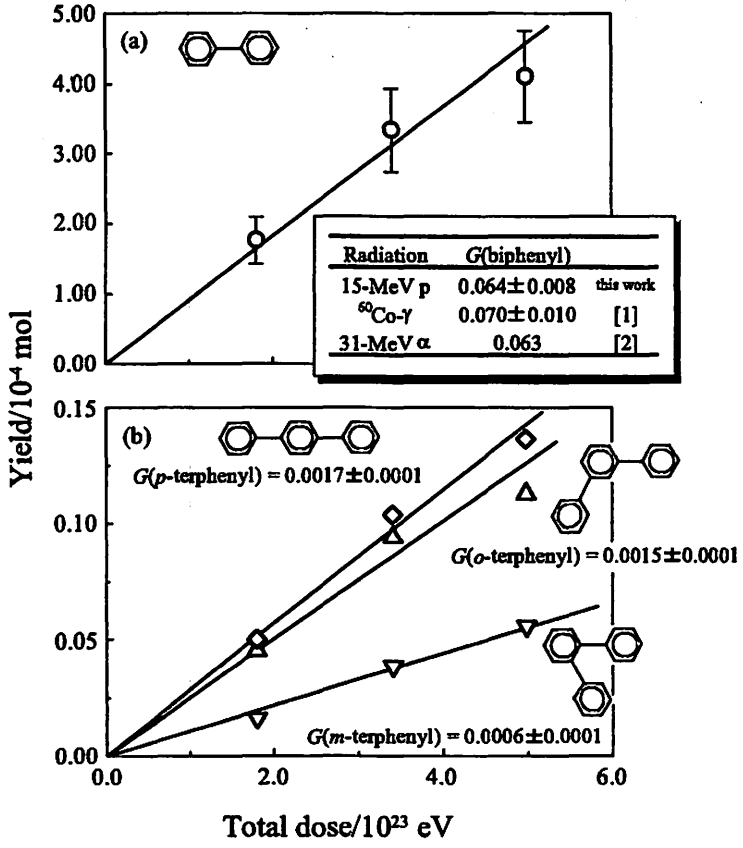

Fig. 2. Dose effects on the yields of (a) biphenyl and (b) terphenyl produced by the proton irradiation of liquid benzene.

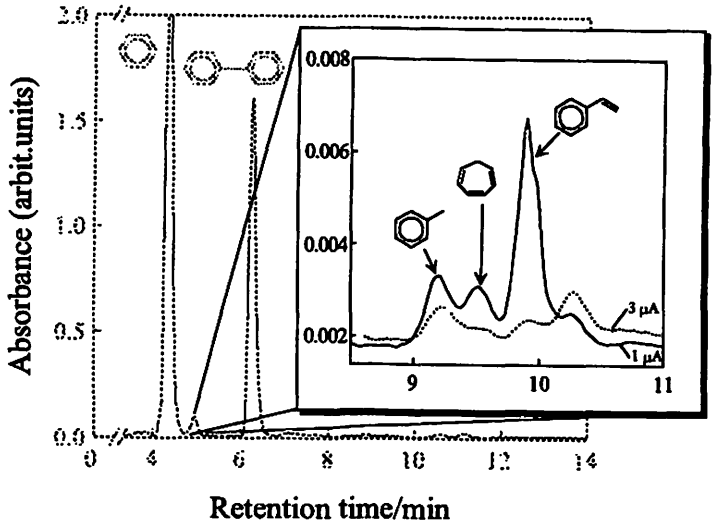

Fig. 3. HPLC chromatogram of the proton-irradiated benzene. Column: μBondapak C_{18} (1/4 inchϕ × 1 feet, Waters). Eluate: CH_3CN/H_2O (v/v = 1/1). Flow rate: 1.0 ml min^{-1}. Detection: UV (λ = 254 nm). The proton currents are 1 μA (solid line) and 3 μA (dotted line), respectively.

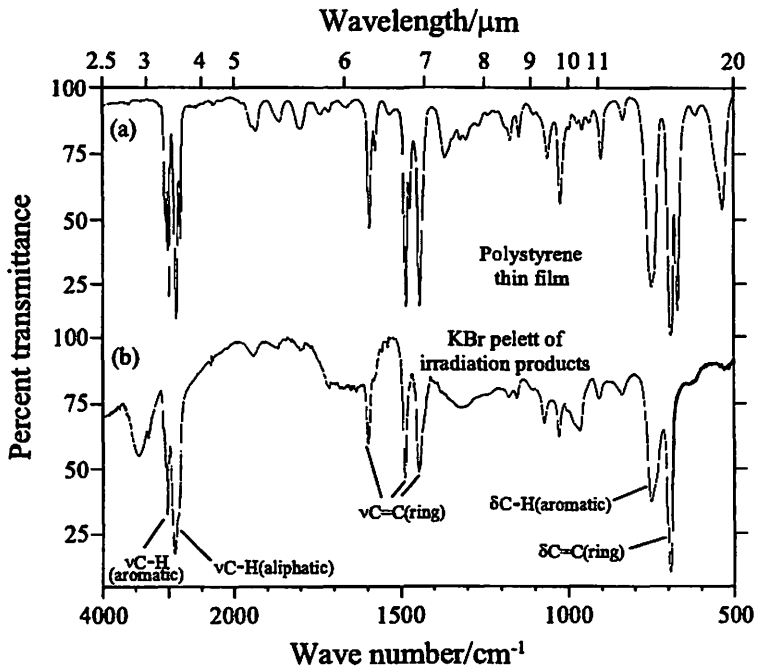

Fig. 4. IR spectra of (a) polystyrene thin film and (b) the ethanol-insoluble fraction of the proton-irradiated benzene.

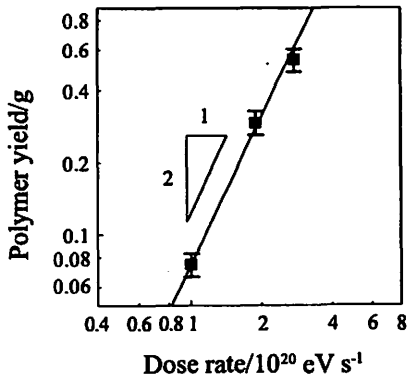

Fig. 5. Dose rate effect on the yield of polymer produced by the proton irradiation of liquid benzene.

III. 2. Analysis of Brain Alpha Rhythm with Multi-channel EEG Machine

Ozawa T., Nagasawa M., Ishii K., Yamazaki H., Matsuyama S., Itoh M., and Orihara H.**

Department of Quantum Science and Energy Engineering, Tohoku University
*Cyclotron and Radioisotope Center, Tohoku University**

Introduction

The brain-generated currents produce electrical potentials on the scalp. The recording of these potentials and the changes in time is the well known as electroencephalogram (EEG). A clinical investigation of 3-dimensional localization of focal epilepsy has been performed by using a multi-channel EEG machine[1-5]. An approach to mapping the electrical fields by simultaneously measuring with dozen of electrodes also affords a definitive description of electric brain activity over the scalp and provides a fundamental informations in the neural network controlling highly intellectual functions.

Two-dimensional analysis of phase difference

The alpha rhythm (the most prominent activity, and approximately 10 c/sec) can be frequently seen in EEGs over the head in normal condition without visual inputs. And when the alpha rhythm is strongly observed, a certain kind of correlation: the similarity of waveform and the stable of phase difference are realized between any two selected EEGs[6].
Here, we consider that the most prominent electric brain activity, alpha rhythm, is the characteristic rhythm of human brain in a stable condition. An analysis of EEG's trajectories at different points was carried out to investigate the correlation of electrical brain potentials. In this two–dimensional analysis of EEGs, the amplitudes of two EEG data at the same time are plotted on the X-Y plane. Figure 1 shows typical trajectories for some correlations ,where the phase difference between two EEGs is constantly 0,90,180,270 degrees.

Experimental

Brain activity of a young adult (male) was recorded with a 20-electrode EEG machine (Bio-logic System Corp.,Model BRAIN ATRAS-2.3). Twenty EEG-disc electrodes were applied on the head in the same array as an international 10-20 system with the electrical reference on the earlobes in the dark room. The analog bandwidth was 1.6-60Hz. The data of each channel were digitized at 67Hz. Eye-closed data were measured for

two minutes, and both portions with and without strong alpha rhythm were mainly investigated in terms of the 2-D analysis of phase difference.

Results and discussion

Figure 2 shows the EEGs at F3 and P4 of the international 10-20 electrodes system reference, and the results of 2-D analysis phase difference. Both typical patterns with and without strong alpha rhythm are presented for 0.5sec region of EEGs. In the case of strong alpha rhythm (a), we can find the 90 degree correlation in the phase difference between F3 and P4 (see Fig. 1). On the other hand, in the case of weak alpha rhythm (b), the phase correlation shows a random trajectory which seems to be the Lorentz attractor. These two types of trajectory's patterns appeared in other EEG data of two minutes. An interval time on transition from the strong correlation to the random pattern was a few minutes at the longest.

Intrinsic oscillation of brain expresses a simple function of the network system consisting of 10^8 neurons. The dynamic system of brain oscillator, which is distinct from mechanical oscillator, cannot maintain a harmonic oscillating mode in a long period.

The correlated EEGs of F3 and P4 were considerably disturbed by both a visual input and a somatic stimulus even in the existence of strong alpha rhythm. Then the change of phase difference could be observed in this case. In conclusion, the two-dimensional analysis of EEGs at two different points gives us visual inspection results on the change in brain-activity correlation.

References

1) Cohen D. and Cuffin B. N., Electroenceph. Clin. Neuropysiol. **47** (1979) 131.
2) Cohen D. and Cuffin B. N., Electroenceph. Clin. Neuropysiol. **56** (1983) 38.
3) Paul L. Nunez., Electroenceph. Clin. Neuropysiol. **63** (1986) 75.
4) Huttunen J. and Kobal G., Electroenceph. Clin. Neuropysiol. **64** (1986) 347.
5) Ricci G. B., and Romani G. L., Electroenceph. Clin. Neuropysiol. **66** (1987) 358.
6) Chapman R., Ilmoniemi R., Electroenceph. Clin. Neuropysiol. **58** (1984) 569.

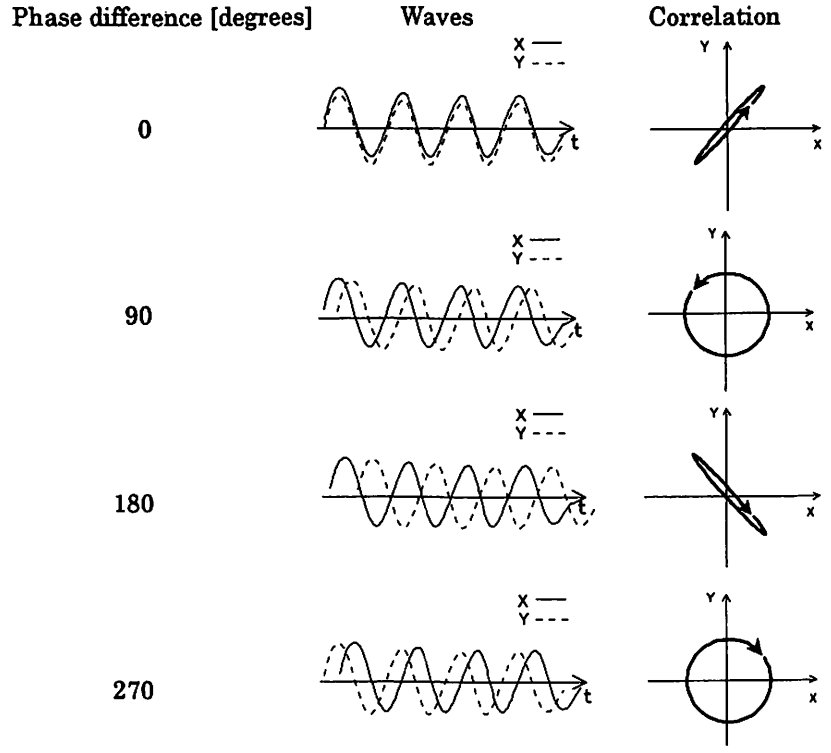

Fig. 1. The trajectory on four typical correlation.

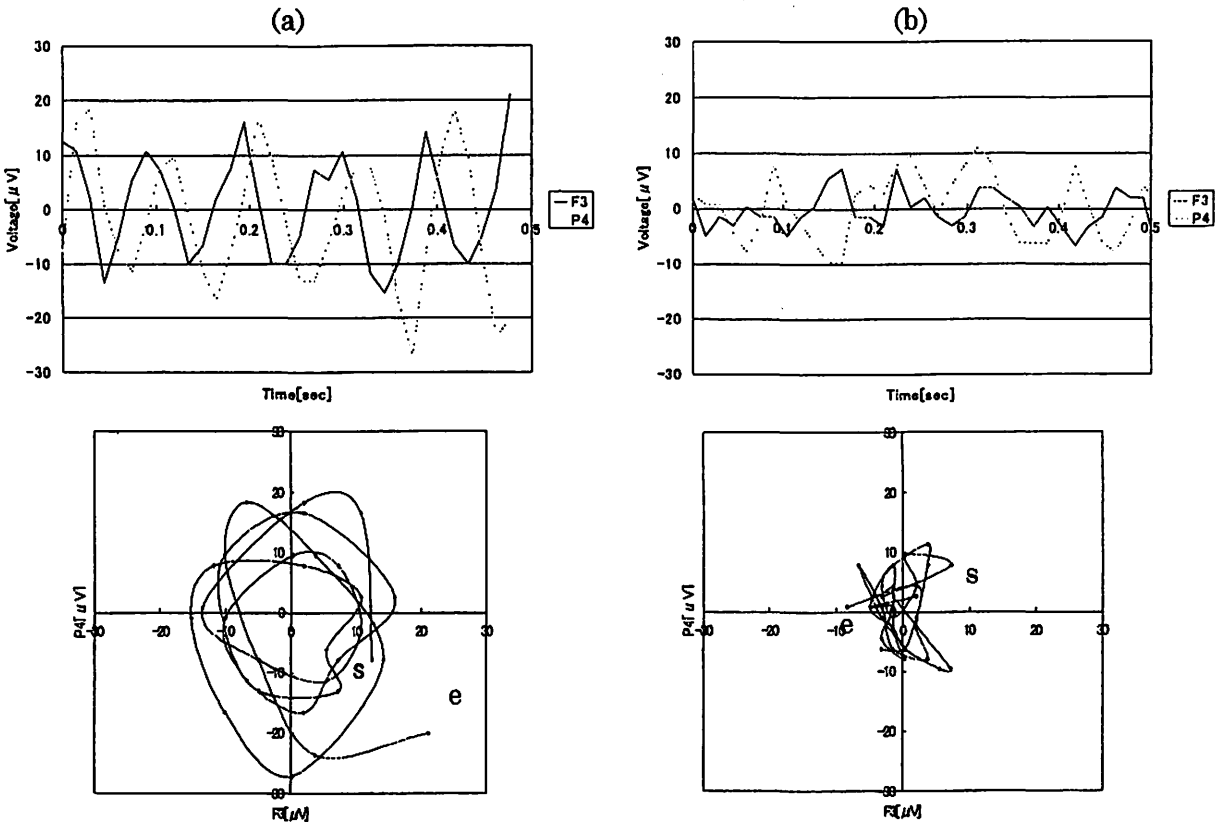

Fig. 2. The EEGs of F3 and P4 electrode and their trajectory plots (a) and (b) are respectively a strong alpha rhythm and a weak one. The symbol of "s "and "e" denote the starting and the end points respectively.

IV. MEDICINE AND BIOLOGY (Basic)

IV. 1. Production of PET Radionuclides with a Cypris HM12 Cyclotron at CYRIC.

Iwata R., Ishikawa Y., Funaki Y., Wada H., Ido T., Nagatsu K. , Morita T.* and Tanaka A.**
CYRIC, Tohoku University

*Quantum Equipment Business Center, Sumitomo Heavy Industries, Ltd**

The 680 AVF Cyclotron was shut down for renewal in April 1998, and a Cypris HM 12 Cyclotron, a prototype machine made by Sumitomo Heavy Industries (SHI), was introduced to resume PET clinical studies as soon as possible. In August 1998, it was installed in the target room-1, where one of the two beam line and the rotating target exchange system attached to it had been removed to make room for the new cyclotron (see Fig. 1). The HM 12 Cyclotron, dedicated to the production of PET radionuclides, ^{11}C, ^{13}N, ^{15}O and ^{18}F, accelerates H^- ions at 12 MeV and D^- ions at 6 MeV with beam intensities up to 50 μA and 30 μA, respectively. Since this was the first experience of CYRIC in use of such a low energy and high beam current machine, we accommodated ourselves to it and then evaluated it for routine production of $[^{11}C]CO_2$, $[^{15}O]O_2$, $[^{15}O]CO_2$, and $[^{18}F]F^-$. One of disadvantages to nuclide productions with a low energy cyclotron is the limitation to the flexibility in beam window thickness which should be chosen so as to minimize energy loss in the window whereas it must be thick enough to resist against the increase in target pressure by high current irradiation. This was especially the case with the $[^{11}C]CO_2$ and $[^{18}F]F^-$ productions. The window thickness and target dimension had to be carefully optimized. Table 1 lists the comparison of target conditions between the old and new systems.

^{11}C production

The saturated thick target yield of $[^{11}C]CO_2$ at the incident energy of 11.3 MeV was estimated to be 84 mCi/μA[1]. When the pure nitrogen gas target (99.999%) was irradiated, the yield was very uncertain and considerably lower than the expected value (Run 1-7 in Table 2), while the O_2-added gas target gave higher and more reproducible yields (Run 8-14). It was therefore concluded that the addition of O_2 was necessary for efficient recovery of ^{11}C as $[^{11}C]CO_2$. A target chamber of a large diameter (25 mm) was finally chosen since the dimension of the irradiation chamber was also observed to affect the production yield. Nearly 2 Ci of high specific activity $[^{11}C]CO_2$ (>10 Ci/μmol at EOB) is now routinely produced with 1-hour irradiation at a beam current of 30 μA.

^{15}O production

The incident energy of deuteron available for the $^{14}N(d, n)^{15}O$ reaction is calculated at 4.8 MeV after passing through two beam window foils (totally 20 μm thick Havar foils). The saturated thick target yield of ^{15}O with this energy was estimated to be 25 mCi/μA, almost half of that with the old system (the incident energy was 6.7 MeV). The decrease in yield, however, was compensated for by decreasing the target volume from 600 mL (100 mL × 6 kg/cm^2) to 60 mL (20 mL × 3 kg/cm^2), and thus the extracting yield of ^{15}O from the chamber with 10 μA irradiations was expected to be 67 mCi/min at a continuous flow rate of 300 mL/min. The production yield experimentally determined was slightly lower but well compatible. For the old system the target N_2 gas contained 0.2% carrier O_2 or CO_2, but with those gases the yield was lower by 20% than the expected one. Therefore the content of O_2 was increased up to 0.5% and that of CO_2 to 2.5% to improve the production yield. Approximately 25 mCi/min/10 μA of ^{15}O was obtained at the PET site, to which the ^{15}O was transferred from the target chamber through the 100 m stainless steel tube (2.0 mm inner diameter). Two target chambers are separately used for the production of $[^{15}O]O_2$ and $[^{15}O]CO_2$ for rapid exchange between these two radioactive gases.

^{18}F production

The incident energy of 11.2 MeV is high enough for the ^{18}F production by the $^{18}O(p, n)^{18}O$ reaction. The saturated thick target yield of $[^{18}F]F^-$ with 88 atom% ^{18}O -enriched water was estimated to be 135 mCi/μA[3]. The target vessel, made by SHI, consists of a titanium body electron beam welded to two titanium foils (depth: 2.4 mm thick; diameter: 15 mm). It takes 0.4 mL of $[^{18}O]$water without no expansion space. As seen in Table 3, production efficiencies were in the range from 70 to 80% within the beam current of 30 μA. However, the pressure was observed to rise up to almost 50 kg/cm^2 at 30 μA. Neither cooling of the beam window with a cold He flow nor that of the vessel with a cold water flow was practically effective on suppressing this pressure increase. A bigger target with expansion space is scheduled to be evaluated with over 30 μA irradiations in near future. Therefore, for the moment a beam current of 20 μA is used for routine productions.

All the productions of PET radionuclides and labelled compounds except $[^{18}F]F_2$ have been rapidly and successfully restored by introducing the HM 12 cyclotron. $[^{18}F]$Fluorine was produced by the deuteron irradiation of the neon target containing F_2. As the deuteron energy available from the cyclotron is too low for the $^{20}Ne(d, \alpha)^{18}F$ reaction (threshold energy for this reaction is 3.1 MeV), an alternative is the so-called two shot method[4] using $[^{18}O]O_2$ as the target for the $^{18}O(p, n)^{18}F$ reaction. The collaborative development of an automated production system is now in progress.

References

1) Bida G. T., Ruth T. J., Wolf A. P., Radiochem. Acta **27** (1980) 181.
2) Sajjad M., Lambrecht R., Wolf A. P., Radiochem. Acta **38** (1985) 57.
3) Ruth T., Wolf A. P., Radiochem. Acta **26** (1979) 21.
4) Roberts A. D., Oakes T. R., Nickles R. J., Appl. Radiat. Isot. **46** (1995) 87.

Table 1. Irradiation conditions for PET nuclide production.

Nuclide	680 cyclotron			HM 12 cyclotron		
	Accelerated particle	Beam window	Incident energy	Accelerated particle	Beam window	Incident energy
	(MeV)	(μm)	(MeV)	(MeV)	(μm)	(MeV)
^{11}C	p-18	Al-800	12	H^--12	Havor-25	11.3
^{15}O	d-11	Al-250	6.7	D^--6	Havor-10	4.8
^{18}F	p-18	Ti-50	17	H^--12	Ti-50	11.2

Table 2. Production of $[^{11}C]CO_2$ with the HM 12 cyclotron.

Run No.	Target	charged pressure	Target chamber	Beam current	$[^{11}C]CO_2$ yield
1	N_2	16 kg/cm^2	A	10 μA	40 mCi/μA
2	N_2	21 kg/cm^2	A	5 μA	44 mCi/μA
3	N_2	16 kg/cm^2	B	20 μA	54 mCi/μA
4	N_2	10 kg/cm^2	B	20 μA	27 mCi/μA
5	N_2	10 kg/cm^2	B	28 μA	44 mCi/μA
6	N_2	11 kg/cm^2	C	20 μA	43 mCi/μA
7	N_2	10 kg/cm^2	C	30 μA	33 mCi/μA
8	0.2% O_2+N_2	15 kg/cm^2	A	15 μA	67 mCi/μA
9	0.2% O_2+N_2	12 kg/cm^2	B	20 μA	38 mCi/μA
10	0.2% O_2+N_2	16 kg/cm^2	B	20 μA	54 mCi/μA
11	0.2% O_2+N_2	10 kg/cm^2	B	30 μA	39 mCi/μA
12	0.2% O_2+N_2	15 kg/cm^2	B	30 μA	51 mCi/μA
13	0.2% O_2+N_2	11 kg/cm^2	C	30 μA	61 mCi/μA
14	0.2% O_2+N_2	11 kg/cm^2	C	30 μA	67 mCi/μA

Chamber dimension: (A) ϕ16 mm × L. 120 mm; (B) ϕ16 mm × L. 180 mm;
(C) ϕ25 mm × L. 180 mm

Table 3. [^{18}F]Fluoride production.

Current	Irradiation time	Argon overpressure	Pressure during irradiation	^{18}F yield (EOB)	^{18}F saturated yield
10 μA	60 min	11.0 kg/cm^2	12.5 kg/cm^2	354 mCi	112 mCi/μA
15 μA	60 min	11.5 kg/cm^2	17.3 kg/cm^2	447 mCi	95 mCi/μA
15 μA	60 min	16.0 kg/cm^2	19.4 kg/cm^2	512 mCi	108 mCi/μA
15 μA	60 min	21.0 kg/cm^2	25.0 kg/cm^2	444 mCi	93 mCi/μA
20 μA	60 min	15.5 kg/cm^2	23.5 kg/cm^2	637 mCi	105 mCi/μA
30 μA	60 min	16.0 kg/cm^2	49.0 kg/cm^2	830 mCi	95 mCi/μA

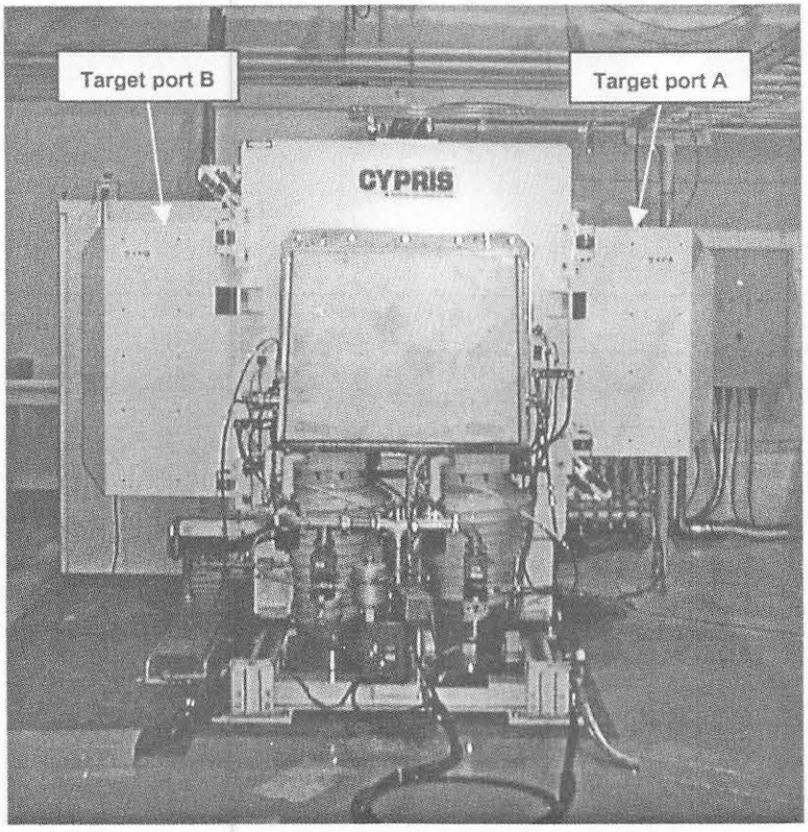

Fig. 1. Cypris HM 12 Cyclotron in the target room No. 1.

IV. 2. Synthesis of 1-*O*-(8-[^{18}F]fluorooctanoyl)-2-*O*-palmitoyl-*rac*-glycerol for PET Imaging of Intracellular Signaling

Furumoto S., Iwata R. and Ido T.

Cyclotron and Radioisotope Center, Tohoku University

Introduction

Investigation on the human brain functions by positron emission tomography (PET) is generally conducted by measuring cerebral blood flow, metabolism, and neurotransmitter-receptor systems. However, these measuring have the difficulty in imaging directly the overall neuronal activities. To make a breakthrough in the problem, Imahori *et al.* focused on the 1,2-*O*-diacylglycerols (1,2-DAGs) playing an important role in the postsynaptic intracellular signal transduction system and have developed a fundamental concept for the PET imaging of postreceptor signaling by using carbon-11 labeled 1,2-*O*-diacylglycerol (1,2-[^{11}C]DAG)[1].

Other DAG analogues labeled fluorine-18 were also developed for imaging the postsynaptic neuronal activities. Among them, our designed DAG analogue, 1-*O*-(8-[^{18}F]fluorooctanoyl)-2-*O*-palmitoyl-*rac*-glycerol (*rac*-1,2-[^{18}F]FDAG), showed unique character[2]: The administered *rac*-1,2-[^{18}F]FDAG is mainly metabolized into phosphatidylethanolamine and phosphatidylcholine different from the case of [^{11}C]DAG. Since the metabolic turnover is considered to be modulated by phospholipase D, *rac*-1,2-[^{18}F]FDAG is expected to be used as a novel PET tracer for evaluating the activity. To make use of *rac*-1,2-[^{18}F]FDAG to clinical research, however, we had to optimize the previous synthetic route because the multi radiosynthetic steps and the complicated operations limit its application to the automated synthesis. This manuscript reports an improved method for the synthesis, that is, the radiosynthetic steps are shorter and simpler than previous ones.

Methods

Synthesis of New Precursors for [^{18}F]FDAG

Two types of new precursor, **6a** and **6b** were synthesized from isopropylidene-*rac*-glycerol (**1**) following the general route to construct 1,2-DAG structure with two different acyl chains (Fig. 1). The intermediate **4a** was prepared according to a modification of the procedure described by Watts *et. al*[3]. The methoxyethoxymethyl (MEM) protecting group was introduced into the glycerol **1** by treatment of MEM chloride with diisopropylethylamine

(DIEA). The hydrolysis of the isopropylidene group in 10% aqueous acetic acid provided the diol **2**. Treatment of the diol **2** with one equivalent of 8-bromooctanoic acid in the presence of dicyclohexylcarbodiimide and dimethylaminopyridine (DMAP) at 0 °C afforded the intermediate **4a**. The intermediate **4b**, on the other hand, was synthesized according to a modification of the another procedure described by Kodali *et. al*[4]. Acylation of glycerol **1** with 8-bromooctanoyl chloride and triethylamine was done at first. Then the isopropylidene group was removed by acid gel-type resin in refluxing ethanol. The resulting diol **3** was treated with trityl (Tr) chloride in the presence of DIEA to give the intermediate **4b**. Treatment of the intermediates **4a** and **4b** with palmitoyl chloride and DMAP gave the protected diacylglycerols **5a** and **5b**. The synthesis of the corresponding precursors **6a** and **6b** was accomplished by converting the bromides of **5a** and **5b** into the *p*-toluenesulfonates by treatment with silver *p*-toluenesulfonate in refluxing acetonitrile.

Radiosynthesis of [^{18}F]FDAG

The new method of radiosynthesis for *rac*-1,2-[^{18}F]FDAG consists of radiofluorination and deprotection. To optimize the reaction times, the radiochemical yield in each process were monitored by radio thin layer chromatography.

^{18}F-Fluorination of the precursors (**6a** and **6b**) was carried out by NCA [^{18}F]KF and Kryptofix 222 in refluxing acetonitrile. The changes of radiofluorination yield with time were examined and the results were summarized in Figure 2. After quenching with water, radioactive crude products were extracted using Sep-Pak C18 column. The products were dissolved in CH_2Cl_2 and the deprotections were performed by B-bromocatecholborane (4 eq. to **6a**) to **7a** or BF_3·MeOH (4 eq. to **6b**) to **7b** as deprotection reagents. The changes in deprotection yield with time were also examined (Fig. 2). After stopping the deprotection with water, the mixed solution was passed through Extrelut and Sep-Pak dry column and then the CH_2Cl_2 solutions were evaporated *in vacuo*. The radioactive residues were applied to radio-HPLC to purify *rac*-1,2-[^{18}F]FDAG.

Results and Discussion

Each precursor was labeled with fluorine-18 in a good yield (about 70%) for 5 min and thereafter the yields did not increase. The sufficient time for the radiofluorination was concluded to be 5 min under the above conditions. The deprotection yields of **7a** and **7b** were achieved to 78% and 60% respectively for 1 min. After that the yield of *rac*-1,2-[^{18}F]FDAG decreased gradually with time due to the isomerization of *rac*-1,2-[^{18}F]FDAG to *rac*-1,3-[^{18}F]FDAG. The optimal reaction time was determined to be 1 min under the above conditions. The total radiochemical yields using **6a** and **6b** were 23% and 36% respectively, and the total synthesis time was about 90 min including final preparative HPLC separation. Compared to the previous synthesis, the yield was increased by about 10%

(using **6b**) and the synthesis time was reduced by about 30 min.

References

1) Imahori Y. and Ido T., Med. Chem. Res., **5**, **97** (1995).
2) Ido T., Imahori Y. *et al.*, J. Label. Compd. Radiopharm., **40**, **631** (1995).
3) Duralski A. A., Watts A. *et al.*, Tetrahedron Lett., 264, **1483** (1989).
4) Kodali D. R. and Duclos, Jr. R. I., Chem. and Phys. of Lipids, **61**, **169** (1992).

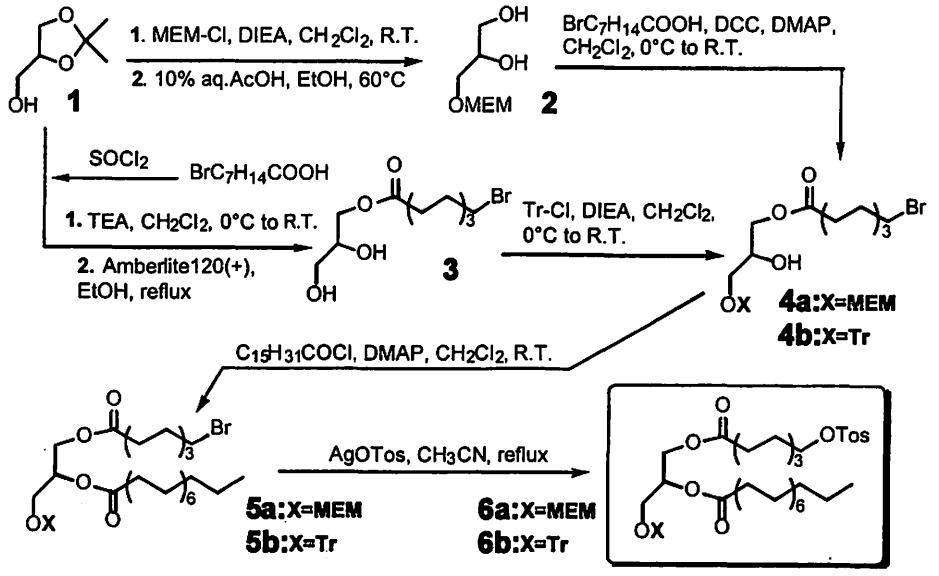

Fig. 1. Synthesis of 1-*O*-methoxyethoxymethyl-2-*O*-palmitoyl-3-*O*-(8-*O*-tosyloctanoyl)-*rac*-glycerol (**6a**) and 2-*O*-palmitoyl-1-*O*-(8-*O*-tosyloctanoyl)-3-*O*-trity-*rac*-glycerol (**6b**) from isopropylidene-*rac*-glycerol

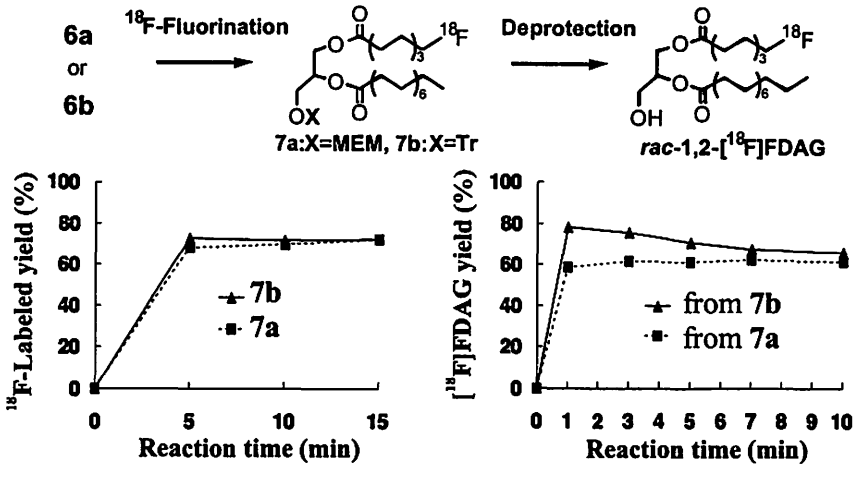

Fig. 2. Scheme of radiosynthesis of *rac*-1,2-[^{18}F]FDAG and the results of radio-TLC analysis of ^{18}F-fluorination to **6a** and **6b** (left graph) and the deprotection of **7a** and **7b** (right graph).

IV. 3. A Convenient Method for the Preparation of 4-[^{18}F]fluorobenzyl Bromide, a Versatile ^{18}F-labeling Precursor

*Iwata R., Ido T. and Yanai K.**

CYRIC, Tohoku University
*School of Medicine, Tohoku University**

Now that [^{18}F]fluoride can be easily produced in a large scale from a ^{18}O-enriched water target by proton irradiation, a various kind of ^{18}F-labeled compounds have been increasingly synthesized from this ^{18}F-labeling precursor. Much effort has also been made to extend its usefulness by developing ^{18}F-labeled intermediates which can be used as a versatile labeling precursor. 4-[^{18}F]Fluorobenzyl bromide is one of such promising candidates since it can provide many useful ^{18}F-labeled compounds by simple [^{18}F]fluorobenzylation as [^{11}C]methyl iodide by [^{11}C]methylation. It was first developed at CYRIC[1], and later several methods have been reported[2-4]. However, they all require such troublesome, time-consuming procedures as condensation, evaporation and extraction which make them inconvenient for routine use. Our new method consists of a simple on-column reduction and a mild, rapid bromination as shown in Fig. 1.

No-carrier-added [^{18}F]fluoride was produced by 12 MeV proton irradiation of [^{18}O]water (0.4 mL) with a Sumitomo Cypris HM12 cyclotron at CYRIC. The whole synthesis was performed using the semi-automated system illustrated in Fig. 2. An aliquot (0.2-0.3 mL) of the [^{18}F]fluoride solution was added to Kryptofix 222 (15 mg) dissolved in acetonitrile (1 mL) in an open round-bottom vessel. The vessel was then dipped in an oil bath (120℃) using a motored jack and the solvent evaporated under a stream of He (200 mL/min). The residue was dried by azeotropic evaporation with dry acetonitrile (1 mL×3 times) to ensure complete removal of water. A solution of the substrate **1** (6-8 mg), prepared according to the literature[5], in dry DMSO (1 mL) was added to the residue and the mixture was then allowed to react at the same temperature for 8-10 min.

After reaction the vessel was lifted up from the oil bath and the reaction was quenched by adding HCl (0.2 M, 8 mL). The whole solution was first sucked up into a 10 mL plastic syringe driven by a pneumatic cylinder and then pushed out through a Sep-Pak C18 Plus cartridge to retain the aldehyde **2**. The C18 cartridge was washed with water (10 mL) in the same manner *via* the vessel. After switching the 6-way valve, $NaBH_4$ (15 mg) dissolved in 0.5 mL of water was passed through the C18 cartridge for the on-column

reduction of the aldehyde **2** to the alcohol **3** and discarded onto an Extrelut column. 4-[^{18}F]Fluorobenzyl alcohol **3** was then eluted from the C18 cartridge with 4 mL of CH_2Cl_2 and the eluate was dried by passing with an He flow (200 mL/min) through an Extrelut column and a short $MgSO_4$ (0.5 g) column. The organic solution was collected in a second reaction vessel containing Ph_3PBr_2 (60 mg). After 5 min stirring at room temperature, the entire solution was passed through a silica cartridge followed by rinsing with an additional 1 mL of CH_2Cl_2, and *ca.* 2-3 mL of a colorless solution of **4** in CH_2Cl_2 were obtained in a vial. The whole synthesis was completed within 30 min after EOB.

The almost quantitative reduction of **2** to **3** was performed directly on the C18 cartridge. This on-column procedure considerably simplifies the method and hence facilitates its automation. Furthermore, the next halogenation step could be now directly carried out in the same solvent, CH_2Cl_2, used for eluting **3**.

The conversion of **3** to **4** in CH_2Cl_2 was investigated with Ph_3PBr_2[6]. 4-[^{18}F]Fluorobenzyl bromide was obtained in >98% radiochemical yields at room temperature within 5 min. The conversion yield was found to be strongly affected by the dryness of the reaction solvent. The ^{18}F-labeling precursor could be effectively purified by simple elution through a Sep-Pak silica cartridge.

4-[^{18}F]Fluorobenzyl bromide was prepared in 50-60% overall radiochemical yields (radiochemical yields of **2**: 70-80%) within 30 min from EOB using this simplified method. The present study clearly demonstrates that this method can be easily adapted to automated synthesis of the labeling precursor.

References

1) Hatano K., Ido T., Iwata R., J. Labelled. Cmpd. Radiopharm. **29** (1991) 373.
2) Damhaut P., Cantineau R., Lemaire C., *et al.*, Appl. Radiat. Isot. **43** (1992) 1265.
3) Mach R. H., Elder S. T., Morton T. E., *et al.*, Nucl. Med. Biol. **20** (1993) 777.
4) Dence C. S., John C. S., Bowen W. D., Welch M. J., Nucl. Med. Biol. **24** (1997) 333.
5) Wilson A. A., Dannals R. F., Ravert H. T., Wagner, Jr. H. N., *J.* Labelled. Cmpd. Radiopharm. **28** (1990) 1189.
6) Coe D. G., Landauer S. R., Rydon H. N., J. Chem. Soc. (1954) 2281.

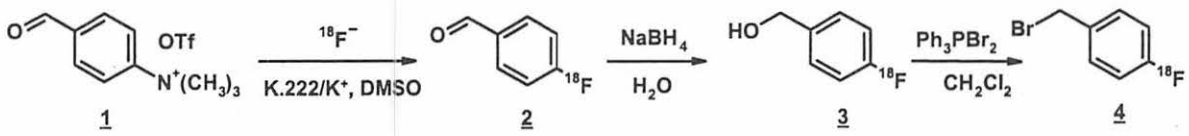

Fig. 1. Synthesis of 4-[^{18}F]fluorobenzyl bromide from [^{18}F]fluoride.

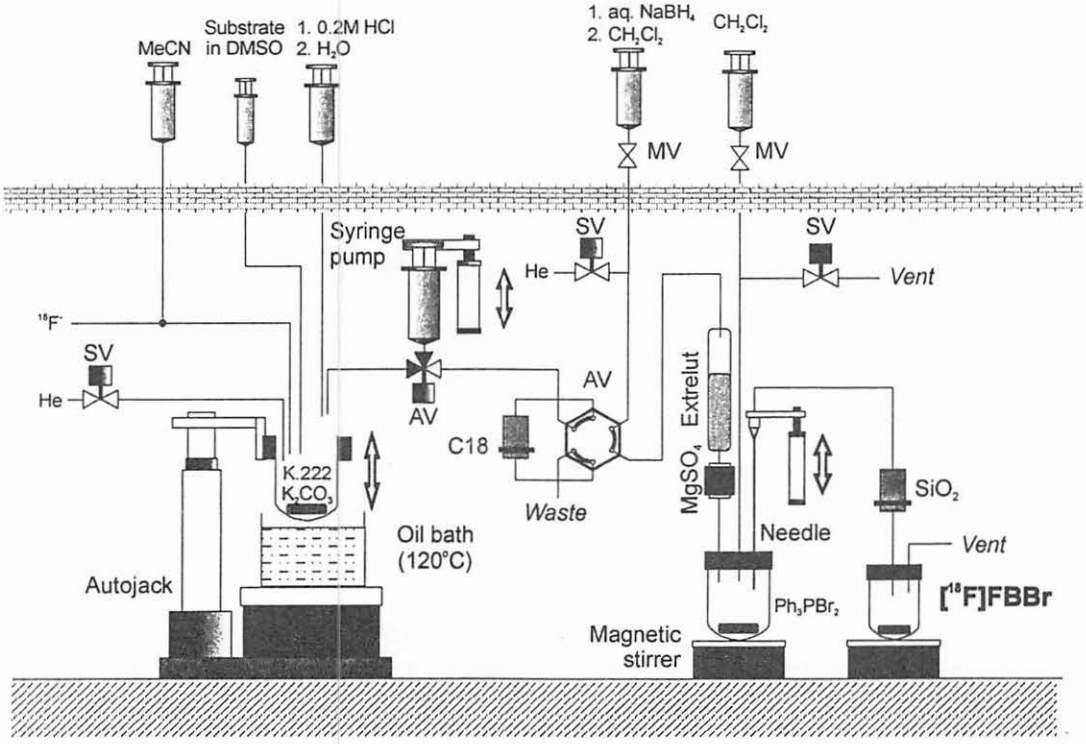

Fig. 2. A semi-automated system for the preparation of 4-[^{18}F]fluorobenzyl bromide.

IV. 4. Sequential Changes of Dopamine Uptake Sites in the Mouse Brain after MPTP Treatment

Tanji H., Araki T., Nagasawa H. and Itoyama Y.*

Department of Neurology, Tohoku University School of Medicine
*Miyagi University **

Introduction

There have been many studies showing that 1-methyl-4-phenyl-1,2,3,6-tetrahydropyridine (MPTP) induces neuronal damage in the nigrostriatal dopaminergic system in humans and in some animal species and that the clinical features are quite similar to those observed in Parkinson's disease. Moreover, some of these studies have demonstrated that mice, especially the C57BL mouse strain, are highly susceptible to the neurotoxic effects of MPTP and are useful as animal models of Parkinson's disease[1-5].

The neurotoxic effects of MPTP are thought to be initiated by the 1-methyl-4-phenylpyridinium ion (MPP^+), which is a metabolite formed by monoamine oxidase (MAO) B mediated oxidation of MPTP[6]. MPP^+ is known to be actively accumulated by dopamine neurons[7,8], where it is further concentrated within mitochondria by an energy-dependent mechanism[9]. The inhibition of mitochondrial electron transport at Complex I results in decreased oxygen consumption, and ATP production and a disruption of ion homeostasis[9-18]. Additionally, it is also suggested that the oxidative stress induced by MPP^+ may potentiate its toxicity to dopamine neurons[19-21]. Recent reports also suggest that the toxic effects of MPP^+ are mediated, in part, through an excessive production of nitric oxide (NO)[22,23].

In the present study, to clarify the process of functional damages of dopaminergic neurons after MPTP treatment, we investigated the sequential changes of dopamine uptake sites as a good marker for dopaminergic nerve terminals in brains of MPTP-treated parkinsonian mice, using quantitative autoradiographic method.

Materials and Methods

Thirty C57BL male mice (SPF strain), 23-26g in weight and 10 weeks old, were used for this study. MPTP-HCl (Sigma, U.S.A.) was dissolved in 0.9% sterile saline. The mice received intraperitoneal injections of MPTP (10 mg/kg) four times at intervals of 60 min, the total dose per mouse being 40 mg/kg. The mice were sacrificed at 6 hours and 1, 3, 7 and 21 days after the injection, and the brains were quickly removed, frozen in powdered

dry-ice and stored at -80℃ until receptor assay. Control mice were injected with only normal saline according to the same protocol as the MPTP-treated mice. Coronal sections, 12 μm in thickness, were cut at the level of the striatum and the substantia nigra of MPTP-treated and control mouse brains on a cryostat (HM500, Zeiss, Germany) and thaw-mounted onto silane-coated cover glasses.

RECEPTOR AUTORADIOGRAPHY

Autoradiographic distribution of dopamine uptake sites was determined using [^{3}H]mazindol according to the method of Przedborski et al.[24] with minor modifications[25]. The sections were pre-incubated for 15 min at 4℃ in 50 mM Tris-HCl buffer (pH 7.9) containing 120 mM NaCl and 5 mM KCl. The sections were then incubated with 15 nM [^{3}H]mazindol (New England Nuclear; specific activity, 24 Ci/mmol) in 50 mM Tris-HCl buffer (pH 7.9) containing 300nM NaCl, 5 mM KCl and 0.3 μM desmethylimipramine (Sigma, U.S.A.). Desmethylimipramine was added to block the binding of [^{3}H]mazindol to norepinephrine uptake sites, as described previously[26]. After incubation, the sections were washed twice in fresh buffer for 3 min at 4℃ and dipped in ice-cold distilled water. Non-specific binding was determined using 30 μM benztropine (Sigma, U.S.A), and it was about 25% of total binding.

DATA ANALYSIS

The sections were quickly dried under a cold airstream and then exposed for 1-3 weeks with [^{3}H]-labeled graded standards (Amersham, U.K.) to tritium-sensitive imaging plates (Fuji Photo Film, Japan) coated with minute crystals of photostimulable phosphor. A computer-assisted image-processing system, BAS5000 (Fuji Photo Film, Japan), was used for the quantitative analysis of radioactivity. Regions of interest (ROIs) on the autoradiograms were placed at the medial and lateral parts of the striatum separately and in the whole substantia nigra according to an atlas of mouse brain[27]. The radioactivity of each ROI was quantified using the calibration lines obtained from the [^{3}H]-labeled graded standards, and the values for radioactivities were converted to fmol/mg tissue. Specific binding activities of each ligand in the striatum and the substantia nigra were calculated by subtracting the non-specific binding from the total binding. All values were expressed as mean±S.E. and statistical significance was evaluated using an analysis of variance (ANOVA) followed by Dunnett's multiple range test (two-side).

Results

Representative autoradiograms of [^{3}H]mazindol binding sites in the striatum and substantia nigra of control and MPTP-treated mice are shown in Fig. 1, and chronological changes of each binding activity are presented in Table 1 and Fig. 2.

[^{3}H]Mazindol binding sites decreased in the lateral and medial parts of the striatum starting at 6 hours after MPTP administration, and the lowest levels of binding activity were observed at 3 and 7 days (18% of the control values in the medial part and 30% in the lateral part), as shown in Fig. 1A, Table 1 and Fig. 2A. In the substantia nigra, such binding also decreased significantly starting at 6 hours, and the lowest level of binding activity was observed at 1 day (20% of the control values) after MPTP administration (Fig. 1B, Table 1 and Fig. 2B).

Discussion

Javitch et al. [26] reported that dopamine uptake sites, as evidenced by the specific binding of [^{3}H]mazindol, were highly concentrated in the striatum, nucleus accumbens, olfactory tubercle, subthalamic nucleus, ventral tegmental area and pars compacta of the substantia nigra in rat brains, and that they were located on the pre-synaptic terminals of dopaminergic axons in the striatum. Therefore, measuring dopamine uptake sites is useful for detecting functional changes of dopaminergic neurons in Parkinson's disease or in animal models of Parkinson's disease. Several studies on dopamine uptake sites in patients with Parkinson's disease using autopsied brains have demonstrated marked decreases in the striatum[28-30] and significant decreases in the substantia nigra[30]. Also many studies have reported marked reductions of dopamine uptake sites in the striatum, pars compacta of the substantia nigra, ventral tegmental area or the nucleus accumbens in MPTP-treated animals, such as monkeys[31], cats[32] and marmosets[33]. Alexander et al[31] reported that there was a good correlation between the decreases in [^{3}H]mazindol binding sites and in tissue dopamine levels in the striatum or nucleus accumbens. In the present study, [^{3}H]mazindol binding was already decreased in the striatum and the substantia nigra at 6 hours, and the lowest levels of binding activity were observed in the striatum at 3 and 7 days and in the substantia nigra at 1 day after MPTP administration. These results demonstrate that the decrease of dopamine uptake sites, indicating damage of dopaminergic neurons, occurs in a very early stage after MPTP administration. Furthermore, of particular interest in this study is that [^{3}H]mazindol binding went down in the substantia nigra somewhat more abruptly than in the striatum. This observation suggests that cell bodies may be affected by MPTP at an early phase, as compared with nerve terminals. We also observed that dopamine uptake sites had slightly recovered at 21 days, such finding may indicate that dopaminergic neurons recover or regenerate in the chronic phase. A previous study reported that intrastriatal injection of 6-hydroxydopamine in rats could cause severe decrease in [^{3}H]mazindol binding in the medial part of the striatum, as compared with the lateral part[34]. Therefore, our findings that dopamine uptake sites were more decreased in the medial part of the striatum than in the lateral part also indicate the severer damage of pre-synaptic dopaminergic neurons in the medial part. These differences between the medial and lateral parts of the striatum may be due to different patterns of anatomical distribution or to different susceptibility to MPTP toxicity in the mouse

brain.

References

1) Heikkila R. E., Hess A. and Duvoisin R. C., Science **224** (1984) 1451.
2) Zimmer J. and Geneser F. A., Neurosci. Lett. **78** (1987) 253.
3) Arai N., Misugi K., Goshima Y., et al., Brain Res. **515** (1990) 57.
4) Date I., Felten D. L. and Felten S. Y., Brain Res. **519** (1990) 266.
5) Muthane U., Ramsay K. A., Jiang H., et al., Exp. Neurol. **126** (1994) 195.
6) Tipton K. F. and Singer T. P., J. Neurochem. **61** (1993) 1191.
7) Irwin I. and Langston J. W., Life Sci. **36** (1985) 207.
8) Javitch J. A., D'amato R. J., Strittmatter S. M., et al., Proc. Natl. Acad. Sci. USA **82** (1985) 2173.
9) Ramsay R. R., Salach J. I., Dadgar J., et al., Biochem. Biophys. Res. Commun. **135** (1986) 269.
10) Nicklas W. J., Vyas I. and Heikkila R. E., Life Sci. **36** (1985) 2503.
11) Ramsay R. R., Salach J. I. and Singer T. P., Biochem. Biophys. Res. Commun. **134** (1986) 743.
12) Di Monte D., Jewell S. A., Ekström G., et al., Biochem. Biophys. Res. Commun. **137** (1986) 310.
13) Vyas I., Heikkila R. E. and Nicklas W. J., J. Neurochem. **46** (1986) 1501.
14) Denton T. and Howard B. D., J. Neurochem. **49** (1987) 622.
15) Hollinden G. E., Ramos J. R. S., Sick T. J., et al., Brain Res. **475** (1988) 283.
16) Scotcher K. P., Irwin I., DeLanney L. E., et al., J. Neurochem. **54** (1990) 1295.
17) Chan P., DeLanney L. E., Irwin I., et al., J. Neurochem. **57** (1991) 348.
18) Gluck M. R., Krueger M. J., Ramsay R. R., et al., J. Biol. Chem. **269** (1994) 3167.
19) Hasegawa E., Takeshige K., Oishi T., et al., Biochem. Biophys. Res. Commun. **170** (1990) 1049.
20) Chiueh C. C., Miyake H. and Peng M. T., Adv. Neurol. **60** (1993) 251.
21) Chiueh C. C. and Rauhala P., Adv. Pharmacol. **42** (1998) 796.
22) Schulz J. B., Matthews R. T., Muqit M. M. K., et al., J. Neurochem. **64** (1995) 936.
23) Przedborski S., et al., Proc. Natl. Acad.Sci. USA **93** (1996) 4565.
24) Przedborski S., Lewis V. J., Yokoyama R., et al., J. Neurochem. **57** (1991) 1951.
25) Araki T., Kato H., Shuto K., et al., J. Neurol. Sci. **148** (1997) 131.
26) Javitch J. A., Strittmatter S. M. and Snyder S. H., J. Neurosci. **5** (1985) 1513.
27) Sidman R. L., Angevine J. B. and Pierce E. T., Harvard University Press, Cambridge, MA, (1971).
28) Chinaglia G., Alvarez F. J., Probst A., et al., Neuroscience **49** (1992) 317.
29) Joyce J. N., Brain Res. **600** (1993) 156.
30) Murray A. M., Weihmueller F. B., Marshall J. F., et al., Ann. Neurol. **37** (1995) 300.
31) Alexander G. M., Schwartzman R. J., Brainard L., et al., Brain Res. **588** (1992) 261.
32) Frohna P. A., Rothblat D. S., Joyce J. N., et al., Synapse **19** (1995) 46.
33) Gnanalingham K. K., Milkowski N. A., Smith L. A., et al., Eur. J. Pharmacol. **277** (1995) 235.
34) Przedborski S., Levivier M., Jiang H., et al., Neuroscience **67** (1995) 631.

Table 1. Time course of the changes in [^{3}H]Mazindol binding in the striatum and the substantia nigra of the mouse brain after MPTP administration

			MPTP treatment				
		Control (n=12)	6 hours (n=6)	1 day (n=6)	3 days (n=6)	7 days (n=6)	21 days (n=6)
Striatum	lateral	141±4	124±8	87±7**	42±6**	44±5**	56±4**
	medial	120±4	101±8*	60±6**	21±4**	22±4**	34±5**
Substantia nigra		37±3	22±2**	7±3**	18±3**	13±3**	17±4**

Values are given in mean±S.E. fmol/mg tissue. n: number of animals
*$p < 0.05$, **$p < 0.01$ vs. control (Dunnett's multiple range test, two-side)

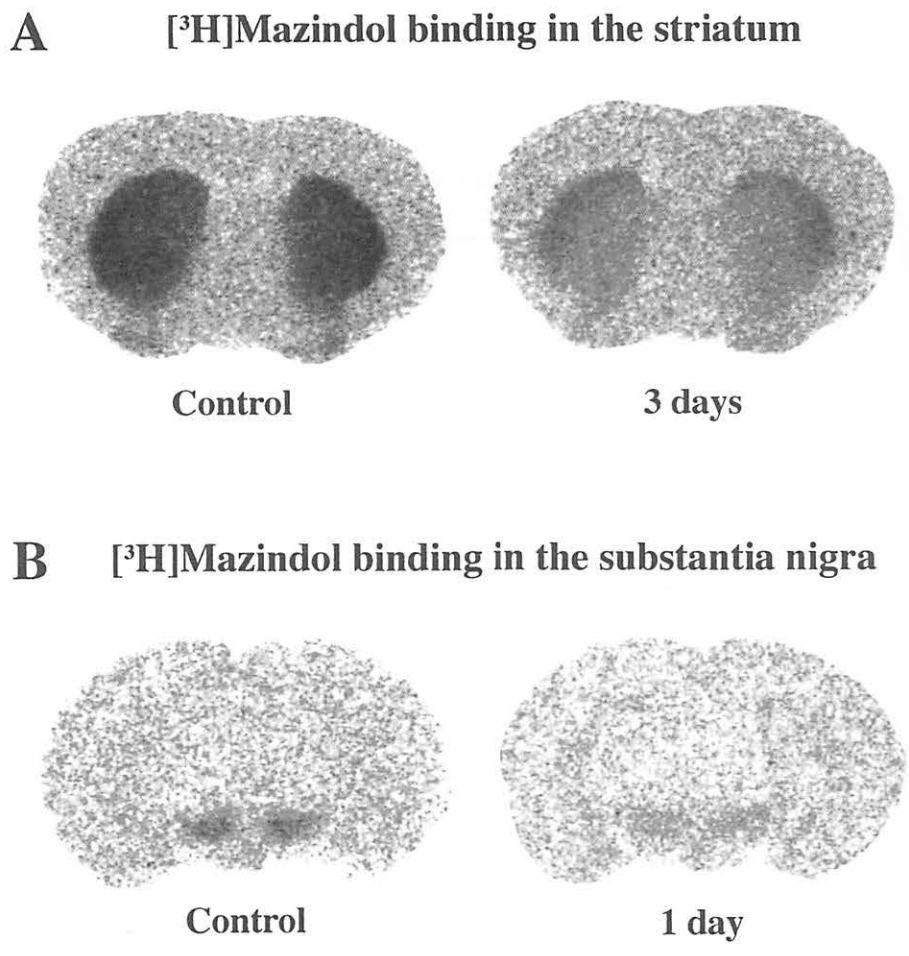

Fig. 1. Representative autoradiograms of [^{3}H]mazindol binding sites in the striatum (A) and the substantia nigra (B) of control mice and MPTP-treated mice at 3 days and 1 day after administration, respectively.

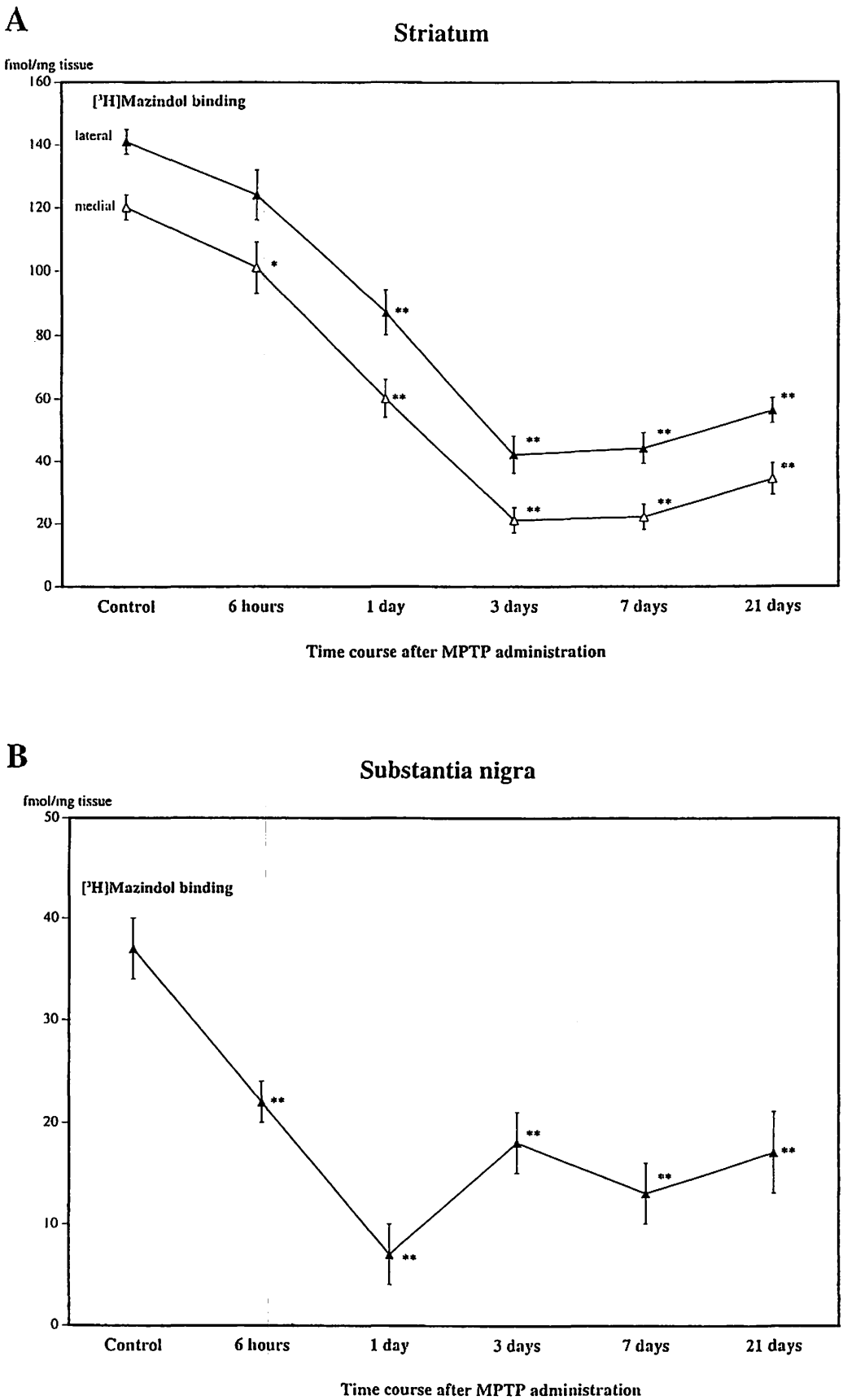

Fig. 2. Time course of [^{3}H]mazindol binding in the lateral (filled triangles) and medial (open triangles) parts of the striatum (A) and the substantia nigra (B) after MPTP administration. Each point shows the mean±S. E. fmol/mg tissue, using 6 MPTP-treated mice and 12 normal controls. Statistical significances: * $p < 0.05$, ** $p < 0.01$ vs. control (Dunnett's multiple range test, two-side).

IV. 5. Myotoxin *a*, a Rattlesnake Venom, Causes Ca^{2+} Release from Skeletal Muscle Sarcoplasmic Reticulum with a Novel Mechanism Common to DIDS, a Stilbene Derivative

Hirata Y., Nakahata N., Ohkura M., and Ohizumi Y.

Department of Pharmaceutical Molecular Biology,
Graduate School of Pharmaceutical Sciences, Tohoku University

Molecular mechanism of Ca^{2+} release by myotoxin *a* (MTYX), a polypeptide toxin isolated from the venom of prairie rattlesnakes (*Crotalus viridis viridis*), was investigated in the heavy fraction of sarcoplasmic reticulum (HSR) of rabbit skeletal muscles. [^{125}I]MYTX bound to four HSR proteins (106, 74, 53 and 30 kDa) on polyvinylidene difluoride (PVDF) membrane. DIDS, 4,4'-diisothiocyanatostilbene-2,2'-disulfonic acid, bound predominantly to 30 kDa protein on PVDF membrane, molecular weight of which was similar to one of MYTX binding proteins. The maximum $^{45}Ca^{2+}$ release induced by caffeine (30 mM) was further increased in the presence of MYTX (10 μM) or DIDS (30 μM), whereas that induced by DIDS (30 μM) was not affected by MYTX (10 μM). MYTX inhibited [^{3}H]DIDS binding to HSR in a concentration-dependent manner. Furthermore, [^{125}I]MYTX binding to 30 kDa protein was inhibited by DIDS in a concentration-dependent manner. These results suggest that MYTX and DIDS release Ca^{2+} from HSR in a common mechanism. The 30 kDa protein may be a target protein for Ca^{2+} releasing action of MYTX and DIDS.

Introduction

Release of Ca^{2+} from intracellular stores is a key step in signal transduction and regulated by several intrinsic proteins, such as calsequestrin (CS), triadin, junctin, FKBP, 30 kDa protein and mitsugumin29[1]. To establish the role of these proteins, excellent pharmacological tools are eagerly to be found. Recently, we found that myotoxin *a* (MYTX), which was isolated from prairie rattlesnakes (*Crotalus viridis viridis*) venom[2], strongly induced Ca^{2+} release from heavy fraction of SR (HSR) containing ryanodine receptor (RyR)[3]. Since [^{125}I]MYTX did not bind to the purified RyR[4] but the MYTX-induced Ca^{2+} release was abolished by pretreatment with ryanodine[5], MYTX is assumed to bind to important regulatory proteins in Ca^{2+} release, which are distinct from the RyR.

DIDS, a stilbene derivative known as an anion channel blocker[6], was shown to

modulate RyR[7,8]. It is reported that [^{3}H]DIDS binding protein is not the Ca^{2+} release channel but the 30 kDa protein in junctional face membrane in SR[7]. However, the properties of DIDS-induced $^{45}Ca^{2+}$ from HSR remains unknown.

To characterize the molecular mechanism of MTYX-induced Ca^{2+} release from HSR, we compared the properties of MYTX and DIDS in Ca^{2+} release.

Materials and Methods

Material

HSR enriched in Ca^{2+} release activity was prepared from rabbit skeletal muscle[9] with a minor modification. MYTX was purified from crude prairie rattlesnake venom as described previously[10]. [^{125}I]MYTX was prepared by the method of chloramine-T[4]. Other chemicals or drugs were of reagent grade or highest quality available.

Analysis of [^{125}I]MYTX and [^{3}H]DIDS binding proteins on PVDF membrane.

SDS-PAGE was conducted by the method described by Laemmli[11]. After HSR proteins (50 μg) were separated on 12% SDS-PAGE, they were transferred to PVDF membranes. The membranes were blocked by incubation with 90 mM KCl, $CaCl_2$ equivalent to 100 nM free Ca^{2+} and 50 mM MOPS-Tris (pH7.4)(Buffer A) containing 1% BSA for 60 min and were washed three times with Buffer A for 5 min. Then, they were incubated with [^{125}I]MYTX (0.3 μM) or [^{3}H]DIDS (3 μM) for 60 min at 0°C. After incubation with radioactive materials. blots were washed three times for 5 sec in ice-cold 50 mM MOPS-Tris (pH7.4)(Buffer B). Analysis of [^{125}I]MYTX binding to HSR proteins was performed by using with an image analyzer (Molecular Imager GS-363, Bio-Rad). Analysis of [^{3}H]DIDS binding to HSR proteins was performed by exposure to film after enhancement using Enlightning (NEN Research Products).

Measurement of $^{45}Ca^{2+}$ release

The $^{45}Ca^{2+}$ release from HSR passively preloaded with $^{45}Ca^{2+}$ was measured at 0°C as described previously[3].

[^{3}H]DIDS binding assay

[^{3}H]DIDS binding was examined as followed. HSR (100 μg/ml) was incubated with various concentrations (0.1-100 μM) of [^{3}H]DIDS in Buffer A in a final volume of 200 μl. After incubation at 0°C for 1 h. ice-cold Buffer B in a volume of 2.5 ml was added to each tube and the reaction mixture was immediately filtered under reduced pressure through a Whatman GF/C glass fiber filter which was then washed twice with ice-cold Buffer B (2.5 ml). Nonspecific binding was determined in the presence of 100 μM unlabeled DIDS.

Data analysis.

The data were expressed as means ± S. E. M. The statistical difference of the values was determined by Student's *t*-test.

Results

In order to identify the proteins bound to [^{125}I]MYTX, HSR proteins were separated by SDS-PAGE, transferred to PVDF membrane, and incubated with [^{125}I]MYTX [^{125}I]MYTX bound to four proteins (106, 74, 53 and 30 kDa) after transferring to PVDF membrane, although many proteins were identified by Coomassie staining (Figs. 1A and B). Two proteins were assumed to be Ca^{2+}-pump[12,13] and CS[4], which had been previously shown as proteins associated with MYTX. Other two [^{125}I]MYTX binding proteins (30 and 74 kDa) have not been identified. On the other hand, [^{3}H]DIDS markedly bound to 30 kDa protein on PVDF membrane after SDS-PAGE. The molecular size (30 kDa) of the protein was similar to that of a [^{125}I]MYTX binding to protein (Fig. 1C).

Fig. 2 shows the concentration-response curves for DIDS, MYTX and caffeine in $^{45}Ca^{2+}$ release from HSR at pCa 7. DIDS markedly accelerated $^{45}Ca^{2+}$ release in a concentration-dependent manner with the EC_{50} value of approximately 8 μM. The EC_{50} values of MYTX and caffeine were approximately 0.5 μM and 2 mM, respectively. Thus, DIDS is 250 times more potent than caffeine and 16 times less potent than MYTX. The maximal $^{45}Ca^{2+}$ release induced by DIDS was slightly larger than that induced by MYTX or caffeine. Fig. 3 shows the interrelations of the $^{45}Ca^{2+}$-releasing activities among MYTX, DIDS and caffeine at pCa 8. The maximum response of $^{45}Ca^{2+}$ release induced by caffeine (30 mM) was further increased in the presence of MYTX (10 μM) or DIDS (30 μM), whereas that induced by DIDS (30 μM) was not affected by MYTX (10 μM).

In order to determine whether MYTX and DIDS had the common binding sites, [^{3}H]DIDS binding to HSR was studied in the presence of MYTX. As shown in Fig. 4, MYTX inhibited [^{3}H]DIDS binding to HSR in a concentration-dependent manner. Furthermore, [^{125}I]MYTX binding to 30 kDa protein on PVDF membrane was studied in the presence of DIDS. [^{125}I]MYTX binding to 30 kDa protein was inhibited by DIDS in a concentration-dependent manner (Fig. 5).

Discussion

Recently, it has been postulated that RyR, Ca^{2+} release channel, is regulated by some intrinsic proteins such as CS, triadin, junctin and 30 kDa protein in the SR[1]. However, the detailed mechanism of the regulation of RyR by intrinsic proteins remains to be solved. Since [^{125}I]MYTX did not bind to the purified RyR[4] but MYTX-induced Ca^{2+} release was abolished by pretreatment with ryanodine[5], MYTX is assumed to bind to important regulatory proteins of RyR. We found new two MYTX binding proteins (30 and 74 kDa)

other than Ca^{2+}-pump[12,13] and CS[4] by binding of [^{125}I]MYTX to HSR proteins on PVDF membrane after SDS-PAGE. The 30 kDa protein was also a target protein for [^{3}H]DIDS.

DIDS, a stilbene derivative known as amino modifier and an anion exchanger blocker in red blood cell[6], is shown to modulate the SR Ca^{2+} channel[7,8]. Although MYTX and DIDS were powerful potentiators of Ca^{2+} release from HSR, the $^{45}Ca^{2+}$ release induced by caffeine was further increased in the presence of MYTX or DIDS. However, DIDS-induced $^{45}Ca^{2+}$ release was not affected in the presence of MYTX. Therefore, it is suggested that MYTX and DIDS, but not caffeine, have a common mechanism in Ca^{2+} release from HSR. In fact, [^{3}H]DIDS binding to HSR was inhibited by MYTX (Fig. 4), and [^{125}I]MYTX binding to the 30 kDa protein on PVDF membrane was inhibited by DIDS in a concentration-dependent manner (Fig. 5). Thus, MYTX and DIDS are assumed to commonly bind to 30 kDa protein.

In conclusion, MYTX causes Ca^{2+} release through RyR with a mechanism common to DIDS. The target protein for Ca^{2+} releasing action of MYTX may be 30 kDa protein, to which DIDS also binds. MYTX is a useful probe for elucidating the functional role of 30 kDa protein in excitation-contraction coupling of skeletal muscle.

Acknowledgments

This work was partly supported by Research Fellowships of the Japan Society for the Promotion of Science for Young Scientists and by Grant-in-Aid for Scientific Research from the Ministry of Education, Sciences and Culture of Japan.

References

1) Mackrill J. J., 1999, Biochem. J. **337**, 345-361.
2) Ownby C. L., Cameron, M S. and Tu A T., Am. J. Path. **85** (1976) 149-166.
3) Furukawa, K-I., Funayama K., Ohkura M., Oshima Y., Tu A.T. and Ohizumi Y., Br. J. Pharmacol. **113** (1994) 233-239.
4) Ohkura M., Ide T., Furukawa K-I., Tu. A. T. and Ohizumi Y., Eur. J. Pharmacol. Mol. Pharmacol. **268** (1994) R1-R2.
5) Ohkura M., Ide T., Furukawa K-I., Kawasaki T., Kasai M. and Ohizumi Y., Can. J Physiol. Pharmacol. **73** (1995) 1181-1185.
6) Cabantchik Z. I., Knauf P. A., and Rothstein A., Biochim. Biophys. Acta. **515** (1978) 239-302.
7) Yamaguchi N., Kawasaki M. and Kasai M., Biochem. Biophys. Res. Commun. **210** (1995) 648-653.
8) Oba T., Koshita M. and Van-Helden D. F., Am. J. Physiol. **271** (1996) C819-824.
9) Seino A., Kobayashi M., Kobayashi J., Fang Y.-I., Ishibashi M., Nakamura, H. and Ohizumi Y., J. Pharmacol. Exp. Ther. **256** (1991) 861-867.
10) Cameron D. L., and Tu A.T., Biochemistry **16** (1977) 2546-2553.
11) Laemmli U. K., Nature **277** (1970) 680-685.
12) Volpe. P., Damiani E., Maurer A., and Tu A. T. Arch. Biochem. Biophys. 246 (1986) 90-97.
13) Utaisincharoen P., Baker B. and Tu A. T., Biochemistry **30** (1991) 8211-8216.

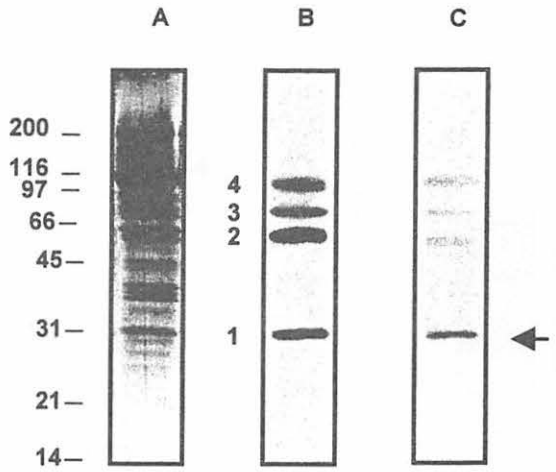

Fig. 1. Identification of the binding proteins to [^{125}I]MYTX and [^{3}H]DIDS. HSR proteins (50 μg) were separated on 12% SDS-PAGE and transferred to PVDF membrane. Coomassie-stained HSR proteins on PVDF membrane (A). The PVDF membrane was incubated with [^{125}I] MYTX (B, 0.3 μM) or [^{3}H]DIDS (C, 3 μM) for 1 h at 0°C after blocking with 1% BSA. Bands: 2, CS; 4, Ca^{2+}-pump; 1 and 3, unknown proteins.

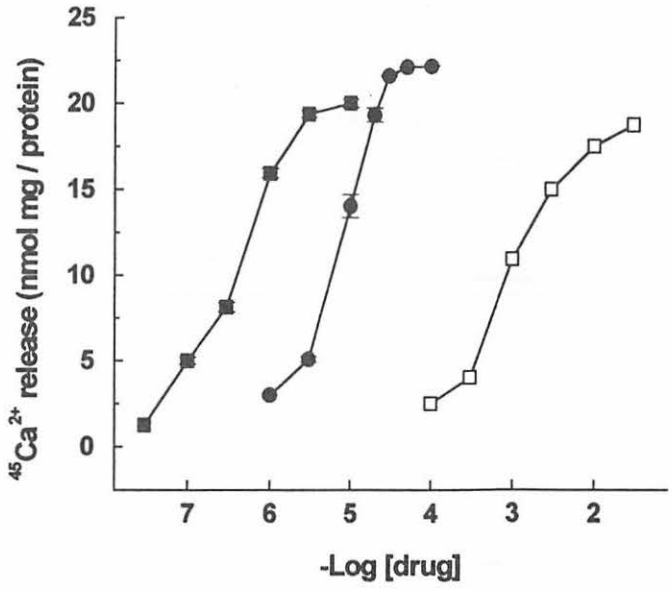

Fig. 2. Concentration-dependent acceleration of $^{45}Ca^{2+}$ release from HSR by MYTX, DIDS and caffeine. The amount of released $^{45}Ca^{2+}$ was obtained from the decrease in the $^{45}Ca^{2+}$ content in HSR vesicles during 1 min after dilution. Each value was calculated by subtracting the amount of released $^{45}Ca^{2+}$ measured in the presence of the test substance from that measured in the absence of it. MYTX (■); DIDS (●); caffeine (□). Values are means ± S. E. M. (n=3).

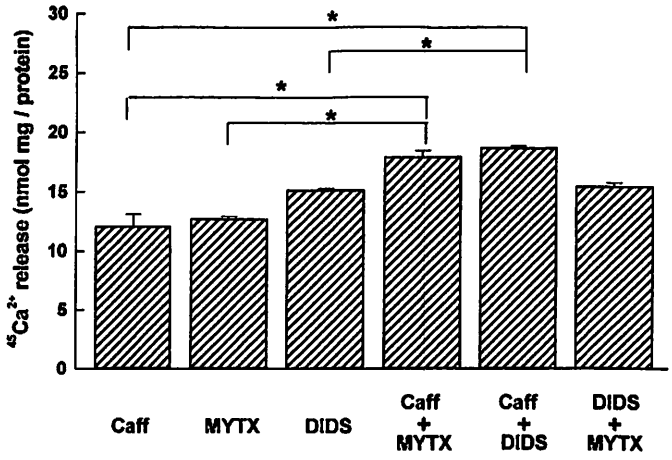

Fig. 3. Interrelations among the Ca^{2+}-releasing activities of MYTX, DIDS and caffeine. Experimental protocols were the same as those for Fig. 2. The amount of $^{45}Ca^{2+}$ released from HSR for 1 min after dilution into the medium was obtained at pCa 8. The concentrations of caffeine (Caff), MYTX and DIDS were 30 mM, 10 μM and 30 μM, respectively. Values are means ± S. E. M. (n=3). *Significantly (*p<0.01) different between the values

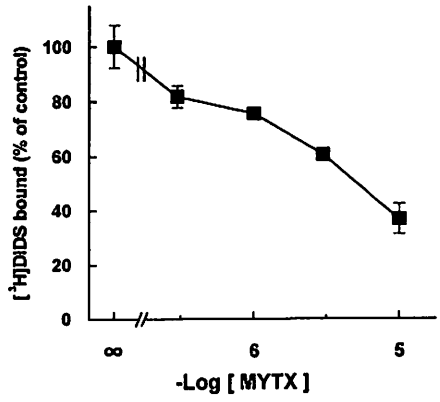

Fig. 4. Concentration-dependent inhibition of [^{3}H]DIDS binding by MYTX. HSR was incubated with 3 μM [^{3}H]DIDS in the presence of various concentrations of MYTX for 1 h at 0°C, as described in experimental procedures. Nonspecific binding was determined in the presence of 100 μM unlabeled DIDS. Values were expressed as % to the presence of 100 μM unlabeled DIDS. Data are means ± S. E. M. (n=3).

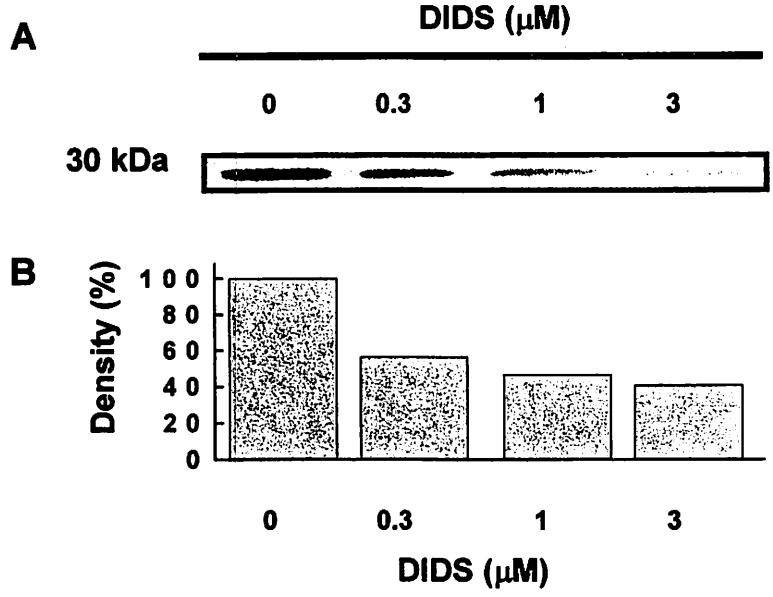

Fig. 5. Inhibition of [^{125}I]MYTX binding to 30 kDa protein by DIDS on PVDF membrane. Experimental protocols were the same as those for Fig. 1. In A, the PVDF membrane was incubated with [^{125}I]MYTX (0.3 μM) in the presence of DIDS (0-3 μM) for 1 h at 0°C after blocking with 1% BSA. In B, the date are expressed as % to the density of [^{125}I]MYTX binding to 30 kDa protein in the absence of DIDS.

IV. 6. Intra-tumoral Accumulation of Technetium-99m Sestamibi Compared to Carbon-14 Deoxyglucose in Mouse Breast Cancer Models

Ohira H., Kubota K., Ohuchi N., Satomi S., Fukuda H.**

The Second Department of Surgery, Tohoku University School of Medicine
*Department of Nuclear Medicine and Radiology, Institute of Development, Aging and Cancer, Tohoku University**

INTRODUCTION

Technethium-99m methoxyisobutylisonitrile (MIBI) is a tracer that is widely used as myocardial perfusion agent. Since the first article on ^{99m}Tc-MIBI uptake in breast cancer appeared in 1992[1], ^{99m}Tc-MIBI scintimammography has been used for tumor detection, evaluation of chemotherapeutic response and prediction of multidrug-resistance[2-8]. P-glycoprotein (P-gp) is well known to play an important role for the excretion of MIBI from tumor cell[9,10]. However, little is known about intra-tumor accumulation of ^{99m}Tc-MIBI. The purpose of this study is to evaluate the intra-tumor accumulation of ^{99m}Tc-MIBI, to compare it with 2-deoxy [^{14}C] glucose (^{14}C-DG) using animal tumor models and to investigate uptake pattern of MIBI in the three different characteristic tumors.

MATERIALS AND METHODS

Animals, Tumor Growth Study

Male 6-weeks-old C3H/He or ddy mice were injected subctaneously on their left thighs with a 0.1 ml suspension containing $0.5\times10^7 - 1.5\times10^7$ cells of syngenic mouse breast cancer models of FM3A, MM48 and Ehrlich. The solid tumors were measured using a vernier calipers every day. The product of the three principal diameters of each tumor was designated as tumor volume[11]. Irradiation was performed when the tumor size reached about 10 mm in diameter. Mice were anesthetized with intraperitoneal 1 mg sodium pentobarbital, then fixed with adhesive tape to place the tumor-bearing thigh in the field of irradiation[12]. The tumors were exposed to a single dose of 20 Gy X-rays (150 kV, 20 mA, Hitachi Medical Corp., Japan) at a dose rate of 1.50 Gy/min with a copper aluminum filter[13]. Non-irradiated tumors in mice, handled in the same manner were used as control. The two groups of eight mice each were used for tumor growth study with or without irradiation.

Macro-autoradiography

Approximately 10 days following transplantation, C3H/He mice with FM3A or MM48 tumors and ddy mice with Ehrlich tumors were injected intravenously with a mixure of 3 mCi (111MBq) of ^{99m}Tc-MIBI (Daiichi Radioisotope Labs., Ltd., Tokyo, Japan) and 10 μCi (0.37MBq) of ^{14}C-DG (Amarsham International plc, Buckinghamshire, UK). Previously we searched the linear correlation of radioactivity and autoradiographic density of ^{99m}Tc , a pure gamma emitter, and decided the injection dose (3 mCi/mouse) for ARG with mice (Fig. 1). The mice were killed with over anesthesia for ARG at 30 min. This time point was determined from time-course tissue distribution experiment. Tumors were dissected and embedded in a frozen block with O.C.T. compound (Miles Inc., Elkhart, IN), the sample blocks were sectioned on a cryostat at -25°C[14]. Several 10 μm-thick sections were mounted on clean glass slides, air-dried and directly contacted with ARG films (Kodak Biomax MS Film) for 6 hr in order to produce ^{99m}Tc-MIBI images. Three days later (about 12 half-lives of ^{99m}Tc), when ^{99m}Tc had decayed, the same sections were contacted with other films for seven days to produce ^{14}C-DG images. Sections on the slides were stained with hematoxylin and eosin, and examined under a system microscope.

Analysis Autoradiograms

Intra-tumor distribution of two tracers within the same sections was analysed using co-registered double-tracer ARG images and image analysis software (Win ROOF Ver. 3.2, Mitani Corp., Fukui, Japan) on a personal computer (PC) system. ARG images were digitized and transferred to the PC through a CCD camera system. Each intra-tumor tissue components were covered with square region of interest (each ROI was 0.5 × 0.5 – 1.0 × 1.0 cm) compared with histology, quantitative evaluation of autoradiograms was done by measuring optical density after background subtraction in the ROIs. Then, regional radioactivity of two tracers of the same ROI at the same section was analysed.

RESULT

Tumor Growth Curve

Figure 2 shows the effect of radiation on the growth and growth rate of each tumor. MM48 tumor was the most radioresistant; these tumors continued to enlarge even after 20 Gy irradiation. The pattern of FM3A tumor growth showed swelling for two days after irradiation (Day 9, 10), followed by shrinking until Day 16 (eight days after irradiation), and regrowth was seen on Day 17 (nine days after irradiation). Erhlich tumor was the radiosensitive tumor which showed decrease in size after irradiation immediately. These tumors were not measurable on Day 17 (ten days after irradiation). MM48 was the rapid growing tumor with doubling time of about 2.0 days. The doubling time of FM3A and Ehrlich was about 2.5 days and 3.8 days respectively, as measured from the beginning of the

irradiation.

Double-tracer Macro-autoradiography with ^{99m}Tc-MIBI and ^{14}C-DG

Figure 3 shows representative autoradiograms of ^{99m}Tc-MIBI (A) and ^{14}C-DG (B) as double tracer study, the same histologic tumor sections (C) and the sketch illustrations of the micrograph (D).

In the upper low, FM3A tumor shows similar uptake pattern of ^{99m}Tc-MIBI and ^{14}C-DG. It's histology shows viable cancer cells almost occupied within the tumor and the dense area with the both ARG corresponding to the viable cancer cells.

In the middle low, MM48 shows high uptake of both tracers by viable cancer cells than degenerating cancer cells and connective tissue. Almost no tracer accumulation is seen in necrotic tumor tissue in both images.

The lower low, ^{99m}Tc-MIBI uptake is the highest by muscle but a little accumulation by viable and degenerating cancer cells is also seen. On the other hand, ^{14}C-DG accumulated within cancer cells largely, while muscle and connective tissue showed equal tracer accumulation. Each tracer showed little uptake by necrotic tissue as well.

Optical Density of Different Tissue Components

Figure 4 shows the results of macroautoradiograms with ^{99m}Tc-MIBI and ^{14}C-DG images. The grain numbers were expressed in values relative to the highest value for each tracer. ^{99m}Tc-MIBI image showed higher tracer uptake by muscle than that by other components in all tumor models, while ^{14}C-DG image showed very high uptake by viable cancer cells. Necrotic tissue area had the lowest tracer uptake in both images in all tumors.

DISCUSSION

Recently, positron emission tomography (PET) using 2-deoxy-2-^{18}F-fluoro-D-glucose (^{18}F-FDG) has become well established in the diagnosis and follow up of breast cancer[15,16]. Increased glycolysis is one of the most important characteristics of the cancer cells. In tumor cells, ^{14}C-DG is similarly phosphorylated by the intracellular hexokinase enzyme, but not further metabolized and trapped in cells as ^{14}C-DG-6 phosphate. Therefore the glycolysis level of the tissue can be measured by the accumulation of ^{14}C-DG.

Concerning ^{99m}Tc-MIBI uptake mechanism it has been reported that ^{99m}Tc-MIBI accumulates within mitochondria on the basis of electrical potentials generated across the membranes. Since malignant tumors maintain a more negative transmembrane potential, ^{99m}Tc-MIBI accumulation increases[17-19]. However, the presence of multidrug-resistance mediated P-gp energy-dependent excludes ^{99m}Tc-MIBI accumulation. The tumors with P-gp expression show lower uptake and faster clearance of ^{99m}Tc-MIBI than that tumor without P-gp, further the clearance has been started within 5 min[20]. In this study we did not examine

the expression of P-gp in three tumor models. If we compare to the known P-gp positive tumor P388VCR, it is suggested that all these tumors are without of P-gp. If they have P-gp, ^{99m}Tc-MIBI image 30 min after injection would show higher uptake by connective tissue rather than that by viable cancer cells.

Comparing two tracers uptake by viable cancer cells and connective tissue, ^{99m}Tc-MIBI uptake by connective tissue in FM3A tumor was 25.5% relative to that by viable cancer cells, it was 31.6% and 44.1% in MM48 and Ehrlich respectively. On the other hand, ^{14}C-DG uptake by connective tissue relative to viable cancer cells in FM3A, MM48, Ehrlich was 53.3%, 54.2%, 54.0% respectively. In short, connective tissue/viable cancer cells ratio of ^{14}C-DG image was higher than that of ^{99m}Tc-MIBI image in all tumors. Therefore, it was suggested that intra-tumor accumulation of ^{99m}Tc-MIBI represents the presence of viable cancer cells more selectively than that with ^{14}C-DG. ^{99m}Tc-MIBI image showed similar intra-tumor distribution pattern irrespective to the different tumor characteristics, growth rate and radiosensitivity.

In this study ^{14}C-DG uptake by viable cancer cells was higher than ^{99m}Tc-MIBI. It has been demonstrated that the glycolysis level in pathological connective tissue around cancer cells is higher than that in normal connective tissue. Therefore, a boundary of tumor may be indistinct on the film.

ACKNOWLEDGMENT

This study was supported by Grants-in-aid (09470195) from the Ministry of Education, Science, Sports and Culture, Japan, and from Daiichi Radioisotope Labs., Ltd., Tokyo, Japan.

References

1) Waxman A., Ashock G., Kooba A., et al., Clin. Nucl. Med. **9** (1992) 761.
2) Prats E., Aisa F., Abos M. D., et al., J. Nucl. Med. **40** (1999) 296.
3) Uriarte I., Carril JM., Quirce R., et al., Eur. J. Nucl. Med. **25** (1998) 491.
4) Joaquim AI., Sagarra A. J., Ramos CD., et al., Clin. Nucl. Med. **22** (1997) 638.
5) Scopinaro F., Mezi S., Ierardi M., et al., Int. J. Oncol. **12** (1998) 661.
6) Reinhold T., Klaus T., Harald S., et al., J. Nucl. Med. **39** (1998) 849.
7) Francesco S., Orazio S., Wolf U., et al., Anticancer Res. **17** (1997)1631.
8) Rao VV., Chiu ML., Kronauge J. F., et al., J. Nucl. Med. **35** (1994) 510.
9) Kostakoglu L., Ruacan S., Ergun E. L., et al., J. Nucl. Med. **39** (1998) 1021.
10) Piwnica-Worms D., Chui ML., Budding M., et al., Cancer Res. **53** (1993) 977.
11) Kubota K., Kubota R., Matsuzawa T., Cancer Res. **43** (1983) 787.
12) Kubota K., Matsuzawa T., Takahashi T., et al., J. Nucl. Med. **30** (1989) 2012.
13) Abe Y., Matsuzawa T., Fujiwara T., et al., Eur. J. Nucl. Med. **12** (1986) 325.
14) Kubota R., Yamada S., Kubota K., et al., J. Nucl. Med. **33** (1992) 1972.
15) Palmed H., Bender H., Grunwald F., et al., Eur. J. Nuclv Med. **24** (1997) 1138.
16) Oshida M., Uno K., Suzuki M., et al., Cancer. **82** (1998) 2227.
17) Chui M. L., Kronauge J. F., Piwnica-Worms D., et al., J. Nucl. Med. **31** (1990) 1646.

18) Moretti J. L., Caglar M., Duran-Cordobes M., et al., Eur. J. Nucl Med. 22 (1995) 97.
19) Maffioli L., Steens J., Pauwels E., et al., Tumori. 82 (1996) 12.
20) Kubota K., Yamada S., Fukuda H., et al., CYRIC Annual Report. (1996) 129.

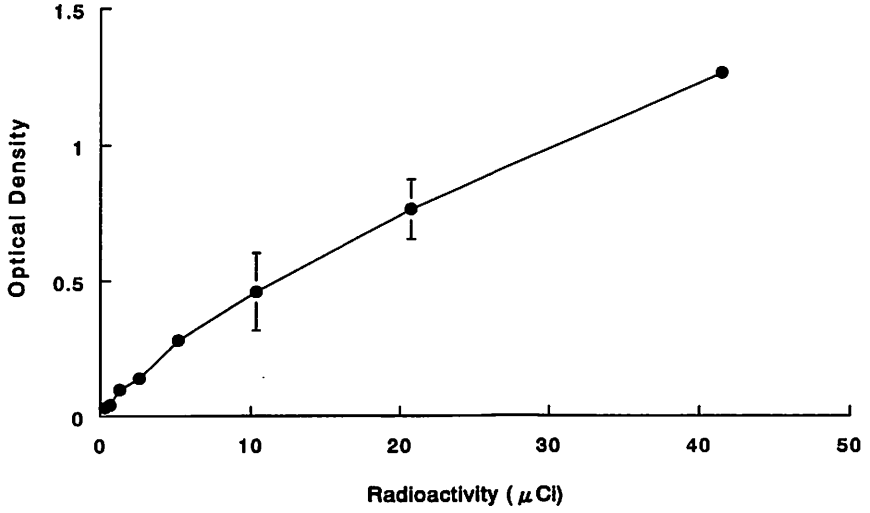

Fig. 1. Response curve of macroautoradiographic film to ^{99m}Tc, 6 hr exposure. In the experimental dose range, the optical density was almost linearly related to the ^{99m}Tc radioactivity.

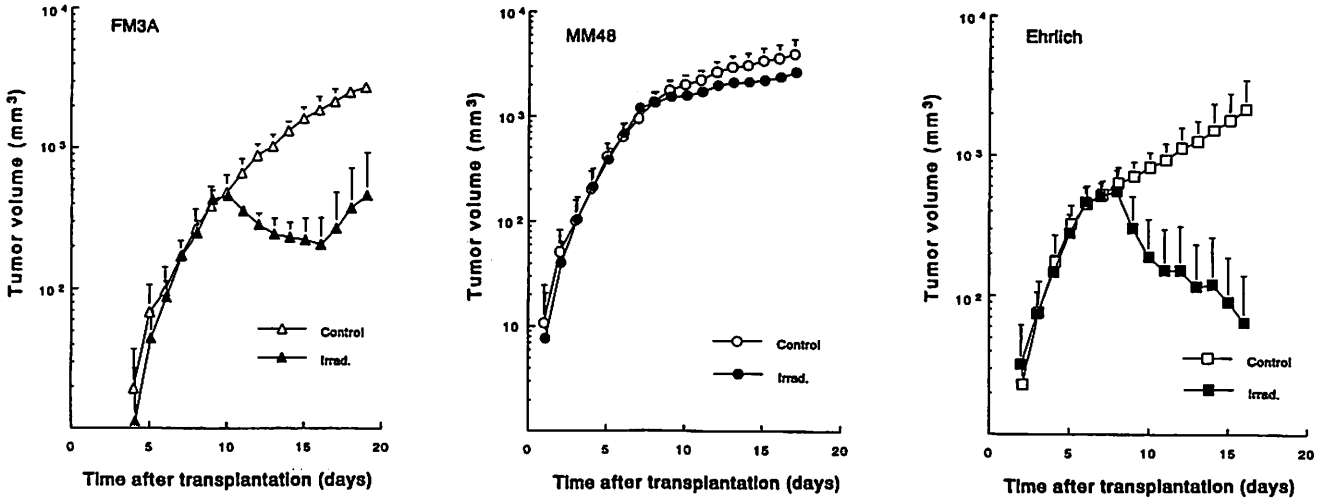

Fig. 2. Each tumor response growth curve after a single dose of 20 Gy irradiation. Day 0 is the day when the tumor cells were transplanted on the thighs of mice. Irradiation was performed on Day 6 in MM48 tumor, Day 8 in FM3A, Day 7 in Ehrlich respectively. Each point shows the mean of eight tumors.

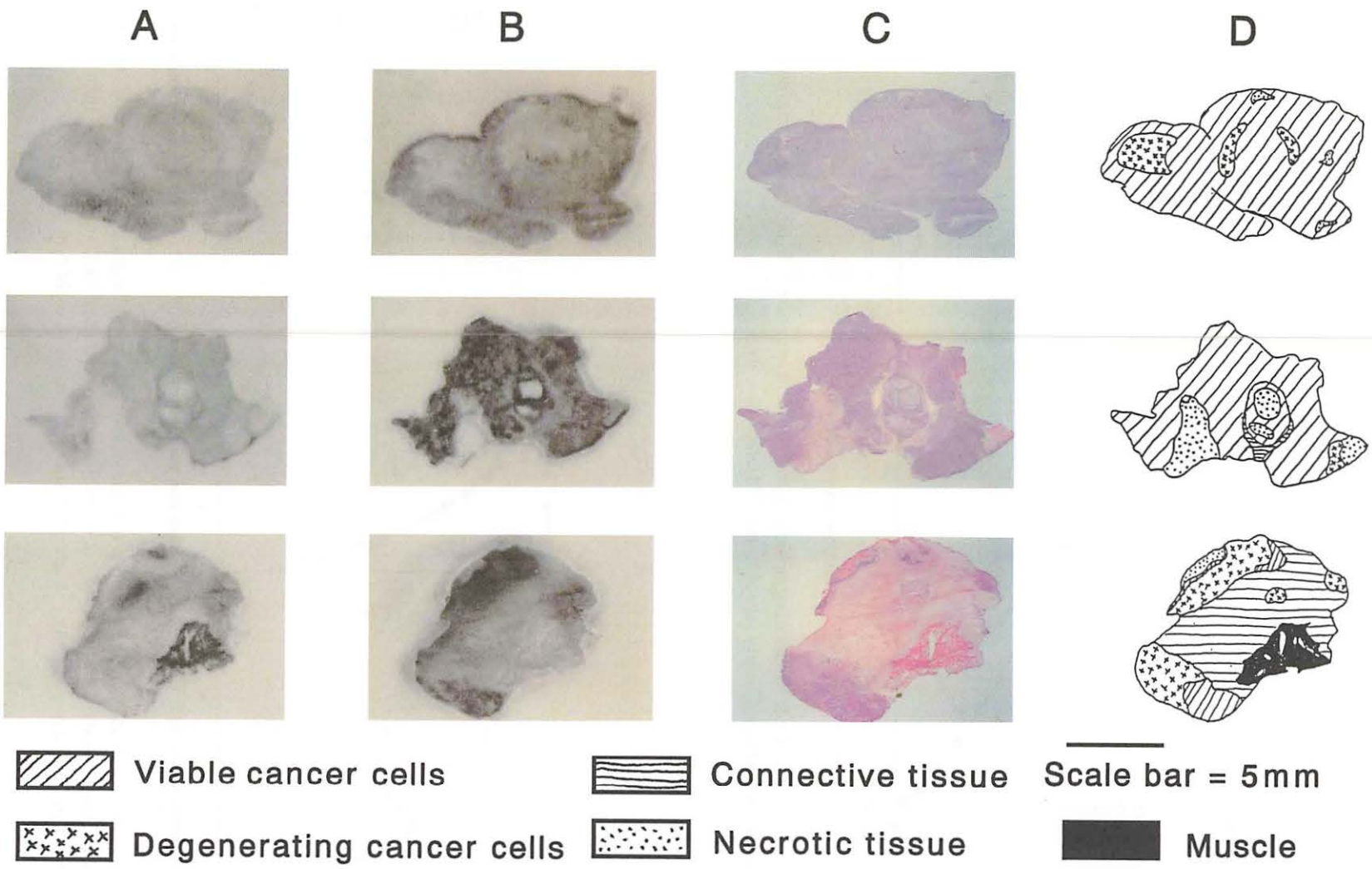

Fig. 3. A combination of double tracer macroautoradiograms and microscopy. Images of ^{99m}Tc-MIBI distribution (A) and ^{14}C-DG (B), and a photomicrograph of the hematoxylin and eosin stained specimen (C) used for production of autoradiograms and illustration of the micrograph (D). Upper: FM3A tumor; Middle: MM48 tumor; Lower: Ehrlich tumor.

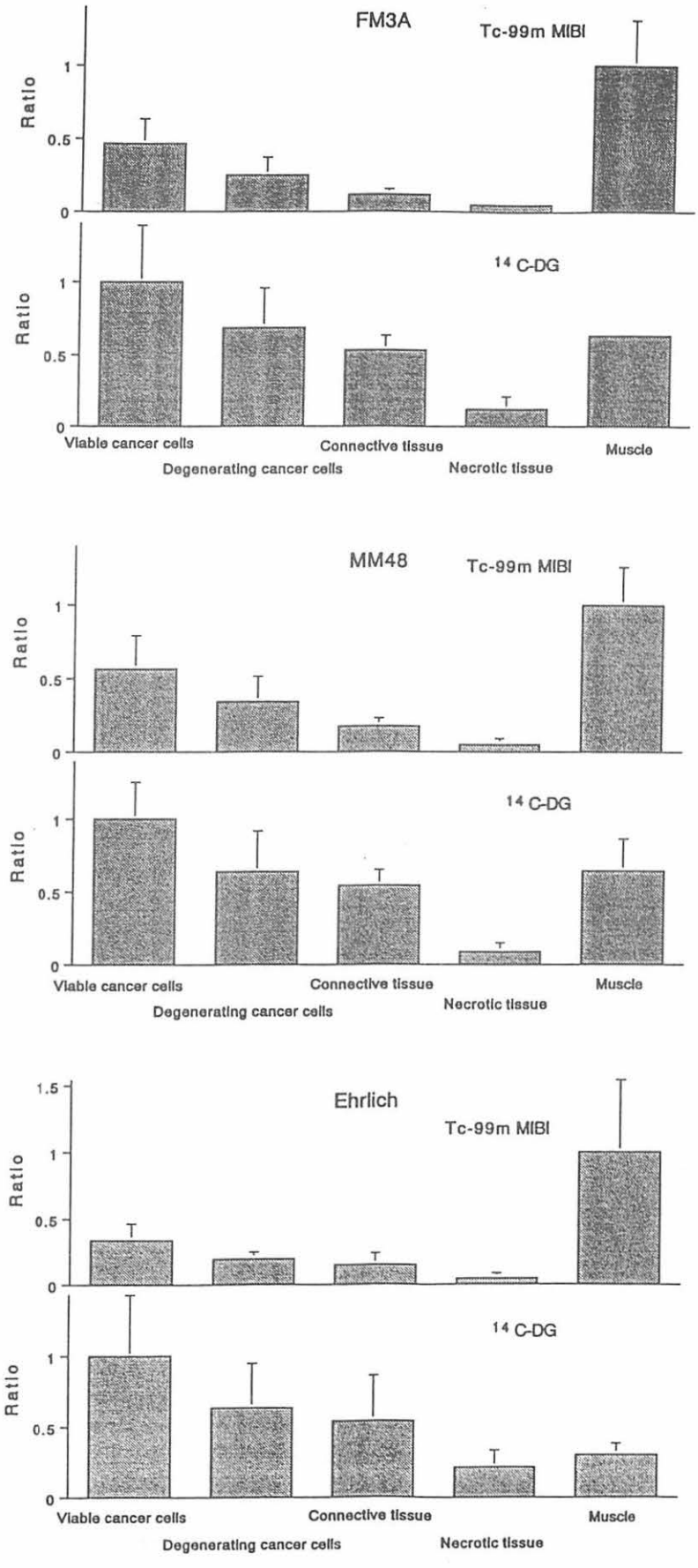

Fig. 4. Comparison of intra-tumor cellular uptake ratio, relative to the highest that of the tissue component with ^{99m}Tc-MIBI and ^{14}C-DG 30 min after injection.

V. MEDICINE AND BIOLOGY (Clinical)

V. 1. Standardization of the Head-neck PET Images

Nishiura H., Rikimaru H., Yamaguchi K.,Watanabe M. and Itoh M.*

Cyclotron and Radioisotope Center, Tohoku University
*Department of Geriatric Dentistry, School of Dentistry, Tohoku University**

Introduction

Masticatory jaw movement and swallowing are controlled by the cooperative masticatory muscles and tongue activities[1,2]. In order to clarify the cooperative stomatognathic system, the activities of the masticatory muscles and tongue has been analyzed. The most common approach for this purpose uses electmyograph. However, it has been very difficult to record simultaneous activities of various muscles and/or many parts of ones.

Our purpose is to quantitatively visualize activities of masticatory muscles and tongue during mastication using by positron emission tomograghy (PET), by pixel-base. In this report, we generated a standerdized three-dimensional head-neck PET images by using spatial normalization technique (Friston et al.).

Subjects and methods

This study protocol was approved by the Human Ethics Review Committee of this institution and written informed consent was taken from all subjects.

1: Spatial standardization of the head-neck transmission images

We used the head-neck transmission images of 20 healthy Japanese male volunteers (19-48y). The transmission scans were obtained by using external rotating line source (^{68}Ge/^{68}Ga). The twenty transmission images were visually registered to the standard plane; namely the Frankfort plane (include the lower orbital point and the bilateral external auditory miatus), the mid-sagital plane and the miatal perpendicular plane (perpendicular to the Frankfort plane through external auditory miatus). These registered images were averaged to form a raw template images (T0). Then each original transmission images were spatially normalized onto the raw template (T0) using linear transformations provided by the Statistical Parametric Mapping software (SPM 96). The final template (T1) was generated by averaging of these 20 transformed images (Fig. 1).

2: Spatial standardization of the head-neck emission images

The head-neck [^{18}F]Fluorodeoxyglucose (FDG) emission images (original emission image E0) were spatially normalized using the original transmission images T0. The parameters for the linear affine components and non-linear transformations were then used to transform emission images. The smoothing kernel of 8 mm FWHM filter was used to reduce possible errors in the transformation[3]. Emission images of fourteen healthy Japanese male volunteers (21-29y) were used. They were divided into two groups, 6 volunteers masticated voluntarily, and the remaining 8 subjects masticated on the right side. Each subject chewed gums for 30 min after the intravenous injection of FDG (approximately 1.79mCi).

Results

The standardized head-neck transmission images were shown in Fig. 1. The skull and external auditory miatus of the standardized transmission image (T1) are more clear-cut than those of registered transmission image T0. However, variance was found in the periphery of menton.

The standardized head-neck emission images of voluntary and right-side mastication groups are shown in Fig. 2 and 3, respectively. Masseter, lateral pterygoid muscles and tongue activities can be confirmed clearly. Moreover, the parts activated high or low were shown in the same muscles. In the voluntary mastication group, the activities of the bilateral lateral pterygoid muscles, left medial pterygoid and masseter muscles were observed. Whereas the activities of the only left lateral pterygoid muscle, right medial pterygoid and masseter muscles were recoded in the right-side mastication group.

Discussion

We suggest the potential use of standardization of the PET head-neck images to visualize activity of masticatory muscles, especially masseter, lateral pterygoid muscle and tongue in this study. Moreover, the differences of activities according to the parts of the same muscle were confirmed clearly. However, in order to standardize more various masticatory muscles and parts of ones, and to become highly precise, it needs to record and analyze more PET images of various quantitative jaw movements.

References

1) Moller E., Acta Physiol Scand. **69**, 1-229 (1966).
2) Ramsey G. H. et al., Radiol. **64**, 498-518 (1955).
3) Friston K. J., Human Brain Mapping **3**, 165-189 (1995).

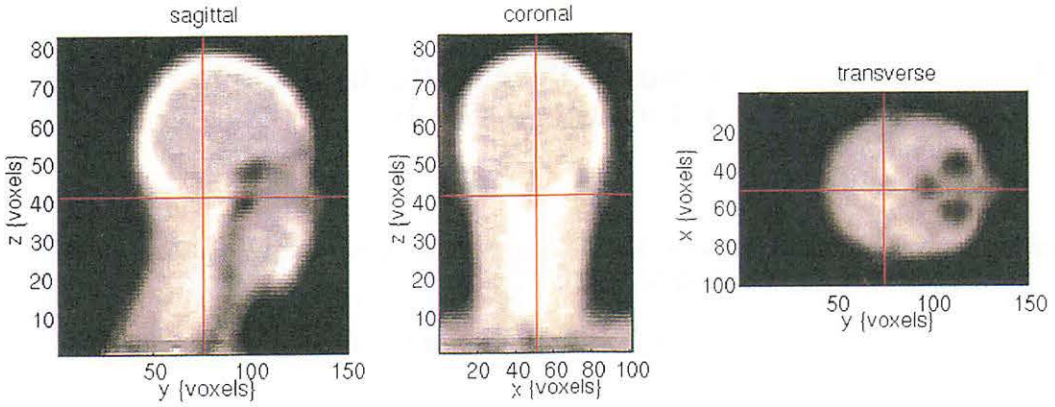

Fig.1. Standardized transmission images.

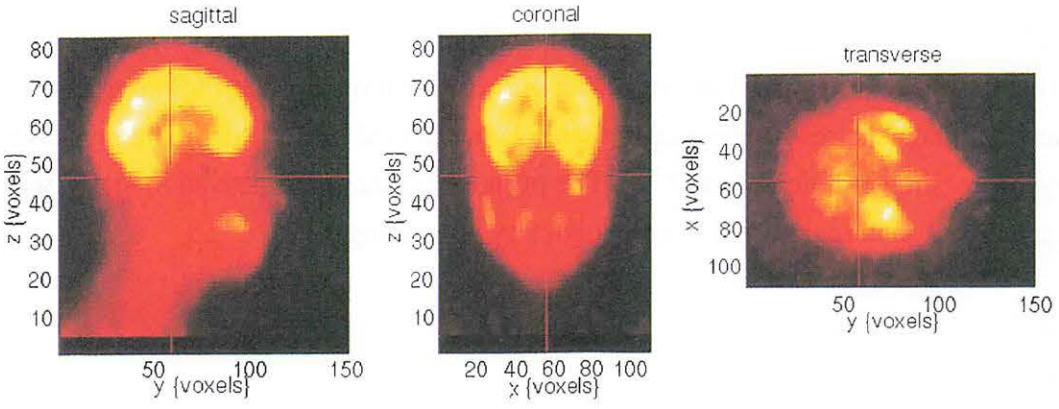

Fig.2. Standardized emission images of the voluntary mastication group.

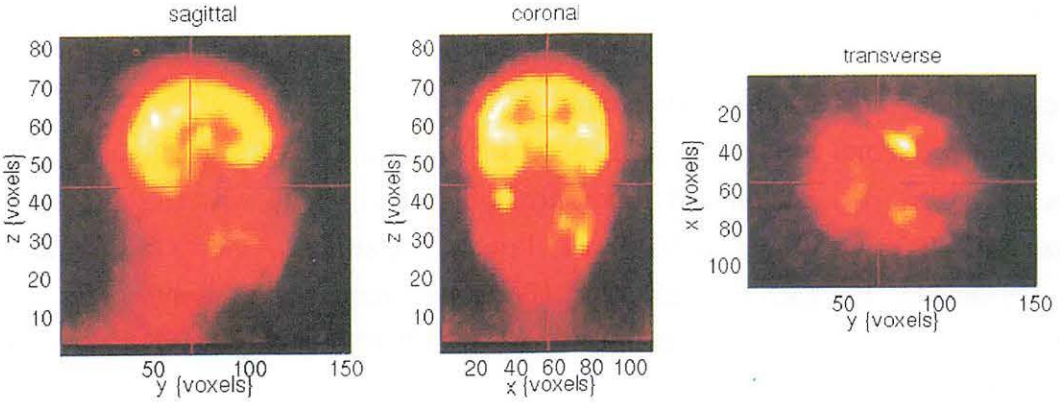

Fig.3. Standardized emission images of the right-side mastication group.

V. 2. Olfactory Stimulus Processing by Human Brain- A Functional Study

Qureshy A., Kawashima R., Imran M. B., Sugiura M., Goto R., Okada K., Inoue K., Itoh M., and Fukuda H.,*

Department of Nuclear Medicine & Radiology, Institute of Development, Aging and Cancer (IDAC), Tohoku University
*Cyclotron and Radioisotope Centre, Tohoku University**

Introduction

Memory of odours is associated with certain objects, incidents and emotions[1]. Due to the lack of an appropriate animal model the analysis of human olfactory processing had been difficult. Recent advances in neuroimaging i.e., positron emission tomography (PET) and functional magnetic resonance imaging (fMRI) has helped in unraveling the mysteries of olfactory processing in human brain[2,3]. The purpose of this PET activation study was to determine human brain regions involved in olfactory processing.

Methods

Subjects

Eight right handed, male volunteers (age 18-26 years) participated in this study after written informed consent. The subjects were screened for right handedness, colour vision and any history of ailments affecting olfaction. The study conformed with the principles of the Declaration of Helsinki and was approved by the medical ethics committee of the Tohoku University. All the subjects underwent MRI scanning using T1-sensitive SPGR sequence within a week of their PET studies. All had normal reported MRI scans.

PET Scanner Description and Study Procedure

Regional cerebral blood flow (rCBF) was determined in all 8 subjects using $H_2{}^{15}O$ PET for six tasks (two control and four activation). PET study was carried out on a Shimadzu SET2400SW Scanner in 3-D mode. Prior to the study a ^{68}Ge-^{68}Ga transmission scan was obtained. For each task 200 MBq $H_2{}^{15}O$ was administered intravenously. The PET data was acquired for 60 seconds in each task with 8-10 minutes interval between two consecutive tasks.

Task Procedures

In each task 8 couplets of olfactory and visual stimuli were presented. Each couplet consisted of simultaneous presentation of an odour and a pair of pictures for 6 seconds followed by a 4 second interval for the response from the subject. To keep the eye movements to a minimum, subjects were asked to fix their gaze all the time on the red cross in the centre of the field of view. Odour was presented birhinally with a self designed 'sniffing stick' held 2-3 cm in front of the anterior nares of the subject. Coloured visual stimuli were presented with help of a head mounted display (HMD Eyetrek FM011F, Olympus) connected to Macintosh PowerBook G3 computer. Presentation and withdrawal of olfactory and visual stimuli were simultaneous. Subjects were asked to breath through nose at their normal respiratory rate with no attempt to sniff.

With a pre-PET psychophysical test, two groups of odours were defined. One group, selected for the ON task, was familiar to the local population. The other group of odours was found unfamiliar and it was used in tasks C2, VN, OD and VD.

Control task 1 (C1) consisted of keeping eyes on red cross with no cognition involved. No olfactory or other visual stimuli were presented.

Control task 2 (C2) consisted of looking at a scrambled picture (without any specific shape or design) and breathing an unspecified odour. No cognition was involved.

In Olfactory Naming Task (ON) an olfactory stimulus was presented simultaneously with a scrambled picture for 6 seconds. Concentrating on the olfactory stimulus only, the subject was required to name or categorize it in the following 4 seconds or say PASS, if undecided.

In Visual Naming Task (VN) a picture (having a pair of same image) was presented simultaneously with an olfactory stimulus. Subject was required to concentrate on the picture only and name it in the following 4 seconds or say PASS if undecided.

In Olfactory Delayed Matching to Sample Task (OD) a target odour was presented 2 minutes before the actual task. Subject was required to 'memorize' it. During the task the target odour was presented thrice among eight cycles of olfactory-visual couplets. Attention to the simultaneously presented scrambled visual stimulus was not required.

In Visual Delayed Matching to Sample Task (VD) two target scrambled pictures were presented 2 minutes before the actual task. Subject was required to 'memorize' their characteristics (colours and design). During the task the target visual stimuli were presented thrice among eight cycles of olfactory-visual couplets. Attention to the simultaneously presented olfactory stimulus was not required.

In OD and VD tasks answer was to be given as 'yes, no or pass' when presented stimulus matched or did not match the target stimulus or when undecided, respectively. The tasks were presented in a counterbalanced manner.

Image Processing and Statistical Analysis

Each PET image was anatomically normalized using Automated Image Registration (AIR)[4] and the Elastic transformation[5]: each subject's MRI was normalized into the standard brain MRI of Human Brain Atlas (HBA)[6] using affine transformation of AIR followed by application of the 3-D deformation field of the Elastic transformation, and these parameters were subsequently used to transform each subject's PET image and MRI into the standard brain anatomy. Statistical Parametric Mapping (SPM96, Wellcome department of Cognitive Neurology, London)[7] software was used for smoothing and statistical analysis. A 3-D Gaussian filter of 16 mm was used for image smoothing. For each comparison, voxels with Z values>3.1 ($p<0.001$) were considered to denote regions of significantly increased rCBF. Anatomical localization of the activated areas was made in relation to the mean reformatted MRI of the eight subjects and expressed in the stereotactic space defined by Talairach and Tournoux[8].

Results

In the statistical analysis first ON, VN, OD and VD tasks were subtracted from C1 and C2 tasks respectively. Then conjunction analysis was carried between different subtraction sets. The results are presented in table 1 and figures 1 to 4.

ON-C2 with ON-C1 conjunction analysis show areas activated by olfactory recognition, and naming. This revealed significant activation in the left insula, the right anterior cingulate gyrus, the left basal ganglia, the left cuneus, and the bilateral cerebellum (Fig. 1).

VN-C2 with VN-C1 conjunction analysis show areas activated by visual recognition, and naming. This analysis showed activation in the left insula, the right anterior cingulate gyrus, the right basal ganglia, the left cuneus, the bilateral cerebellum and left fusiform gyrus (Fig. 2).

OD-C2 with OD-C1 conjunction analysis show areas activated by olfactory delayed-matching-to-sample task. This analysis showed activation in the left insula, the left cuneus, the right anterior cingulate, the right middle temporal gyrus, and the bilateral cerebellum. (Fig. 3).

VD-C2 with VD-C1 conjunction analysis show areas activated by visual delayed-matching-to-sample task. This analysis showed activation in the left insula, the left cuneus, the right anterior cingulate, the right inferior temporal gyrus, the bilateral cerebellum, and the right lateral occipital lobe (Fig. 4).

Discussion

In this study aim was to locate the human brain regions involved in the olfactory processing by functional PET imaging. Attempt was made to sort the regions which are involved in the olfactory naming and short-term memory. The results showed that in

addition to the limbic system structures, the cerebellum was also activated during the olfactory processing. This is a new finding which has been not reported previously.

Among the areas activated in olfactory recognition with naming, the insula, and the cingulate gyrus are part of limbic system and are known to be activated during olfactory stimulation[9] and attention related tasks[10,11] respectively. The cuneus is part of the secondary visual cortex and is involved in the visual imagery tasks, which may be required in the olfactory naming process as well.

In the olfactory short term memory task analysis, additional activation is seen in the middle temporal gyrus, and lateral occipital lobe. In a clinical study carried out in patients of right temporal lobe resection, Jones-Gotman et al have reported loss of odor memory over a period of time[12].

Cerebellar activation during the olfactory tasks is a new finding and have not been reported in any of the previously published olfactory PET studies[13]. However a recent fMRI study has revealed cerebellar involvement in olfactory perception[14]. The authors found cerebellar activation at different locations during sniffing and passive smelling tasks. They concluded that cerebellum had a role in the olfactory processing by controlling the sniff volume. In our data analysis it was noted that C2-C1 subtraction analysis did not show activation in the cerebellar region. While all the other tasks involving cognition during olfactory stimulation showed cerebellar activation. Data from other recent functional imaging experiments in humans have indicated that the cerebellum has a number of additional functions e.g., tactile sensory discrimination, attention and cognitive function. Our results indicate that cerebellum has some role in cognitive processing of olfactory stimulus.

References

1) Nolte J., The Human Brain. An introduction to its functional anatomy. III rd Edition. Mosby-Year Book Inc. (1993).
2) Zatorre R. J. et al., Nature **360** (1992) 339-340.
3) Levy L. M. et al., J. Comput. Assist. Tomogr., **21** (1997) 849-856.
4) Woods R. P. et al., J. Comput. Assist. Tomogr., **22** (1998) 153-165.
5) Schormann et al., Lecture Notes in Computer Science (1996), 1131:337-342.
6) Roland P. E. et al., Human Brain Mapping **1** (1994) 173-184.
7) Friston et al., Human Brain Mapping **2** (1995):189-210.
8) Talairach J. & Tournoux P., Co-planar stereotactic atlas of the human brain. Stuttgart: Thieme
9) Royet J. P., et al. J. Cogn. Neurosci., **11** (1999):94-109.
10) Pardo J. V. et al., Proc. Natl. Acad. Sci. USA. (1990) **87**: 256-259.
11) Posner M. I., Annu. Rev. Neurosci. (1990). **13**: 25-42.
12) Jones-Gotman M. et al., Brain Cognition. (1993). **22** (2): 182-198.
13) Yousem D. M. et al., Radiology. **204** (1997) 833-838.
14) Sobel N. et al., Neurosci. **18** (21): (1998), 8990-9001.

Table 1: Activated regions related to processing of olfactory and visual tasks.

Analysis	Regions	Talairach coordinates			
	ACTIVATION	x	y	z	Z score
ON-C2 with ON-C1	Right cerebellum posterior Medial lobule	-20	-75	-45	5.49
	Left cuneus	2	-88	25	5.16
	Left posterior lateral cerebellum	36	-81	-26	5.00
	Left insula	32	23	14	4.91
	Right anterior cingulate gyrus	-8	32	11	4.87
	Left anterior Medial cerebellum	40	-38	-32	4.76
	Left Basal Ganglia	7	9	15	4.74
VN-C2 with VN-C1	Right anterior cingulate gyrus	-8	14	23	5.00
	Left insula	22	23	0	4.47
	Right posterior medial cerebellum	-23	-74	-40	4.44
	Left fusiform gyrus	50	-53	-15	4.36
	Right posterior Medial cerebellum	-14	-82	-35	4.21
	Left cuneus	7	-88	33	4.03
	Right anterior cingulate gyrus	-6	20	45	4.02
	Right Basal ganglia	-4	-17	1	3.82
	Left insula	37	25	14	3.75
OD-C2 with OD-C1	Left cuneus	9	-71	8	5.10
	Right Posterior Medial Cerebellum	-21	-75	-39	4.56
	Left anterior Lateral Cerebellum	37	-40	-36	4.49
	Right Posterior Medial Cerebellum	-12	-81	-34	4.34
	Left insula	24	25	4	4.18
	Right anterior cingulate gyrus	-8	35	8	4.11
	Right anterior cingulate gyrus	-6	20	45	3.95
	Right middle temporal gyrus	-66	-29	-11	3.67
VD-C2 with VD-C1	Right anterior cingulate gyrus	-9	35	6	5.40
	Left cuneus	6	-87	30	5.02
	Right lateral Occipital lobe	-42	-66	30	4.77
	Left Cuneus	18	-64	5	4.75
	Left anterior lateral cerebellum	40	-35	-32	4.73
	Right lateral occipital	-25	-77	43	4.38
	Right Inferior Temporal gyrus	-56	-26	-11	4.33
	Left Insula	33	20	13	4.22

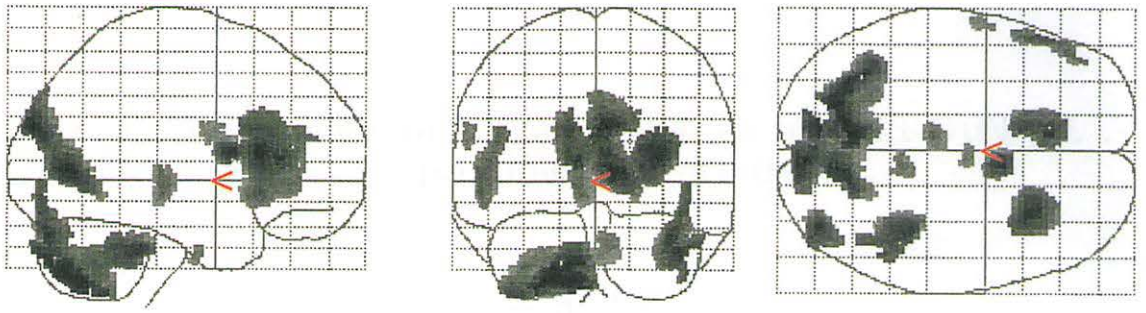

Fig. 1. Conjunction analysis results of ON-C2 with ON-C1.

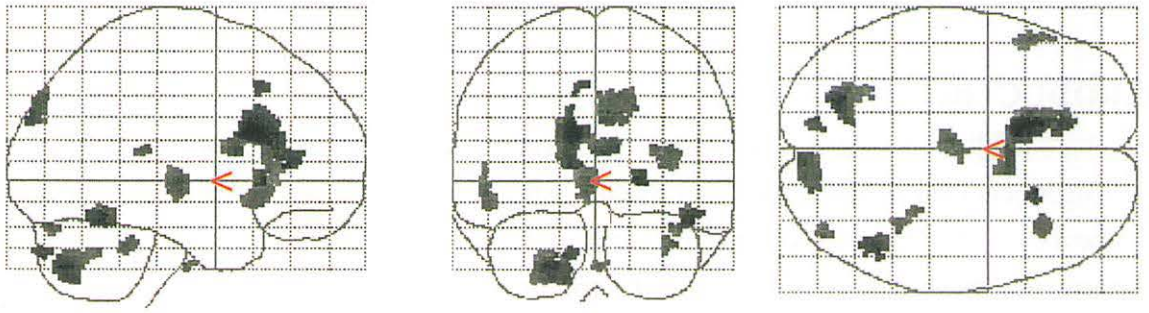

Fig. 2. Conjunction analysis results of VN-C2 with VN-C1.

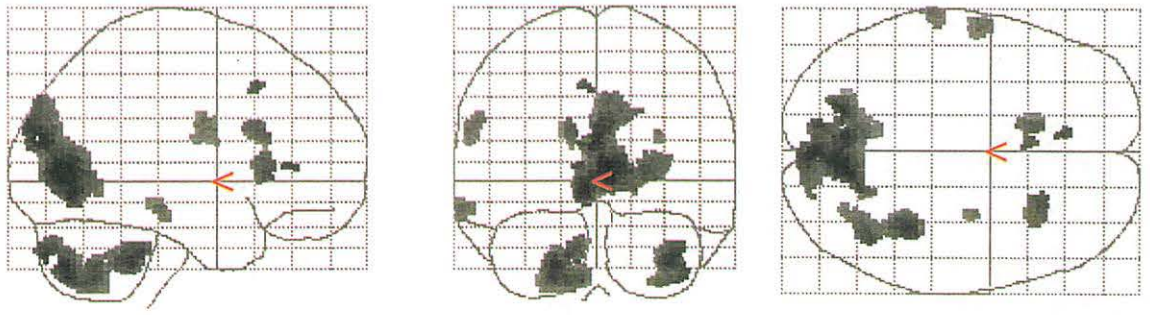

Fig. 3. Conjunction analysis results of OD-C2 with OD-C1.

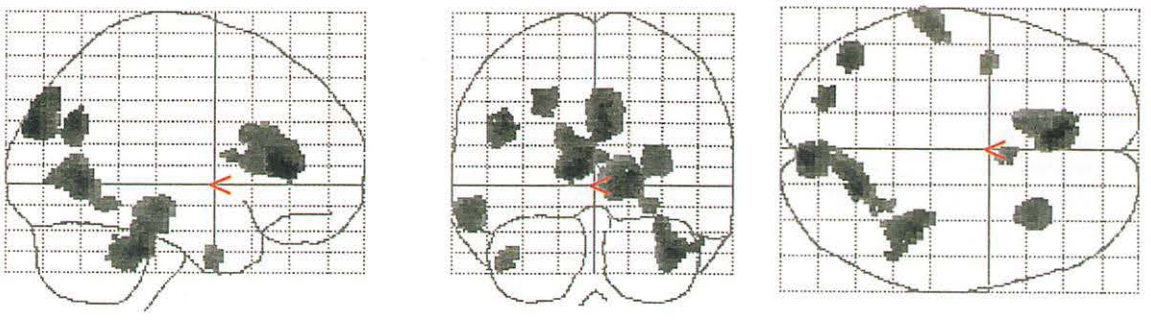

Fig. 4. Conjunction analysis results of VD-C2 with VD-C1.
Brain regions showing rCBF changes in different conjunction analyses. The results are in three 2-Dimensional planes (sagittal, transverse, coronal projections). The superimposed dotted grid represents Talairach and Tournoux[8] coordinate space.

V. 3. FDG-PET for the Evaluation of Residual and Regrowth During Chemotherapy

Yoshioka T., Fukuda H., Akaizawa T.*, Kanamaru R.*

Departments of Clinical Oncology, Nuclear Medicine and Radiology, Institute of Development, Aging and Cancer, Tohoku University*

INTRODUCTION

[^{18}F]Fluorodeoxyglucose (FDG) and PET may be more suitable for follow-up after cancer treatment than morphological approaches, since it reflects tumor viability[1]. Here, we describe a case of abdominal lymph node metastases from a colon cancer in a patient receiving chemotherapy after colectomy. FDG-PET tumor images in this case changed along with the clinical progress, while morphological examination did not show any clear response.

A CASE REPORT

A 43-yr-old male suffering from lumbago and abdominal pain underwent clinical examinations, which revealed an adenocarcinoma of the transverse colon. He underwent resection of the cancer and lymphnode, but lymphnode metastases surrounding the abdominal aorta were unresectable. He was therefore admitted to our hospital for chemotherapy aimed at eradicating the residual lymphnodal metastases.

The patient complained of severe lumbago and abdominal pain. CT revealed abdominal lymphnodal metastases at the level of the bilateral renal hilus with a maximum diameter of 10 cm (Fig. 2A). Laboratory findings revealed a high level of LDH and slightly increased CEA (Fig. 1). Administration of Camptotesin 150 mg/m^2 on day 1 and 5-fluorouracil (5FU) 500 mg/m^2 on day 2 started from the 7th day after admission once every two or three weeks. After the first administration, the lumbago and abdominal pain improved and the LDH value normalized (Fig. 1). After the second administration, the diameter of the tumor was reduced by 10 % on CT (Fig. 2B). On the 63th day after the start of the chemotherapy, this reduction was observed to have persisted with no further change (Fig. 2C). On the same day, PET was carried out. Imaging 40 minutes after the injection of 247.9 MBq of FDG revealed little accumulation of label in the area corresponding to the mass and only a hot spot representing urinary excretion (Fig. 3A). Regions of interest (ROI) were set and the standard uptake value, which is the uptake of FDG normalized for the dose administrated and the weight of the patient, was calculated as follows:

SUV = Activity in ROI (mCi/ml) / injected dose (mCi) / patient's weight (Kg)
The calculated value was 1.8.

On the 113th day after the start of chemotherapy, there was no change in the size of the tumor on CT (Fig.2D). On the 145th day, acute pleuritis occurred, accompanied by an increase in the LDH value, but this could be controlled by administration of antibiotics for one week.

However, the lumbago and elevated LDH again appeared from about the 190th day after the start of chemotherapy. On the 198th day, CT (Fig. 2E) and PET (Fig. 3B) were carried out. There was little change in the size of the tumor on CT, but PET imaging 40 minutes after the injection of 314.5 MBq of FDG revealed a high accumulation of label with a SUV of 5.4. Thereafter the lumbago worsened and LDH continued to increase and CT images showed growth of the tumor and progressive disease on the 244th day (Fig. 2F).

DISCUSSION

FDG uptake reflects the viability of tumor cells[1], and its use in experimental studies has allowed demonstration of cytotoxic effects of chemotherapy and radiation therapy causing metabolic arrest of cancer cells before necrosis and reduction in tumor size[2,3]. Therefore, FDG-PET is suitable for follow up purposes after cancer treatment.

In the present case, the limited variation in size of the metastatic tumor measured with CT would be judged as "NC" (no change) with adaptation of the WHO criteria[4]. Differences in the X-ray absorption values of the mass on CT might reflect changes in its structure, but exact interpretation of such images is very difficult. With FDG-PET, in contrast, the data were clear: little accumulation of FDG in the initial phase of chemotherapy suggesting that the number of viable tumor cells was decreased, with replacement by fibrotic tissue, and subsequent high uptake mirroring progressive growth. These PET studies thus showed large variation in glycolytic metabolism in the tumor along with subjective symptoms (lumbago and abdominal pain) and biologic data such as LDH and CEA values, although the actual change in tumor size was small.

In this case, LDH was the most reliable serum marker for judgement of disease progression, but it is not specific, as evidenced by the temporary elevation with acute pleuritis. CEA is generally a good tumor marker but the level was not high in this case, and far more precise information was obtained with the FDG-PET.

There are several reports of recurrent detection with FDG-PET in brain[5], head and neck[6], lung[7] and colorectal cancers[8,9], but these were after radiotherapy or surgery. Stephens et al[10]. and Reinhardt et al[11]. evaluated residual masses of postchemotherapy germ cell tumors. Kubota et al[12]. suggested PET to be more useful than CT in long-term follow-up during radiotherapy, using ^{11}C-methionine as a PET tracer. To our knowledge, this is the first case of FDG-PET evaluation of residual masses and regrowth during long-term follow-up and chemotherapy, with a CT comparison.

Unfortunately, we did not have the opportunity to estimate the pretreatment state of this case with FDG-PET, but the available findings nevertheless clearly showed that metabolic change measured in this way may reflect the clinical course more exactly than morphologic alterations during chemotherapy.

ACKNOWLEDGMENT

This work was supported in part by Grant-in-Aid (No. 10670820 and No. 09470196) from the Ministry of Education, Science and Culture, Japan. We would like to thank the staff of the Cyclotron Radioisotope Center, Tohoku University.

References

1) Higashi K., Clavo A. C., Wahl R. L., J. Nucl. Med. **34** (1993) 414-419.
2) Abe Y., Matsuzawa T., Fujiwara T., et al., Eur. J. Nucl. Med. **12** (1986) 325-328.
3) Yoshioka T., Takahashi H., Oikawa H., et al., J. Nucl. Med. **38** (1997) 714-717.
4) Miller A.B., Hoogstraten B., Staquet M., et al., Cancer **47** (1981) 207-214.
5) Patronas N. J., Di Chiro G., Brooks R. A., et al., Radiology **144** (1982) 885-889.
6) Lapela M., Grenman R., Kurki T., et al., Radiology **197** (1995) 205-211.
7) Duhaylongsod F. G., Lowe V.J., Patz E. F., et al., J. Thorac. Cardiovasc. Surg. **110** (1995) 130-140.
8) Straus L. G., Clorius J. H., Schlag P., et al., Radiology **170** (1989) 329-332.
9) Ito K., Kato T., Tadokoro M., et al., Radiology **182** (1992) 549-552.
10) Stephens A. W., Gonin R., Hutchins G. D., et al., J. Clin. Oncol. **14** (1996) 1637-1641.
11) Reinhardt M. J., Muller-Mattheis V. G. O., Gerharz C. D., et al., J. Nucl. Med. **38** (1997) 99-101.
12) Kubota K., Yamada S., Ishiwata K., et al., Clin. Nucl. Med. **17** (1991) 877-881.

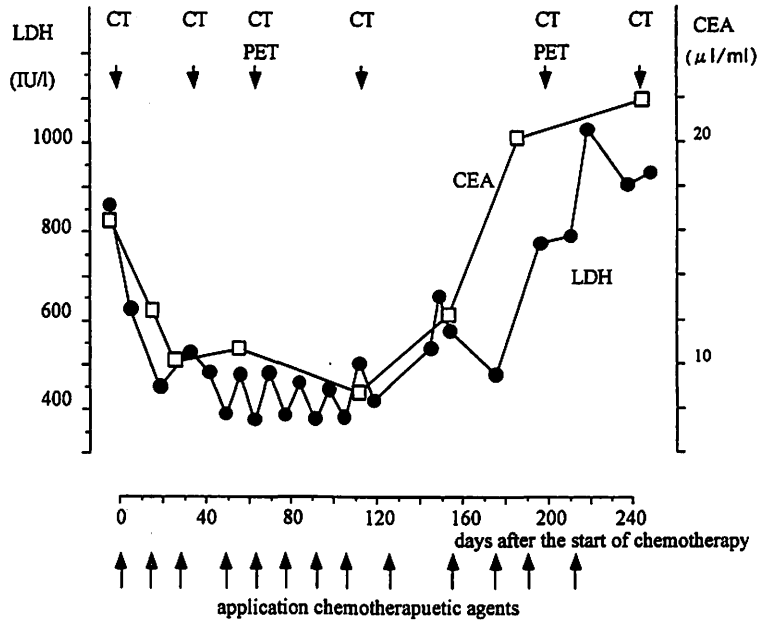

Figure 1. The clinical course after the start of cancer chemotherapy. The normal range of LDH values is 240 to 470 IU/l, and CEA is less than 5.0 ng/ml.

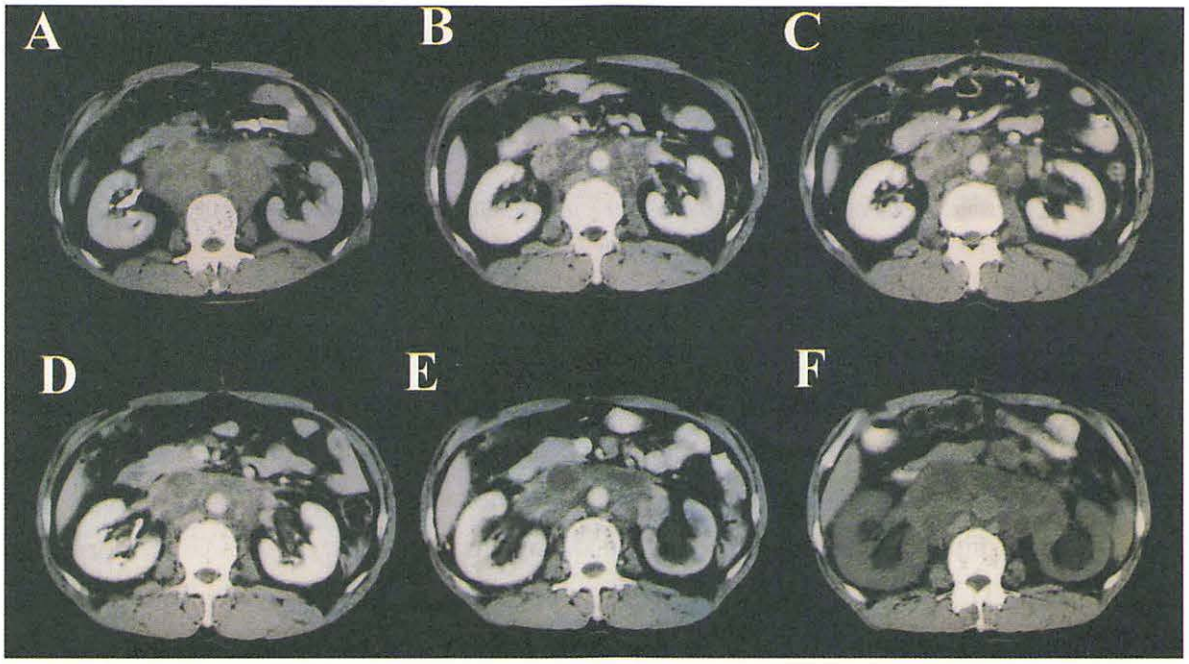

Figure 2. CT images. Note the lymphnodal metastases surrounding the abdominal aorta at the level of the bilateral renal hilus. Ratios of maximum tumor size before and after chemotherapy were: (A) pretreatment, 100%; (B) 22th day, 91%; (C) 63th day, 86%; (D) 113th day, 90%; (E) 198th day, 95%; (F) 244th day, 118%. The day numbers are from the start of chemotherapy.

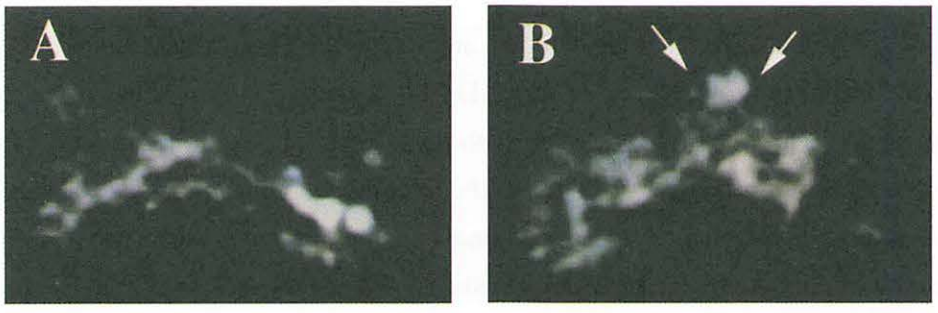

Figure 3. PET images. (A) 63rd day from the start of chemotherapy. The regions corresponding to the metastases are cold. Hot spots represent urinary excretion of ^{18}FDG. (B) 198th day. The tumors are visualized as hot spots, indicated by arrows.

V. 4. Attenuation Correction in 3-D PET

Mizuta T., Watanuki S., Yamazaki H., Matsuyama S., Ishii K., Itoh M.*, and Orihara H.**

Department of Quantum Science and Energy Engineering, Tohoku University
*Cyclotron and Radioisotope Center, Tohoku University**

Introduction

Acquisition of all possible coincidence lines in the cylindrical geometry of positron emission tomograph (PET), commonly referred to as full volume imaging of 3-D mode, affords a large increase in sensitivity over slice-collimated 2-D mode[1,2]. In PET studies accurate attenuation correction is essential in quantitative analysis. Attenuation correction factors for 3-D PET is obtained in 2-D mode transmission scan with the septa in. Unfortunately, this approach leads to a drawback of a long acquisition time to achieve adequate statistical quality. With the view to overcoming this drawback, we introduce a method for attenuation correction, which dose not need transmission scan and is based on extraction of an object contour from emission images without attenuation correction. Here we will discuss the accuracy of this method.

Attenuation Correction Method

Usually, attenuation correction factors are obtained from transmission $T(r,\theta)$ and blank $B(r, \theta)$ scan data. These two scan data are acquired by rotating an external source with and without a patient in the gantry. In the 2-D PET, attenuation correction factors are given by the ratio of $B(r, \theta)/T(r, \theta)$. However in the 3-D PET, attenuation correction factors are obtained by the following procedure. First, the transmission and the blank data are acquired in the 2-D mode. Second, two-dimensional images of attenuation coefficients μ are reconstructed with $\ln[B(r, \theta)/T(r, \theta)]$, in each slice. Third, these 2-D μ-images are forward-projected to all possible 3-D PET LORs and attenuation correction factors for 3-D PET are obtained.

The emission image reconstructed without attenuation correction reproduces the contour of the patient body since it is emphasized due to reduction of attenuation of γ-ray nearby the surface of the body. We can obtain the μ-image by assigning the theoretical μ value to the pixels in the extracted contour.

Experimental

To evaluate the validity of this attenuation correction method, we adopted clinical brain scan data acquired with multi-ring high resolution PET PT931/04-12 (CTI Inc, USA). A patient was healthy male volunteer and was administered 8,2mCi of ^{18}FDG. Emission scan time was 5-min and transmission scan time was 10-min. Three protocols were applied to attenuation correction for emission images, (1)10-min transmission scan (the standard method for attenuation correction), (2)theoritical extraction of μ-image which is based on the assumption that brain region including skull has a uniform attenuation coefficient (μ=0.095[cm^{-1}]), and (3)another one of μ-image which consisting of uniform brain region, skull (bones) (μ=0.105[cm^{-1}]) as a reduced copy of brain contour, and head rest. The μ-image of head rest was obtained by separate measurement of 120-min transmission scan. A quantitative comparison of the three techniques was made in terms of the x and y profiles across the origin of the plane of reconstructed images.

Results and Discussion

Figure1 shows the emission image of human brain without attenuation correction(1A) and the three images corrected for attenuation. Attenuation correction factors are determined respectively with the use of 10-min transmission scan data(1B), μ-image based on the assumption that brain has a uniform attenuation coefficient(1C), and μ-image which incorporates the existence of both skull and head rest to the uniform object of brain(1D). These corrected images are quite similar to each other. The extracting contour method based on a uniform region seems practical for attenuation correction without transmission scan especially in the case of brain which has a simple structure of attenuator. Figure.2 depicts the x and y profiles taken from the corrected images of 1B, 1C, and 1D. In both profiles, the difference in pixel values between B and D is smaller than that between B and C.

In the present method, this is a serious problem that the attenuation coefficients for individual persons will be different each other. For this situation, we have a promising procedure which is a combination of segmented attenuation correction with short transmission scan[3]. Short transmission scan gives a μ-image with poor statistical precision and can not be directly used. We discriminate lungs, soft tissue (blood, muscle, and fat), and bones using the distribution histogram of this μ-image[4]. Then theoretical or average μ values are assigned to each region. Now we are investigating the performance of this method for complex distribution of attenuator with the aim to establish an exact attenuation correction method. Furthermore, we are developing an attenuation correction method using the resultant information of scattering objects for scatter correction in 3-D PET.

References

1) Townsend D. W., Spinks T., Jones T., Geissbuhler A., Defrise M., Gilardi M. C., and Heather J., IEEE Trans. Nucl. Sci., **36**, 1056-1065 (1989).

2) Townsend D. W., Bailey D. L., Defrise M., and Kinahan P. E., IEEE NSS/MIC Short Course, 1-54 (1994).
3) Xu E. Z., Mullani N. A., Gould K. L. and Anderson W. L., J. Nucl. Med. **32**, 161-165 (1991).
4) Xu M., Luk W. K., Cutler D. C. and Digby W. M., IEEE Trans. Nucl. Sci., **41**, 1532-1537 (1994).

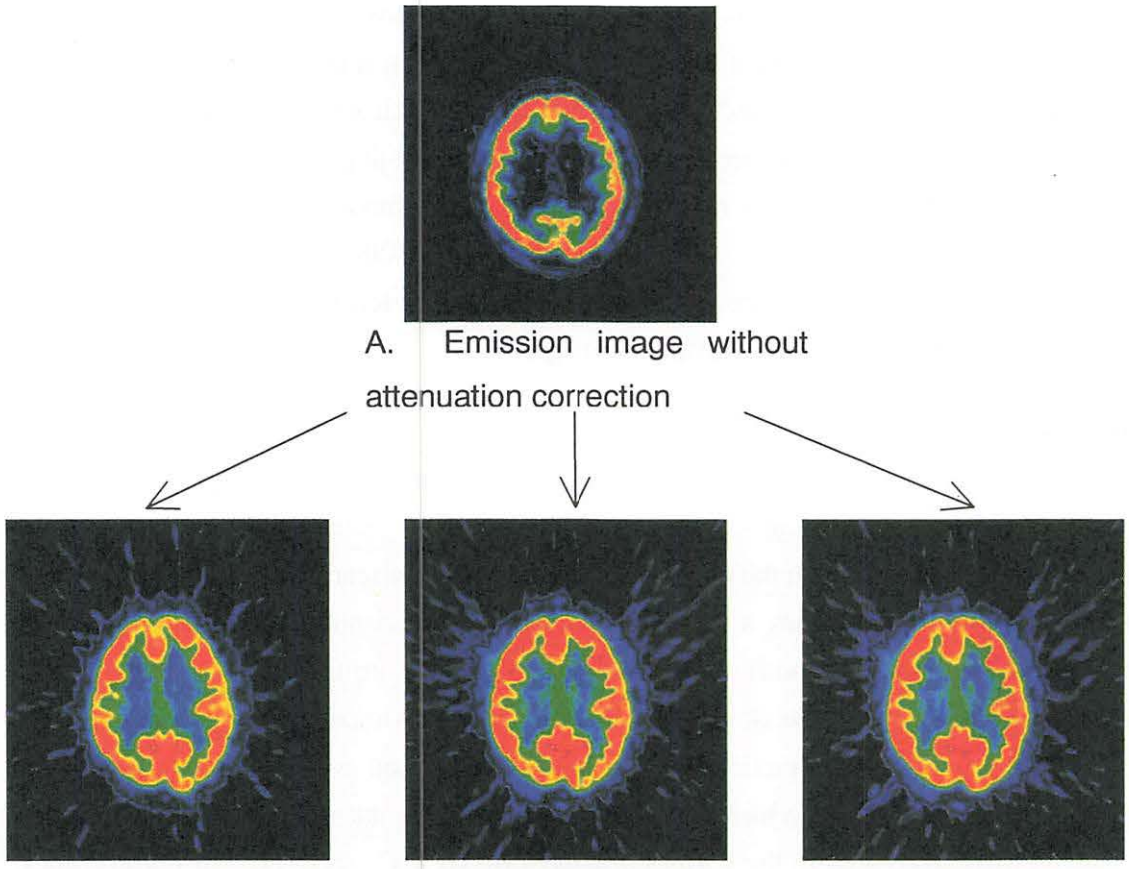

Fig. 1. Original emission image of brain without attenuation correction(A) and images corrected with 10-min transmission scan data(B), with μ-image based on the assumption that brain has uniform attenuation coefficient (C), and with μ-image which incorporates the existence of skull and head-rest (D).

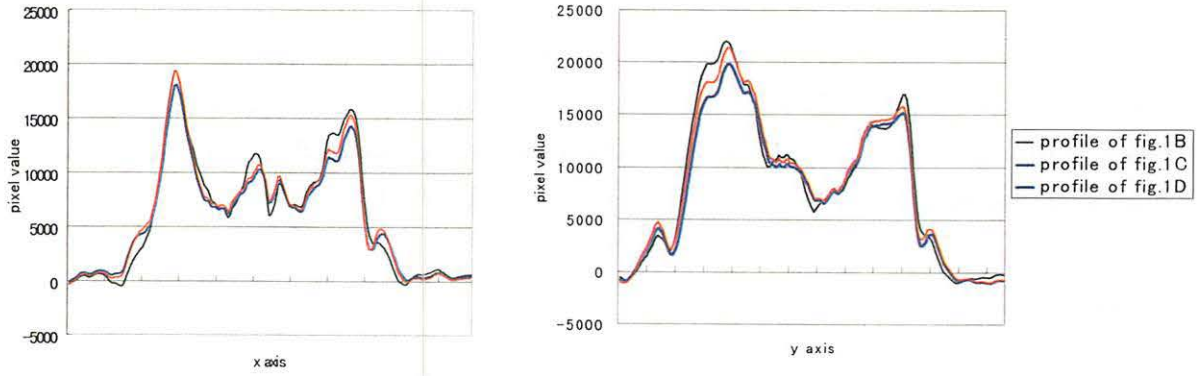

Fig. 2. Profiles of corrected images.

V. 5. A Research of Image Reconstruction for 3-D PET Based on Fourier Rebinning Algorithm

Oishi Y., Watanuki S., Ishii K., Yamazaki H., Matsuyama S., Itoh M.*, Orihara H.**

Department of Quantum Science and Energy Engineering, Tohoku University
*Cyclotron and Radioisotope Center, Tohoku University**

Introduction

The quest for increased sensitivity in positron emission tomography (PET) has led to interest of acquisition of all possible coincidence lines in a gantry. This has become feasible with the advent of commercial scanners equipped with retractable septa. Although this technique significantly improves sensitivity over conventional slice-orientated methods (2-D PET), it comes at the cost of much increased time of image reconstruction. This drawback must be solved in actual clinical application based on dynamic imaging or whole body imaging. The necessary time for 3-D image reconstruction can be significantly reduced with the use of the super computer. However, it can't be always available from the side of cost. So we need some methods to speed up the 3-D reconstruction without using the super computer. Recently, a rebinning algorithm has been proposed as a promise approach in overcoming time-consuming reconstruction of images in 3-D PET. An axial view is about 8 to 16cm, for most of current PET scanners with a ring-diameter of 60 to 100cm, and the maximum axial acceptance angle is rarely beyond 10 degrees. With regard to small solid angles in the axial view, 3-D data can be rebinned into a stack of ordinary 2-D data sets. These rebinned data can therefore be reconstructed by applying the 2-D filtered-backprojection methods. Hence, some rebinning algorithms are promised to reduce processing time of image reconstruction[1].

In this report, we especially make notice to the Fourier rebinning (FORE) algorithm which was implemented in Shimadzu SET-2400W scanner at Cyclotron and Radioisotopes Center of Tohoku University (CYRIC). This is an approximate algorithm which can be lead from the frequency-distance relation. After image reconstruction is performed with the 3-D reprojection (3DRP) algorithm and the FORE algorithm, we evaluate quality and quantification for the images with the use of the two algorithms.

Fourier rebinnig algorithm

For a PET scanner with N rings, the data acquired in 3-D mode consist of N^2 sinograms, in which N direct sinograms (θ=0) and $N(N-1)$ oblique sinograms are included. The four variables s, ϕ, z and δ are defined as follows:s is the distance between the axis of the scanner and a projection line onto a transaxial plane, ϕ is an angle of the projection direction with respect to a y-axis on the transaxial plane, z is the axial coordinate of the point midway between two detectors. The δ coordinate is defined as the tangent of the angle θ between a line of response and the transaxial plane (See Fig. 1)[1].

We take the Fourier transform of oblique and directed sinograms with respect to the parameters of s, ϕ and z. In the 3-D Fourier transform, $P(\omega, k, \omega_z, \delta)$, ω is the radial frequency, k is the Fourier index, and ω_z is the axial frequency. The exact rebinning algorithm yields the following relation between the 3-D Fourier transforms of oblique and direct sinograms[2,3].

$$P(\omega,k,\omega_z,\delta) = \exp(-i\Delta\phi)P(\omega\chi,k,\omega_z 0)$$

In this relation, $\Delta\phi$ is the phase shift: $\Delta\phi = k$ arctan α, and χ is the frequency scaling:

$$\chi = \sqrt{1+\alpha^2} .$$

For the fast implementation, an approximation can be derived by considering the first-order truncation Taylor expansions in α of the phase shift and of the frequency scaling factor.

$$P(\omega,k,\omega_z,\delta) \cong \exp(-i\frac{k\delta}{\omega}\omega_z)P(\omega,k,\omega_z,0) .$$

As the only dependence on the axial frequency ω_z is a linear phase shift, it is possible to calculate the inverse 1-D Fourier transform of $P(\omega, k, \omega_z, \delta)$, with respect to ω_z,

$$P(\omega,k,z,\delta) \cong P(\omega,k,z-\frac{k\delta}{\omega},0) .$$

This Fourier rebinning approximation relates the 2-D Fourier transform of an oblique sinogram (z, δ) to the 2-D Fourier transform of a slice shifted axially by a frequency-dependent offset $\Delta z = -k\delta/\omega$. The Fourier rebinning equation is regarded as the frequency-distance relation stating that the value of P at the frequency (ω, k) receives contributions mainly from sources located at a fixed distance $t = -k/\omega$ along the lines of integration. Note that t represents the signed distance measured on a transaxial projection of line response (LOR) from the midpoint f the LOR. The Fourier rebinning does not require execution of an axial Fourier transform with respect to z. This property considerably simplicity the implementation not only because of the small number of Fourier transforms, but more

importantly because the data need no longer be known for all values of z, and hence the truncated data need not be estimated[2].

After all projection data is rebinned to parallel slices on the frequency space, inverse 2-D Fourier transform is calculated to return sinogram $P_{2D}(s, \phi, z, 0)$. Finally, 2-D image reconstruction is performed.

Experimental

The 3-D PET data were obtained with the Shimadzu SET-2400W scanner, which has the axial view of 20cm and 32 slices, in CYRIC. Commonly, a lot of data collected with this PET system is sent to SX4/44R super computer in the computer center of Tohoku University. However, in this experiment, image reconstruction was performed using workstation TITAN2 in CYRIC for the purpose of estimating reconstruction time without super computer. Both the 3DRP and the FORE algorithms used in this experiment, were implemented in the Shimadzu SET-2400W. The time required for reconstruction in the FORE algorithm is found to be ten times less than that in 3DRP (Table 1).

Figure 2-1 shows two kinds of using phantoms. In the first experiment mainly designed to evaluate image quality, the activity injected in the phantom (a) was F-18 300μCi (1.0μCi/ml) and scan time was 15 minutes. In the second experiment for the quantification evaluation, the activity injected in the phantom (b) was 0.1μCi/ml in the part of A and was 0.0255μCi/ml in the part of B. Scan time was 20 minutes.

Result and Discussion

Evaluation for image quality

Figure 3 shows standard deviation for pixel value of the plane phantom in the region of interest (ROI) indicated in Fig. 2-2. The standard deviation is consistently higher in FORE than in 3DRP, but a large difference is not observed between FORE and 3DRP in the region of $\pm$ 20 slices from the center slice No.32 in the cylindrical scanner of SET-2400W. This region corresponds to about 60% of all slices. In contrast, the edge standard deviation in FORE suddenly raises out of this region. This may be caused by the following reason. This abrupt increase in the standard deviation in FORE can be ascribed to the reduction of rebinned data at a distant from the center of cylindrical scanner. The FORE can not be easily adopted to the region having small number of rebinned data, as a low activity is possibly buried in noise. On the other hand, noise in 3DRP doesn't increase significantly in the whole region, apart from the edge, due to data supplement.

Evaluation of Quantification

Figure 4 shows profile across center of the middle slice (Fig.2-2) in the non-uniform phantom. The pixel value in profiles based on the FORE and 3DRP algorithms changes

almost the same way along the x-axis except for the edge values. The FORE produces negative quantities at the edge free from activity, while such negative values does not generated by the 3DRP algorithm. The production of negative quantity for pixel values may be ascribed to an unexpected ill effect reconstruction filter when, in non-uniform axial distribution, a distant existence of strong activity is rebinned to pixels of low activity. This indicates the limit of the FORE algorithm from the standpoint of quantification.

References

1) Tanaka E., RADIOISOTOPES, **46** (1997) 33.
2) Kitamura K., Tanaka K., Satoh T. and Amano M., SHIMADZU REVIEW, **55** (1998) 199.
3) Michel Defrise., P. E. Kinahan et al., IEEE Trans. Med. Imag., **15** (1997) 145.

Table 1. Reconstruction time.

Algorithm	Reconstruction time
3DRP	4 hours
FORE	26 minutes

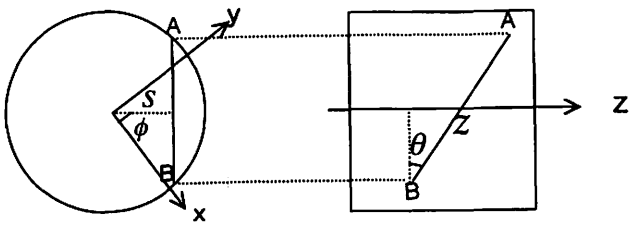

Fig. 1. Parameters.

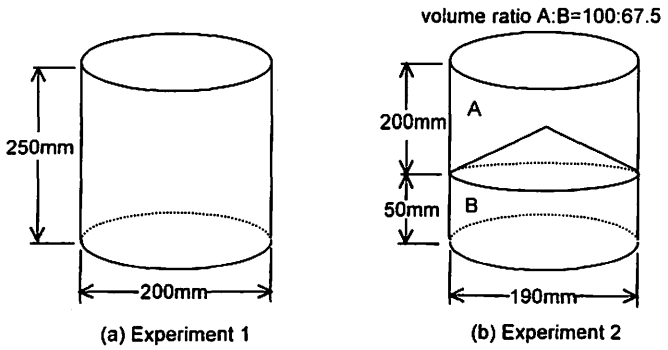

Fig. 2-1. Shape of phantom.

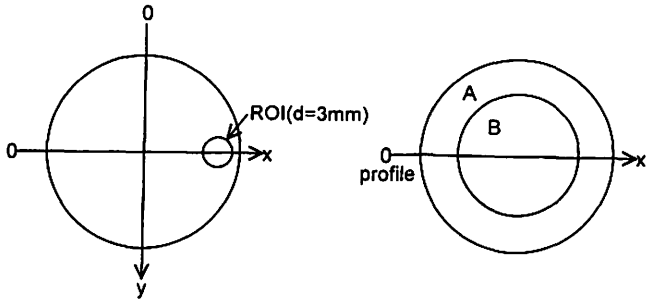

Fig. 2-2. ROI and profile axis.

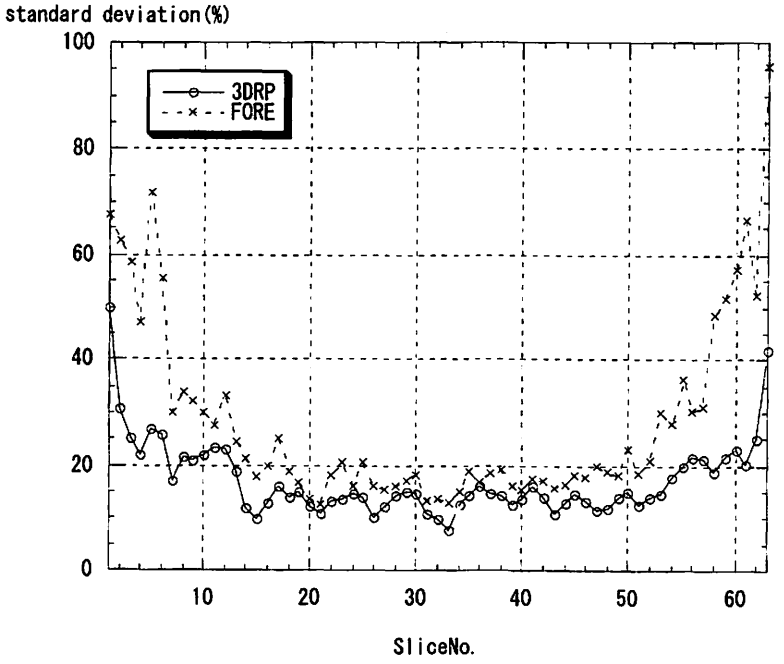

Fig. 3. Standard deviation in ROI.

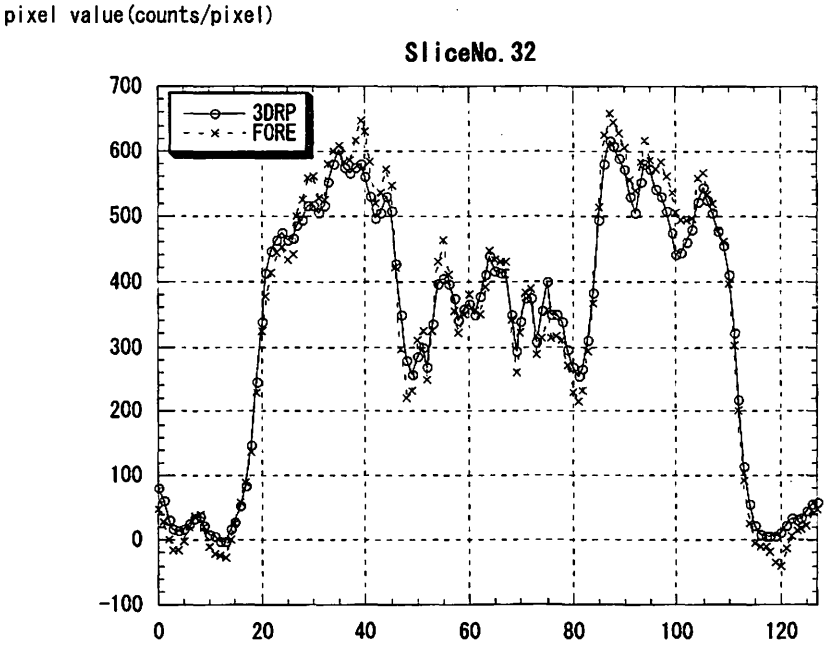

Fig. 4. Profile (Slice No. 32).

V. 6. Transmission scan conditions in Positron Emission Tomograph SET-2400W

Watanuki S., Ishii K., Miyake S., Itoh M., and Orihara H.

Cyclotron and Radioisotope center, Tohoku University

Introduction

Accurate attenuation correction is essential for the quantification in positron emission tomography (PET). Most of PET systems utilize the attenuation correction factors (ACFs) which are the ratios of transmission scan events and blank scan events measured with an external radioactive source. This method is a theoretically perfect to determine the ACFs, but the noise in the transmission data is inevitably propagated to PET image[1-3]. This noise propagation can be reduced by increasing the duration of transmission and blank scan and also by smoothing ACF data[3]. However, this increase in scan duration leads to a longer examination time and is less tolerable for patients especially in case of a whole body scan. Therefore, it is important to find appropriate scan duration for each study. In this work, we investigate relations between the image quality and transmission scan duration, and also data smoothing in PET system (SET-2400W Shimadzu Co., Japan).

Methods

Measurement in this study was performed with SET-2400W, which has 2D and 3D data acquisition capability. A blank scan was made with an external rotating line source with 275 MBq ^{68}Ge-^{68}Ga, and its duration was taken long enough so that the contribution of noise to ACFs is negligible. A cylindrical phantom was used for all the experiments. A phantom of 20cm bore and 25 cm long, was filled with water and placed at the center of FOV. Transmission data were acquired in 2D mode with the line source. The transmission scan duration varied from 2, 3, 5, 10, 20 to 30 minutes. For the emission scan, 18F-solution was injected into the phantom. The 2D mode dynamic emission scans were made in 12 frames, for 1 hour per each frame. The total counts were 2-120 M counts per frame. The 3D-mode emission scan was made to accumulate 120 M counts per frame.

A set of ACFs was obtained from blank data and six transmission data. This set of ACFs was smoothed either by a simple smoothing procedure with 8, 16 and 32 mm cutoff length filters or by a non-linear smoothing procedure[4] with 8 mm cutoff. These sets of ACFs were reconstructed as images of attenuation map of the phantom. The 2D mode

emission data of 120 M counts were corrected for attenuation by using each ACFs set and were reconstructed under the 8 mm cutoff smoothing filter. The 3D mode emission data were corrected by using the ACFs of 16mm cutoff and reconstructed under a 8mm cutoff filter.

The mean and standard deviation (SD) values were obtained by drawing a circular (10cm diameter) region of interest (ROI) at the center of phantom in all transmission and emission images. The mean values of ROI in transmission image were normalized to that of the transmission image obtained by the 30 minutes scan. In emission data, the mean values of ROI were normalized to that of the emission image corrected by the ACFs of 30 minutes transmission scan. The coefficients of variance (COV) was calculated by dividing the ROI SD by the ROI mean.

The effect of transmission duration on the COV in emission image depended on the total counts of emission data. Then, The 2D mode dynamic emission data were reconstructed with the set of the ACFs smoothed by 16mm cutoff and the COVs were obtained in order to examine this relation. The sets of COV values were normalized so that the COV with 30 minutes transmission is made to be 1.0 in each set.

Results

Figure 1 shows transmission images in scan duration and in smoothing types. Figure 2 shows the relationship between the COV and scan duration in each smoothing condition. The COV increases with decrease in scan duration and it was remarkable in the duration of less than 5 minutes. The smoothing reduces COV and it depends on the size of cutoff filter. The decreases in the COV correlated with the scan duration similarly. The decrease of COV was the factor of 0.53(0.21) in COV of cutoff of 16(32) for cutoff of 8, while the image of phantom surface blurs in dependence on cutoff length. The non-linear smoothing greatly reduces COV without blurring of the phantom edge. Figure 3 shows the relations between the ROI mean and the transmission scan duration in each cutoff, which related to each other. However the mean values in the scan duration of less than 3 minutes were slightly underestimated.

Figure 4 is 2D and 3D mode emission images of 120M total counts. Figure 5 shows relations between COV and transmission scan duration in each cutoff parameter. In the 2D mode emission image corrected with the ACFs simply smoothed, the increase in the scan duration and also the smoothing cutoff value reduces COV. But the dependence of COV on the scan duration is different from each other. The smaller the cutoff parameters become, the steeper the slope of COV in the scan duration becomes. In the 2D mode image corrected with the non-linear smoothing, owing to the high smoothing effect in ACFs, the value of COV does not depend on the scan duration. The COV of 3D mode image was lower than that of the 2D mode images, in spite of the use of same ACFs data and total emission counts for both mode. Figure 6 shows relations between ROI mean values of

emission image and transmission scan duration in each smoothing. The mean values in 2D mode emission image had a tendency to be underestimated in the transmission scan duration of less than 3 minutes. In the case of 3D mode, this tendency is remarkable, and the underestimation occurs at the scan duration of less than 5 minutes.

In Fig. 7, the reciprocals of COV for counts are shown as a function of transmission scan duration. The effect of increasing transmission duration is less, as total count of the emission data decreases.

Discussion

The transmission measurement should be done over 5 minutes in order to avoid a marked increase in the COV value of transmission images and 2D mode emission images(Figs. 2 and 5). The smoothing technique reduces well the COV value, but a blur in images is produced for the simple smoothing with 32mm cutoff as shown in Fig. 1. On the other hand, in the case of the non-linear smoothing, there is no increase of the COV value, and the blur is small (see Figs. 2,4 and 5). Our results suggested that the non-linear smoothing technique enables to do the transmission measurement within 5 minutes.

The effect of transmission duration for COV reduced with decrease in the total emission counts(Fig. 7). The total counts of head scan is usually 12M~15M counts for 10 minutes data acquisition, at 45 minutes of after the administration of 185MBq FDG. In this case, the COV value is not reduced below 20%, even if the transmission scan duration is taken long enough.

The 3D mode images show the COV values, which are smaller than those of the 2D images using 32 mm cutoff ACFs data. This result may be due to the low axial resolution, the difference of the reconstruction filter function of the 3D image and the procedure to get ACFs from those of 2D mode images.

The absorption coefficients are underestimated when the transmission scan duration becomes less than 3 minutes (Fig. 3). This lead about underestimation of the emission image values (Fig. 6). This underestimation originates from processing of the zero values in the transmission data. Since the zero values of ACF results a strong artifact in the emission image, they are usually replaced by an arbitrary value in order to avoid this artifact. If this value is lager than true values, the ACF will be underestimated. Since the underestimation of the oblique direction is added, this underestimation is enhanced in the 3D image. This will be a serious problem in the quantitative analysis of PET images.

In a whole body study, 10 minutes per 1 position will be practically the upper limit of the transmission scan duration. In consideration of the COV value, the lower limit will be 5 minutes when the smoothing of 16mm cutoff is used. The non-linear smoothing is expected to reduce shortest scan time less than 5 minutes. However, the measurement should be done over 5 minutes in 2D mode and 3 minutes in 3D mode, if the image quantity is

required (see Fig. 6).

References

1) Huang S. C., Hoffman E. J. et al., J. Comput Assist Tomo. **3** (1979) 804-814.
2) Dahlbom M., Hoffman E. J. et al., IEEE Trans. NS **34** (1987) 288-293.
3) Starns C. W., Wck D. C., IEEE Trans MI **12** (1993) 287-292.
4) Aurich V. et al., . Proceed 17, DAGM-Symposium, Bielefeld, Springer (1995)538-545.

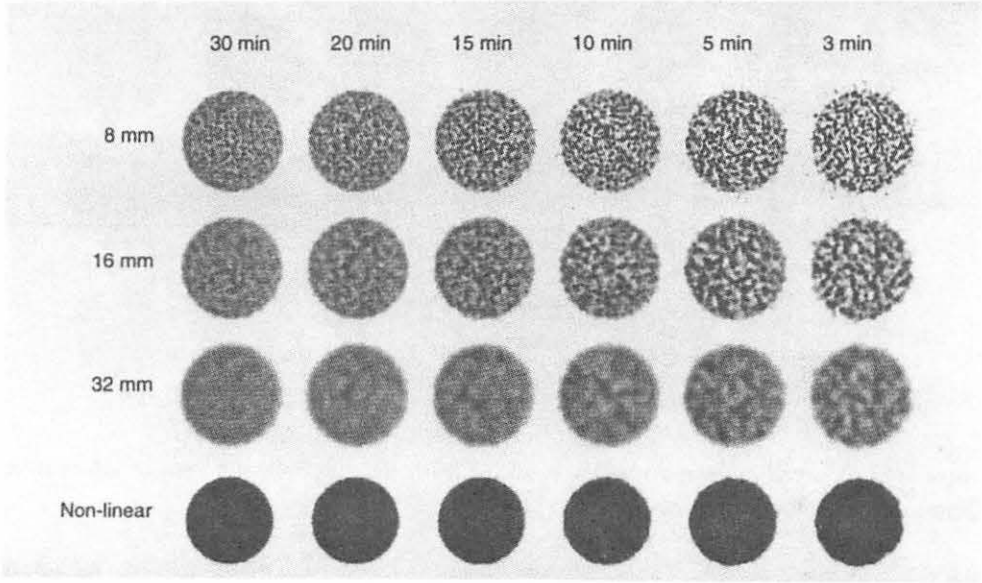

Fig. 1. Comparisons between transmission images of different scan duration, smoothing parameters and smoothing types.

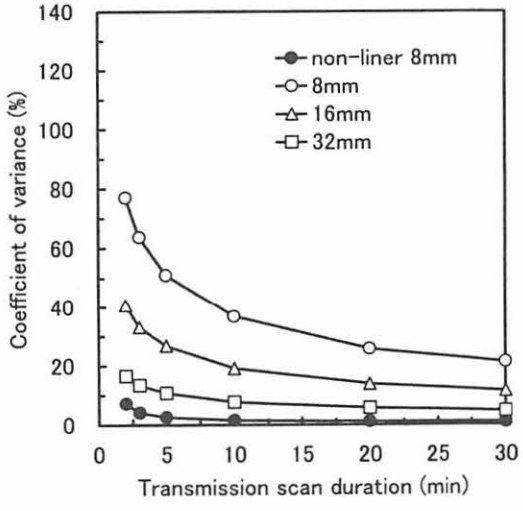

Fig. 2. COV value of transmission image as a function of scan duration for different smoothing parameters and a non-linear smoothing.

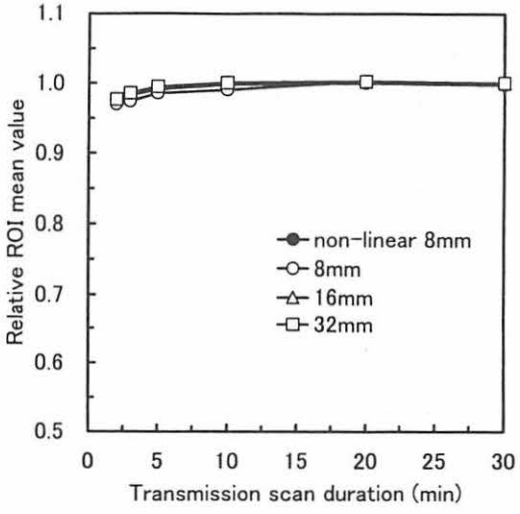

Fig. 3. ROI mean value of transmission image as a function of transmission scan duration for different smoothing parameters and the non-linear smoothing.

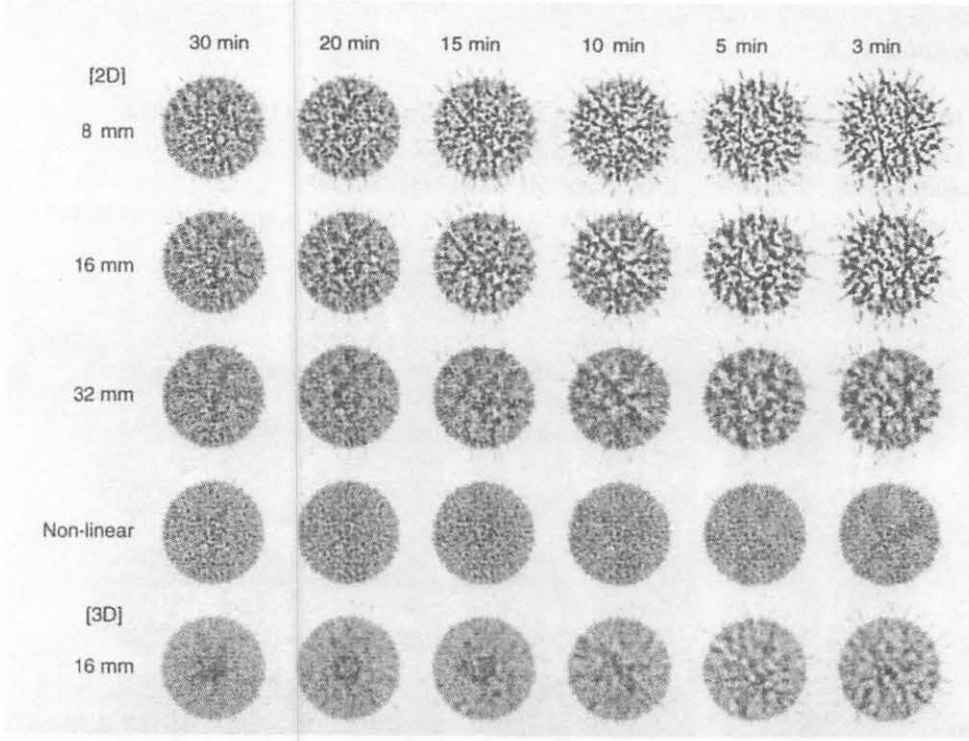

Fig. 4. Comparisons between emission images corrected with the transmission data of different duration, smoothing parameters and smoothing types.

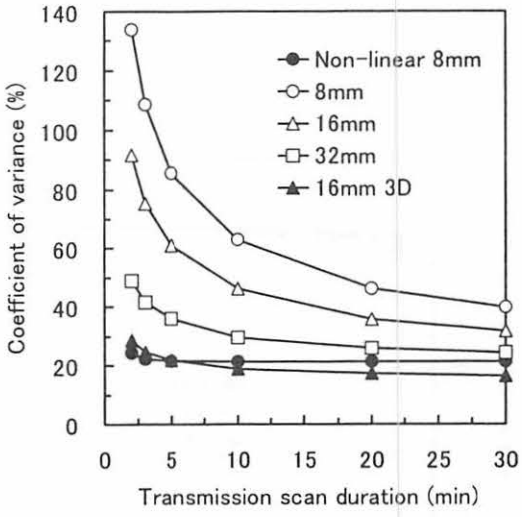

Fig. 5. COV value of emission image as a function of transmission scan duration for different smoothing parameters and a non-linear smoothing.

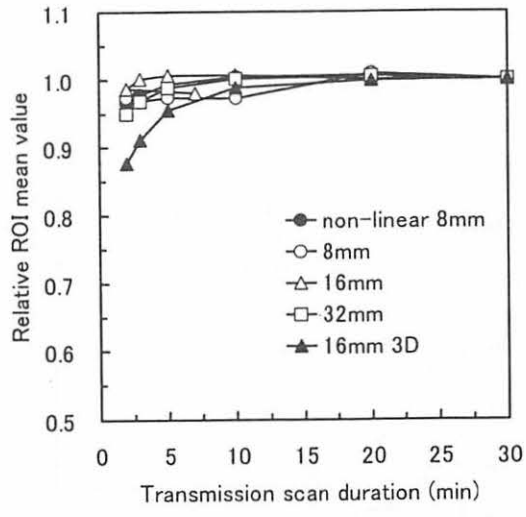

Fig. 6. ROI mean value of emission image as a function of transmission scan duration for different smoothing parameters and smoothing types.

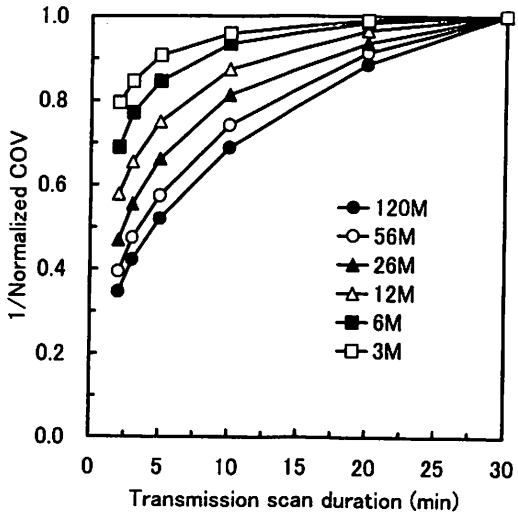

Fig. 7. Reciprocals of COV value as a function of transmission scan duration for different total counts of emission scan.

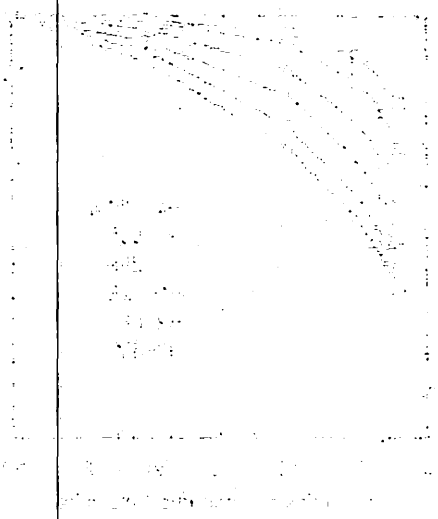

VI. RADIATION PROTECTION AND TRAINING OF SAFE HANDLING

VI. 1. Fast Neutron Profiling with Imaging Plate (3)

Yamazaki T., Sanami T., Baba M., Miura T., Hirasawa Y., Saito K., Hirakawa N. Yamadera A., Taniguchi S.*, and Nakamura T.**

Quantum Science and Energy Engineering, Tohoku University
*Cyclotron Radioisotope Center, Tohoku University**

Introduction

We have continued a study of fast neutron profile measurement using an imaging plate (IP) coupled with a polyethylene plate (IP-CH_2)[1,2] which will be useful for fast neutron radiography, non-destructive inspection of bulk objects, and medical applications. In this method, neutrons are converted to protons by a polyethylene converter and detected in IP, and the effects of γ-ray backgrounds can be eliminated by taking difference between the data with and without the converter. We have reported[1,2] that this device is useful to measure profiles of 5, 15 MeV neutrons, while not so sensitive to 1-2 MeV neutrons. Following the above studies, we extended the study to 1) an effective dynamic range of the sensitivity in a neutron field, 2) spatial resolution, and 3) applied the method to radiography of bulk media. Improvement of the sensitivity to lower energy neutrons was also attempted.

Experiments were carried out using a 4.5 MV Dynamitron accelerator at Fast Neutron Laboratory[3]. Figure 1 shows an experimental setup. Incident neutrons of 5 and 15 MeV were utilized for experiments. They were produced via the D(d,n) and T(d,n) reactions[3].

The IPs employed were X-ray type from Fuji Film Co. Ltd. (BAS-UR), 12.5 cm×12.5 cm. Polyethylene or polypropylene converters with appropriate thickness were placed in front of IP in a stepwise or flat shape. The flat converter was employed to correct for the effect of neutron flux non-uniformity on the converter. The IP was scanned to analyze a PSL (Photo Stimulated Luminescence) distribution using BAS-3000 system (Fuji Film Co. Ltd.) at CYRIC. Scanning was done about one hour after irradiation to reduce the effect of fading. Scanning parameters were the same for all the scanning, i.e., latitude 4, sensitivity 10000, and gradation 4096.

Dynamic Range

Dynamic range of IP is known to be larger than 10^4 for X-rays. In the case of neutron irradiation, however, much more γ-rays may be present in the field and reduce the

effective dynamic range for neutrons. We measured the dynamic range of IP-CH_2 for 5 MeV neutrons. The neutron (proton) fluence incident on IP-CH_2 was varied over a digit by 1) placing the IP in three different distances from the neutron target, 245 mm, 345 mm and 725 mm, and 2) employing converters with five steps between 60 μm and 300 μm thick (60 μm steps). The exposure time was about one hour with a 3.7 μA direct beam current.

Figure 2 shows the results for net PSL versus neutron fluence[3], where net PSL means PSL value subtracted with γ-ray backgrounds. In the figure, the linearity between PSL and fluence is confirmed from 10^7 to 10^9 neutron fluence. Consequently, the dynamic range is larger than 10^2 even in this neutron field. Furthermore, we can expect that the ultimate dynamic range is larger than 10^3 if we take account of the fact that the largest PSL in this measurements is only about one half of the allowable upper limit, 4096, and the detectable low limit is a few PSL[4].

Spatial Resolution

Spatial resolution which is of prime importance for a two dimensional detector is 50 μm for the present IP. In the case of neutron profiling, however, several factors degrade the spatial resolution, e.g., dispersion of recoil-angles and ranges. Therefore, we inspected the influences of these factors experimentally.

The spatial resolution was measured from the dispersion of PSL in a sharp cutoff of neutron beam provided by an iron shadow-bar (10 cm thick). The target-IP distance was extended to about 800 mm, and one half of the IP-CH_2 was irradiated by 5, 15 MeV neutrons with the other half being shadowed by the iron block. The converters for 15 MeV neutrons were 0.5 mm to 2.5 mm thick in 0.5 mm steps.

Table 1 summarizes the results. The spatial resolution is given in FWHM which was evaluated in the manner shown in Fig. 3. The spatial resol account. Among the factors for resolution degradation, the dispersion in recoil-angles will be dominant one because it introduces about 0.1 and 0.6 mm spatial spread for 5 and 15 MeV neutron, respectively. The result for 15 MeV neutrons is accounted for by the factor, but only about 10 % in the case of 5 MeV neutrons. Mis-alignment of neutron beam from the iron block edge will be the main reason of the discrepancy because the observed edge of the iron block deviated from the center of the beam. Consequently, the intrinsic resolution for 5 MeV neutrons will be much higher than observed. The spatial resolution was found not to be very sensitive to the converter thickness, while average ranges of recoil protons depend on the converter thickness.

Fast Neutron Radiography

The IP-CH_2 was applied to radiography for 5 and 15 MeV neutrons. Converter thicknesses were 0.5 mm and 2.5 mm for 5 and 15 MeV neutrons, respectively. Objects of

radiography were an iron block with voids (hidden holes) shown in Fig. 4 and cans filled with water partially.

Figure 5 shows the radiography image and the PSL distribution for the iron block by 5 MeV neutrons. The voids in the iron block is distinguished clearly, and the PSL distribution corresponds reasonably to the cylindrical shape of hole and voids. This fact suggests that smaller voids will also be detected by the present system. The result was also good for cans with water. Therefore, the IP-CH_2 method enables fast neutron radiography of thick metal and water which are too thick for the X-ray radiography.

The image contrast for 15 MeV neutrons were found to be generally lower than that for 5 MeV ones, probably because of too high penetrability of 15 MeV neutrons for the object thickness. Therefore, there should be optimum neutron energy corresponding to the macroscopic cross section and thickness of each object.

In some cases, PSL distribution deviates from the neutron transmission particularly in the edge region. It is attributed to the effects of scattered neutrons and charged-particles emitted from the objects. It is difficult to eliminate by the IP-CH_2 method unless the energy and species of particles are known. To solve the problem, we are developing a neutron counter which is position sensitive in two-dimensions and sensitive to the energy deposited in the counter.

Improvement for 1 MeV Neutron Detection

The low sensitivity of the IP-CH_2 to 1-2 MeV neutrons is attributed to short ranges of recoil protons and proton attenuation in the protection layer on the IP surface made of PET (Polyethylene Terephtalete). Improvement of the sensitivity was attempted by employing a BAS-TR film which has no protection layer. A BAS-TR film coupled with converters of 4 μm to 20 μm in 4 μm steps was irradiated by 1 MeV neutrons via the T(p,n) reaction. A signal-to-noise ratio (S/N) was improved about three times by using BAS-TR. Nevertheless, absolute PSL value was still too small to obtain clear images with practical irradiation time (a few hours).

References

1) Sanami T., Baba M., Saito K., Ibara Y., Hirakawa N., Yamadera A., Taniguchi S., and Nakamura T., Proc. of 11th Workshop on Radiation Detectors and Their Uses (1997 KEK, Japan) p.74.
2) Sanami T., Saito K., Yamazaki T., Baba M., Ibara Y., Sato J., Hirakawa N., Yamadera. A., Taniguchi S., and Nakamura T., CYRIC ANNUAL REPORT 1998, (1998) p.138.
3) Baba M., Takada M., Iwasaki T., Matsuyama S., Nakamura T., Ohguchi H., Nakao N., Sanami T., and Hirakawa N., Nucl. Instrum. Methods. **A376** (1996) 115.
4) Nohtomi A., Terunuma T., Kono R., Takada Y., Hayakawa Y., Maruhashi A., Proc. 1998 Spring Meeting of Japan Atomic Energy Society **C25** (March 1998) p.115.

Table 1. Relation of converter thickness and spatial resolution (FWHM).

En = 5MeV

Converter Thickness (μm)	60	120	180	240	300
Resolution (mm)	1.42	1.32	1.25	0.99	0.87

En = 15MeV

Converter Thickness (mm)	0.5	1.0	1.5	2.0	2.5
Resolution (mm)	(0.67)	0.79	0.90	0.90	0.68

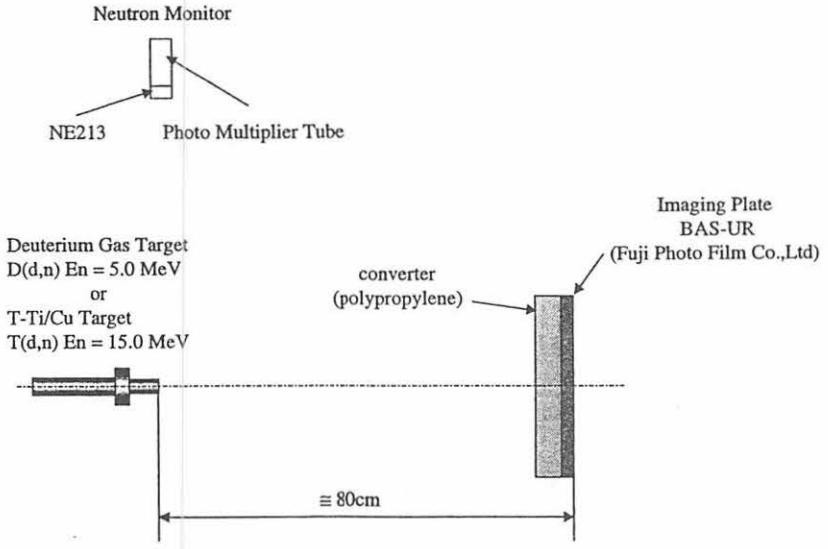

Fig. 1. Experimental setup in the present experiment.

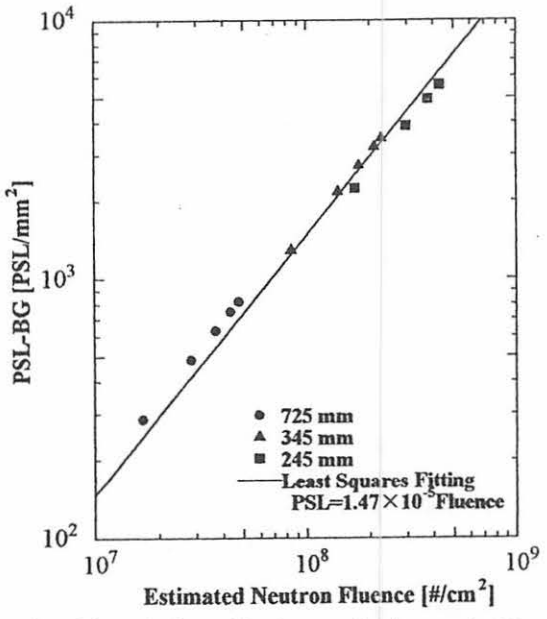

Fig. 2. The relation of background-subtracted PSL versus neutron fluence.

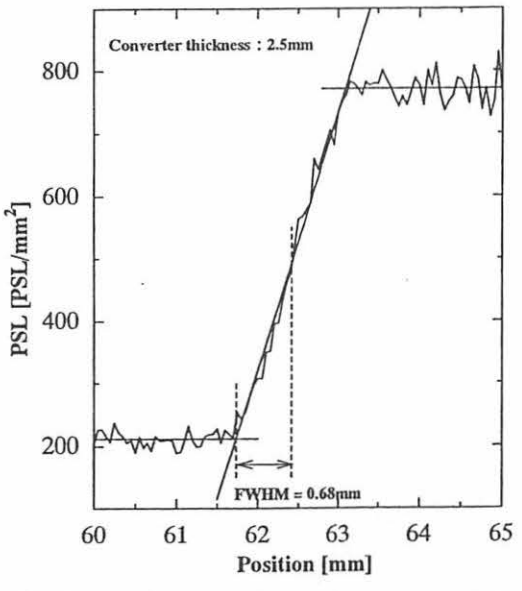

Fig. 3. Evaluation scheme of spatial resolution: The low value in the left corresponds to PSL for shadowed region and the higher values in the right to un-shadowed region.

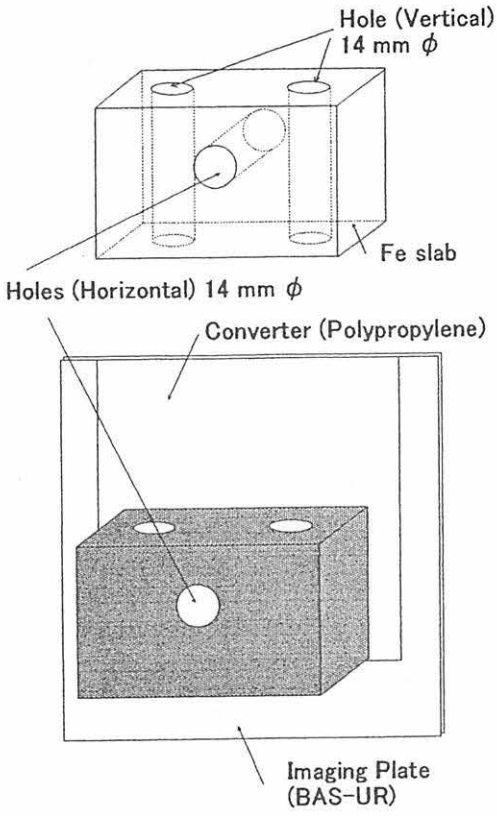

Fig. 4. Schematic view of iron block object and the setup of the IP-CH_2 for neutron radiography.
A neutron beam is incident perpendicularly to the block from the front side of the block.

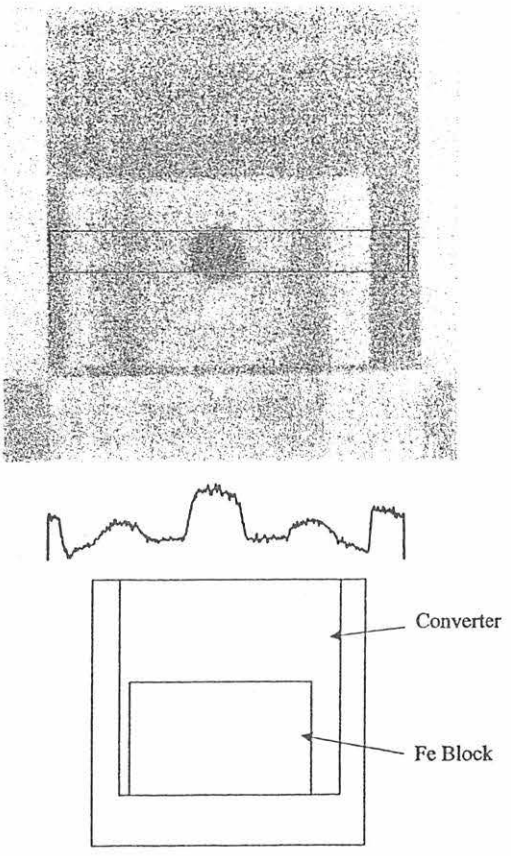

Fig. 5. Radiography image (upper) and PSL distribution (middle) for iron block in fig.4.
The PSL distribution shows values in the area surrounded by lines in the image figure.

VI. 2. The Functional Equation for the Fading Correction of Imaging Plate

*Ohuchi H., Yamadera A. * and Nakamura T. **

Graduate School of Pharmaceutical Sciences, Tohoku University
Cyclotron and Radioisotope center, Tohoku University

Several experiments were performed in order to investigate the effect of the temperature on the fading for commercial imaging plate, IP (BAS-UR). The fading characteristics were measured under the temperature control between 0°C - 60°C after irradiation with ^{238}U alpha-ray and ^{60}Co gamma-ray sources. Applying the Arrhenius' equation to the experimental results, we could find out a universal functional equation which includes two variables of the elapsed time(t) and the temperature(K). The PSL values calculated by this equation showed good agreement with the experimental ones between 0°C - 40°C. From this equation, the activation energies of the fading curve are estimated to be about 0.9eV for both ^{238}U alpha-ray and ^{60}Co gamma-ray sources.

Introduction

The imaging plate (IP) made of $BaFBr:Eu^{2+}$ phosphor is a two-dimensional detector which has the wide dynamic range (more than 10^5), the sensitivity of more than 100 times higher than that of the X-ray film and the high spatial resolution[1-3]. These properties made it possible to apply as an integral type detector, such as radiation monitoring during a certain period. For this purpose, however, the IP has a defect of the large fading effect which brings about a serious hindrance for quantitative measurements[4].

Several reports on the measurements of the fading effect have been published, expressing the fading effect as the following equation which is the sum of a couple of exponentially-decaying components [5-7].

$$(PSL)_t / (PSL)_0 = A_1 \cdot \exp(-\ln 2 / T_1 \cdot t) + A_2 \cdot \exp(-\ln 2 / T_2 \cdot t) + A_3 \cdot \exp(-\ln 2 / T_3 \cdot t), \quad (1)$$

where $(PSL)_t$ and $(PSL)_0$ mean the PSL values of the elapsed time t and 0 after irradiation, respectively, A_1 to A_3 are the component amplitudes and T_1 to T_3 are the half-lives of each component.

The formulas shown in Refs. 5-7 give quite different A_1 to A_3 and T_1 to T_3 values.

Here in this study, we aimed to find out a new universal formula for the fading correction by irradiating the IP with ^{238}U alpha-ray and ^{60}Co gamma-ray sources.

Experimental

The IP used in our experiments is the commercial IP BAS-UR (Fuji Film Co.). A ^{238}U planchet source (specific radioactivity of 10.8Bq/cm^2) was used as an alpha-ray source and a ^{60}Co point source (10.8mGy/h at 1m, on Nov. 1st, 1998) was used as a gamma-ray source. The IP held in the aluminium IP cassette was set inside an incubator in which the temperature was maintained constant within ± 1°C. The fading characteristics were measured with varying the temperature at every 10 °C between 0 °C and 60 °C.

Experimental Results

Measurement of the Fading Characteristics

In order to investigate the effect of the temperature on the fading effect, several fading curves were obtained in the temperature range of 0 °C -60 °C for ^{238}U alpha rays and 0°C -50 °C for ^{60}Co gamma rays. Figs. 1 and 2 show the temperature dependence of the fading of the latent image after irradiation with ^{238}U and ^{60}Co sources, respectively. These results imply us that the fading curves may be divided into three components, hereafter called the first, the second and the third one in order of half-life, which can be expressed in Eq.(1).

Functional Fading Equation

As in this study, at some time elapsed after the irradiation until the first component fades out,the fading equation should be written as

$$(PSL)_t / (PSL)_0 = A\cdot\exp(-\lambda_a\cdot t) + B\cdot\exp(-\lambda_b\cdot t), \qquad (2)$$

where $\lambda = \ln 2/T_{1/2}$ and $T_{1/2}$ is the half-life.

Now paying attention to the strong temperature dependence of the fading effect shown in Figs. 1 and 2, the fading effect is considered to be a kind of a thermal reaction, and the change of reaction rate with the temperature can be expressed by the Arrhenius' equation.

The Arrhenius' equation is well known to be defined by the following relation

$$d\ln\lambda / dK = E/(RK^2), \qquad (3)$$

where λ is the rate constant, E the activation energy, R gas constant, and K the absolute temperature.

Integrating this equation, we obtain

$$\lambda = C\exp\{-E/(RK)\}. \qquad (4)$$

By putting J = E/R, Eq.(2) is expressed as

$$(PSL)_{t,k} / (PSL)_{0,k} = A\cdot\exp\{-a\cdot t\cdot\exp(-J_a/K)\}+B\cdot\exp\{-b\cdot t\cdot\exp(-J_b/K)\}. \qquad (5)$$

Combining Eqs. (2) and (5) , we obtain

$$a = 0.693/\{T^{a}_{1/2} \cdot \exp(-J_a/K)\} \quad (6)$$

$$b = 0.693/\{T^{b}_{1/2} \cdot \exp(-J_b/K)\} \quad (7)$$

Assuming that both A and B in Eq.(5) are independent on the temperature, that is, the ratio of the second to the third component does not depend on the temperature, J_a, J_b, a and b can be obtained from the half-lives of two different fading curves.

Analysis of the Fading Characteristics

In order to get the values of half-lives of the fading curves at each temperature, we analyzed the fading curves in Figs. 1 and 2 as shown in Fig. 3;

1. We choose a certain PSL value(A) on the fading curve at 40 °C as a reference curve which typically consists of the second and the third components in Eq.(1). We then select the value at the elapsed time e = 46 hours after irradiation as a reference point.
2. We find out an elapsed time (d) at which the same PSL value is given on the different fading curve as on the reference curve (in Fig. 3, the fading curve at 50 °C is shown as an example).
3. We obtain the ratio of e to d, r = e/d.

By multiplying the elapsed time by the r values, we can normalize the PSL values of different fading curves to those of the reference curve at 40 °C, in order to get the universal fading curve.

Figs. 4 and 5 show the thus-obtained universal fading curves of the latent images for ^{238}U alpha rays and ^{60}Co gamma rays, respectively. It is clearly shown that all the fading curves converge on a single universal curve for both cases, except at 50 °C for ^{60}Co gamma rays.

This result means that the ratio of the second component to the third one inEq.(2) is almost independent on the temperature, which verified that our preceding assumption that A and B in Eq.(2) is independent on the temperature.

Table 1. shows the r values and half-lives (hours) $T^{a}_{1/2}$, $T^{b}_{1/2}$ of the second and the third components of Eq.(5) at each temperature for ^{238}U and ^{60}Co sources, where the half-lives are obtained by multiplying the half-lives at 40 °C by the r values. The r values for both sources are almost the same.

Fading Correction Equation

Using four values of half-lives at 20 °C, at which the fading effect becomes remarkable, and at 60 °C for ^{238}U alpha-ray source shown in Table 1, J_a, J_b, a and b values in Eqs.(6) and (7) were calculated. In order to obtain the B value in Eq.(5), the intersection point of the extrapolated line of the third component of a universal fading curve in Fig. 4 was read out and the B value of 0.513 was thus-obtained.

Eq.(5) could finally be written as

$$(PSL)_{t,k}/(PSL)_{0,k} = 0.487\exp\{-2.18\times10^{14}\cdot t\cdot\exp(-1.11\times10^{4}/K)\} + 0.513\exp\{-3.18\times10^{13}\cdot t\cdot\exp(-1.11\times10^{4}/K)\} \quad (8)$$

The PSL values calculated from Eq.(8) are compared with the experimental results in Fig. 6. Both are in quite good agreement in the temperature range of 0 °C -40 °C.

In the same way, J_a, J_b, a and b values in Eqs.(6) and (7) for ^{60}Co gamma-ray source were calculated with four values of half-lives at 20 °C and 50 °C shown in Table1. The B value in Eq.(5) was obtained from a universal fading curve in Fig. 5.

Eq.(5) could also be written as

$$(PSL)_{t,k}/(PSL)_{0,k} = 0.439\exp\{-7.73\times10^{13}\cdot t\cdot\exp(-1.08\times10^{4}/K)\}\} + 0.561\exp\{-9.99\times10^{12}\cdot t\cdot\exp(-1.08\times10^{4}/K)\} \quad (9)$$

The comparison between calculated PSL values from Eq.(9) and the experimental results is shown in Fig. 7. Quite good agreement of both values in the range of 0 °C -40 °C is also found.

Activation Energy

The activation energies were obtained from Eqs.(6) and (7). The results are E≒ 0.96eV and 0.93eV for both second and third components for ^{238}U alpha rays and ^{60}Co gamma rays, respectively.

Conclusion

In this study, we investigated the temperature dependence of the fading effect for commercial IP (BAS-UR). Applying the Arrhenius' equation to the experimental results, we could first find out a new functional equation which includes two variables of the elapsed time(t) and the temperature(K). The PSL values calculated by this equation gave quite good agreement with the experimental ones between 0 °C - 40 °C. This equation makes possible to correct the PSL values measured at different elapsed time after irradiation at different temperature, so that it may be used for a long-term fading correction in applying the IP as an integral type detector.

From this equation, the activation energies of the second and the third components of the fading curve are estimated to be about 0.9eV for both ^{238}U alpha-ray and ^{60}Co gamma-ray sources. This result indicates that there might be an another lower energy level to induce the fading besides the PSL process and it may be a clue to the fading mechanism.

References

1) Sonoda M. et al., Radiology **148** (1983) 833-838.
2) Amemiya Y. et al. Science **237** (1987) 164-168.
3) Amemiya Y.and Miyahara J., Nature **336** (1988) 89-90.
4) Bücherl T., Rausch C. and von Seggern H., Nucl. Instrum. & Methods, **A333** (1993) 502-506.
5) Mori C. and Matsumura A., Nucl. Instrum. & Methods, **A312** (1992) 39-42.
6) Yamadera A. et al., RADIOISOTOPES, **42** (1993) 676-682.
7) Oikawa T., Taniyama A. and Shindo D., Ionizing Radiat., **23** (1997) 97-102.

Table 1. The r values and half-lives (hours) $T^{a}_{1/2}$, $T^{b}_{1/2}$ of the second and the third components of Eq. (5) at each temperature for ^{238}U and ^{60}Co sources are shown. The half-lives are obtained by multplying the half-lives at 40 °C by the r values, which are almost the same for both sources.

<U-238>

temperature (℃)	0	10	20	30	40	50	60
r value	0.01	0.03	0.1	0.318	1	2.72	9.46
$T^{a}_{1/2}$: the second component(h)	910	303	91	28.6	9.1	3.3	0.96
$T^{b}_{1/2}$: the third component(h)	6,130	2,043	613	193	61.3	22.5	6.48

<Co-60>

temperature (℃)	0	10	20	30	40	50
r value	0.01	0.03	0.11	0.36	1	3.3
$T^{a}_{1/2}$: the second component(h)	900	300	82	25	9.0	2.7
$T^{b}_{1/2}$: the third component(h)	6,000	2,000	545	167	60	18.2

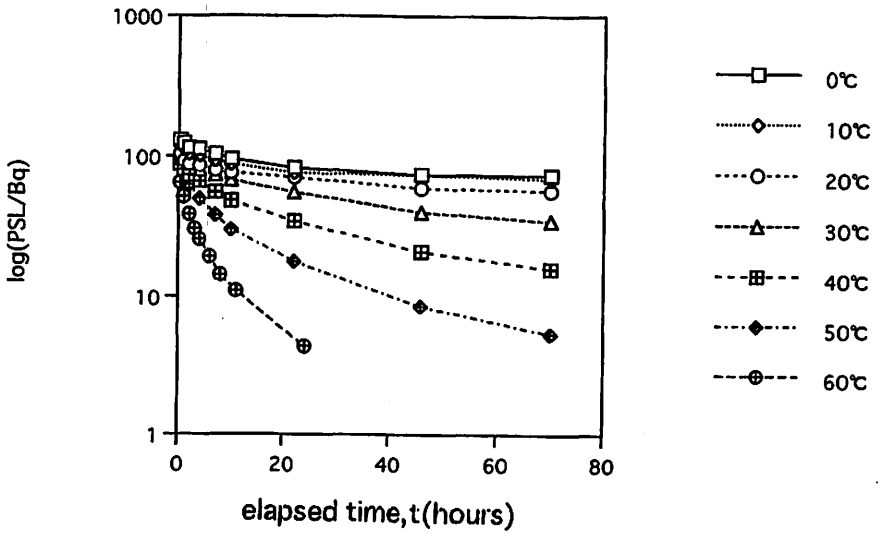

Fig. 1. Temperature dependence of the fading effect of the latent image after the irradiation with ^{238}U alpha-ray source, varying the temperature at every 10 °C between 0 °C - 60 °C. The fading effect becomes stronger as the temperature increases.

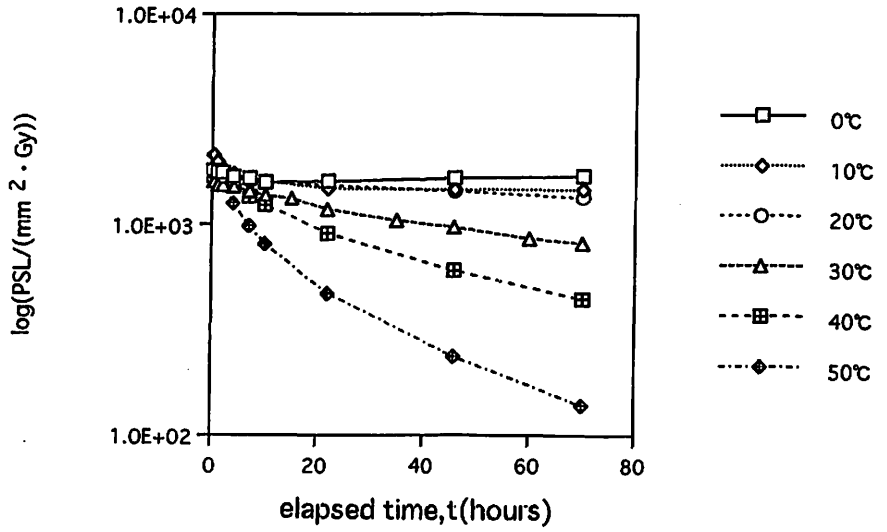

Fig. 2. Temperature dependence of the fading effect of the latent image after the irradiation with ^{60}Co gamma-ray source, varying the temperature at every 10 °C between 0 °C - 50 °C. The same tendency as Fig. 1 is observed.

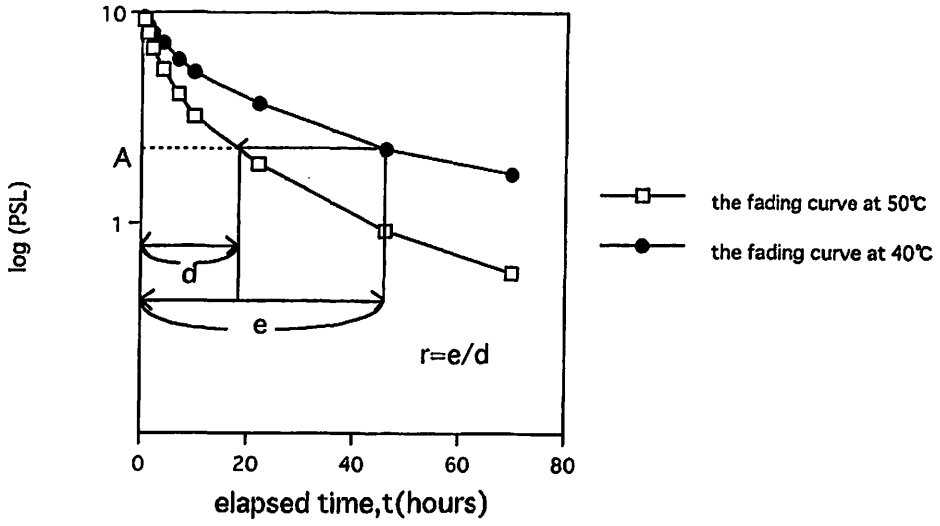

Fig. 3. Illustration explained a method of data analysis. The fading curve at 40 °C as a reference curve is shown by ● mark and the one at 50 °C as an example is shown by □ mark. The r value is obtained as the ratio of e to d, r=e/d.

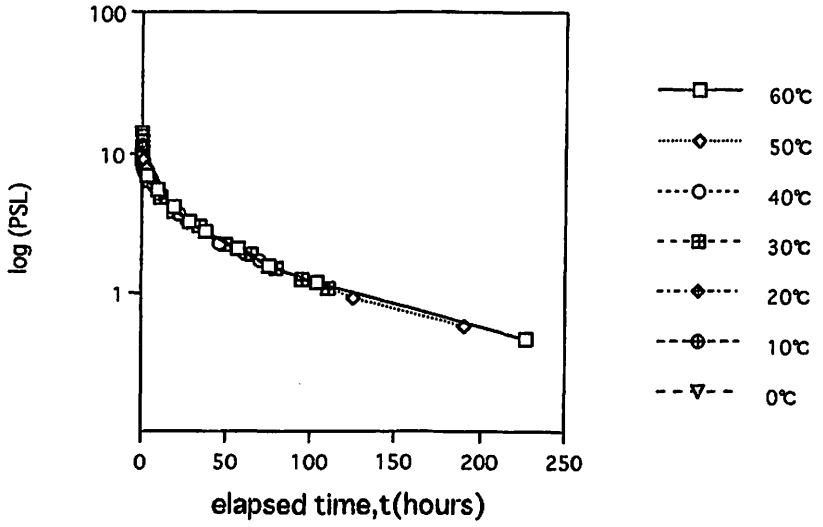

Fig. 4. Universal fading curve of the latent image for ^{238}U alpha rays. All the fading curves converge on a single universal curve.

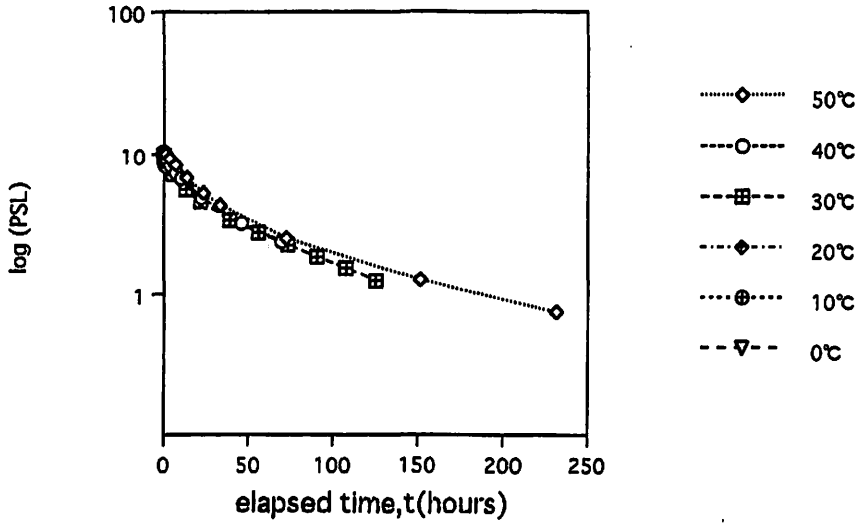

Fig. 5. Universal fading curve of the latent image for ^{60}Co gamma rays. All the fading curves converge on a single universal curve except at 50 °C.

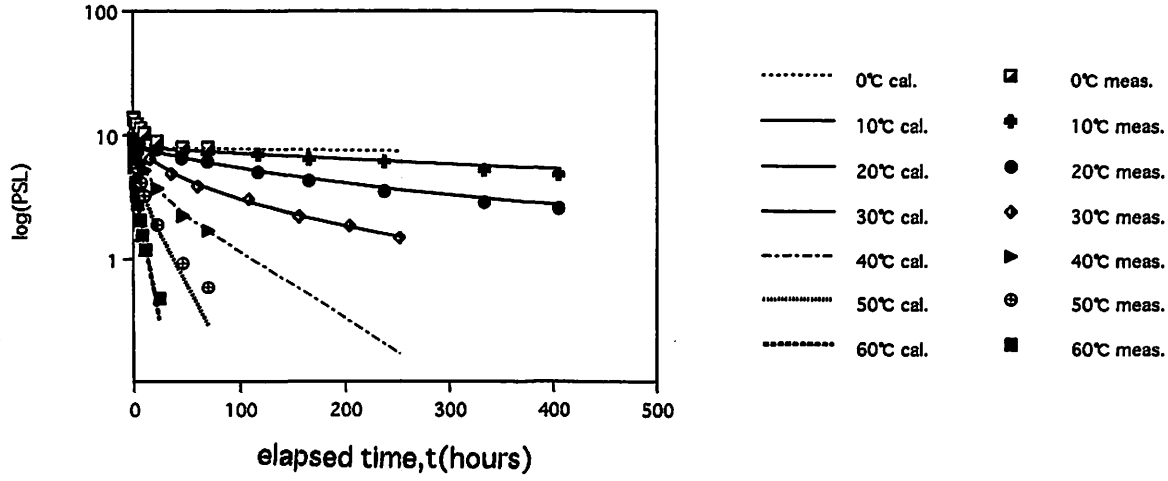

Fig. 6. Comparison of the PSL values for ^{238}U alpha rays calculated from Eq.(8) and the experimental results. The former are shown by each dotted line and the latter are shown by each mark at different temperature. Both are in quite good agreement in the temperature range of 0 °C -40 °C.

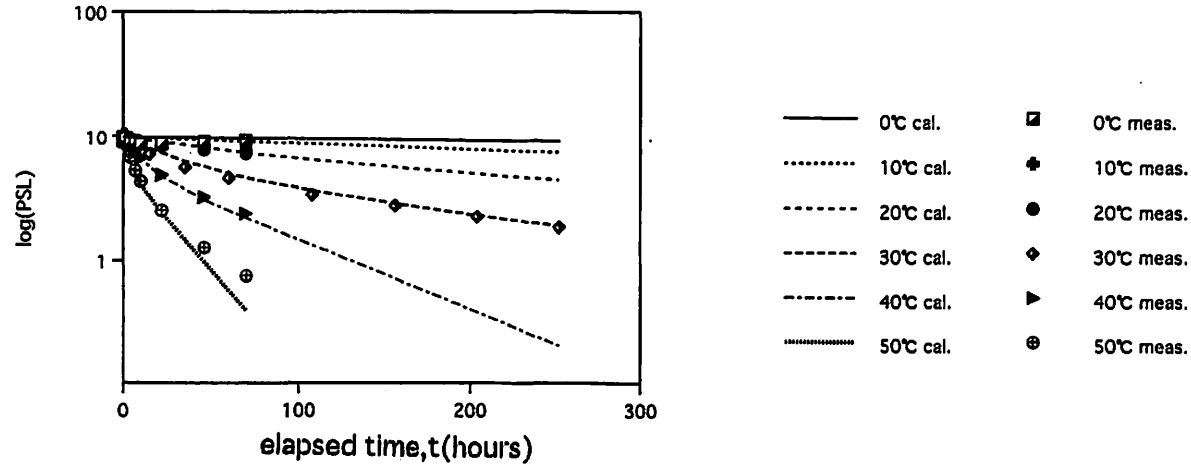

Fig. 7. Comparison of the PSL values for ^{60}Co gamma rays calculated from Eq.(9) and the experimental results. The former are shown by each dotted line and the latter are shown by each mark at different temperature. Both are in quite good agreement in the temperature range of 0 °C-40 °C.

VI. 3. Training for Safehandling of Radiation and Radioisotopes and X-Ray Machines for Beginners in Tohoku University

Nakamura T., Yamadera A. and Miyata T.

Cyclotron and Radioisotope Center, Tohoku University

Training for safehandling of radiation and radioisotopes for beginners has been conducted twice a year from 1977 in Tohoku University. The contents of lectures and practices are shown in Table 1. In 1998 the training was performed for 499 persons. The departments to which they belong are given in Table 2.

Training for safehandling of X-ray machines and electron microscopes began from the end of 1983. The training is scheduled to be held twice a year at the same time as the safehandling of radiation and radioisotopes. Only lectures are given and not practices. The contents of the lectures and the distributions of trainees are shown in Tables 3 and 4, respectively.

Training for safehandling of synchrotron radiation began from the end of 1995. The contents of the lectures are the same as safehandling of radiation and radioisotopes for beginners and not practices. In 1998 the training was performed for 76 persons.

Table 1. Contents of lectures and practices for safehandling of radiation and radioisotopes in 1998.

Lectures (one day)	
Radiation physics and measurements	1.5 (hours)
Chemistry of radioisotopes	1.0
Radiological protection ordinance	1.5
Effects of radiation on man	1.0
Safehandling of radioisotopes	1.5

Practices (one day)	
Treatment of unsealed adioactive solution	4.0 (hours)
Measurements of surface contamination and decontaminatio	1.0
Measurements of gamma rays and beta rays	2.0

Table 2. Distribution of trainees for safehandling of radiation and radioisotopes in 1998.

Department	Staff	Student	Total
Medicine	12	100	112
Dentistry	0	16	16
Pharmacy	5	42	47
Science	4	82	86
Engineering	3	66	69
Agriculture	1	90	91
Research Institutes	4	59	63
The others	0	15	15
Total	29	470	499

Table 3. Contents of lectures for safehandling of X-ray machines and electron microscopes in 1998.

Safehandling of X-ray machines	1.5 (hours)
Radiological protection ordinance	1.0
VTR for safehandling of radiation and radioisotopes	1.0

Table 4. Distribution of trainees for safehandling of X-ray machines and electron microscopes in 1998.

Department	Staff	Student	Total
Science	1	19	20
Engineering	3	99	102
Research Institutes	8	109	117
Total	12	227	239

Table 5. Distribution of trainees for synchrotron radiation in 1998.

Department	Staff	Student	Total
Science	0	12	12
Engineering	1	28	29
Research Institutes	6	29	35
Total	7	69	76

VI. 4. Radiation Protection and Management

*Miyata T., Yamadera A., Nakamura T. and Watanabe N.**

Cyclotron and Radioisotope Center, Tohoku University
*Japan Radiation Protection Co., Ltd.**

(1) Unsealed radionuclides used in the center

The kinds and activities of unsealed radionuclides handled in the center in 1998 are shown in Table 1. The table includes the isotopes produced by the cyclotron, purchased from the Japan Isotope Association and took over from another RI institutes.

(2) Individual monitoring

The exposure doses of the workers in the center in 1998 is given in Table 2. They were less than the permissible doses.

(3) Monitoring of the workplace

Radiation dose rates inside and outside of the controlled areas were monitored periodically and as needed. They were below the legal permissible levels. Surface contamination levels of the floors inside the controlled areas were measured by smear method and with survey meters periodically and as needed. They also cleared under the legal regulation levels.

(4) Wastes management

The radioactive wastes delivered to the Japan Radioisotope Association in 1998 are shown in Table 3. The concentration of radioisotopes in the air released after filtration from the stack was monitored with stack gas monitors. The levels were less than the legal regulation levels. The radioactive water was storaged at the tanks at least for 3 days and then released to the sewerage after confirming that the concentration was less than permissible levels.

The treated volume of radioactive waste of organic scintillator was 694 l by the incinerator made by Fujikogyo Co., Ltd.

Table 1. Unsealed radionuclides used in the center in 1998.

(a) Cyclotron	Building (kBq)	(b) RI Building (kBq)			
group 3		group 1		group 4	
^{11}C	239,501,000.000	^{90}Sr	1,440.000	^{3}H	64,048.352
^{13}N	7,030,000.000			^{14}C	829,917.480
^{15}O	555,000.000	total	1,440.000	^{18}F	151,626,000.000
^{111}In	1,630,760.000	group 2		^{201}Ti	5,550.000
		^{60}Co	4,597.030	total	152,525,515.832
		^{137}Cs	19,676.400		
		^{65}Zn	7,718.000		
total	248,716,760.000	^{68}Ge	73,115.000		
group 4		^{22}Na	370.000		
^{18}F	979,182,800.000	^{125}I	399,996.797		
total	979,182,800.000	total	505,473.227		
(c)Research	Building (kBq)	group3			
group3		^{131}I	94,002.600		
^{15}O	24,790,000.000	^{32}P	1,331,286.501		
		^{35}S	145,782.346		
		^{99m}Tc	37,000.000		
total	24,790,000.000				
group 4		total	1,608,071.447		
^{18}F	1,998,000.000				
total	1,998,000.000				

Table 2. Occupational radiation exposures at the center in 1998.

Dose range (mSv)	Number ofindividuals
No measurable exposure	41
Measurable exposure less than 1.0	6
1.0 to 3.1	3
Total persons monitored	50

Table 3. Radioactive wastes delivered to the Japan Radioisotope Association in 1998.

Wastes	Container	Number
solids		
Combustible Type I	50 ℓ drum	24
Combustible Type I	50 ℓ drum	18
Incombustibles	50 ℓ drum	5
Annimal carcasses	50 ℓ drum	17
Filters	1 ℓ /unit	454
liquids		
inorganic liquids	25 ℓ PE bottle	13

Type I: Cloth and Paper made of natural cellulose.
Type II: Combustible Plastics such as Polyethylene and Polypropylene.

VII. PUBLICATION

VII. PUBLICATIONS

(January 1998 ~ December 1998)

A

1. Isospin Mixing in the Isobaric Analog State Derived from the (p,$n_{IAS}p$) Reaction on ^{140}Ce, ^{172,174,176}Yb, and ^{208}Pb
   H. Orihara, C. C. Yun, A. Terakawa, K. Itoh, A. Yamamoto, K. Kawami. H. Suzuki, Y. Mizuno, H. Kamurai, Y. Tajima, K. Ishii, Y. Fujii, H. Sagawa, T. Suzuki, and H. Ohnuma
   Physical Review Letters vol.81, Number 17, (1998) 3607-3610

2. Estimation of absorbed dose for 2-[F-18]fluoro-2-deoxy-D-glucose using whole-body positron emission tomography and magnetic resonance imaging
   Hossain M. Deloa, Takehiko Fujiwara, Miho Shidahara, Takashi Nakamura, Hiroshi Watabe, Yuichiro Narita, Masatoshi Itoh, Masayasu Miyake, Shoichi Watanuki
   European Journal of Nuclear Medicine, Vol. 25, No., pp. 565-574, (1998)

3. Estimation of internal absorbed dose of L-[methyl-^{11}C]methionine using whole-body positron emission tomography
   Hossain M. Deloar, Takehiko Fujiwara, Takashi Nakamura, Masatoshi Itoh, Daisuke Imai, Masayasu Miyake, Shoichi Watanuki
   European Journal of Nuclear Medicine, Vol. 25, No. 6, pp 629-633, (1998)

4. Simulation study of a Hydrostat Design for Detecting Underground Leakage of Water Supply using Neutron Backscattering
   TADAHIRO KUROSAWA, TAKASHI NAKAMURA, TAKASHI SUZUKI, YASUHIRO OKANO and HARUO CHISAKA
   Appl. Radiat. Inst. Vol. 49, No. 12, 1729-1735, (1998)

5. Measurement of radiation tracks for particle and energy identification by using imaging plate
   Shingo Taniguchi, Akira Yamadera, Takashi Nakamura, Akifumi Fukumura
   Nucl. Instr. and Methods in Physics Research A, Vol. 413, pp. 119-126, (1998)

6. Development and characterization of real-time personal neutron dosemeter with silicon detectors
   M. Sasaki, T. Nakamura, N. Tsujiimura, O. Ueda, T. Suzuki
   Nucl. Instr. and Methods in Physics Research A418, 465-475(1998)

7. Estimation of organ cumulates activities and absorbed doses on intakes of several ^{11}C labelled radiopharmaceuticals from external measurement with thermoluminescent dosimeters
   Takashi Nakamura, Yoshiharu Hayashi, Hiroshi Watabe, Masaki Matsumoto, Tohru Horikawa, Takehiko Fujiwara, Masatoshi Ito and Kazuhiko Yanai
   Phys. Med. Biol. 43, 389-405 (1998)

8. Measurements of Neutron Spoliation Cross Sections of ^{12}C and ^{209}Bi in the 20-to 150-MeV Energy Range
   E. Kim, T, Nakamura, and A. Konno, Y. Uwamino and N. Nakanishi, M. Imamura,

N. Nakao, and S. Shiibata, and S. Tanaka
NUCLEAR SCIENCE AND ENGINEERING 129, 209-223(1998)

B

9. Measurements of the total reaction cross section using the sum-of-differences method
T. Yamaya, H. Ishiyama, A. Yamazaki, J. Tojima, M. Katoh, T. Kuzumaki
H. Yahata, K. Suzuki, K. Kotajima, T. Shinozuka, M. Fujioka
Physics Letters B417, 7-12 (1998)

10. Insertion of Xe and Kr Atoms into C_{60} and C_{70} Fullerenes and the Formation of Dimers
Tsutomu Ohtsuki, Yutakaa Maruuyama, Kazuyoshi Masumoto
Physical Review Letters vol. 81, NUMBER 5 967-970(1998)

11. Most probable charge of fission products in 24MeV proton induced fission of ^{238}U
H. Kudo, M. Maruyama, and M. Tanikawa, T. Shinozuka and M. Fujioka
PHYSICAL REVIEW C 57, 1788-1888 (1998)

12. Helium implantation effect on mechanical properties of SiCf/SiC composites
A. Hasegawa, M. Saito, K. Abe, R. H. Jones
Journal of nuclear Materials, Vol. 253, pp. 31-35, (1998)

13. Cerebral blood flow correlated with carotid blood flow in neurologically normal elderly with severe white matter lesions
Kenichi Meguro, Jun Hatazawa, Masatoshi Itoh, Hidemitsu Miyazawa,
Taiju Matsuzawa and Atsushi Yamadori
European Journal of Neurology, Vol. 5, No. 2, pp. 143-149, (1998)

14. Lesion-to-Background Ratio in Nonattenuation-Corrected whole-Body FDG Pet Images
Muhammad Babar Imran, Kazuo Kubota, Susumu Yamada, Hiroshi Fukuda,
Kenji Yamada, Takehiko Fujiwara and Masatoshi Itoh
The Joural of Nuclear Medicine , Vol. 39, No. 7, pp. 1219-1223

15. Participation of the prefrontal cortices in prospective memory: evidence from a PET study in humans
Jiro Okuda, Toshiikatsu Fujii, Atsushi Yamadori, Ryuta Kawashima,
Takashi Tsukiura, Reiko Fukatsu, Kyoko Suzuki, Masatoshi Ito, Hiroshi Fukuda
Neuroscience Letters 253 127-130 (1998)

16. 20-31. PET Study of Pointing With Visual Feedback of Moving Hands
KENTARO INOUE, RYUTA KAWASHIMA, KAZUNORI SATOH,
SHIGEO KINOMURA, RYOI GOTO, MASAMICHI KOYAMA,
MOTOAKI SUGIURA, MASATOSHI ITO, HIROSHI FUKUDA
J.Neurophysiol 79, 117-125 (1998)

17. Heterogeneous fatty acid uptake early after reperfusion in rat hearts
YURIKO YAMAME, NOBUMASA ISHIDE, YUTAKA KAGAYA,
DAIYA TAKEYAMA, NOBUYUKI SHIBA, MASANOBU CHIDA
TETSUJI NOZAKI, TOSHIHITO TAKAHASHI, TATSUO IDO,
AND KUNIO SHIRATO
Am. J. Physiol. , Vol. 274, (Hear Circ. Physiol. 43), pp. H923-H929, (1998)

18. The role of the left inferior temporal cortex for visual pattern a PET study
Ryuta Kawashima, Kazunori Satoh, Ryoi Goto, Kentaro Inoue, Masatoshi Itoh and Hiroshi Fukuda

Neuroreport, Vol. 9, No. 7, pp. 1581-1586, (1998)

19. Pet study of striatal fluorodopa uptake and dopamine D_2 receptor binding in a patient with juvenile parkinsonism
H. Tanji, H. Nagasawa, T. Araki, J. Onodera, S. Tkase, M. Itoh and Y. Itoyama
European Journal of Neurology, Vol. 5, No. 3, pp. 243-248, (1998)

VIII. MEMBERS OF COMMITTEE

VIII. Members of Committees (as of Jan. 1, 1999)

General

(Chairman)	Hikonojo	Orihara	(CYRIC)
	Osamu	Hashimoto	(Graduate School of Science)
	Hiroshi	Kudo	(Graduate School of Science)
	Kohshi	Yoshimoto	(Graduate School, Division of Medicine)
	Tadashi	Yamada	(Faculty of Dentistry)
	Tetsuya	Terasaki	(Faculty of Pharmaceutical Sciences)
	Katsunori	Abe	(Graduate School of Engineering)
	Masahiro	Hata	(Faculty of Agriculture)
	Reimon	Hanada	(Institute for Materials Research)
	Minoru	Issiki	(Institute for Advanced Materials Processing)
	Hiroshi	Fukuda	(Institute for Development, Aging and Cancer)
	Jirohta	Kasagi	(Laboratory of Nucler Science)
	Syogo	Yamada	(University Hospital)
	Manabu	Fujioka	(CYRIC)
	Tatsuo	Ido	(CYRIC)
	Takashi	Nakamura	(CYRIC)
	Masatoshi	Itoh	(CYRIC)
	Ren	Iwata	(CYRIC)
	Akira	Yamadera	(CYRIC)
	Keizo	Ishii	(Graduate School of Engineering)
	Tadao	Saitou	(Faculty of Agriculture)
	Sadaei	Yamaguchi	(Institute for Materials Research)
	Michiharu	Katoh	(Institute for Chemical Reaction Science)

Research Program

(Chairman)	Takashi	Nakamura	(CYRIC)
	Takemi	Nakagawa	(Graduate School of Science)
	Tsutomu	Sekine	(Graduate School of Science)
	Takehiko	Watanabe	(Graduate School, Division of Medicine)
	Kohshi	Yoshimoto	(Graduate School, Division of Medicine)
	Hidetada	Sasaki	(Graduate School, Division of Medicine)
	Katsunori	Abe	(Graduate School of Engineering)

	Reimon	Hanada	(Institute for Materials Research)
	Hiroshi	Fukuda	(Institute for Development, Aging and Cancer)
	Manabu	Fujioka	(CYRIC)
	Tatsuo	Ido	(CYRIC)
	Keizo	Ishii	(Graduate School of Engineering)
	Masatoshi	Itoh	(CYRIC)

Cyclotron

(Chairman)	Manabu	Fujioka	(CYRIC)
	Osamu	Hashimoto	(Graduate School of Science)
	Takemi	Nakagawa	(Graduate School of Science)
	Toshio	Kobayashi	(Graduate School of Science)
	Satoru	Kunii	(Graduate School of Science)
	Tsutomu	Sekine	(Graduate School of Science)
	Kazushige	Maeda	(Graduate School of Science)
	Ken	Abe	(Graduate School of Engineering)
	Keizo	Ishii	(Graduate School of Engineering)
	Akira	Hasegawa	(Graduate School of Engineering)
	Reimon	Hanada	(Institute for Materials Research)
	Minoru	Issiki	(Institute for Advanced Materials Processing)
	Tatsuo	Ido	(CYRIC)
	Takashi	Nakamura	(CYRIC)
	Masatoshi	Itoh	(CYRIC)
	Ren	Iwata	(CYRIC)
	Tsutomu	Shinozuka	(CYRIC)
	Astuki	Terakawa	(CYRIC)

Radiation Protection and Training of Safe Handling

(Chairman)	Tadashi	Yamada	(Faculty of Dentistry)
	Yoshiaki	Fujii	(Graduate School of Science)
	Hiroshi	Kudo	(Graduate School of Science)
	Yoshio	Hosoi	(Graduate School, Division of Medicine)
	Yoshihiro	Takai	(University Hospital)
	Kazuo	Ouchi	(Faculty of Pharmaceutical Sciences)
	Naohiro	Hirakawa	(Graduate School of Engineering)
	Toshiyasu	Yamaguchi	(Faculty of Agriculture)
	Masayuki	Hasegawa	(Institute for Materials Research)
	Hiroshi	Fukuda	(Institute for Development, Aging and Cancer)

	Manabu	Fujioka	(CYRIC)
	Takashi	Nakamura	(CYRIC)
	Akira	Yamadera	(CYRIC)
	Akira	Nagamuma	(Faculty of Pharmaceutical Sciences)

Life Science

(Chairman)	Tatsuo	Ido	(CYRIC)
	Kazuo	Yamamoto	(Graduate School of Science)
	Yasuhito	Itoyama	(Graduate School, Division of Medicine)
	Kazuie	Iinuma	(Graduate School, Division of Medicine)
	Syogo	Yamada	(Graduate School, Division of Medicine)
	Reizo	Shirane	(Graduate School, Division of Medicine)
	Masahiko	Yamamoto	(Graduate School, Division of Medicine)
	Michinao	Mizugaki	(University Hospital)
	Makoto	Watanabe	(Faculty of Dentistry)
	Kazuo	Ouchi	(Faculty of Pharmaceutical Sciences)
	Keizo	Ishii	(Graduate School of Engineering)
	Satoshi	Yokota	(Faculty of Agriculture)
	Hiroshi	Fukuda	(Institute for Development, Aging and Cancer)
	Kazuo	Kubota	(Institute for Development, Aging and Cancer)
	Shin	Maruoka	(College of Medical Sciences)
	Manabu	Fujioka	(CYRIC)
	Takashi	Nakamura	(CYRIC)
	Masatoshi	Itoh	(CYRIC)
	Kei-ichiro	Yamaguchi	(CYRIC)
	Yoshihito	Funaki	(CYRIC)

Prevention of Radiation Hazards

(Chairman)	Takashi	Nakamura	(CYRIC)
	Takemi	Nakagawa	(Graduate School of Science)
	Tsutomu	Sekine	(Graduate School of Science)
	Ken	Abe	(Graduate School of Engineering)
	Manabu	Fujioka	(CYRIC)
	Tatsuo	Ido	(CYRIC)
	Akira	Yamadera	(CYRIC)
	Iwao	Suzuki	(CYRIC)
	Takamoto	Miyata	(CYRIC)

IX. PERSONNEL

IX. Personnel (as of Jan. 1, 1999)

Director Hikonojo Orihara

Division of Accelerator

Manabu	Fujioka
Osamu	Hashimoto[1)]
Tsutomu	Shinozuka
Minoru	Tanigaki
Masahiro	Fujita
Shizuo	Kan[6)]
Shizuo	Chiba[6)]

Division of Instrumentations

Hikonojo	Orihara
Keizo	Ishii[2)]
Astuki	Terakawa
Toshiyuki	Misu
Sho-ichi	Watanuki
Tsutomu	Ichikawa

Division of Radiopharmaceutical Chemistry

Tatsuo	Ido
Ren	Iwata
Yoshihito	Funaki
Hiroaki	Wada
Akari	Kagaya
Hideo	Takahashi
Yo-ichi	Ishikawa[7)]

Division of Cyclotron Nuclear Medicine

Masatoshi	Itoh
Kei-ichiro	Ymaguchi
Kazuhiko	Yanai[4)]
Kaoru	Ozaki
Hiroto	Nishiura
Masayasu	Miyake

Division of Radiation Protection and Safety Control

Takashi	Nakamura
Akira	Yamadera
Takamoto	Miyata
Noboru	Watanabe[7)]

Graduate Student and Researcher

Yasumori	Kanai	(Graduate School, Division of Science)
Tsuyoshi	Hoshino	(Graduate School, Division of Science)
Takero	Baba	(Graduate School, Division of Science)
Tetu	Sonoda	(Graduate School, Division of Science)
Asaki	Yamamoto	(Graduate School, Division of Science)
Hiroshi	Suzuki	(Graduate School, Division of Science)
Gen	Kamurai	(Graduate School, Division of Science)
Hideyuki	Mizuno	(Graduate School, Division of Science)
Yasuo	Saito	(Graduate School, Division of Science)
Yu-ji	Kikuchi	(Graduate School, Division of Science)
Takehiko	Sizuki	(Graduate School, Division of Science)
Shinji	Nagata	(Faculty of Pharmaceutical Sciences)
Takehisa	Kawata	(Faculty of Pharmaceutical Sciences)
Yoshitaka	shimizu	(Faculty of Pharmaceutical Sciences)
Syozou	Furumoto	(Faculty of Pharmaceutical Sciences)
Ryo	Kosaka	(Faculty of Pharmaceutical Sciences)
Kenntaro	Wakayama	(Faculty of Pharmaceutical Sciences)
Manabu	Tashiro	(Graduate School, Division of Medicine)
Md. MEHEDI MASUD		(Graduate School, Division of Medicine)
Eun Ju Kim		(Graduate School, Division of Engineering)
Tadahiro	Kurosawa	(Graduate School, Division of Engineering)
Shingo	Taniguchi	(Graduate School, Division of Engineering)
Osamu	Satoh	(Graduate School, Division of Engineering)
Yoshihiro	Nakane	(Graduate School, Division of Engineering)
Akifumi	Fukumura	(Graduate School, Division of Engineering)
Michiya	Sasaki	(Graduate School, Division of Engineering)
Miho	Shidahara	(Graduate School, Division of Engineering)
Sayaka	Satoh	(Graduate School, Division of Engineering)
Tomoya	Munomiya	(Graduate School, Division of Engineering)
Hiroshi	Iwase	(Graduate School, Division of Engineering)
Tomoyuki	Shiomi	(Graduate School, Division of Engineering)
Yoshifumi	Azeyanagi	(Graduate School, Division of Engineering)

Syunji	Takagi	(Researcher)

Office Staff

Iwao	Suzuki
Hiroshi	Syoji
Hashime	Wako
Kyoko	Fujisawa
Seiji	Kikkukawa
Keietsu	Aizawa
Fumiko	Mayama
Mitsuko	Endo
Yu-ko	Yamashita
Yuri	Okumura
Noriko	Suzuki
Hitomi	Inoue
Toshiyuki	Watanabe[7)]

1) Graduate School of Science
2) Graduate School of Engineering
3) Institute for Materials Research
4) Graduate School, Division of Medicine
5) Institute for Development, Aging and Cancer
6) SUMI-JU Accelerator Service Ltd.
7) Japan Radiation Protection Co., Ltd.